AGH

AGH UNIVERSITY OF SCIENCE AND TECHNOLOGY

FIELD OF SCIENCE: Natural Sciences

SCIENTIFIC DISCIPLINE: Physical Sciences

DOCTORAL THESIS

Characterization of novel semiconductor structures for tracking detectors in high-energy physics experiments using the TCT method

Author: Fasih Zareef

Supervisor: dr hab. inż. Agnieszka Obłąkowska-Mucha - prof. AGH

Completed in: AGH University of Krakow

Faculty of Physics and Applied Computer Science

Department of Particle Interactions and Detection Techniques

Kraków 2026

Declaration of the author of this dissertation

Aware of legal responsibility for making untrue statements, I hereby declare that I have written this dissertation myself and that all the contents of the dissertation have been obtained by legal means.

signature date

Declaration of the thesis Supervisors

This dissertation is ready to be reviewed.

Signature of thesis Supervisor date

Contents

List of Abbreviations

AC-LGAD	Alternating Current Capacitively Coupled Low Gain Avalanche Detector
APD	Avalanche PhotoDetector
ATLAS	A Toroidal LHC Apparatus
BNL	Brookhaven National Laboratory
CB	Conduction Band
CC	Collected Charge
CCE	Charge Collection Efficiency
CFD	Constant Fraction Discriminator
CMS	Compact Muon Solenoid
CNM	Centro Nacional de Microelectrónica
CV	Capacitance vs reverse bias Voltage
DJ-LGAD	Deep Junction Low Gain Avalanche Detector
DRIE	Deep Reactive Ion Etching
DUT	Device Under Test
EIC	Electron Ion Collider
ELI	Extreme Light Infrastructure
ETL	Endcap Timing Layer
FCC	Future Circular Collider
FF	Fill Factor
FWHM	FullWidth at HalfMaximum
GL	Gain Layer
HEP	High Energy Physics
HGTD	High Granularity Timing Detector
HL-LHC	High Luminosity Large Hadron Collider

HPK	Hamamatsu Photonics K.K.
IDUB	Excellence Initiative - Research University
iLGAD	inverse Low Gain Avalanche Detector
IR-LIT	Infrared Lock-In Thermography
IPD	Inter Pad Distance
IR	InfraRed
IV	Current Intensity vs reverse bias Voltage
JTE	Junction Termination Extension
LGAD	Low Gain Avalanche Detector
LHC	Large Hadron Collider
MII	Mean Ion Integral
mip	minimum ionizing particle
NCN	National Science Center
NIEL	Non-Ionizing Energy Loss
OPA	Optical Parametric Amplifier
PIN	P-type – intrinsic silicon – N-type detector
R&D	Research and Development
SEM	Scanning Electron Microscopy
SIMS	Secondary Ion Mass Spectroscopy
SNR	Signal to Noise Ratio
SPA	Single Photon Absorption
TCAD	Technology Computer Aided Design
TCT	Transient Current Technique
TI-LGAD	Trench Isolated Low Gain Avalanche Detector
ToA	Time of Arrival
TPA	Two Photon Absorption
UV	Ultra Violet
VB	Valence Band
VELO	VErtex LOcator

Acknowledgements

I am deeply thankful to my supervisor, Agnieszka Obłąkowska-Mucha, for her immense support, which began even before I arrived in Krakow and continued until this very day as I dust my hands off this PhD. She always went the extra mile to accommodate and support me. Her guidance, patience, expertise, and, most importantly, her trust gave me the confidence to overcome all the challenges I faced during my PhD journey.

I am sincerely grateful to my mentor, Tomasz Szumlak, who has always been there to support me, boost my confidence, and trust me with my ideas. I am immensely thankful to this remarkable problem-solver. Despite the demands of serving as Head of the Department, you always created an environment in which we felt welcomed and supported.

I extend my regards to one-of-a-kind Neil "the" Moffat. He turned my PhD upside down—or rather, downside up. Without him, it might have been a disaster. Thank you for bumping into me!

I am thankful to all collaboration members, in no particular order: Richard Bates, Dima Maneuski, Mark Williams, Marco Gersabeck, Alexander Oh, Oscar Francisco, Parisa, Enoch, Ben, and the rest, for their valuable discussions and suggestions.

A special thanks to the fellows at the University of Glasgow and the Centro Nacional de Microelectrónica (CNM), Barcelona, for hosting me and supporting my research activities.

I am grateful to Piotr Wiacek, Przemek, and Andrzej for their constant support with wire-bonding and other engineering work.

To the most beloved person who genuinely cared for me during my hardest times and supported me in every aspect of life, my wife, Saliha, this would not have been possible without you. You helped me through the most difficult days and were always there to take responsibilities off my shoulders when I was overwhelmed. This journey felt easier because you were by my side.

To my parents, siblings, and family members, whose continued support and prayers gave me the strength to achieve my goals—your confidence in me kept me going, even thousands of miles away, while feeling close to you in every moment.

I thank all my friends for believing in me and for the emotional support they provided during difficult times, my colleagues for the useful discussions over coffee, and everyone who has been directly or indirectly involved in this work.

A special thanks to the Excellence Initiative – Research University AGH IDUB 6275, the Polish National Science Center under agreement numbers NCN 2023/49/N/ST2/02314 and UMO-2023/51/B/ST2/02313, for supporting my research and travel expenses.

Finally, I dedicate this thesis to my beloved father, **Haji Zareef Ahmed**, who never skipped a day without asking about my work and praying for my success. He was always eager to see me become a doctor and was proud of even my smallest achievements. He passed away a few months before the submission of this thesis. I hope he is witnessing this moment and is proud of me.

Streszczenie

Krzemowe detektory od kilku już dekad stanowią kluczowy element infrastruktury badawczej w fizyce wysokich energii i w zastosowaniach medycznych. Precyzyjne pomiary torów cząstek z użyciem detektorów śladowych oraz czasu życia hadronów wymagają znakomitej zdolności rozdzielczej zarówno przestrzennej, jak i czasowej. Nowa generacja eksperymentów, a w szczególności modernizacja Wielkiego Zderzacza Hadronów (High-Lumi LHC) oraz eksperymenty na akceleratorze Elektronowo-Jonowym (EIC), stawiają rygorystyczne wymagania wobec technologii detekcyjnych. Obejmują one osiągnięcie rozdzielczości czasowej poniżej 50 ps, wysokiej rozdzielczości przestrzennej oraz wysokiej odporności na uszkodzenia radiacyjne — przy jednoczesnej integracji tych parametrów w ramach stosunkowo łatwo dostępnej technologii.

Przedmiotem niniejszej pracy jest rozwój oraz kompleksowa charakteryzacja detektorów lawinowych o niskim wzmocnieniu (Low-Gain Avalanche Detectors, LGAD), przeznaczonych do pracy w środowiskach radiacyjnych o wysokich fluencjach. Ze względu na globalny charakter prowadzonych badań, działania realizowano w ścisłej współpracy z międzynarodowymi ośrodkami naukowymi oraz wyspecjalizowanymi fabrykami półprzewodników, co umożliwiło wspólne projektowanie, wytwarzanie i testowanie opracowywanych struktur detekcyjnych.

W pracy przeprowadzono systematyczne badania odporności radiacyjnej oraz parametrów czasowych detektorów LGAD o różnej grubości i odmiennych strukturach. Szczególną uwagę poświęcono zagadnieniu zwiększenia gradualności oraz maksymalizacji współczynnika wypełnienia w pikselowych detektorach, co stanowi jedno z kluczowych wyzwań współczesnej mikroelektroniki detekcyjnej. W tym kontekście opracowano oraz poddano analizie detektory Trench-Isolated LGAD, stanowiące strategię segmentacji kompatybilną z architekturami odczytowymi Timepix oraz Medipix. Optymalizacja współczynnika wypełnienia została przeanalizowana zarówno dla cząstek o wysokiej, jak i niskiej zdolności penetracji, z uwzględnieniem niejednorodności pola elektrycznego, efektywności multiplikacji ładunku oraz skuteczności separacji pola między pikselami.

W perspektywie przyszłych infrastruktur badawczych, takich jak Future Circular Collider (FCC), w których przewidywane poziomy fluencji przekroczą wartości charakterystyczne dla HL-LHC, szczególnego znaczenia nabierają detektory 3D, uznawane za technologię o podwyższonej odporności radiacyjnej. W niniejszej pracy dokonano oceny ich właściwości czasowych w kontekście zastosowań do rozróżnienia czasu, w którym cząstki docierają do sensorów, wykorzystując dwustronny proces technologiczny oraz analizując różnorodne geometrie pikseli.

Całość przeprowadzonych badań obejmuje projektowanie i symulacje numeryczne struktur półprzewodnikowych, ich wytwarzanie w różnych wariantach technologicznych, a także szczegółową charakteryzację elektryczną, jak również odpowiedź na wzbudzenie laserem. Opracowane konfiguracje detektorów zostały zoptymalizowane pod kątem specyficznych zastosowań zarówno w fizyce wysokich, jak i niskich energii, stanowiąc wkład w rozwój nowej generacji szybkich i odpornych radiacyjnie systemów detekcyjnych.

Abstract

Silicon radiation detectors have a wide range of applications in high-energy physics and synchrotron science, where accurate spatial and temporal measurements must be made under extreme radiation environments. The next generation of collider experiments, including the High-Luminosity Large Hadron Collider (HL-LHC) and the Electron–Ion Collider (EIC), demands detector technologies capable of delivering < 50 picosecond timing resolution, high spatial granularity, and long-term radiation tolerance within a single integrated platform.

This thesis focuses on the development of low-gain avalanche detectors (LGADs) for implementation in such environments. Since these efforts are being pursued worldwide, we extended our collaboration with various institutes and semiconductor foundries to contribute collectively to the development and characterization of suitable detectors. The radiation hardness and timing performance of the LGADs with varied detector thicknesses and detector design is investigated. A major contribution of this work addresses the challenge of achieving high granularity and enhanced fill factor in pixelated timing detectors. In this context, trench-isolated LGADs (Ti-LGADs) are developed and studied as a segmentation strategy compatible with TimePix and MediPix readout architectures. The optimization of fill factor for both high- and low-penetrating particles is investigated, balancing electric field uniformity, charge multiplication efficiency, and inter-pixel isolation.

Looking toward future facilities such as the Future Circular Collider (FCC), where radiation levels will exceed those of the HL-LHC, the 3D detectors proved to be a sustainable technology in terms of radiation hardness. Their timing performance is evaluated in this work using a double-sided fabrication process for timing applications, based on different pixel geometries. Overall, this work comprises electrical and laser characterizations, device design and simulations, and the fabrication of various detector configurations, each tailored to address a specific issue in high- and low-energy physics.

Author's contribution

Projects

The author won a grant as a principal investigator (PI) of the following project funded by the National Science Centre (NCN) in Poland:

- *TCT study of new types of radiation hard silicon sensors for future high energy experiments.*, project number: UMO-2023/49/N/ST2/02314, project type: PRELUDIUM 22 - NCN grant, the amount awarded: 82 472 PLN, project start date: 2024-01-29, project end date: ongoing project.

The author worked as a researcher in the following project funded by IDUB Excellence Initiative – Research University (IDUB):

- *Preparation of the test stand and measurement of silicon sensors using the Transient Current Technique (TCT) method.*, project number: 6275, project type: IDUB, the amount awarded: 148 000 PLN, project start date: 2023-08-30, project end date: 2025-08-30.

The author worked as a researcher for 1 year in the following project funded by the National Science Centre (NCN) in Poland:

- *Novel 4D reconstruction for the flavour physics in HL-LHC era.*, project number: 608010, project type: NCN-OPUS 26, project start date: 2024-11-01, project end date: 2025.12.31.

Internships

- Internship for a period of 2 weeks at Jozef Stefan Institute, Ljubljana, on the training of commissioning and operation of TCT setup under the supervision of Gregor Kramberger [July 2022].

- Internship for a period of 2 months at CERN under the supervision of Michael Moll (SSD Group at CERN) [Oct–Dec 2022].
- Internship for a period of 2 weeks at the University of Glasgow under the supervision of Richard Bates to perform characterizations on TI-LGADs [August 2023].
- Internship for a period of three months at CNM Barcelona to learn TCAD simulations under the supervision of Neil Moffat [Nov 2023 - Jan 2024].
- Internship for a period of 3 weeks at the University of Glasgow under the supervision of Richard Bates to perform wafer-level testing on version-2 of TI-LGADs [November 2024].
- Internship for a period of 2 weeks at CNM Barcelona to perform post-fabrication etching of double-sided 3D column detectors under the supervision of Neil Moffat [September 2025].

Talks and Poster Presentations

- Fasih Zareef (on behalf of RD50), *Silicon Detectors Beyond LHC- RD50 Status Report*, 23rd International Workshop on Radiation and Imaging Detectors (IWoRID), Riva del Garda, Italy, June 2022. [Poster presentation]
- Fasih Zareef (et al.), *Gain degradation study after neutron and proton irradiations in Low Gain Avalanche Diodes*, 42nd RD50 Workshop, Tivat, Montenegro, 20-24, June 2023. [Talk]
- Fasih Zareef (et al.), *Characterization of Ultra-Fast Silicon Detectors (UFSD) for high energy physics applications*, The 13th International Conference on Position Sensitive Detectors, Oxford, United Kingdom, 03-08, September 2023. [Poster presentation]
- Fasih Zareef (et al.), *First characterisation of Trench Isolated LGADs fabricated at Micron Semiconductor Ltd*, 1st DRD3 week on Solid State Detectors R&D , CERN, Geneva, 17-21, June 2024. [Talk]
- Fasih Zareef (et al.), *Performance Evaluation of Ultra-Thin Low Gain Avalanche Diodes (LGADs) for Fast Timing and 4D Tracking*, 26th International Workshop

on Radiation and Imaging Detectors (IWoRID), Bratislava, Slovakia, 06-10, July 2025. [Poster Presentation]

Publications

- F. Zareef et. al., *Fill-factor optimization of trench-isolated low gain avalanche diodes (TI-LGADs) for low penetrating particles* (**under review**). [Journal Article: First/corresponding author]
- F. Zareef et. al., *Achieving near 100% Fill factor for small pixel LGADs: Study of First Trench Isolated LGADs fabricated at Micron Semiconductor Ltd*, JINST 20 (2025) 07, P07037. [Journal Article: First/corresponding author]
- E. Currás Rivera, A. La Rosa, M. Moll and F. Zareef *Gain layer degradation study after neutron and proton irradiations in Low Gain Avalanche Diodes*, JINST 18 (2023) 10, P10020. [Journal Article: Main contributor]
- F. Zareef, A. Oblakowska-Mucha and T. Szumlak *Silicon detectors beyond LHC — RD50 status report*, 2022 JINST 17 C11004. [Conference proceedings: First/corresponding author]
- F. Zareef, et. al., *Characterization of Ultra-Fast Silicon Detectors (UFSD) for high energy physics applications*, Nucl.Instrum.Meth.A 1061 (2024) 169085, Contribution to: PSD13. [Conference proceedings: First/corresponding author]

Trainings and Certifications

- EUROPRACTICE Introduction to Technology CAD (TCAD) course on 22-24 February 2022

Participation in summer schools

- 7th Barcelona TechnoWeek: Course on semiconductor detectors, Barcelona, Spain, 03–07 July, 2023.
- Advanced UK Instrumentation Training, May-July 2025, UK, Online

- Advanced UK Instrumentation Training, April-June 2024, UK, Online
- Advanced UK Instrumentation Training, May-July 2023, UK, Online

Other important activities

- XIV International Conference on Beauty, Charm and Hyperon Hadrons, 5-11, June 2022, Kraków, Poland, Organizing Committee;
- "Accelerating Science" CERN's Flagship Exhibition in Krakow, 11-26, May 2024, Kraków, Poland, Volunteer;

Teaching and supervision

- Tutorial classes for Physics-II course for AGH students
- Co-supervision of a Bachelor's (engineer) project
- Co-supervision of 2 Master's projects

Motivation

4D tracking imposes simultaneous demands on timing precision, spatial granularity, and radiation tolerance. Thin LGADs provide intrinsically fast signals suitable for precision timing, but their performance is ultimately limited by irradiation-driven gain-layer degradation, which changes the achievable gain, noise, and bias headroom over time. At the same time, realizing fine segmentation for tracking requires robust electrical isolation and minimal dead regions, motivating trench-isolated LGAD concepts. This thesis unifies these aspects by treating timing performance as the common metric: first quantifying gain degradation, then establishing operating points for thin sensors, and finally evaluating trench isolation as the segmentation strategy that preserves timing and efficiency throughout the detector lifetime. Looking beyond the HL-LHC, future facilities such as the FCC will impose even more extreme radiation environments while demanding timing resolutions at the level of tens or even units of picoseconds. Meeting these conditions requires exploring alternative detector technologies with enhanced radiation tolerance. For this reason, this thesis also investigates 3D silicon detectors, which are strong candidates for applications such as the LHCb VELO Upgrade-II at the HL-LHC. Their geometry decouples depletion depth from electrode spacing, offering enhanced radiation hardness while maintaining fast charge collection, which is an essential ingredient for next-generation 4D tracking.

Introduction

Silicon-based semiconductor detectors have emerged as crucial components in high-energy-physics (HEP) experiments, particularly for vertexing and precision tracking applications. Their sub-micron spatial resolution [1] enables precise reconstruction of charged particle trajectories near the point of collision, which is essential for identifying particles with short lifetimes and studying complex decays. A key advantage of the semiconductor detectors is that they are energy efficient. The generation of an electron-hole pair in silicon requires only $\sim$ 3.6 eV, an order of magnitude less than the ionization energy required in gaseous detectors. This allows for increased charge production from minimal thickness, contributing to both outstanding resolution and cost-effectiveness in tracking systems.

Moreover, silicon detectors exhibit higher stopping power, aiding the fabrication of very thin sensors without sacrificing detection efficiency. Their fast signal collection is due to the high mobility of charge carriers in silicon, which allows for signal formation within nanoseconds. These attributes collectively make silicon detectors especially well-suited for high-rate environments where spatial granularity, timing precision, and radiation tolerance are critical. However, the planned upgrade of the Large Hadron Collider (LHC) to the high-luminosity LHC (HL-LHC), expected to commence data-taking in 2030, will drastically increase the collision rate. The projected instantaneous luminosity represents a fivefold increase over the current LHC luminosity for proton-proton collisions, mounting to 7.5×10^{34} cm^{-2}s^{-1}, leading to an average pile-up of 140-200 interactions per bunch crossing [2].

This increased pile-up imposes major challenges for event reconstruction, as spatially overlapping tracks from multiple collisions become difficult to disentangle using spatial resolution alone. To address this, the next generation of silicon detectors is being designed with both high spatial and temporal resolution, enabling four-dimensional tracking (4D-tracking). This approach couples precise hit position with time stamps of the order of 30

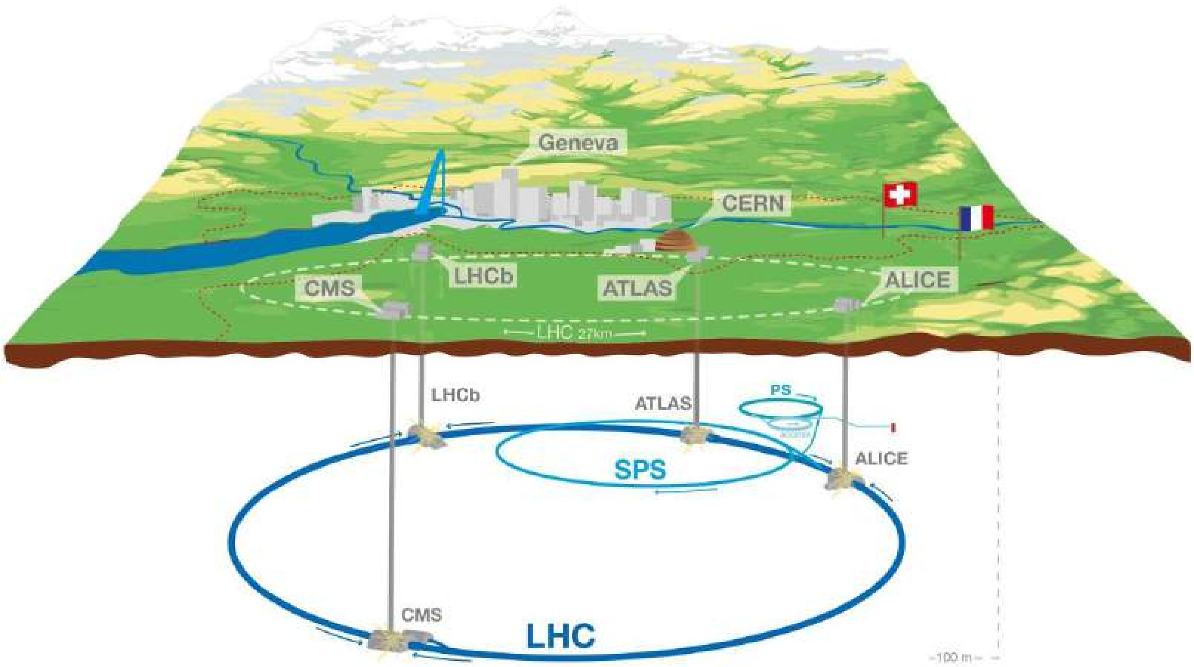

Figure 1: An overview of the LHC with its 4 main experiments [3].

– 50 ps, allowing events to be distinguished based on their interaction time within the same bunch crossing. The schematics of the LHC are shown in Figure 1.

Among the promising technologies being developed are Low Gain Avalanche Diodes (LGADs), which provide internal charge multiplication and fast signal rise times, making them ideal candidates for precision timing layers in future tracker upgrades. LGAD technology is based on a silicon PIN diode. The LGAD stands out from the PIN diode with an extra doping layer underneath the junction implant, which, under reverse bias conditions, causes a high field region at the junction between these two implants. The electric field near the junction implants can be tailored to allow impact ionization by controlling the doping profile precisely, which results in charge multiplication for negatively charged carriers crossing this high field region. The design and operation of the LGADs are similar to the Avalanche Photodiodes (APDs), except that the LGADs have a low gain, in the range of 5 - 20, as compared to the APDs that have a gain of 100's. The preference of LGADs over APDs is because the sensors with higher gain tend to have large sensor noise and are difficult to segment. Moreover, APDs are typically not operated in full depletion mode.

However, LGADs with a significantly lower gain (~ 20), increased slew rate and fine segmentation, are optimal for timing detectors. LGADs are already slated for deployment in the timing detectors of ATLAS High Granularity Timing Detector (HGTD) [4] and the CMS Endcap Timing Layer (ETL) [5], where they will play a crucial role in pile-up mitigation. Active thickness of the LGAD plays a pivotal role in the timing performance of the technology, since thinner sensors offer a fast rise time. LGADs with a thickness of $\sim$ 50 μm have been shown to give a time resolution of 30 ps [6]. Given the above-mentioned timing capabilities, LGADs have become highly attractive for hybrid sensor architectures, where a dedicated LGAD array is bonded to a readout ASIC or a spatially segmented sensor to provide both timing and position information. This hybrid approach is adopted not only in high-energy physics experiments but also in soft X-ray imaging, ultra-fast photon science, and synchrotron-based experiments where high timing resolution, spatial granularity, and low signal-to-noise ratio (SNR) are required. For synchrotron application, there is a desire to reduce the minimum detectable energy to a range of $1 - 5$ keV. Potential application of LGADs combined with hybrid pixel technology can result in larger signals in response to low-energy deposition, improved SNR, hence, improving the image quality [7].

Hybrid detectors have already been implemented in single photon counting pixel detectors, which are used for numerous applications, such as X-ray diffraction and X-ray crystallography. Inclusion of LGAD with fine segmentation to match the available readout electronics of this technology can enhance the detection capabilities. Internal gain of the LGAD can allow sub-threshold detection of low-energy photons, for example, a gain of 4 could generate a meaningful output signal from X-ray interaction of 1 keV. Along with the fast response of the readout chip with timing resolution of 1.6 ns [8], it should be possible to have a detector with good spatial and timing resolution to detect sub-keV photons. LGADs hold significant potential for a broad range of synchrotron-based experiments operating in the low-energy X-ray regime. Techniques such as low-energy X-ray diffraction [9] and spectromicroscopy [10] stand to benefit from the enhanced timing and sensitivity offered by LGADs.

However, applying LGADs to finely segmented hybrid detectors comes with a limitation, known as reduced fill factor. In conventional segmented LGADs, adjacent pixels must be separated from each other to have isolation between the pixels and maintain spatial resolution. The separation comes with a region where there is no multiplication occurring, making them inactive or dead region. Consequently, the detection efficiency is compromised in this region. Overcoming this fill factor limitation requires the design and fabrication of the LGADs capable of delivering consistent performance regardless of where a particle interacts within the sensor. To address this, trench-isolated LGADs (TI-LGADs) were developed, forming the central focus of this thesis. In TI-LGADs, the isolation implants are replaced by etching trenches physically in the silicon. This can potentially reduce the dead region from tens of micrometers to a few micrometers, which helps in increasing the fill-factor and improved detection efficiency [11].

Another concept is three-dimensional (3D) silicon pixel detectors that are high-performance radiation detectors whose geometry – channeling electrodes directly into the silicon bulk - allows for very short carrier drift distances (typically 30-70 μm), faster signal collection, low depletion voltages, and exceptional radiation tolerance, capable of withstanding fluences up to approximately 10^{16} n_{eq}/cm^2 or more. These features make them highly attractive for the innermost layers of high-energy physics experiments.

While LHCb's current VELO (Vertex Locator) upgrade I employs planar hybrid pixel sensors, future upgrades (e.g., VELO Upgrade II) are exploring alternative technologies—including 3D sensors—due to the extremely high radiation levels expected near the beam [12], which may exceed 6 x 10^{16} neq/cm^2 at an inner radius of 5.1 mm. Simulation studies and R&D on sensor longevity, timing, and readout integration continue to evaluate the feasibility of such designs for future high-luminosity operations.

In this chapter, the basic principles of LGAD technology were introduced in terms of achieving low-gain detectors and enhancing their fill-factor for segmentation. Their applications in particle identification for high-energy physics and in synchrotrons for the detection of low penetrating particles are also discussed. 3D silicon radiation detectors are also introduced, which are a potential candidate for future upgrades in HL-LHC. The thesis is organized into chapters, as described below:

- Chapter 1 gives an overview of the fundamental properties of the semiconductor detectors. Also digging into the detector types like PIN, LGADs, and 3D detectors.

- Chapter 2 is dedicated to discussing the experimental techniques that are used in this work to characterize the above mentioned sensor technologies. This work also involved the commissioning of the TCT setup present in the AGH University of Krakow, which was carried out by the author after taking an extensive 2-week training at Jozef Stefan Institute, Ljubljana, Slovenia.

- Chapter 3 presents the results of neutron and proton irradiation on LGADs fabricated by HPK and CNM. A comparative study is carried out in terms of gain layer degradation by calculating the acceptor removal coefficient post-irradiation. This work was performed in the Solid State Detector (SSD) group at CERN, where the author secured a 2-month internship. This exposure helped the author gain experience with detector characterization and data analysis techniques from one of the well-developed groups in the detector development for LHC. This experience is further applied throughout the author's research activities.

- Chapter 4 introduces the radiation hardness study of the ultra-thin LGADs produced by BNL with 20 μm and 30 μm active thicknesses for timing layers and high pile-up environments. Timing resolution studies are performed pre- and post-irradiation. This work is carried out as a result of a strong collaboration made by our group with the Institute of Nuclear Physics (IFJ), AGH Krakow, and Brookhaven National Laboratories (BNL), USA. This collaboration turned out to be a great blend of fabrication resources (BNL), irradiation facilities (IFJ), and a well-developed detector characterization lab at AGH Krakow.

- Chapter 5 focuses on the development and characterization of TI-LGADs. Fabrication, characterization, and TCAD simulations are carried out in detail. This helps in increasing the fill-factor and provide solution for the detection of low-penetrating particles. This work highlights the most extensive work during the doctoral studies, carried out in the framework of PixeLGAD collaboration, consisting of the University of Glasgow, Edinburgh, Manchester, Oxford, and AGH Krakow. The author joined this work halfway through and became an integral part of the characterization and simulation responsibilities. This work involved several internships in Glasgow and Centro Nacional de Microelectronica (CNM), Barcelona, test beams at ELI beamlines, Prague, and presenting results at several collaboration meetings and well-reputed conferences. The author also spent 3 months at CNM Barcelona to learn TCAD simulations, which are implemented throughout the research activities.

- Chapter 6 presents the detailed characterization of double-sided 3D column detectors. Charge collection and time of arrival studies are performed by using the TCT setup at AGH University of Krakow. This is a vast project involving many institutes and universities, including CNM, LHCb, the University of Glasgow, and many others. AGH also became a part of this project, and now characterizations are performed here as well. The characterizations were planned to be carried out at ELI beamlines with the TPA-TCT setup as a function of depth. But the biasing of the detectors was not possible due to a mistake in the process of backside metal removal. Therefore, this work also involved an internship at CNM Barcelona to remove the backside metal by leaving a Ti layer for biasing. Therefore, laser characterizations were carried out at AGH.

- Chapter 7 summarizes the findings of the thesis and contains the conclusions based on the research work carried out in the above-mentioned chapters.

All experimental measurements, simulations, and data analyses presented in this thesis were primarily performed by the author at AGH University of Krakow. In addition, selected electrical characterizations were carried out at the University of Glasgow (UK) and at CNM, Barcelona, within the framework of collaborative research activities. The measurements conducted at ELI Beamlines, Prague, were performed as part of a collaborative group effort, with the author actively contributing to both the experimental execution and the subsequent analysis.

Chapter 1

Silicon sensors for radiation detection

Silicon is one of several semiconductor materials used for radiation detection, but it stands out as the most extensively studied and widely implemented, particularly in high-energy physics (HEP) and synchrotron-based applications. Silicon has been widely used as the detector material primarily due to a well-established understanding of its electrical behavior and the maturity of its fabrication technologies. For any novel sensor development, leveraging existing knowledge and infrastructure is crucial, and silicon offers a solid foundation in both areas. Its widespread use in the semiconductor industry makes it highly accessible and cost-effective for research and development purposes, allowing multiple fabrication iterations using commercially available wafers.

One of silicon's key advantages is its relatively low ionization energy, which averages around 3.6 eV per electron-hole pair, which contributes to high energy resolution in radiation detection (when doped). Moreover, the material possesses high charge carrier mobilities, enabling fast signal collection, an essential attribute for time-sensitive experiments such as those conducted at particle colliders and synchrotron light sources.

While other semiconductors do offer certain advantages, they often come with notable limitations. For example, diamond detectors are appealing due to their low leakage currents and reduced power consumption, along with a short radiation length that benefits tracking applications. However, along with the high production cost, diamond has a higher ionization energy than silicon, which can lead to smaller signal amplitudes. Germanium, with its narrow bandgap of 0.66 eV, requires cryogenic operation to suppress noise, unlike silicon, which has a more practical 1.12 eV bandgap that allows room-temperature operation.

Gallium Arsenide (GaAs) is another widely known semiconductor, but its performance is hindered by inherent crystal defects and the presence of deep-level traps, which significantly degrade charge collection efficiency and radiation hardness. In contrast, silicon can be manufactured with minimal defects, which reduces carrier trapping and enhances both timing and energy resolution. These properties make silicon the most practical and effective choice for precision particle tracking and spectroscopy in demanding research environments.

1.1 Crystal structure of silicon

Silicon, a Group IV element in the periodic table, possesses four valence electrons in its outer shell, which allows it to form stable covalent bonds with neighboring atoms. These bonds result in a tetrahedral crystal configuration known as the diamond cubic lattice. While elemental silicon does not exist freely in nature due to its high reactivity, highly purified mono-crystalline silicon can be synthesized through controlled crystal growth processes, such as Czochralski or Float-Zone (FZ) methods [13]. These techniques produce large ingots of single-crystal silicon, which are then sliced into thin wafers.

The physical and electrical characteristics of a silicon wafer are influenced not only by the purity and resistivity of the material but also by its crystallographic orientation. The wafer orientation is defined by Miller indices, which describe the atomic arrangement of the crystal surface. Common orientations for detector-grade silicon include <100>, <110>, and <111>, as shown in Figure 1.1. Each of these orientations presents different atomic densities and bonding configurations at the surface, which can influence properties such as charge carrier mobility, radiation hardness, and doping uniformity. For HEP applications, <100> and <111> oriented wafers are generally favored due to their enhanced tolerance to radiation-induced damage, as compared to the radiation hardness of <110> [14].

Another critical factor in the detector design is the bulk resistivity of the silicon wafer. High-resistivity silicon is essential for achieving full depletion at relatively low bias voltages, which ensures that the entire volume of the detector contributes to signal generation. Full depletion refers to the state where all mobile majority charge carriers are swept out of the active region, allowing for maximum charge collection efficiency.

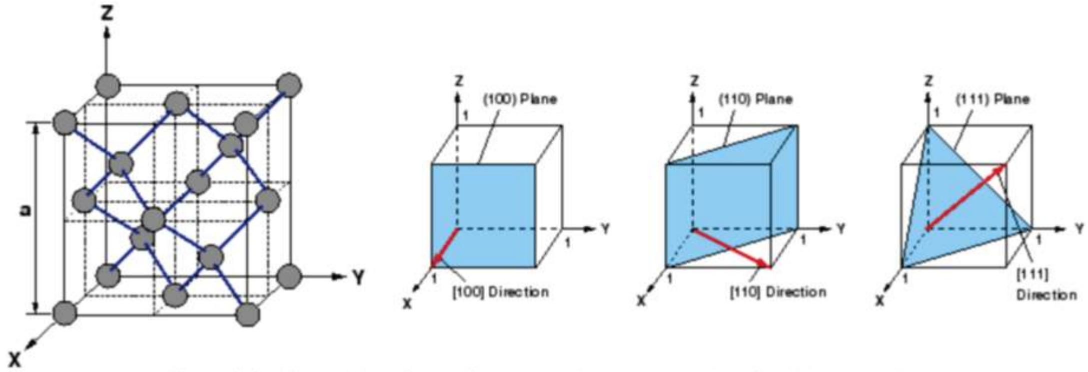

Figure 1.1: From left to right, diamond structure of the silicon crystalline lattice, (100), (110), and (111) lattice orientation planes (blue). The orientations <100>,<110>, and <111> refer to the perpendicular vector to the corresponding plane [15].

1.2 Energy band theory

A solid-state material can be described as an ordered arrangement of atoms forming a periodic crystalline lattice. When the Pauli exclusion principle is applied to such a lattice, it dictates that no two electrons can occupy the same quantum states simultaneously. As a result, the discrete atomic energy levels of individual atoms broaden into sets of allowed energy states, or atomic orbitals, distributed across all atoms in the solid. In a macroscopic crystal, the number of the solid orbitals is extremely large, i.e., on the order of Avogadro's number, and the energy differences between adjacent states are so small that the spectrum can be treated as a continuous distribution, known as an energy band.

In this framework, the electronic structure of solids is typically divided into two main bands: the valence band (VB) and the conduction band (CB). The VB contains the lower-energy states that are generally occupied by electrons, whereas the CB contains higher-energy states that may be partially filled or completely empty, depending on the material. Separating these two bands in a range of energies that electrons cannot occupy is known as the bandgap. The bandgap width, $E_g = E_c - E_v$, is defined as the difference between the conduction band minimum (E_c) and the valence band maximum (E_v) [16]. This energy separation determines the electrical classification of the material into insulators, conductors, and semiconductors, as shown in Figure 1.2, and described below :

- **Insulators:** These materials possess large bandgaps ($E_g \geq 2.5$ eV [17]) due to strongly bound electrons between adjacent atoms. At room temperature, very few electrons gain enough energy to move from the VB to the CB, resulting in extremely low electrical conductivity. Silicon dioxide (SiO_2) is a common example, widely used in semiconductor fabrication because it does not conduct current.

- **Conductors:** Materials that have a very small or zero bandgaps ($E_g = 0$) are known as conductors. The CB is already populated with a large number of electrons, even at low temperatures. This abundance of free electrons enables them to readily conduct electric current.

- **Semiconductors:** These materials fall between insulators and conductors. At $T = 0\ K$, the conduction band is empty, and all electrons remain in the VB, making them poor conductors at very low temperatures. At room temperature, some electrons are thermally excited into the conduction band, creating a moderate density of free charge carriers. A small applied electric field can easily mobilize these carriers, resulting in an electrical current.

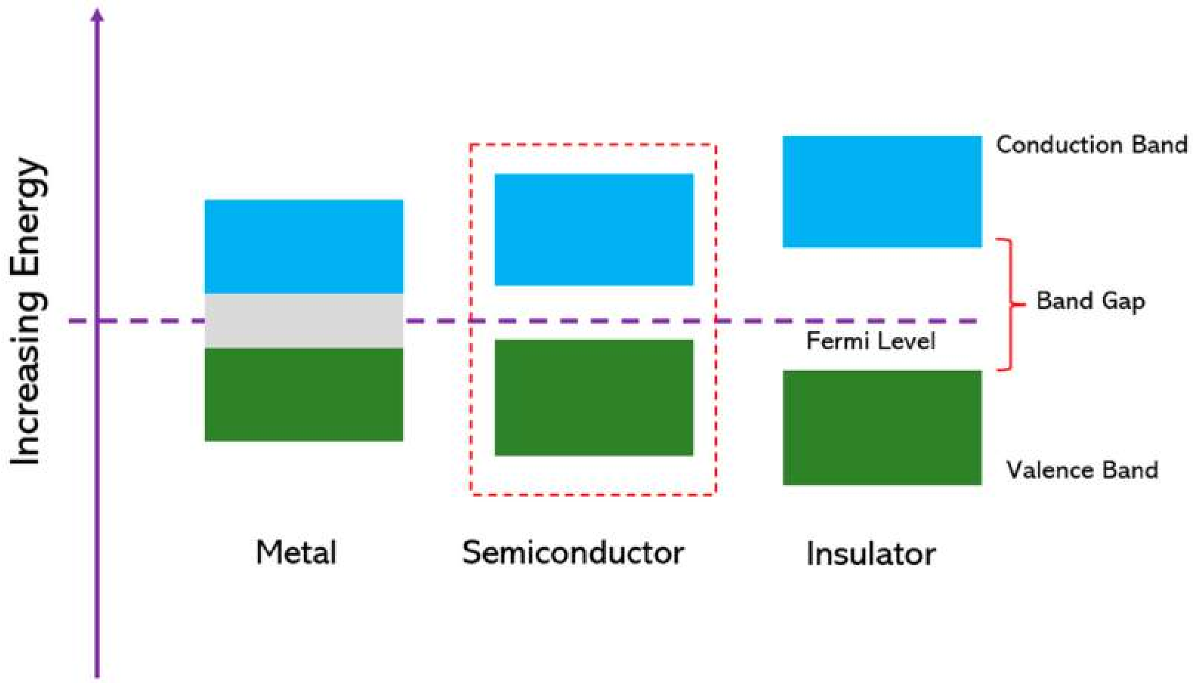

Figure 1.2: Energy band representation of metals, semiconductors, and insulators [18].

Silicon with a bandgap of 1.12 eV is classified as a semiconductor. Based on its purity, semiconductors are categorized as either intrinsic or extrinsic. In practice, all silicon used for particle or X-ray detection contains a controlled number of impurities. Precise control over the doping level is essential for the fabrication and performance of semiconductor devices.

1.3 Carrier concentration

The electrical properties of a semiconductor can be tuned by intentionally introducing specific impurities into the crystal during growth, a process known as doping. The choice of dopant determines the dominant type of charge carrier in the material: dopants that contribute extra electrons to the conduction band are referred to as donors, while those that create holes in the valence band are known as acceptors.

1.3.1 Intrinsic semiconductors

A semiconductor is called intrinsic when the concentration of impurities is lower than that of thermally generated charge carriers, which is the case when no external doping is added. The density of these thermally generated carriers is obtained by integrating over all available density of states in the valence and conduction bands, taking into account both the density of states and the occupation probability given by the Fermi-Dirac distribution [16]. From this, the electron (n) and hole (p) concentrations can be expressed as:

$$p = N_v \exp\left(\frac{E_v - E_f}{kT}\right) \tag{1.1}$$

$$n = N_c \exp\left(\frac{E_c - E_f}{kT}\right) \tag{1.2}$$

where N_v and N_c are the density of states in the valence and conduction bands respectively, k is the Boltzmann constant, T is the temperature in Kelvin, and E_f is the Fermi level. The Fermi level in a semiconductor is the energy at which the probability of finding an electron is exactly one-half. In intrinsic semiconductors, the Fermi level lies approximately midway between the CB minimum (E_c) and VB maximum (E_v), such that $E_c - E_f = E_f - E_v$. Under these conditions, the concentrations of electrons and holes are equal, $n = p = n_i$, where n_i denotes the intrinsic carrier concentration. In case of silicon, $n_i \sim 10^{10}\ p/cm^3$ at room temperature.

1.3.2 Extrinsic semiconductors

Doping refers to the deliberate introduction of controlled amounts of specific impurity atoms into a silicon substrate in order to modify its conductivity by increasing the concentration of either free electrons or holes. By incorporation these impurities into the crystal lattice, the balance of charge carriers can be shifted. This incorporation makes them extrinsic or doped semiconductors.

If the dopant atom donates an extra electron to the lattice, it acts as a donor, and if it accepts an electron, it acts as an acceptor. For instance, when silicon is doped with boron, the boron atom replaces a silicon atom in the lattice. Having only three valence electrons, boron forms covalent bonds with four neighboring silicon atoms by "accepting" an electron, thereby creating a positively charged hole in the VB. This results in a p-type semiconductor, with boron functioning as an acceptor impurity.

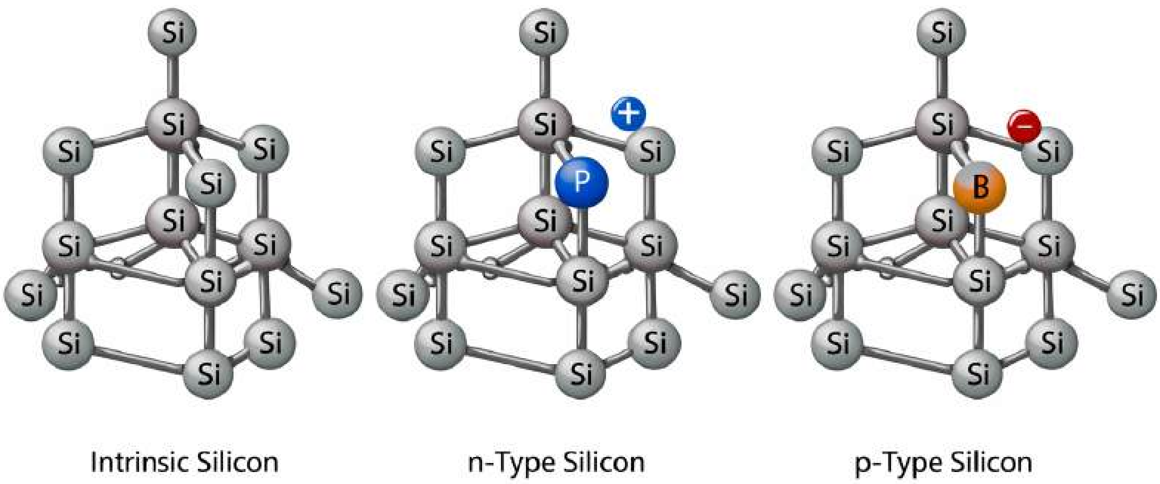

Figure 1.3: Schematics of the electron bonding arrangement in an intrinsic, n-type and p-type silicon crystal lattice.

Conversely, doping silicon with phosphorus introduces atoms that have five valence electrons. Upon replacing the silicon atom, phosphorus forms four covalent bonds with neighboring silicon atoms, leaving one loosely bound electron that is easily donated to the conduction band. This produces an n-type semiconductor due to the increased concentration of negative charge carriers, as shown in Figure 1.3. Doping primarily affects the semiconductor band structure by shifting the Fermi level (E_f) away from its intrinsic position (E_i). Donor impurities cause the E_f to mover closer to the CB, while acceptor impurities shift it toward the VB, as shown in Figure 1.4.

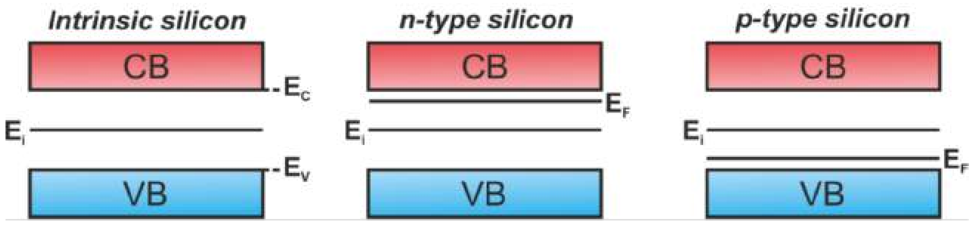

Figure 1.4: Band diagram and E_F level for intrinsic, n-type silicon and p-type silicon [19].

This shift occurs because doping introduces discrete energy levels within the bandgap of the intrinsic semiconductor. Donor level lies just below the CB edge (E_c), allowing electrons in these states to be easily excited into the CB at room temperature. Similarly, acceptor levels are located just above the VB edge (E_v), making it easier for electrons to be thermally excited from the VB into these acceptor states. This behavior is reflected in Eq. 1.3, we can see that:

$$E_f - E_i = kT \ln\left(\frac{n}{n_i}\right) = -kT \ln\left(\frac{p}{n_i}\right) \tag{1.3}$$

Which is 0 for intrinsic silicon ($n = p = n_i$). For doped silicon, the carrier concentration is neutral as a whole, but is given by:

$$n + N_A = p + N_D \tag{1.4}$$

where N_D (or N_A) represents the donor (or acceptor) concentration, which corresponds to the number of fixed positive (or negative) ions in the crystal assuming complete ionization of dopant atoms – typical at room temperature. For n-type silicon, the acceptor concentration $N_A = 0$, and $p << n$, so $n \approx N_D$. Conversely, in p-type silicon, the donor concentration $N_D = 0$, $p >> n$, thus $p \approx N_A$, given by Eq. 1.5:

$$E_F = \begin{cases} E_i & \text{(intrinsic silicon)} \\ E_i + kT \ln\left(\frac{N_D}{n_i}\right) & \text{(n-type silicon)} \\ E_i - kT \ln\left(\frac{N_A}{n_i}\right) & \text{(p-type silicon)} \end{cases} \tag{1.5}$$

1.3.3 Carrier transport processes

Working of a semiconductor device is controlled by combination of various transport processes. The important processes are drift, diffusion, and impact ionization.

Drift:

In thermal equilibrium, electrons in a semiconductor move rapidly in all directions due to thermal motion, undergoing random scattering from collisions with lattice atoms, impurity atoms, and other electrons. Without an external field, this motion results in no net displacement. The average time between collisions is known as the mean free time (τ_c), and the average distance traveled between collisions is the mean free path. When an external electric field E is applied, each electron experiences a force of $-qE$ (where q is the electron charge), accelerating in the direction opposite to the field. The resulting motion combines the random thermal movement with a drift velocity v_d opposite to the electric field, $-qE\tau_c$, to the momentum gained, $m_n v_d$, where m_n is the effective mass of the electron [16]. Equating these terms gives:

$$m_n v_n = -qE\tau_c \tag{1.6}$$

Rearranging 1.6 gives:

$$v_n = -\left(\frac{q\tau_c}{m_n}\right) E \tag{1.7}$$

The electron drift velocity, as given in Eq. 1.7, is directly proportional to the applied electric field. The proportionality constant depends on the mean free time, the electron charge, and the effective mass, and is defined as the electron mobility, μ_n. Mobility quantifies the extent to which an electron's motion is influenced by the electric field. An analogous parameter, the hole mobility, up, describes the motion of holes in the valence band. The drift velocities of electrons and holes can thus be expressed as:

$$n = -\mu_n E, \qquad p = \mu_p E. \tag{1.8}$$

At low electric field strengths, the drift velocity increases linearly with the applied field. However, at higher fields, increased carrier scattering introduces non-linearity, leading to velocity saturation.

When the impurity concentration is low, mobility is primarily limited by lattice scattering, caused by thermal vibrations of the crystal atoms at temperatures above 0 K. These vibrations disturb the lattice and facilitate energy exchange between carriers and the crystal. As the temperature rises, lattice vibrations intensify, resulting in decreased mobility. While, at high impurity concentrations, mobility is increasingly affected by impurity scattering, where carriers undergo Coulomb interactions with dopant ions and lose energy. This effect weakens at high temperatures, as carriers move faster and are less likely to interact. Above $\sim$ 200°C, doping density has little influence on mobility.

At room temperature, mobility is limited by ionized impurity concentration, with a noticeable drop occurring at doping densities $\sim 10^{16}\ cm^{-3}$. In low-impurity devices, such as those used in HEP applications, temperature effects dominate mobility. It is also important to note that hole mobility is lower than electron mobility, largely due to the lower effective mass of electrons.

Diffusion:

When there is a variation of carrier concentration spatially in a semiconductor, an additional transport mechanism arises - diffusion current. This occurs when carriers are unevenly distributed, with regions of high and low concentration. Carriers naturally move from high- to low-concentration regions to establish equilibrium.

The carrier flow rate can be expressed as:

$$F = -v_{\mathrm{th}} l \frac{dn}{dx} \equiv -D_n \frac{dn}{dx} \tag{1.9}$$

where $D_n \equiv v_{th} l$ is the diffusivity, v_{th} is the thermal velocity, and l is the mean free path. Since each electron carries charge $-q$, the resulting current density is:

$$J_n = -qF = -qD_n \frac{dn}{dx} \tag{1.10}$$

Diffusion current stems from random thermal motion in the presence of a concentration gradient and flows in the opposite direction to electrons (hence positive sign). Diffusivity and mobility are related by the Einstein relation for electrons and holes respectively:

$$D_n = \left(\frac{kT}{q}\right)\mu_n \tag{1.11}$$

$$D_p = \left(\frac{kT}{q}\right)\mu_p \tag{1.12}$$

If both electric field and the concentration gradiaent are present, the total current is the sum of drift and diffusion components. For electrons, the total current is:

$$J_n = q\mu_n nE + qD_n \frac{dn}{dx}\mu_n \tag{1.13}$$

and for holes is:

$$J_p = q\mu_p pE - qD_p \frac{dp}{dx}\mu_p \tag{1.14}$$

At high electric fields, the drift term $\mu_n E$ and $\mu_p E$ can be replaced with the respective saturation velocities v_n and v_p [16].

Impact ionization

When the electric field in a semiconductor exceeds a critical value, charge carriers gain sufficient kinetic energy to generate new electron-hole pairs through avalanche process. Consider a free electron in the conduction band: if the field is high enough, the electron can transfer part of its kinetic energy to the lattice during a collision, breaking a covalent bond and promoting an electron from the valence to the conduction band. This creates an additional electron-hole pair. The newly created carriers are also accelerated by the field and may, in turn, generate further pairs. This chain reaction is known as impact ionization. The threshold kinetic energy required for ionization is [20]:

$$E_0 = \frac{1}{2}mv_s^2 = 1.5E_g \tag{1.15}$$

where m is the carrier effective mass, v_s the saturation velocity, and E_g the bandgap energy. In practice, the effective energy required to create an electron-hole pair in silicon is higher: approximately 3.2 E_g for electrons and 4.4 E_g for holes. The mechanism leads to carrier multiplication and therefore signal gain in detectors. The generation rate of electron-hole pairs due to impact ionization can be expressed as [21]:

$$G = \alpha_n n v_n + \alpha_p p v_p \tag{1.16}$$

Here, (n, p), (v_n, v_p), and (α_n, α_p) denote the carrier density, velocity, and ionization rate for electrons and holes, respectively. The ionization rate is strongly dependent on the local electric field E and can be expressed as :

$$\alpha = \frac{E}{E_{th}} \exp\left[-\frac{E_i}{E}\right] \tag{1.17}$$

where E is the high electric field inside the device, E_{th} is the effective ionization threshold energy (for silicon, approximately 3.6 eV for electrons and 5.0 eV for holes), and E_i is the characteristic threshold field associated with ionization [22].

1.3.4 The p-n junction:

A p-n junction is formed when regions of p-type and n-type semiconductor are brought into direct contact. To illustrate its operation, one can first imagine the two regions as isolated, and then joined. The p-type region contains an excess of holes, while the n-type region contains an excess of electrons. Once in contact, carriers diffuse across the junction following the concentration gradient – electrons move from the n-side to the p-side, while holes move in the opposite direction, as illustrated in Figure 1.5.

As carriers diffuse and recombine across the junction, a potential difference defined by V_{bi} develops, to counter further diffusion. This built-in potential is maintained by stationary, ionized donor and acceptor atoms, which form a static space charge region around the junction. Equilibrium is reached when this potential is sufficient enough to balance the diffusion process. The magnitude of V_{bi} is determined by the intrinsic carrier concentration n_i, as well as the concentrations of electrons n and holes p, and is expressed by [21]:

$$V_{bi} = \frac{kT}{e} \ln\left(\frac{np}{n_i^2}\right) \tag{1.18}$$

The region surrounding the p-n junction that is depleted of mobile charge carriers is

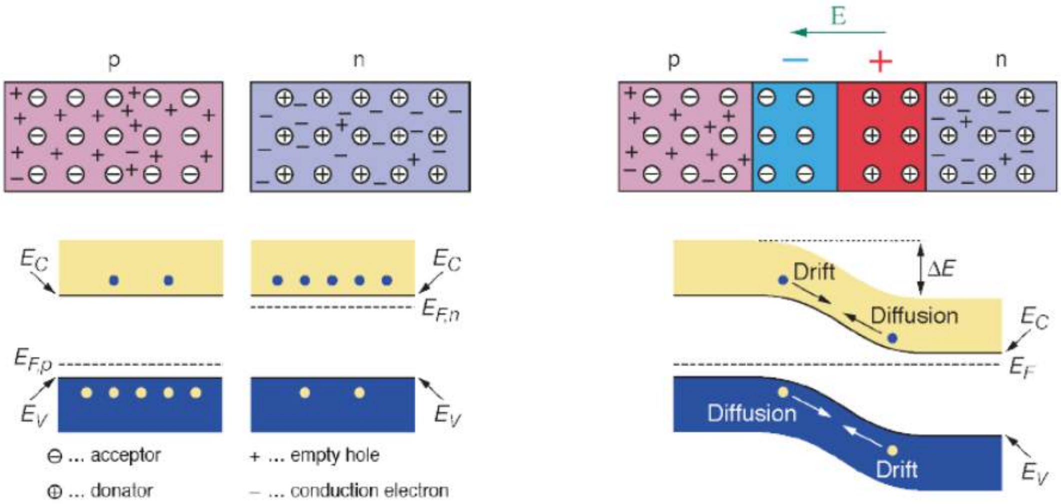

Figure 1.5: Schematic figure of the formation of a p-n junction in thermal equilibrium with zero bias voltage applied. Left: Separate n and p-type semiconductors with their respective energy bands. Right: The p-n junction with the space charge region (SCR) formed around the junction (blue-red) [23].

knows as the *depletion region*, as shown in Figure 1.5. Practically, these junctions are fabricated by introducing controlled impurity dopants into the opposite sides of a silicon wafer, creating either p- or n-type regions. The resulting abrupt junction has a depletion region that extends further into the less heavily doped side. The depletion width can be determined by solving Poisson's equation:

$$\frac{d^2\Psi}{dx^2} = -\frac{q}{\epsilon_s}(N_D - N_A + p - n) \tag{1.19}$$

where Ψ is the electrostatic potential, ϵ_s is the permittivity of silicon, N_D and N_A are the donor and acceptor concentrations, respectively. Since the depletion region is free of charge carriers, Poisson's equation can be simplified to:

$$\frac{d^2\Psi}{dx^2} = +\frac{qN_A}{\epsilon_s} \quad \text{for} \quad -x_p \leq x \leq 0 \tag{1.20}$$

$$\frac{d^2\Psi}{dx^2} = -\frac{qN_D}{\epsilon_s} \quad \text{for} \quad 0 < x \leq x_n \tag{1.21}$$

where x_n and x_p are the depletion widths on the p- and n-sides, respectively. The total depletion width w is then:

$$w = x_p + x_n \tag{1.22}$$

Integrating equations 1.20 and 1.21 gives the electric field in the depletion region, with the maximum field at x = 0:

$$E_m = \frac{qN_D x_n}{\epsilon_s} = \frac{qN_A x_p}{\epsilon_s} \tag{1.23}$$

Further integration yields the total potential variation across the depletion region:

$$V_{bi} = \frac{qN_A x_p^2}{2\epsilon_s} + \frac{qN_D x_n^2}{2\epsilon_s} = \frac{1}{2} E_m w \tag{1.24}$$

Rearranging gives the depletion width:

$$w = \sqrt{\frac{2\epsilon_s (N_A + N_D)}{qN_A N_D}(V_{bi} - V)} \tag{1.25}$$

Applying an external voltage V modifies the depletion width. Under reverse bias, where positive voltage is applied to the n-side, V adds to V_{bi}, and the depletion region widens. Under forward bias, where positive voltage is applied to the p-side, V opposes V_{bi}, and the depletion region shrinks [21].

1.3.5 Operation in forward and reverse bias

In forward bias, the applied external voltage reduces the electrostatic potential across the junction, narrowing the depletion region. When the depletion region vanishes, current can flow freely across the junction. In silicon, the built-in voltage is approximately 0.7 V, depending on doping concentration and temperature [24]. Above this threshold, the current increases exponentially with applied voltage.

Under reverse bias, contrary to the forward bias, the electrostatic potential increases, which widens the depletion region. In an ideal diode, the reverse current remains very low until the electric field reaches a critical value of $\sim$ 300 kV/cm, at which avalanche breakdown occurs [25]. The corresponding current-voltage (IV) characteristic of an ideal p-n junction is shown in Figure 1.6. The Shockley ideal diode equation, or the diode law gives the I-V characteristic of an ideal diode in either reverse, forward or no bias, given by:

$$I = I_0 \left[\exp\left(\frac{q_0 V}{k_B T} \right) - 1 \right] \tag{1.26}$$

where I is the diode current, I_0 is the reverse saturation current, q_0 is the absolute elementary charge, V is the applied bias voltage, k_B is the Boltzmann constant, and T is the absolute temperature in Kelvin.

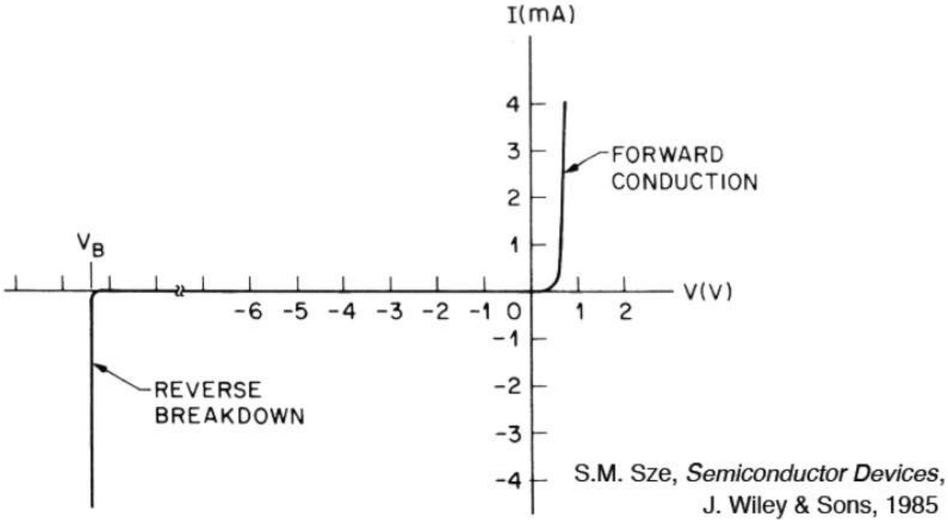

Figure 1.6: IV characteristics of an ideal p-n junction diode [21].

When the depletion region expands to the full detector thickness, the device is said to be fully depleted. The required reverse bias is called the *full depletion voltage*, expressed as:

$$V_{fd} = \frac{q(N_A + N_D)}{2\epsilon} w^2 \tag{1.27}$$

where V_{fd} is the full depletion voltage. Silicon detectors used in HEP applications are always operated under reverse bias, with typical full depletion voltages between 60 - 120 V for 200 - 300 μm thick devices, which increases with time after radiation exposure.

Experimentally, V_{fd} can be determined from capacitance-voltage (CV) characteristics. The depletion region acts as parallel-plate capacitor, with charge $\pm Q$ stored on either sides:

$$C = \frac{dQ}{dV} \tag{1.28}$$

For a depletion width w, the capacitance per unit area is:

$$C = \frac{\epsilon_s A}{w} \tag{1.29}$$

As reverse bias increases, w grows and C decreases, until full depletion is reached. Beyond this point, the capacitance remains constant, and the corresponding voltage defines V_{fd}.

1.4 Radiation-matter interaction

When a particle passes through a semiconductor, it creates a number of electron-hole pairs along its path. Because of the electric field inside the semiconductor detector, the charges are quickly pulled apart and collected by their respective electrodes. The collected charge forms a signal, which tells us that a particle has crossed the detector. This simple mechanism is the basis of how semiconductors work as radiation detectors.

1.4.1 Charged particles

The way ionization happens depends on whether the incoming particle is charged or not. Charged particles lose some of their energy directly by ionizing atoms in the material as they travel, leaving behind a roughly straight track of ionization. In addition, they may also interact with the nuclei of the atoms, which can damage the crystal structure of the semiconductor. Such effects are important to consider when designing detectors, as they can impact long-term performance.

The average energy lost by a charged particle per unit length as it moves through matter is known as the *stopping power*. For fast, heavy charged particles (with relative velocity $\beta > 0.1$), the stopping power can be described by the well-known *Bethe-Bloch formula* (Eq. 1.30) [26] , which depends on the particle's charge, its velocity, and the properties of the material it passes through. Figure 1.7 shows average stopping power of charged particles (muons, pions, and protons) in silicon.

$$-\frac{dE}{dx} \propto \rho \frac{Z}{A} \frac{z^2}{\beta^2} \left[\frac{1}{2} \ln \left(\frac{2 m_e c^2 T_{\max}}{I^2} (\beta\gamma)^2 \right) - \beta^2 + f(\beta\gamma) \right] \tag{1.30}$$

where m_e is the electron's rest mass, T_{max} is the maximum kinetic energy a particle can transfer in a single collision, I is the mean excitation energy of the material, $\gamma = (1 - \beta^2)^{-1/2}$, and $f(\beta\gamma)$ is a correction term that matters at high energies. A charged particle with a energy such that it has the minimum stopping power, is called as a *minimum ionizing particle (mip)*.

For silicon, the stopping power of a mip is about 400 eV/μm. Since it takes about $E_{e,h} \approx 3.6\ eV$ to create a single electron-hole pair in silicon, a mip passing through a detector with a thickness of $\sim 100\ \mu m$ will generate on the order of 10^4 electron-hole pairs. This makes mips a very useful benchmark for calibrating silicon detectors.

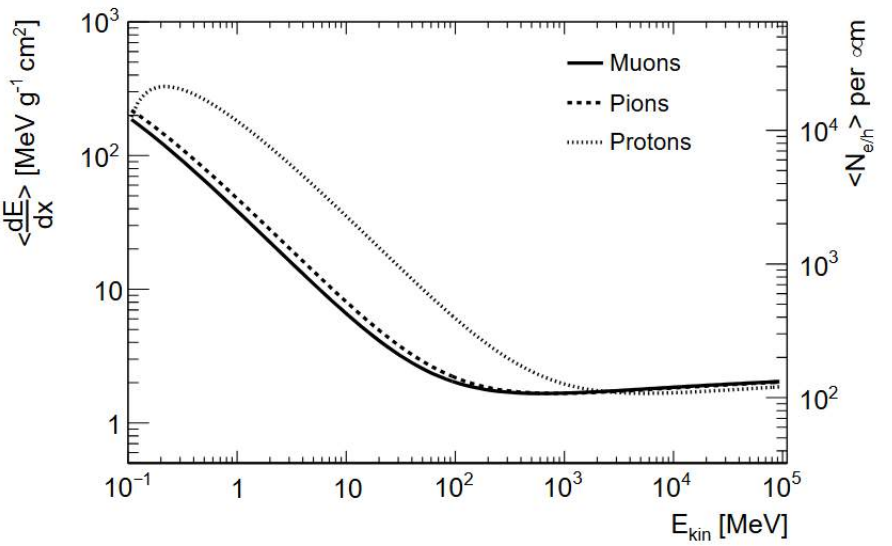

Figure 1.7: Average stopping power of muons, protons and pions in silicon and average number of electron/hole pairs per micrometer as a function of kinetic energy. Figure adapted from [27].

1.4.2 Electromagnetic radiation

Photons behave differently since they cannot ionize directly. They do not have charge, so they do not interact with electrons via Coulomb forces. Instead, they interact through three main processes [28]. For low-energy photons, such an invisible light or x-rays, the dominant interaction is the *photo-electric effect*, where a photon is absorbed by an atom and an electron is ejected. At higher photon energies, up to about 10 MeV, the main process is *Compton scattering*, in which the photon collides with an electron losing part of its energy and imparting recoil to the electron. Finally, for photons with energies above $2m_ec^2 = 1.022\ MeV$, *pair production* becomes possible, where the photon is absorbed and converted into an electron-positron pair. In any of these processes, what really matters for detection is that electrons (and, in the case of pair production, also positrons) are released inside the semiconductor. These secondary particles then cause the actual ionization, generating the electron-hole pairs that generates the detectable signal.

Since, this thesis mainly focuses on the process of photo-electric effect, therefore, the energy of an electron ejected through the photo-electric effect is described by:

$$E_e = h\nu - E_b \tag{1.31}$$

where E_e is the kinetic energy of the emitted electron, h is the Planck's constant, ν is the frequency of photon, and E_b is the binding energy of the electron within its atomic shell.

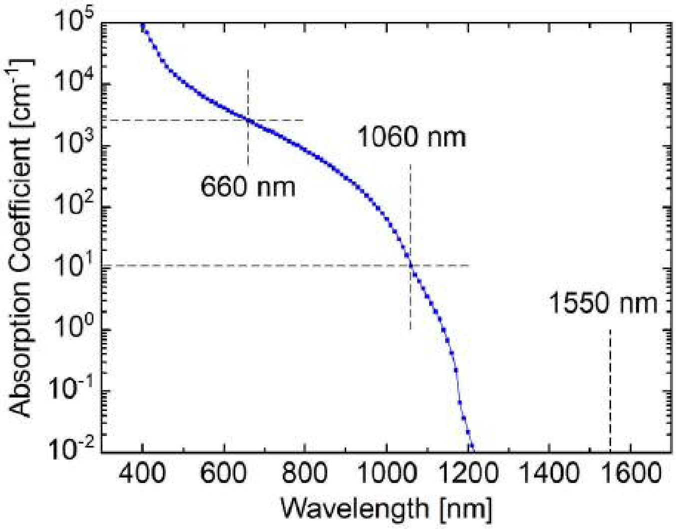

Figure 1.8: Absorption coefficient of silicon against the photon wavelength. The photon wavelengths used in this thesis are marked here [29].

When a photon travels through the silicon bulk, its probability of getting absorbed increases with the increase in depth, resulting in a decrease in light intensity. This reduction follows the Beer-Lambert law:

$$I(x) = I_0 e^{-ax} \tag{1.32}$$

In Eq. 1.32, x is the depth of silicon and $I(x)$ is the intensity at that depth, and a is the absorption coefficient, which depends on the material properties and the wavelength of the photon. Figure 1.8 shows the absorption coefficient versus photon wavelength in silicon.

1.5 Signal formation

When an external electric field is applied to the detector through a bias voltage, the signal is generated by the motion of charge carriers drifting through the silicon bulk toward their respective electrodes with a velocity $\vec{v}_{dr}(\vec{E}(\vec{r}(t)))$, as shown in Figure 1.9. For detectors with more complex geometries, the induced charge can be determined using the Shockley-Ramo theorem [30].

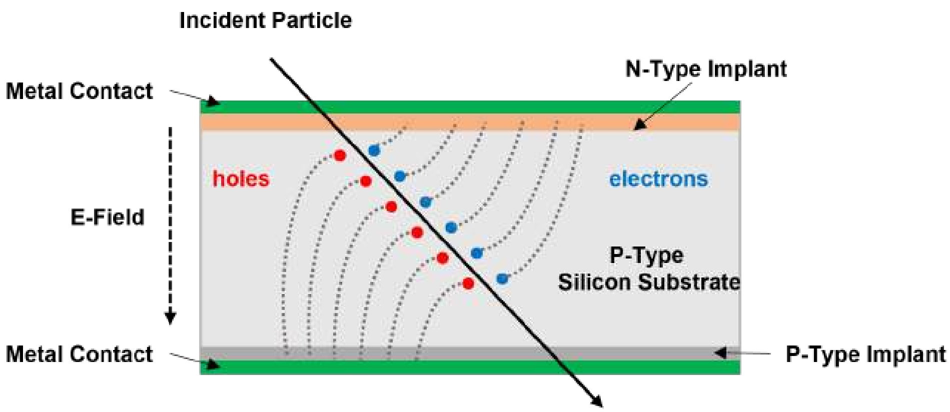

Figure 1.9: Structure of a simple photodiode, showing the charge collection and signal formation from a traversing particle.

This method introduces the concept of the *weighting field*, $\vec{E}_w$, a vector quantity that describes how a charge at a particular point inside the detector couples electrostatically to its electrodes. The associated *weighting potential*, U_w, is obtained by solving Laplace's equation ($\Delta^2 U_w = 0$) under the condition that the sensing electrode is set to unit potential while all others are grounded. From this solution, the weighting field can then be derived as:

$$\vec{E}_w = -\Delta U_w \tag{1.33}$$

The instantaneous signal current induced on the sensing electrode by a point charge q at a given position in the detector, moving with drift velocity $\vec{v}_{dr}$, can be expressed as:

$$i = q\vec{E}_w \cdot \vec{v}_{dr} \tag{1.34}$$

If the charge q travels along a path from its initial position r_0 to a later position $r(t)$, then using Eq 1.33 the total induced charge on the sensing electrode, Q_s, can be written as:

$$Q_s = \int_{t=0}^{t} I\,dt = q\int_{t=0}^{t} \vec{E_w}\vec{v}_{dr}\,dt = q\int_{\vec{r}_0}^{\vec{r}(t)} \vec{E_w}\vec{v}_{dr}\,dt = q\left[U_w(\vec{r}) - U_w(\vec{r}_0)\right] \tag{1.35}$$

As an example, consider a semiconductor detector with a simple parallel-plate geometry (i.e., a non-segmented pad detector). In this case, the electric field is approximately uniform, and solving the Laplace equation gives a linear form for the weighting field: $E_w = -1/d$. As a result, the induced current can be expressed as:

$$i = qv_{dr}E_w = q\mu\frac{V_b}{d}\cdot\frac{1}{d} = q\mu\frac{V_b}{d^2} \tag{1.36}$$

Because both the electric field and weighting field are uniform across the bulk, the induced current remains constant until the charge carriers reach their respective electrodes.

1.6 Radiation damage in silicon

As explained in the section 1.4, radiation can interact with matter by exciting electrons in the lattice, promoting them from valence band to the conduction band and thereby creating electron-hole pairs. Beyond this, radiation may transfer energy directly to the nucleus. If the incoming particle has the energy above the threshold, it can displace atoms from their lattice sites, leading to structural damage. In extreme cases, this process can trigger a chain reaction, causing multiple defects.

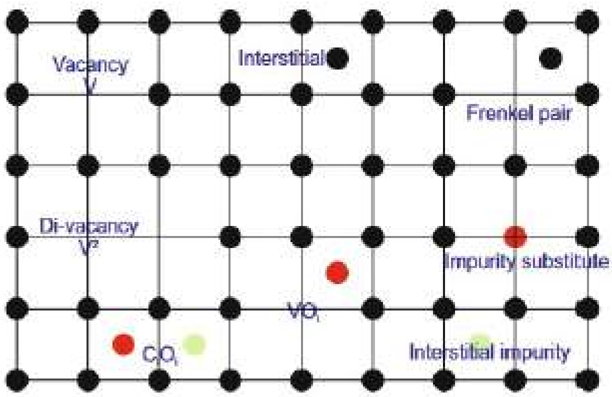

Figure 1.10: Graphical representation of the different type of lattice defects that non-ionizing effects can create in the silicon lattice [31].

Interstitial (I) occur when atoms are displaced into positions outside their normal lattice sites, while *vacancies (V)* represent empty lattice positions where atoms are missing. When several vacancies or interstitial defects are close together, they can form more complex configurations such as bi-vacancies (I^2/V^2), triple defects (I^3/V^3), and so on. A combination of an interstitial and a vacancy is known as a *Frenkel pair*. In some cases, an incoming charged particle may even replace a lattice atom altogether, producing what is called a *substitutional impurity*. Examples of these defect types are shown in Figure 1.10.

The number of defects created in the silicon bulk strongly depends on both the type and the energy of the incident radiation. To allow for a consistent comparison of the damage caused by different particles and energies, the *Non-Ionizing Energy Loss (NIEL) hypothesis* is commonly used. This framework takes into account the amount of energy deposited in the material that does not contribute to ionization but instead leads to atomic displacements and defect formation, independent on the type and energy of the particle. This energy is calculated using the the displacement damage function $D(E)$ given in Eq. 1.37.

$$D(E) = \sum_i \sigma_i(E_{\text{kin}}) \int_0^{E_{R,\max}} f_i(E_{\text{kin}}, E_R) P(E_R)\, dE_R \tag{1.37}$$

where σ_i is the cross-section of the interaction type i, $f_i(E,T)$ is the probability of a collision with a kinetic energy E_{kin}, transferring a recoil energy E_R, and $P(E_R)$ is the Lindhard partition function, which describes the fraction of energy used to displace a silicon atom. For instance, $P(E_R)$ is about 50 % for 10 MeV protons and around 42 % for 24 GeV protons.

Figure 1.11 shows the displacement damage function D(E) normalized to 95 MeV mb for neutrons, protons, pions and electrons. The standard reference for radiation damage is neutrons with 1 MeV of energy, so the standard unit of fluence levels is the *neutron equivalent fluence*, expressed in units of $n_{1,\text{MeV}}/\text{cm}^2$. A conversion factor κ is applied to translate the radiation damage caused by any particle type and energy into the equivalent damage expected from 1 MeV neutrons.

$$\kappa = \frac{\int D(E)\phi(E)\, dE}{95\,\text{MeV} \cdot \text{mb} \cdot \phi} = \frac{\phi_{\text{eq}}}{\phi} \tag{1.38}$$

where $\phi = \int \phi(E)\, dE$ is the total irradiation fluence, and ϕ_{eq} is calculated with units

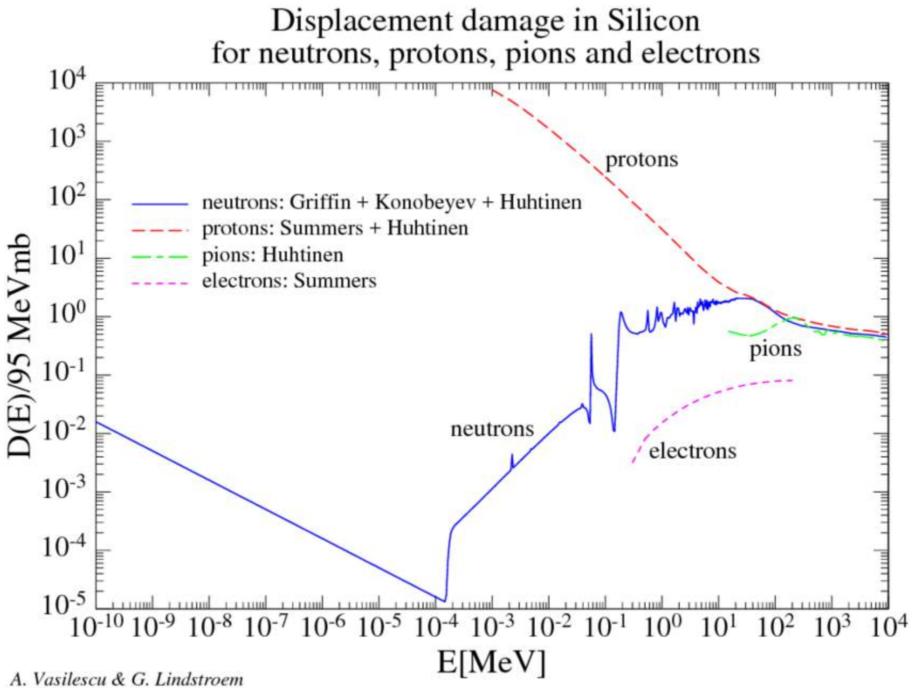

Figure 1.11: Displacement damage function D(E) normalized to 95 MeVmb for neutrons, protons, pions and electrons [32].

of $[\phi_{eq}] = n_{1MeV}/cm^2$, usually written as n_{eq}/cm^2, by:

$$\phi_{\text{eq}} = \kappa\phi = \kappa \int \phi(E)\, dE \tag{1.39}$$

Energy levels in the bandgap are created by the collective effect of the defects that are explained earlier in this section, leading to several macroscopic effects which are described in the following sections.

1.6.1 Increase in depletion voltage

When silicon wafers are exposed to radiation, the atoms in the crystal are displaced from the lattice points, causing them to alter their behavior as donors or acceptors. Therefore, the effective doping changes with irradiation. For n-type silicon, the effective doping concentration decreases until it becomes intrinsic silicon, and after this point it starts increasing with fluence, known as *type inversion* [33], as shown in Figure 1.12. This inversion occurs due to the reduction of donor and acceptor activities [34], and the defects themselves start behaving as donors and acceptors, resulting in a net p-type doping concentration. These changes in effective doping concentrations increases the voltage required to fully deplete the detector thickness.

1.6.2 Increase in leakage current

Defects in silicon that acts as acceptors change the effective doping of the silicon bulk. Thus, the leakage current depends on the density of carriers with in the bulk. Therefore, changes in effective doping concentration will increase the leakage current in the bulk, as shown in Figure 1.12. This increase can be expressed as:

$$\frac{\Delta I}{V} = \alpha \phi_{eq} \tag{1.40}$$

where ΔI is the change in leakage current before and after irradiation, V denotes the active volume, α represents the damage rate related to current, which is estimated to $4 \cdot 10^{-17} A/cm$ [13], and ϕ is the fluence equivalent to 1MeV neutrons.

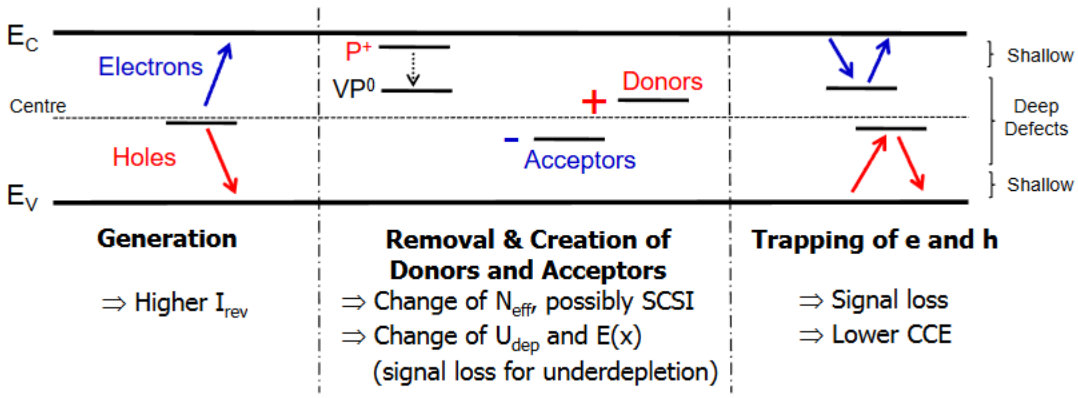

Figure 1.12: Effects of defect levels in the band gap on electrical properties and macroscopic detector parameters: increase in leakage current (left), increase in depletion voltage (middle), decrease in charge collection (right) [35].

1.6.3 Decrease in charge collection

Non-ionizing effects can introduce defects that acts like charge traps, which may trap the charge carriers generated by ionizing particles and release them later. Experimentally, it is demonstrated that charge trapping time has linear dependence with lower fluences, which changes at higher fluences [36].

$$\frac{1}{\tau_{eff,e,h}} = \beta_{e,h} \phi_{eq} \tag{1.41}$$

where β is the traps introduction rate, with

$$\beta = \begin{cases} (4.2 \pm 0.3) \cdot 10^{-16}\,\mathrm{cm}^2/\mathrm{ns} & \text{for electrons} \\ (6.1 \pm 0.3) \cdot 10^{-16}\,\mathrm{cm}^2/\mathrm{ns} & \text{for holes} \end{cases} \tag{1.42}$$

Charge Collection Efficiency (CCE) describes how much charge is actually collected in a detector after irradiation compared to before. If some of the charge carriers get trapped and released too late - outside of the time window when the signal is measured - they will not be taken into the account, hence, reducing the charge collection efficiency, as shown in Figure 1.12. For example, at LHC, the bunch crossing time is 25 ns, which is much larger than the de-trapping time [37]. As a result, more defects and trapped carriers build up, and the collected charge decreases. CCE is defined as:

$$CCE = \frac{Q_{irr}}{Q_0} \tag{1.43}$$

where Q_0 and Q_{irr} are the charges collected before and after irradiation, respectively.

1.6.4 Annealing

Just like silicon atoms can be replaced from their lattice positions, defects inside the bulk material can also move around. These defects may interact with other defects or impurities, forming new structures or even canceling each other out, for example, when a Frenkel pair recombines and fills a vacancy. This process is known as *annealing*, and it depends heavily on temperature. Higher temperature give defects more energy to move, which increases the rate of interaction, while lower temperatures slow down this process.

Annealing affects the material's behavior in three stages. First, short-term annealing helps remove the most mobile defects, which lowers both the leakage current and the full depletion voltage. Then, during the stable phase, the space charge concentration begins to rise. In the final stage, called reverse annealing, the space charge concentration continues to increase [13]. Figure 1.13 shows how the doping concentration changes over time. Typically, newly irradiated sensors are exposed to 60°C for 80 minutes for a beneficial annealing.

Besides doping concentration, annealing also influences leakage current and CCE. Leakage current always goes down with annealing . Short-term annealing can slightly improve or maintain CCE, while long-term annealing tends to reduce it due to increased

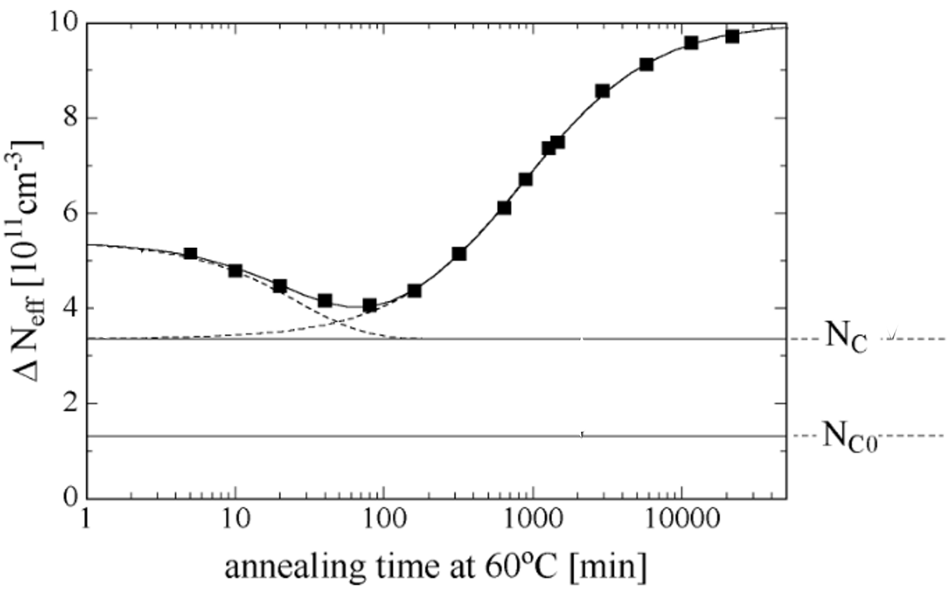

Figure 1.13: Variation of the doping concentration versus annealing time. Figure adapted from [13].

in full depletion voltage.

1.7 Detector technologies

The development of semiconductor detectors was enabled by advancement in crystal growth and microfabrication techniques, which allowed the production of high-purity silicon and reliable detector structures. These detectors are typically fabricated using planar technology, first introduced by Kremmer in 1980 [38,39], and are commonly produced as pad or pixel detectors, depending upon the electrode geometry.

Silicon detectors are widely used in high-energy physics because they combine good energy and spatial resolution with fast response times. To obtain position information, detector electrodes can be segmented so that the signal collected depends on where the ionization occurs, for further help in the track reconstruction of the incoming particle.

1.7.1 PIN diode

The PIN diode represents an evolution from the basic p-n junction, optimized for efficient charge collection and high-speed response in radiation detection. It consists of a lightly doped intrinsic layer (I) inserted between p^+ and n^+ regions, effectively increasing the depletion width. This intrinsic region ensures that under reverse bias, a large volume of the detector is fully depleted even at lower voltages, allowing efficient collection of charge carriers generated by the ionizing particles or photons.

In comparison to the standard p-n diodes, PIN structures exhibit lower junction capacitance, higher sensitivity, and faster timing response, making them suitable for detecting mips and low-energy X-rays.

PIN diodes form the technological foundation for more advanced detectors with internal multiplication. Charge multiplication in semiconductors is a well-known process, arises due to the avalanche process, where charge carriers accelerated by a strong electric field gain enough energy to cause impact ionization, generating additional electron-hole pairs. This internal amplification mechanism is utilized in several silicon-based detectors, like, Avalanche Photodiodes (APDs) with gain around 100s, and Low Gain Avalanche Didoes (LGADs) providing moderate gains of the order of 10s. LGADs have emerged as a development of traditional APDs, with a finely engineered doped gain layer that enable controlled low-level multiplication. In the following sections, the development of LGADs and its flavors for high granularity to mitigate fill-factor limitations will be discussed.

1.7.2 Low Gain Avalanche Diodes

Low-Gain Avalanche Diodes (LGADs) are silicon-based detectors recognized for their internal charge multiplication via impact ionization, typically achieving a low gain of $\mathcal{O}(10)$ [40]. LGADs are based on an n-on-p structure with an additional highly doped p^+ layer sandwiched between the p-bulk and the n-implant ($n^{++} - p^+ - p - p^{++}$), resulting in a high field at the junction between the n^{++} and p^+ layers. The typical doping concentration ranges of p/n, p^+/n^+, p^{++}/n^{++} doped regions are 10^{12} - 10^{13}, 10^{15} - 10^{18}, 10^{18} - 10^{20} cm^{-3}, respectively. Schematics of pin diode and LGAD is shown in Figure 1.14. The doping profile is carefully designed to create an electric field that is high enough to cause impact ionization, and hence charge multiplication, producing larger signals than those from a PIN diode. Subsequently, this enhances the signal-to-noise ratio (SNR), enabling LGADs to produce signals large enough to be separated from the noise, thereby improving the detection efficiency for low-energy or minimally ionizing particles. In the past decade, extensive research and development have been carried out to enhance the spatial and timing resolution of LGADs for precise track reconstruction and to develop these detectors to withstand extreme radiation fluences. 50 μm thick LGADs have demonstrated the capability to achieve timing resolutions below 30 ps [41,42], and tolerate radiation fluences exceeding 10^{15} n_{eq}/cm^2 [43]. LGADs, with their exceptional properties, are not only a candidate for future HEP experiments but also valuable in the fields of synchrotron, medical, and space applications [15,44–46].

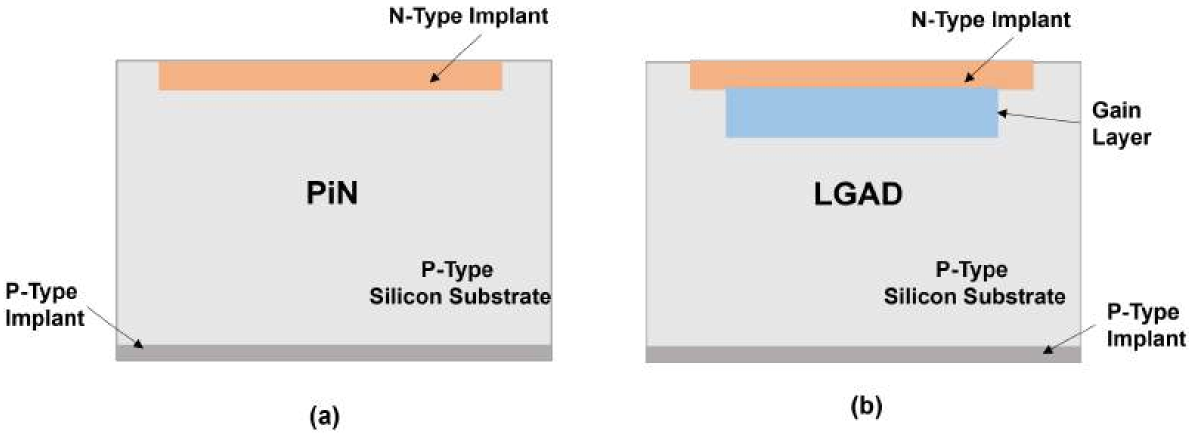

Figure 1.14: Schematics of (a) PiN diode, and (b) standard LGAD structures.

LGADs show strong potential as a key technology for advancing 4D tracking applications [47,48], but are limited by the coarse segmentation of current technologies. To prevent early device breakdown from high electric fields near the periphery of the segmented junction electrodes, standard LGADs incorporate a deep n^+ implantation known as a Junction Termination Extension (JTE), and electrical isolation between the pads is achieved by a p^+ implant (p-stop or p-spray) [49]. A schematic view of the standard LGAD with termination structures is shown in Figure 1.15.

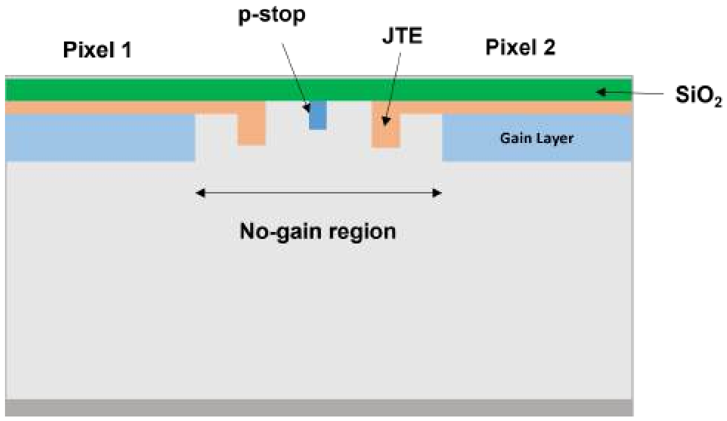

Figure 1.15: Schematics of a pixelated standard LGAD with JTE and p-stop.

There is a discontinuity in the gain layer near the JTE and p-stop implants, which makes this region a *no-gain* area. The gap between the gain layer implants is called the *Inter-Pixel Distance* (IPD). Electrons generated by a laser or a mip that drift into the no-gain region do not experience multiplication, which results in reduced charge detection efficiency [50], consequently, reducing the fill factor (FF). The FF is defined as:

$$FF = \frac{pixel\ area\ with\ multiplication}{total\ pixel\ area} \tag{1.44}$$

The intrinsic trade-off between spatial segmentation and uniform gain has driven the development of several LGAD variants, each aiming to enhance FF and maintain uniform gain across finely segmented geometries, are further discussed in the forthcoming sections.

Inverse-LGAD (iLGAD)

The inverse-LGAD (iLGAD) represents one of the earliest architectural modifications to address the issue of fine-segmentation and increased FF. In an iLGAD, the segmentation is transferred from the multiplication side (n^{++}) to the ohmic side (p^{++}). This design maintains a continuous multiplication layer and n^{++} electrode, ensuring a uniform high-field region across the entire device surface, as shown in Figure 1.16 [51]. This architecture requires double-sided processing on fully depleted float zone (FZ) substrates, which cannot have a thickness as thin as 50 μm due to difficulties in fabrication. In this way, a 100% FF is achieved. However, the timing resolution is worsened due to a thicker active volume [52].

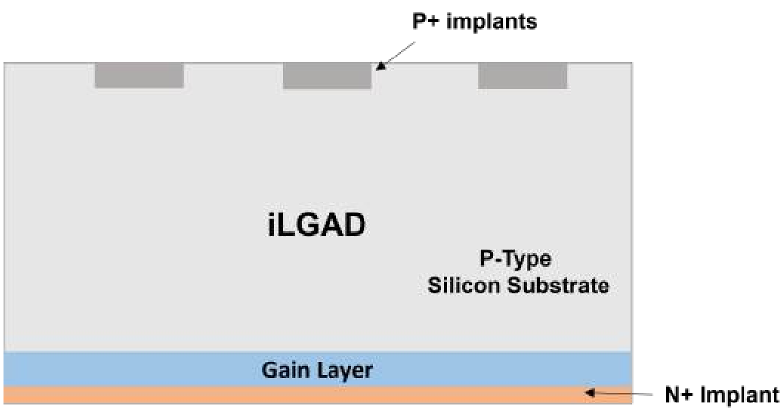

Figure 1.16: Schematics of an inverse LGAD (iLGAD).

AC-LGAD

To overcome the compromise on timing performance, a newer concept known as the AC-LGAD was developed [53]. In this configuration, the n^{++} electrode is made resistive, and a thin dielectric (typically SiO_2 or Si_3N_4) is deposited on top, separating the readout metal pads from the resistive surface. The signal is capacitively coupled from the resistive electrode to the metal readout pads, while charge carriers are collected at the continuous n^{++} layer underneath. Because the gain layer and the n^{++} region are both continuous, the AC-LGAD achieves nearly 100% fill factor while allowing fine segmentation to be defined on the metal pads, as shown in Figure 1.17. This design enable two-dimensional position reconstruction through charge sharing between neighboring pads, as the induced current spreads laterally through the resistive layer. The AC-LGAD concept has demonstrated timing resolutions below 35 ps and spatial resolutions better than 30 μm in prototypes developed at Fondazione Bruno Kessler (FBK), Centro Nacional de Microelectrónica (CNM) and Brookhaven Nationa Laboratory (BNL), making it one of the most promising architectures for 4D tracking applications HEP experiments.

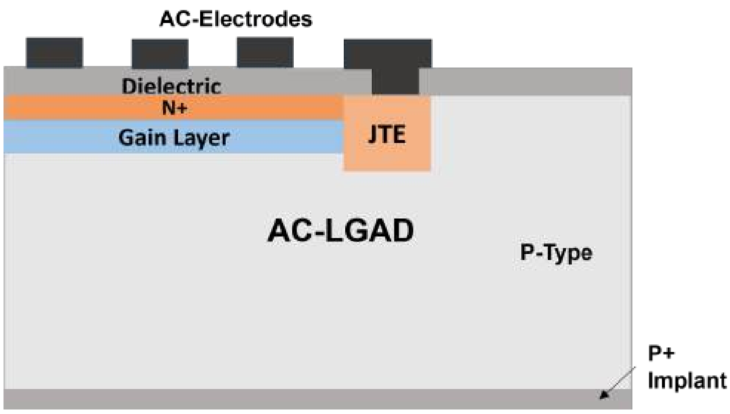

Figure 1.17: Schematic depiction of a part of segmented AC-LGAD (not to scale).

The Resistive Silicon Detector (RSD) builds on the AC-LGAD design by adding resistive and dielectric layers that allow for continuous two-dimensional signal tracking. This structure supports combined spatial, and timing measurements by spreading the induced charge across multiple electrodes. Devices made on 50 μm thick epitaxial silicon have shown fill factors above 98% and time resolutions in the range of 28–32 ps for single mip signals [54].

Deep-Junction LGAD

Another innovative modification is the Deep-Junction LGAD (DJ-LGAD) [55], where the multiplicatoin layer is buried deeper inside the silicon bulk, typically several microns below the surface. This configuration decouples the gain region from electronics at the surface and isolation structures, as shown in Figure 1.18. Additionally, the deeper gain layer provides enhanced radiation tolerance, as surface damage and oxide charge at the interface have reduced influence on the device behavior. The DJ-LGAD, however, requires complex ion implantation and annealing steps to precisely position the buried gain layer, and the deeper field location slightly increases the charge collection time, impacting ultimate timing precision.

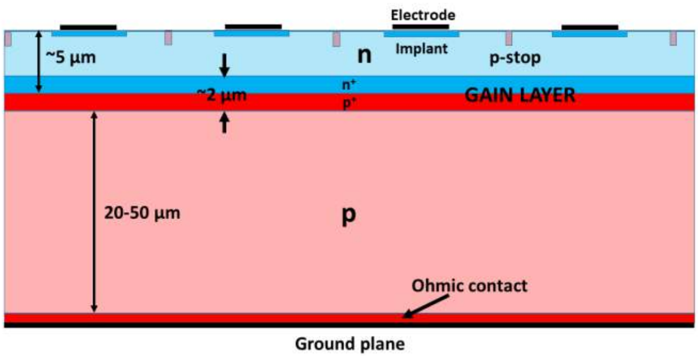

Figure 1.18: Schematic depiction of deep-junction LGAD (DJ-LGAD) [55].

Trench-Isolated LGADs

A significant part of this thesis focuses on an alternative segmentation architecture, known as Trench-Isolated LGAD (TI-LGAD). This architecture has been extensively implemented in CMOS technology [56] as well as in silicon photomultipliers [57] over the years. In this technique, electrical isolation to avoid crosstalk between pixels is achieved by etching physical trenches in the silicon substrate which are subsequently filled with silicon oxide [11,58]. TI-LGADs replace the pixel periphery, consisting of the JTE and p-stop/p-spray, with a single narrow trench ($\approx$ 1-2 μm wide), potentially reducing the IPD to < 10 μm [59]. The schematics of TI-LGAD can be seen in Figure 1.19 compared to the standard LGAD.

TI-LGADs enable IPD to be reduced to a few microns allowing fine segmentation of pixelated devices with a FF $> 90\%$ for 4D tracking applications [60]. In addition to the

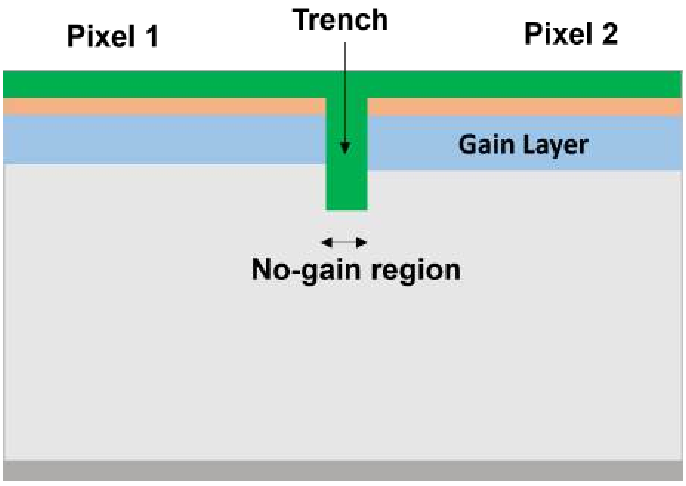

Figure 1.19: Schematic depiction of trench-isolated LGAD (TI-LGAD). Image is not to scale.

efforts put in by FBK in producing several batches of TI-LGADs [61], this work focuses on the development of TI-LGADs by Micron Semiconductors Ltd., UK. In this work, extensive simulation studies are performed using Sentaurus TCAD to optimize the trench parameters, FF, and electrical isolation. Measurements carried out using the Transient Current Technique (TCT) to probe the inter-pixel electrical isolation are discussed along with the calculations of IPD and FF.

1.7.3 3D detector

A novel detector architecture, first proposed by [62], offers several advantages over traditional planar designs by employing a three-dimensional configuration. In this design, the p^+ and n^+ electrodes penetrate through the silicon bulk instead of being confined to the detector surface on the opposite sides [63]. A schematic comparison is shown in Figure 1.20.

In 3D design, the electric field is oriented parallel to the detector surface, which significantly reduces the charge collection distances, leading to faster collection times and reduced full depletion voltages by roughly an order of magnitude for 300 μm thick detectors. These exceptional properties make 3D detectors particularly attractive to be used in extreme radiation environments.

However, the 3D design also presents certain challenges. Fabrication is more complex, and the detectors generally exhibit higher capacitance, leading to an increased electronic

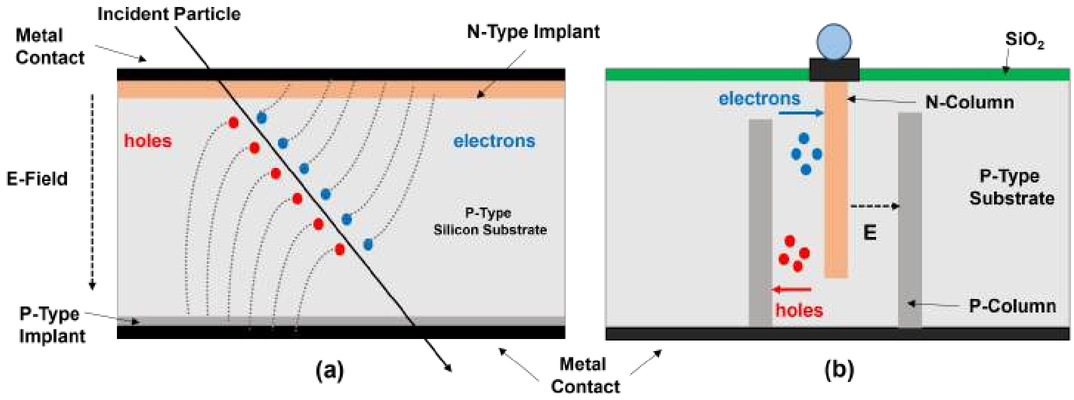

Figure 1.20: Comparison of a PiN diode (a) and 3D column detector (b). Image is not to scale.

noise. Additionally, regions with relatively low electric fields may exist within the structure. Optimizing the production process remains essential to achieve uniform performance and maintain acceptable manufacturing costs.

Chapter 2

Experimental techniques

To gain a deeper understanding of the physics underlying the different detector types and geometries, as well as to study their properties after fabrication, and how these properties evolve before and after irradiation, a range of experimental techniques has been developed. The key parameters are the full depletion voltage (V_{FD}), breakdown voltage (V_{BD}), leakage current (I_{leak}), and charge collection (CC). Monitoring how these parameters change over time helps in understanding how the detector degrades and supports accurate modeling of its performance before and after irradiation.

This chapter describes the electrical and laser-based characterization methods used to extract the key parameters discussed above, which form the basis for analyzing the experimental results in this study.

2.1 Electrical characterization (I/V & C/V)

Electrical characterization is a fundamental approach for evaluating the properties of silicon detectors. It is also widely used by manufacturers as a part of quality assurance (QA) procedures to detect fabrication defects and ensure the reliable operation of the device within desired limits. A straightforward method involves measuring I_{leak} and capacitance, as a function of applied reverse bias voltage − commonly referred to as I/V and C/V measurements. These measurements provide key parameters like V_{BD}, I_{leak} (using the I/V measurements) and V_{FD}, capacitance and effective doping concentration (N_{eff}) (using C/V measurements). The measurement procedure is described in the following section.

2.1.1 Methodology

A reverse-biased silicon detector can be modeled using an equivalent circuit consisting of a capacitor in parallel with a resistor (representing leakage current), connected in series with another resistor that accounts for the undepleted bulk. As reverse bias increases, the depletion region expands, increasing the distance between electrodes and reducing the capacitance. Once full depletion is achieved, the capacitance stabilizes. The undepleted bulk behaves as a resistor whose value also changes with bias voltage, making this model useful for interpreting detector behavior under varying conditions.

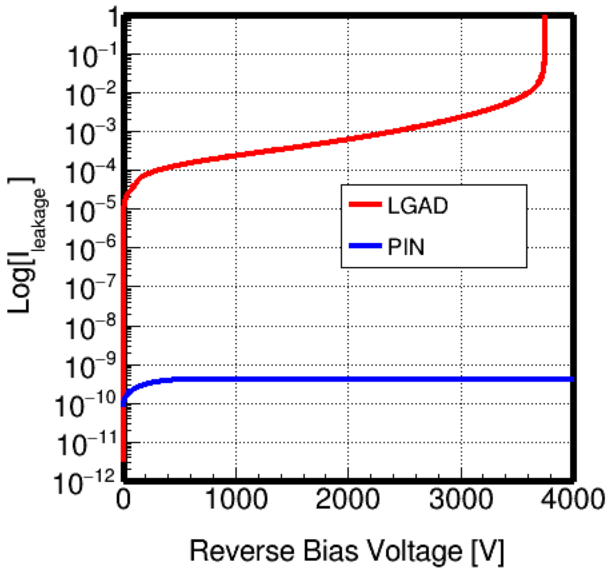

Figure 2.1: Example of an IV measurement of PiN and LGAD [64].

The I/V measurements involve applying a reverse bias voltage across the detector and recording the resulting leakage current. This current is primarily due to thermally generated carriers in the depleted region and is sensitive to material quality, temperature, and radiation-induced defects. The measurement is usually performed using a precision source-meter unit (SMU), which incrementally increases the bias voltage while simultaneously measuring the current. The point where the leakage current begins to rise sharply is identified as the breakdown voltage, indicating the onset of avalanche multiplication. To prevent permanent damage to the device structure, a compliance limit is set on SMU, typically between 10 μA and 1 mA. An example of an I/V measurement is shown in

Figure 2.1.

Capacitance is measured using an LCR meter, which applies a small AC signal superimposed on a DC bias. The amplitude and frequency of the AC signal can be set according to the requirements to get appropriate results. Capacitance is recorded as a function of increasing reverse bias, and the data is converted to - and plotted as inverse-squared capacitance ($1/C^2$) versus bias voltage. The full depletion voltage is extracted from the intersection point between the linear and the plateau region, corresponding to the transition from partially to fully depleted operation, as shown in Figure 2.2. Using the known dielectric properties and thickness of the silicon detector, N_{eff} can also be calculated from the slope of the linear region.

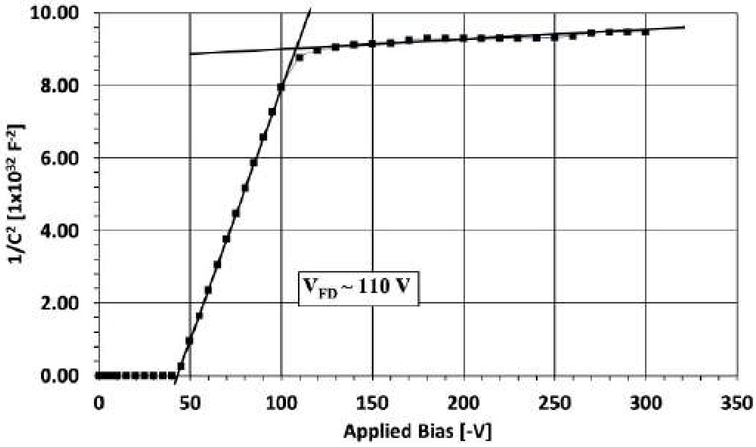

Figure 2.2: Example of CV measurement of LGAD, and method of extraction of full-depletion voltage [65].

2.2 Laser characterization

Laser characterization techniques offer a non-invasive and highly localized method for probing the internal response of silicon detectors. By injecting focused laser pulses into the sensor, these methods simulate the passage of charged particles and allow precise measurement of charge collection dynamics, timing resolution, and spatial uniformity.

One of the key laser-based techniques used throughout this work for sensor characterization is the Transient Current Technique (TCT). In TCT, a short laser pulse is focused onto the detector surface to generate electron-hole pairs. These carriers drift under the influence of the internal electric field, inducing a transient current that is measured using a fast readout system. The amplitude, timing, and shape of the current signal reflect the properties of the sensor, such as carrier mobility, electric field uniformity, and trapping effects. Two configurations of TCT are employed in this work: Single-Photon Absorption TCT (SPA-TCT) and Two-Photon Absorption TCT (TPA-TCT). The following sections provide a detailed description of each method and its implementation.

Before going into the details of the TCT systems, properties of the laser beam and its propagation in silicon are described in the following sections.

2.2.1 Properties of Gaussian laser beam

A Gaussian beam is a type of electromagnetic radiation whose transverse electric field and intensity profiles follow Gaussian distributions. When passed through a lens or lens system, it remains a Gaussian beam but with modified parameters, making this model highly practical and widely used in laser optics.

The beam propagates symmetrically along its axis, with intensity described as:

$$I(r, z) = I_0 \cdot \exp\left(-2 \cdot \frac{r^2}{\omega^2(z)}\right) \tag{2.1}$$

where I_0 is the peak intensity at the beam waist, r is the radial distance from the beam axis, and $\omega(z)$ is the beam radius at position z, defined as the distance from the axis where the amplitude drops to $1/e$, or irradiance to $1/e^2$, of its peak value.

The beam radius evolves along the propagation direction according to:

$$\omega(z) = \omega_0 \cdot \sqrt{1 + \left(\frac{z}{z_R}\right)^2} \tag{2.2}$$

where ω_0 is the minimum beam radius at the waist, and $z_R = \frac{\pi n \omega_0^2}{\lambda}$ is the Rayleigh range [66], with λ being the wavelength of the laser in the propagation medium and n is the refractive index of that medium. Figure 2.3 shows how the Gaussian beam width $\omega(z)$ evolves with distance z along the propagation axis, and highlights key beam parameters described earlier.

For practical analysis, the beam width is often expressed in terms of Full Width at

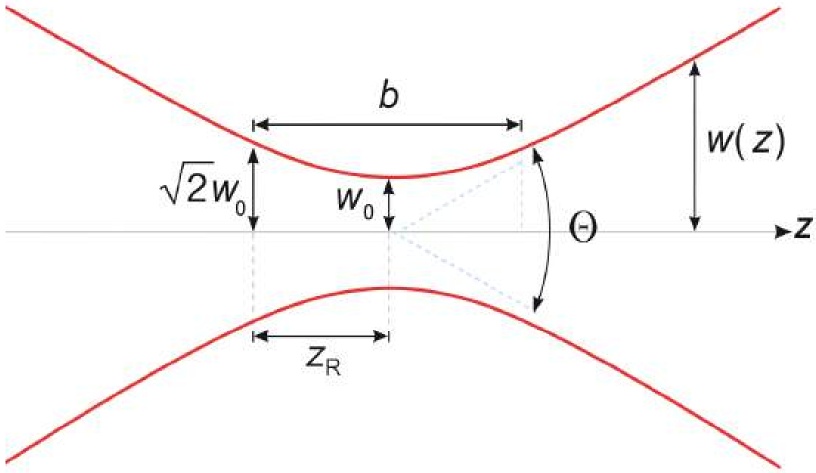

Figure 2.3: Gaussian beam width as a function of distance z along the beam [66].

Half Maximum (FWHM), which relates to the standard deviation σ of the Gaussian distribution as:

$$\text{FWHM} = 2\sqrt{2\ln 2\sigma} \approx 2.35\sigma \tag{2.3}$$

These relationships are essential for estimating the laser spot size and FWHM from the induced current signals in TCT measurements [67].

2.2.2 Propagation of laser in silicon

When a photon enters a semiconductor, it can be absorbed if its energy E_ν exceeds the bandgap E_g. In this case, the photon transfers its energy to an electron, generating an electron-hole (e-h) pair through the photoelectric effect, as explained in section 1.4.2. As the photon beam propagates through silicon, its intensity decreases exponentially with depth z, following:

$$I(z) = I_0 \cdot \exp(-\alpha z) \tag{2.4}$$

where I_0 is the initial intensity and α is the absorption coefficient, which represents the probability of photon absorption per unit length. Figure 2.4 represents experimental data showing how the penetration depth $a = 1/\alpha$ and the mean depth of energy loss vary with photon wavelength near the band edge of silicon [68]. For silicon, the bandgap is

$E_g = 1.12\ eV$, corresponding to a wavelength of approximately 1130 nm. At a wavelength of 1060 nm, the penetration depth is about 800 μm, while the mean energy loss occurs around 130 μm.

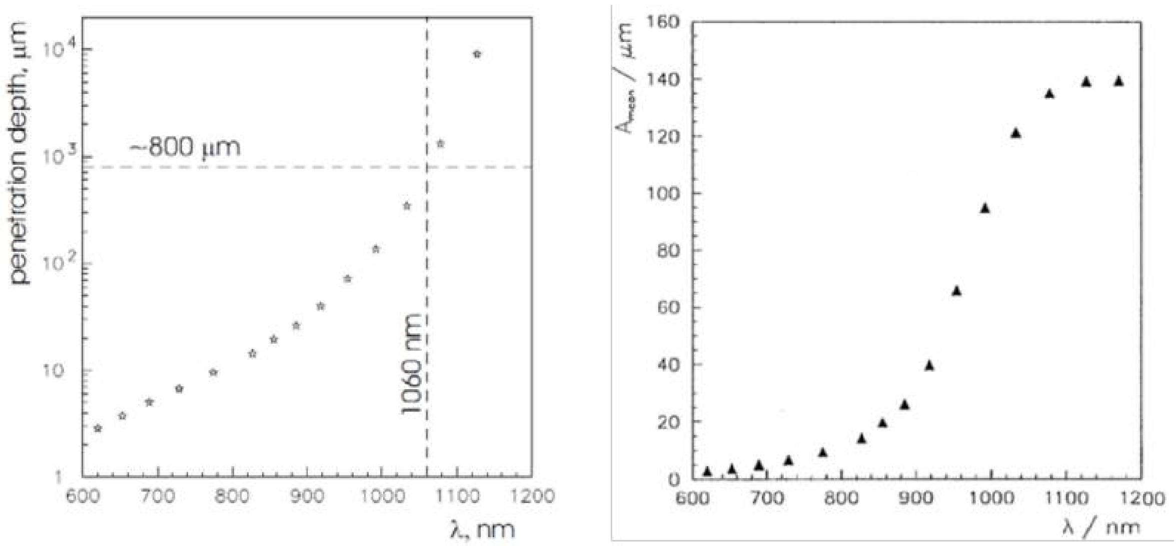

Figure 2.4: Penetration depth of light in silicon depending on the wavelength of a photon (left) and mean depth of energy loss (right). Measurements performed at 298K in high-purity silicon [68].

When a collimated laser beam at 1060 nm passes through a 300 μm thick silicon detector, it generates a cylindrical distribution of e–h pairs along the beam path. This resembles the charge deposition profile of a mip [69], making it a useful tool for simulating particle interactions in silicon detectors.

2.2.3 Transient Current Technique (TCT)

The fundamental principle of the TCT is to generate localized charge carriers within a semiconductor detector and measure the resulting transient current induced by their motion under an applied electric field. This current signal, recorded with sub-nanosecond resolution, carries rich information about the internal electric field distribution, carrier drift velocities, trapping dynamics, and overall charge collection behavior of the device.

By analyzing time evolution and amplitude of the induced current pulse, several above mentioned parameters can be extracted. These quantities are particularly relevant for assessing the impact of radiation damage, validating sensor design, and optimizing operation conditions.

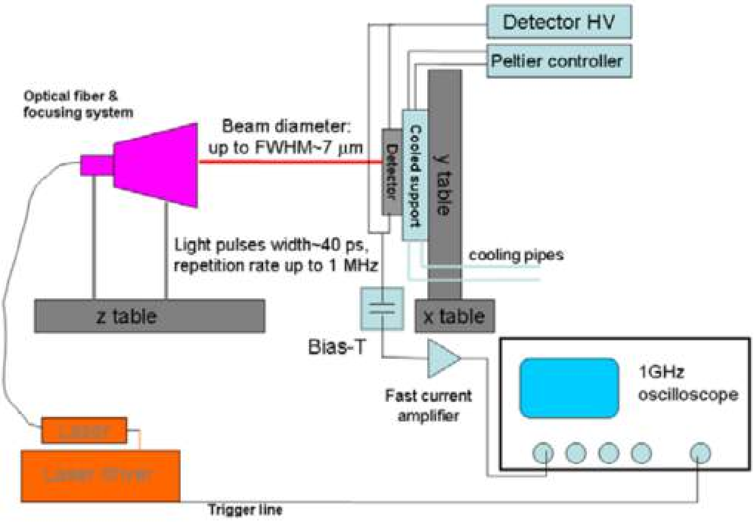

Figure 2.5: Schematic view of the experimental TCT Setup [67].

TCT setup

The TCT setup used in this work is commissioned in AGH University of Krakow, provided by *Particulars* from JSI, Ljubljana [70]. Schematics of the setup are shown in Figure 2.5.

The sensors are mounted on a thermally regulated stage structure composed of aluminum for temperature-dependent measurements, which ensures stable thermal contact during measurements. Temperature control is achieved using a quad 40 W Peltier thermoelectric cooler, capable of maintaining the sample environment within a range of –20°C to 60°C. A custom-built temperature controller regulates the Peltier elements, allowing precise thermal stabilization—particularly important for measurements on irradiated sensors where leakage current and carrier mobility are temperature-sensitive.

High-voltage biasing is provided by a Keithley 2410 source meter, connected to the device under test via a bias-T (Picosecond Pulse Labs, Model 5531). The bias-T serves to decouple the high DC bias from the readout path, allowing simultaneous application of bias voltage and extraction of the fast transient signal. The induced current signal is amplified using a wideband amplifier (MITEQ AM-1309) with a frequency range of 10 kHz to 1 GHz, and subsequently digitized using a 1 GHz bandwidth oscilloscope (Tektronix). To improve the signal-to-noise ratio, each waveform is averaged over several hundred laser pulse repetitions at each spatial scan point.

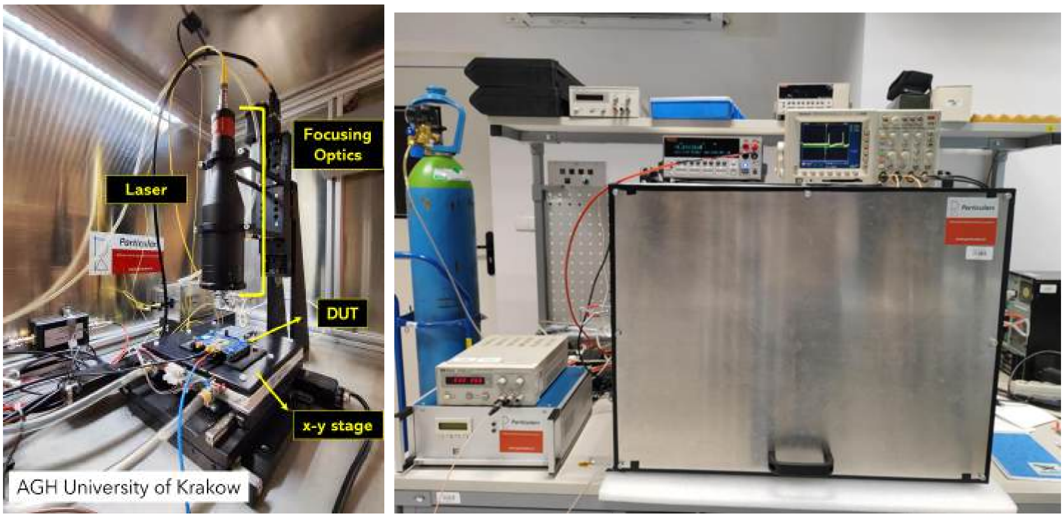

(a) (b)

Figure 2.6: Experimental TCT Setup at AGH University of Krakow (a) inside the TCT Faraday cage, (b) with instrumentation.

Charge carriers are generated using a pulsed red/infrared diode laser (Advanced Laser Diode Systems) operating at a wavelength of 660 nm and 1060 nm, respectively, with a pulse width of 40 ps and a repetition rate of 1 kHz (scalable up to 1 MHz). The short pulse duration is critical for mimicking the fast charge deposition of a mip traversing the detector. The laser beam is focused to a spot size of approximately 8-10 μm (FWHM) at the beam waist using a precision optical system. Beam positioning is controlled by three orthogonal motorized translation stages (XI-Lab), each offering sub-micron resolution. This configuration enables full 3D scanning of the laser injection point within the detector volume.

Photographs of the experimental setup, including the optical distance, focusing optics, sample mount, and translation stages, are provided in Figure 2.6.

Time resolution of TCT setup

This section is an extension of 2.2.3, where the integration of the time resolution measurement setup within the conventional TCT setup will be discussed. Since measuring time resolution with a laser system requires two pulses to have distinct signals, this is achieved by splitting the principal laser beam using an optical splitter. One of the resulting beams is routed through a 25-meter optical fiber, introducing a delay of approximately 120 ns. This ensures that both signals are separated temporally yet still fall in the same acquisition window of the oscilloscope.

The two beams are then combined by a splitter in reverse, which acts as a combiner, to produce a single output containing both pulses. Due to imperfections and losses in the splitting and combining processes, the resulting pulses may differ in amplitude. This imbalance is corrected by a manually tunable attenuator, which helps in maintaining the same amplitude for both pulses.

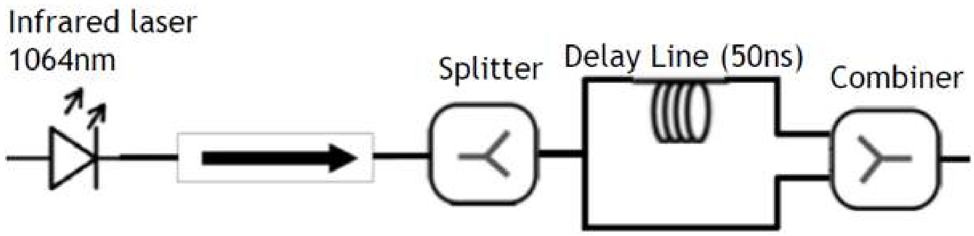

Figure 2.7: Schematic representation of the timing setup within TCT to create a delay in two pulses [71].

Additionally, the first splitter does not transmit 100% of the laser; therefore, an optical isolator is placed before the first splitter that only allows the laser to propagate in one direction and blocks back-reflected laser from reaching the laser generator. A schematic representation of the timing resolution setup is shown in Figure 2.7.

2.2.4 Two-Photon Absorption TCT

TPA technique, also referred to as two-photon excitation, is a technique to characterize sensors based on the simultaneous absorption of two photons. The photon can either have the same or different frequencies. This process excites carriers from initial to higher energy states according to the illustration shown in Figure 2.8. The phenomenon was first predicted by Maria Goeppert-Mayer in 1931 [72], and later confirmed experimentally in 1961 [73]. TPA-TCT is an advanced laser-based technique for characterizing silicon detectors with high spatial precision. Unlike SPA-TCT, which relies on linear absorption of photons with energies higher than the bandgap of silicon, TPA-TCT uses the photon energies within the bandgap and uses non-linear optical absorption. In this process, two photons are simultaneously absorbed at the focal point of a highly-focused femtosecond laser beam, generating e-h pairs only within a confined volume inside the detector bulk.

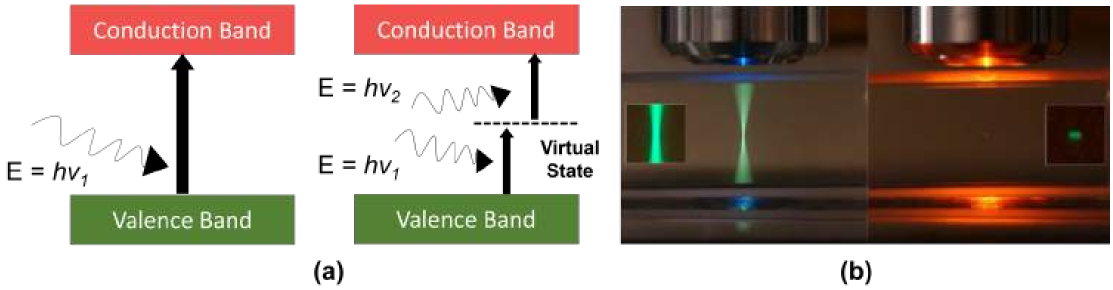

Figure 2.8: Comparison between SPA and TPA. (a) shows excitation of a molecule by a photon in SPA (left) and TPA (right), where E represents the photon energy. (b) shows the laser beam focus in SPA (left) compared to TPA (right) [74].

This non-linear absorption mechanism is highly localized, which occurs only around the beam waist, where photon density is sufficiently high. This brings us the three-dimensional control of where to inject the charge, allowing precise depth-dependent measurements of the electric field and charge collection efficiency. TPA-TCT is os particularly significant for studying sensors with complex geometries, buried structures, and irradiated regions. Another key advantage of TPA-TCT over SPA-TCT is its ability to probe the sensor without interference from the surface effects. TPA-TCT allows selective excitation at any depth, which helps in avoiding the metalization, passivation, and other implants to avoid reflections and scattering, and provides uniform and accurate measurements.

2.2.5 TCT setup at ELI beamlines

To have a better understanding of the results, the TCT setup at Extreme Light Infrastructure (ELI) Beamlines in Prague was used due to its advanced and high-precision components. The schematics of the setup are shown in Figure 2.9. This setup consists of a Titanium:Sapphire (Ti:Sa) laser source (Astrella, Coherent), which delivers femtosecond pulses at a repetition rate of 1 kHz, with pulse energies monitored using a calibrated power meter placed just before entering the objective lens to measure the precise laser power that is injected into the device under test. The fundamental wavelength of 800 nm corresponds to an mip when the laser is focused to $\sim 1.7\ \mu$m spot, creating a dense and localized charge deposition in LGAD with very short time intervals.

The measurement mechanism is similar to that explained in section 2.2.3, while the setup is explained in detail here. Reverse bias to the sensor is applied via a multi-channel

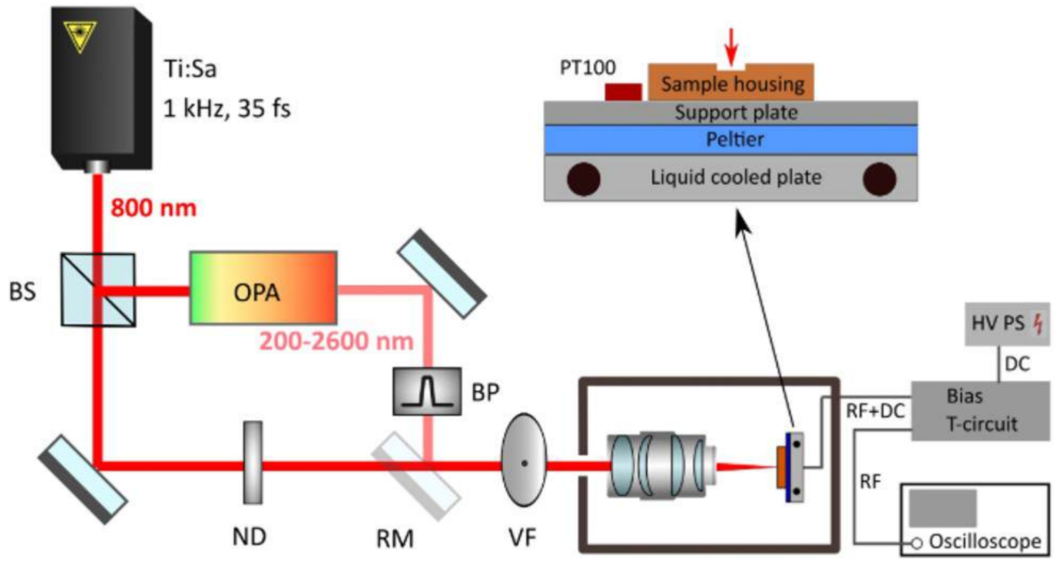

Figure 2.9: Schematic view of the setup for TCT-SPA and TCT-TPA measurements at ELI Beamlines (BS – beamsplitter, OPA – optical parametric amplifier, BP – bandpass filter, ND – neutral density filter, RM – removable mirror, VF – variable filter) [75].

high-voltage power supply by ISEG with a voltage range up to 3 kV, and a low-voltage source is used to power the amplifier(s). The resulting transient pulses are recorded with a fast Keysight Infinium oscilloscope (DSOS604A), having a bandwidth of 6 GHz and a 20 GSa sampling rate. The acquisition is triggered directly by the laser, ensuring that the excitation is synchronized with the readout [76]. The available wavelengths for the excitation range from 200 to 2600 nm, with a repetition rate of 50-300 fs based on the wavelength. The focused waist radius is ~ 0.85 μm for SPA, and 1.5 μm for TPA.

A distinctive feature of the ELI Beamlines TCT setup is the combination of SPA- and TPA-TCT setups. The conventional SPA-TCT is performed using the fundamental 800 nm wavelength with the penetration depth close to the surface. This wavelength can be changed according to the requirement, as we used 400 nm for shallow penetration to mimic low-energy particles. This will be shown in the coming chapters. In addition, TPA-TCT is enabled by an optical parametric amplifier (OPA) that produces a 1550 nm wavelength. In this configuration, free charge carriers are generated through absorption of two sub-bandgap photons at a localized depth in silicon. This dual combination of the techniques benefits us with low penetration and depth-resolved charge creation, providing a comprehensive view of charge transport and electric field behavior.

While using the SPA-TCT configuration, the fundamental wavelength is 800 nm.

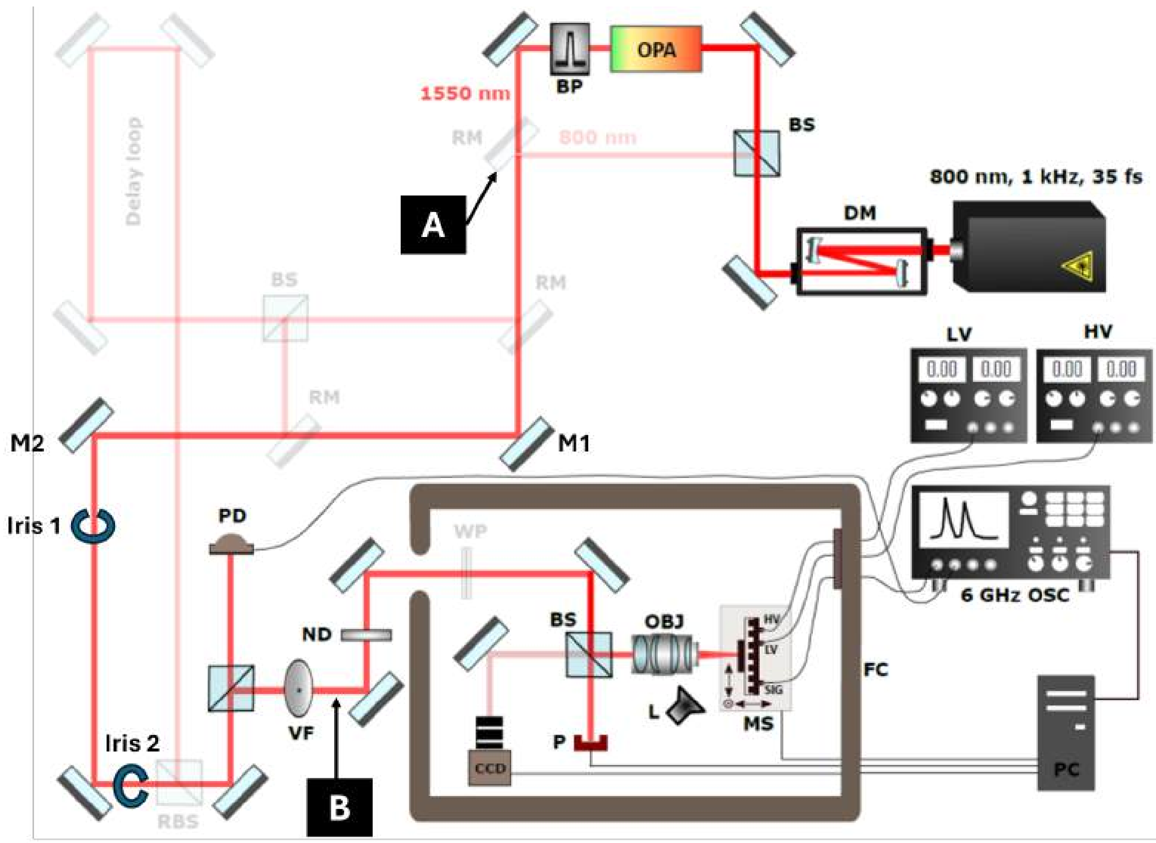

Figure 2.10: Schematic view of the setup for TCT-SPA and TCT-TPA measurements at ELI Beamlines with details of conversion to TPA from SPA and vice versa. The components are: DM – demagnifier, BS – beamsplitter, OPA - optical parametric amplifier, BP - bandpass filter, RM - removable mirror, RBS - removable beamsplitter, PD - reference photodiode, VF - variable gradient ND filter, ND - fixed neutral density filter, WP - half waveplate, P – powermeter, OBJ - 100X objective L- lamp, MS - motorized XYZ stages, LV - low voltage power supply, HV - high voltage power supply, FC - Faraday cage [77].

This can also be converted to other wavelengths using second harmonic generation. The most convenient wavelength for low-penetrating particles was 400 nm, as it is exactly the second harmonic of 800 nm, which is achieved by using a Barium Borate (BBO) crystal sandwiched between half waveplate and band pass filter to let only 400 nm pass through. This alteration is placed at *point* ***B*** in Figure 2.10.

The conversion between SPA- and TPA-TCT setups is quite convenient as the major alteration is the presence or removal of a mirror at *point* ***A*** in Figure 2.10, in order to block or allow the 1550 nm laser beam coming from OPA to use SPA- or TPA-TCT, respectively. After converting SPA to TPA-TCT, or vice versa, it is mandatory to realign the laser beam to enter the objective lens. This can be done by adjusting two irises and two mirrors, alternatively. This means that M1 needs to be adjusted in a way that the laser beam passes through the center of Iris-1, and then M2 needs to be adjusted so that the laser passes through the center of Iris-2. These mirrors and irises are marked in Figure 2.10. Beam alignment can be seen on the screen using a beam profiler (Ophir) and the dedicated software for visualization.

Focusing of the laser beam on the device is carried out using the CCD camera through the objective lens, where the stage is illuminated by a lamp next to it. The best focus is achieved by identifying the sharpest image on the screen. The device is mounted on the hexapod where focusing is carried out in six dimensions, which includes three translational (x, y, z) and three rotational dimensions (r, θ, ϕ).

Beam elongation in silicon

Since TPA occurs at the focus of the laser, it is essential to know the focus position of the laser inside the silicon (DUT). When light travels between media of two different refractive indices, it experiences refraction, as described by Snell's law:

$$n_1 \ \sin\theta_1 = n_2 \ \sin\theta_2 \tag{2.5}$$

where n_1 and n_2 are the refractive indices of two different media, and θ_1 and θ_2 are the angles relative to the surface normal. A beam undergoes bending towards the normal when entering a medium of higher refractive index, and vice versa. In this study, the beam travels from air (lower refractive index) to silicon (higher refractive index). Upon entering silicon, the beam's opening angle decreases relative to the axis. This increases the Rayleigh's length and keeps the beam radius constant, as shown in Figure 2.11.

For air (n_{air}=1) the focal point lies at position z from the surface, whereas for silicon ($n_{Si} > 1$) the focal point shifts to z_1 with a modified angle (θ_1). The relationship between the opening angle and the Rayleigh's length is given by:

$$tan \ \theta_1 = \frac{w_0}{z_R} \tag{2.6}$$

Using Eq. 2.2, 2.5, and 2.6, the new position of the laser focus inside the silicon can be written as:

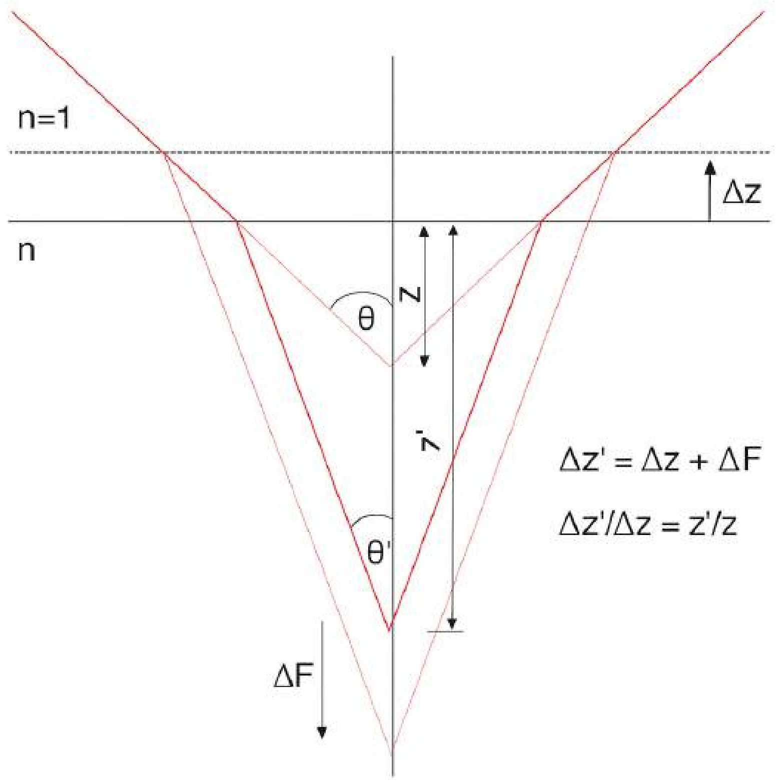

Figure 2.11: Elongation of a laser beam, when entering from air into a material with a higher refractive index. A movement of the sensor surface by Δz results in a shift of the focal point in the opposite direction leading to a total displacement of $\Delta z'$ [29].

$$z_1 = z \cdot \sqrt{\frac{n^2 - NA^2}{1 - NA^2}} \tag{2.7}$$

The ratio z_1/z is referred to as the elongation factor and is shown in Figure 2.12 as a function of Rayleigh's length. For weak focusing, where Rayleigh's length is long, the elongation factor approaches the refractive index and is insignificant to take into account. But for strong focusing, where the Rayleigh's length is $\sim$ 10 - 20 μm, deviations become significant and must be taken into account.

In the case of silicon and air (this study), the calculated elongation factor is 3.97 when using the Rayleigh's length of 7.71 μm for TPA at ELI Beamlines [75]. Therefore, the depths inside the silicon are compensated with this elongation factor in all measurements involving TPA laser beam.

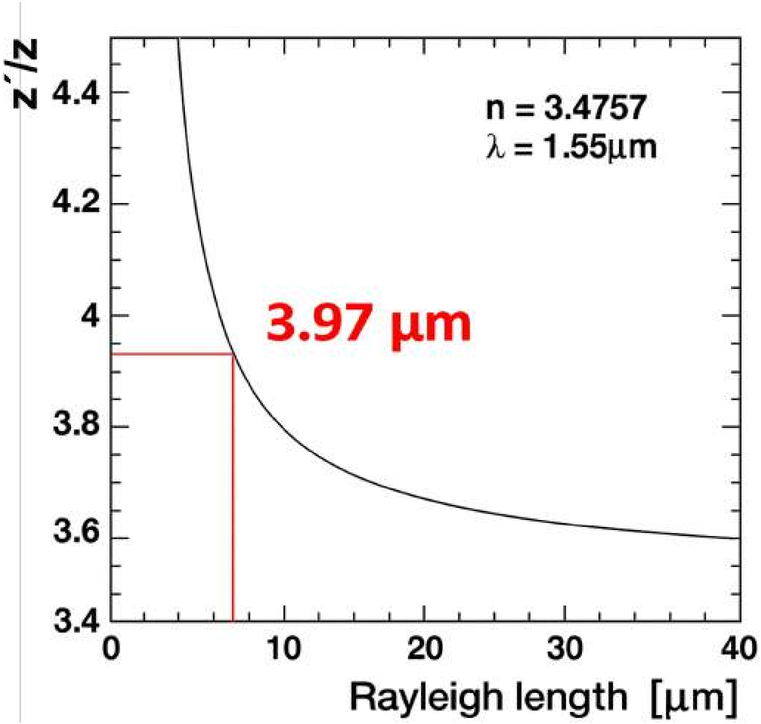

Figure 2.12: Elongation factor z'/z as a function of the Rayleigh length of a focused laser beam in silicon [78].

Chapter 3

Gain layer degradation study after neutron and proton irradiations in Low Gain Avalanche Diodes

3.1 Introduction

Targeting the HL-LHC that is foreseen to start operation near 2030, delivering an integrated luminosity of up to 4000 fb^{-1} during its 10 years of operation. The HL-LHC will operate at an instantaneous luminosity of 5.0×10^{34} cm^{-2}s^{-1}, with an ultimate scenario of 7.5×10^{34} cm^{-2}s^{-1}, as explained in Chapter . For this upgrade, the ATLAS and CMS experiments will include dedicated sub-detectors to perform timing measurements of mips during the HL-LHC operations.

The LGAD structure is described in section 1.7.2, as schematics are shown in Figure 1.14. The timing sub-detectors of CMS and ATLAS are proposed to be built using LGADs with a pixel size of $1.3 \times 1.3\, mm^2$. These detectors will be exposed to radiation levels up to $1.5 \times 10^{15}\, n_{eq}/cm^2$ for CMS endcap timing layer (ETL) and $2.5 \times 10^{15}\, n_{eq}/cm^2$ for ATLAS high granularity timing detector (HGTD), posing a significant challenge for this technology. The radiation fields contains neutrons, but other charged particles are also present in different ratios along the detector dimensions. Therefore, to fully understand the performance of LGADs during the HL-LHC operation, it is essential to investigate the radiation damage produced by all types of particles that are involved. Although similar studies have been conducted with other types of LGADs, a direct comparison between neutrons and 24 GeV/c protons has not been performed yet with the LGADs studied in this work. Most studies in the literature focus primarily on neutrons [79,80].

All the p-type sensors are encountering a particular problem induced by radiation in which boron transforms into defect states that no longer possess the same properties, known as the *acceptor removal effect*. On the macroscopic level, we observe this effect as a change in the gain layer depletion voltage (V_{GL}), a respective change in the effective doping concentration (N_{eff}), a loss of the signal gain, or a loss or increase in the active sensor volume. While on the microscopic level, boron (mostly used in p-type silicon production) is removed from the substitutional lattice sites and bound into defect states i.e., B_iO_i (Boron interstitial – Oxygen interstitial) or B_sO_i (boron substitutional – Silicon interstitial), which no longer hold the properties of shallow acceptor [81]. A study of the acceptor removal effect on the macroscopic level is presented in this chapter.

This chapter also includes the comparison of different methods for the calculation of V_{GL}, the impact of neutron- and proton-irradiation on the degradation of LGADs, and the comparison between the performance of LGADs produced by Hamamatsu Photonics (HPK) and CNM.

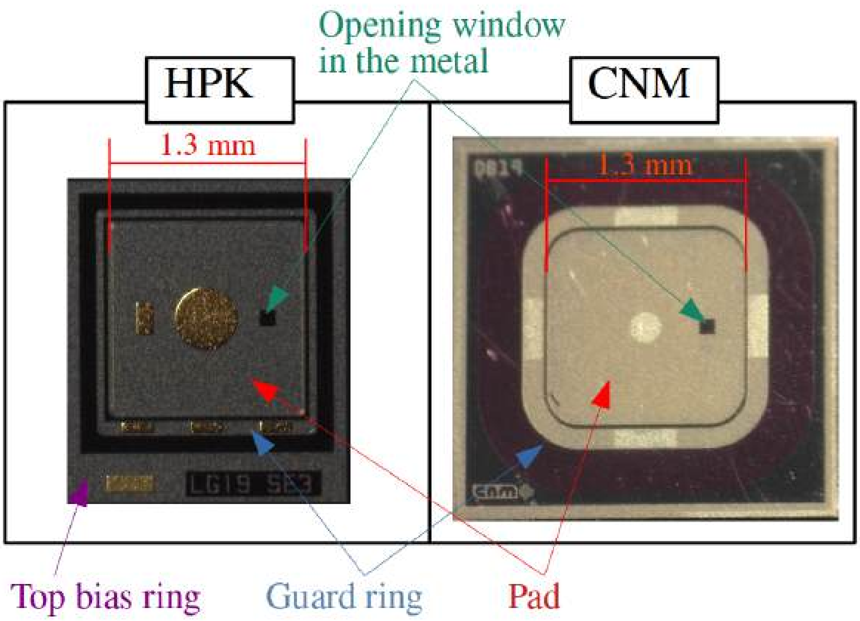

Figure 3.1: Schematic diagram of a standard LGAD. Photographs (not scaled) of the two LGAD types studied in this work.

3.2 Samples description

The samples used for this study were LGAD and PIN sensors produced by HPK and CNM. The only difference between the PIN and LGAD from each producer is the inclusion of the p^+ layer (gain layer) in the case of LGAD. The samples produced by HPK are from the production run S10938-6130 (also called HPK2 or HPK prototype 2) produced on a wafer with a 50 μm thick epitaxial layer on a low resistivity support wafer with a thickness of 150 μm. The samples produced by CNM are from the production run 12916, produced on a 50 μm thick Float Zone wafer bonded to a low resistivity Czochralski support wafer with 300 μm thickness. The HPK LGADs are designed with a deep gain layer doping profile, while the sensors from CNM have a shallow gain layer doping profile.

All samples have an active area of 1.3 x 1.3 mm^2 and a guard ring structure around the central pad. An opening window of 100 x 100 μm^2 in the metallization is provided to allow the laser illumination from the front side (i.e., the top electrode). In Figure 3.1, pictures of sensors from HPK and CNM studied in this work are shown. Key parameters of the sensors from the respective producers are listed in the Table 4.1.

Table 3.1: Main parameters for the LGAD samples used in this work: full depletion voltage (V_{dep}), gain layer depletion voltage (V_{gl}), average breakdown voltage (V_{bd}) at 20°C, capacitance reached above full depletion (C_{end}) and active thickness (d).

Sample	**V_{dep} [V]**	**V_{gl} [V]**	**V_{bd} (20°C) [V]**	**C_{end} [pF]**	**d [µm]**
HPK2-W25	61.7	54.5	145	3.6	48
CNM	42.8	39.4	80 - 100	4.2	42

One set of the samples, including PINs and LGADs, was irradiated at three different fluences at the CERN-PS irradiation facility with 24 GeV/c protons. An error of 7 % is applied to the achieved fluences, and a hardness factor of 0.62 is applied for conversion into 1 MeV neutron equivalent damage [82]. Another set of samples, including PINs and LGADs, was irradiated with neutrons in the TRIGA II reactor at the Jožef Stefan Institute (JSI) in Ljubljana at three different fluences. The fluences were achieved within an error of 10%. Some LGADs and PIN diodes were kept unirradiated for reference measurements. Due to a technical problem during the proton irradiation, the medium fluence was higher than the requested one of 8.0×10^{14} n_{eq}/cm^2. A summary of all the irradiation fluences is shown in Table 4.2. The normalized bulk current extracted from

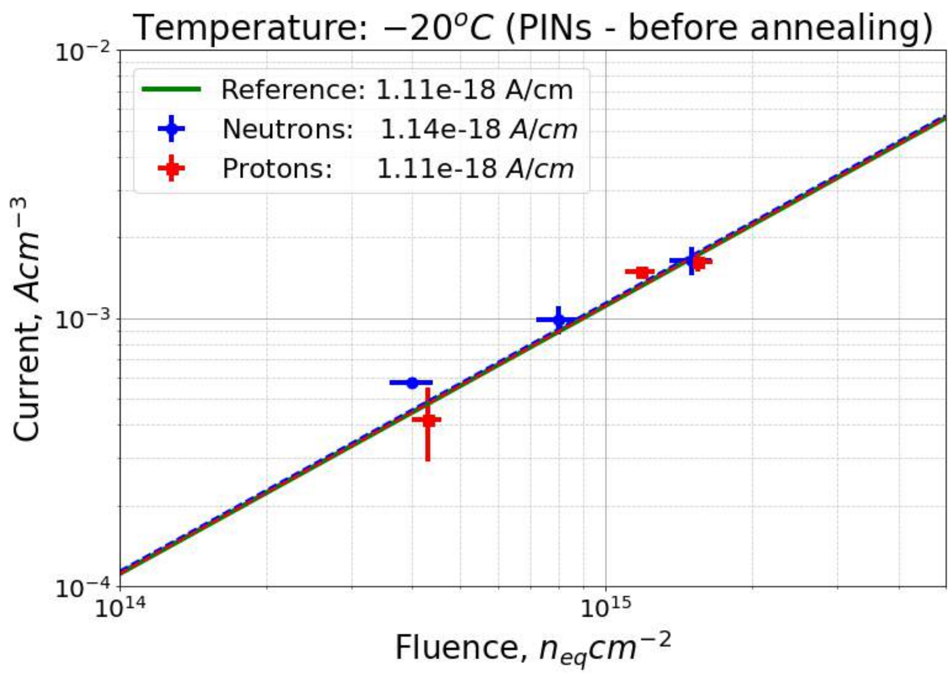

Figure 3.2: Pad current as a function of the fluence, measured with the PIN diodes at -20°C before annealing. Dotted lines represent the linear fit to the data. The reference value is included for comparison [13].

the irradiated PIN detectors after full depletion is plotted as a function of the fluence and is shown in Figure 3.2. Both neutron and proton irradiations are in good agreement with the expected value [13]. After irradiation, all the samples were annealed for 60 minutes at 80°C.

Table 3.2: Table summarizing the irradiations performed in the different LGADs and PINs studied in this work.

Particle	**Low fluence** $[n_{eq}/cm^2]$	**Medium fluence** $[n_{eq}/cm^2]$	**High fluence** $[n_{eq}/cm^2]$
Proton	4.3×10^{14}	1.18×10^{15}	1.55×10^{15}
Neutron	4.0×10^{14}	8.0×10^{14}	1.5×10^{15}

3.3 Electrical characterization

The electrical characterizations were performed at the SSD lab at CERN, where the bare samples before and after irradiation were measured using a probe station, as shown in

Figure 3.3. The samples were placed directly on a temperature-controlled chuck. The leakage current and the capacitance were measured as a function of the reverse bias voltage. The guard ring was always grounded during all of the measurements.

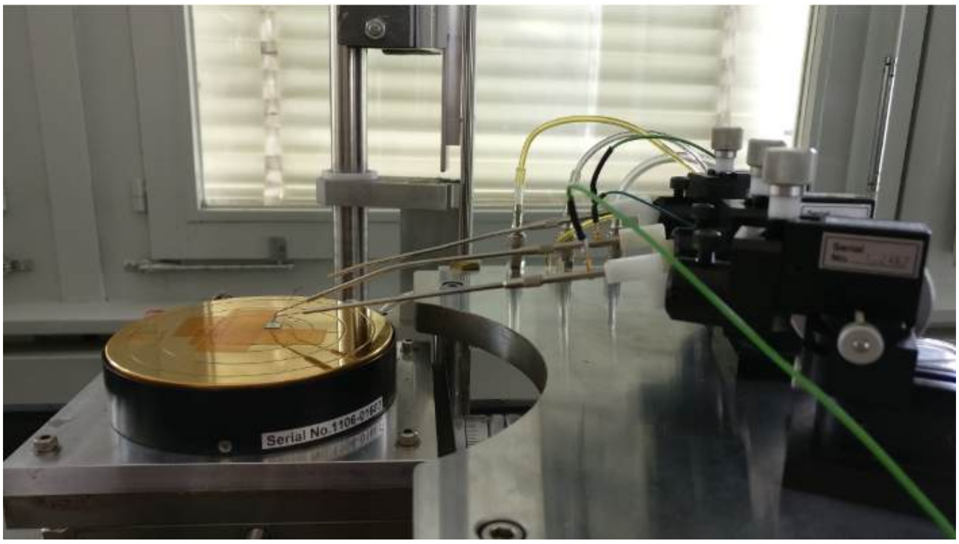

Figure 3.3: Photograph of the probe station at SSD Lab, CERN (Taken from [83]).

The leakage current was measured at 20°C for unirradiated samples, while for the irradiated samples, the temperature was set to -20°C. Figure3.4 (a) shows the pad current for the CNM LGADs, as a function of the reverse bias. For the HPK LGADs, the pad current as a function of reverse bias voltage is shown in Figure 3.4(b).

The capacitance was measured at 20°C for unirradiated samples, while for the irradiated samples, the temperature was set to 10°C. Figure 3.5 (a) shows the inverse squared capacitance for the CNM LGADs as a function of the reverse bias. For the HPK LGADs, the inverse squared capacitance as a function of reverse bias voltage is shown in Figure 3.5 (b). The LCR meter frequency was kept at 1 kHz for both unirradiated and irradiated samples.

During the electrical characterization, a compliance of 10 μA in the total current was set, and the bias voltage was always kept below 600 V.

3.4 Infrared laser measurements

The gain of the devices was measured with the TCT setup of the SSD lab at CERN, using a pulsed IR-laser of 1060 nm and a pulse width of 250 ps. The TCT setup is shown in Figure 3.6. The LGAD sensors are mounted on a customized PCB, which is fixed onto

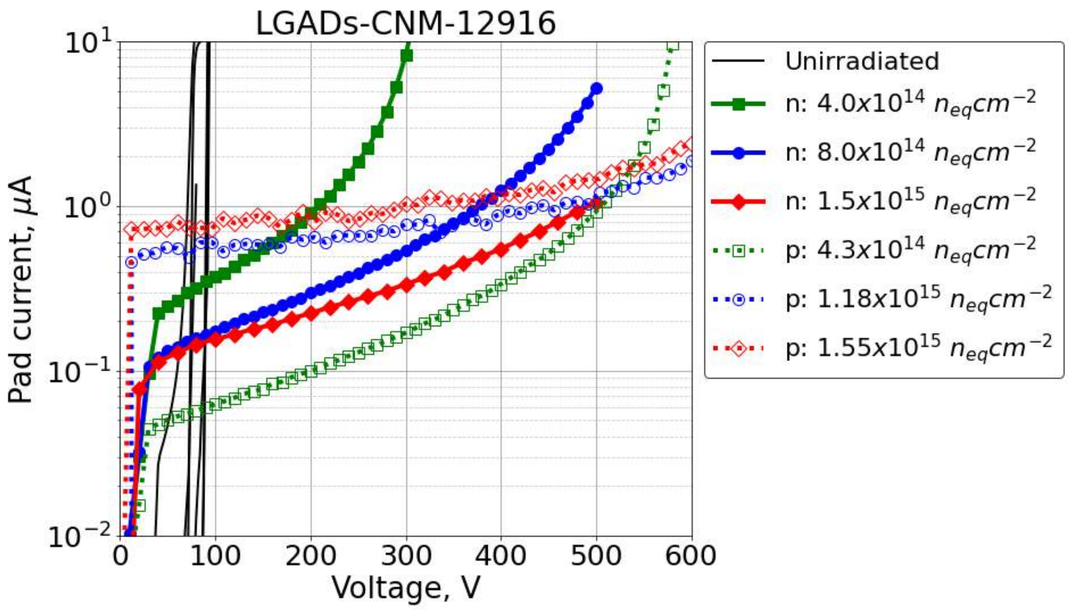

(a)

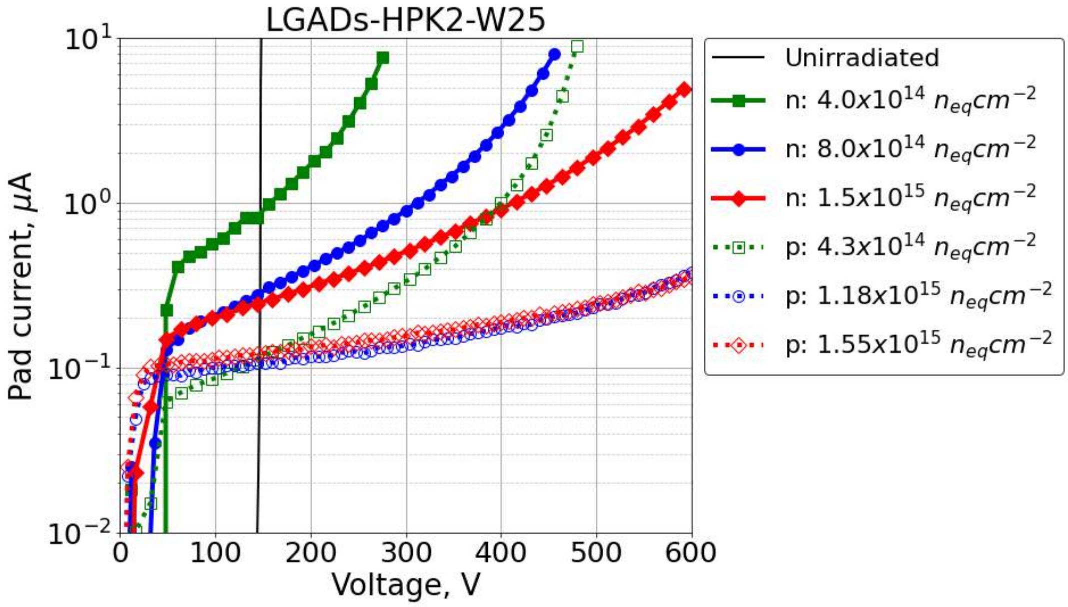

(b)

Figure 3.4: Pad current of the LGADs studied in this work. The figure shows the measurements of the CNM LGADs (a) and the HPK ones (b).

a temperature-controlled metallic support to ensure stable operating conditions during measurements. The laser-induced transient signal is first amplified using a CIVIDEC C2 amplifier with a bandwidth of 2 GHz and a gain of 40 db. Following amplification, the signal is digitized by an Agilent DSO 9254 oscilloscope, offering a bandwidth of 2.5

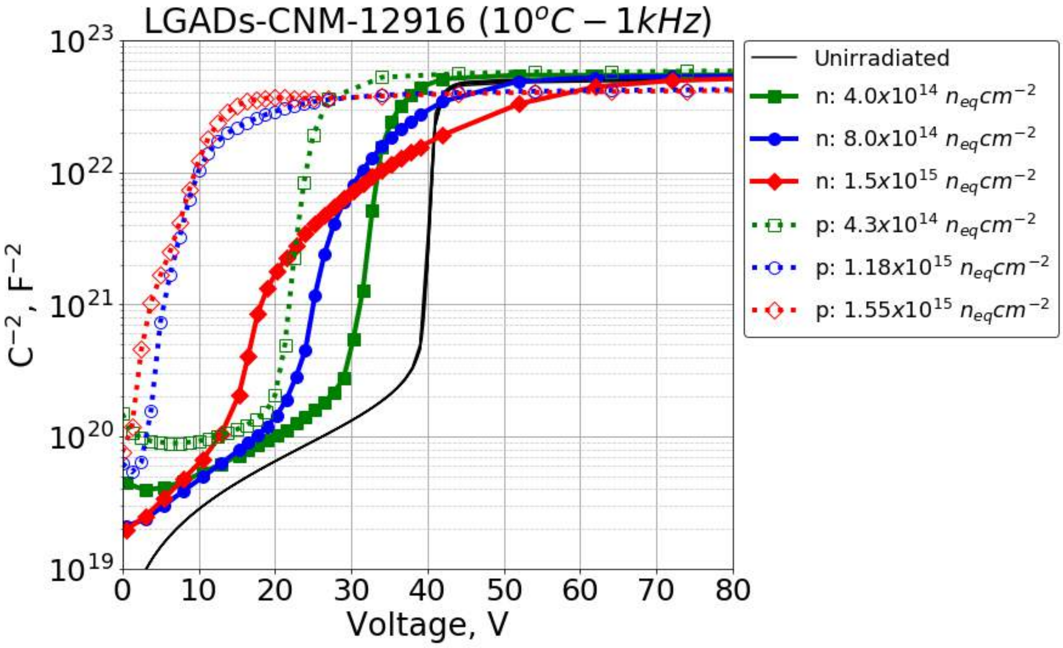

(a)

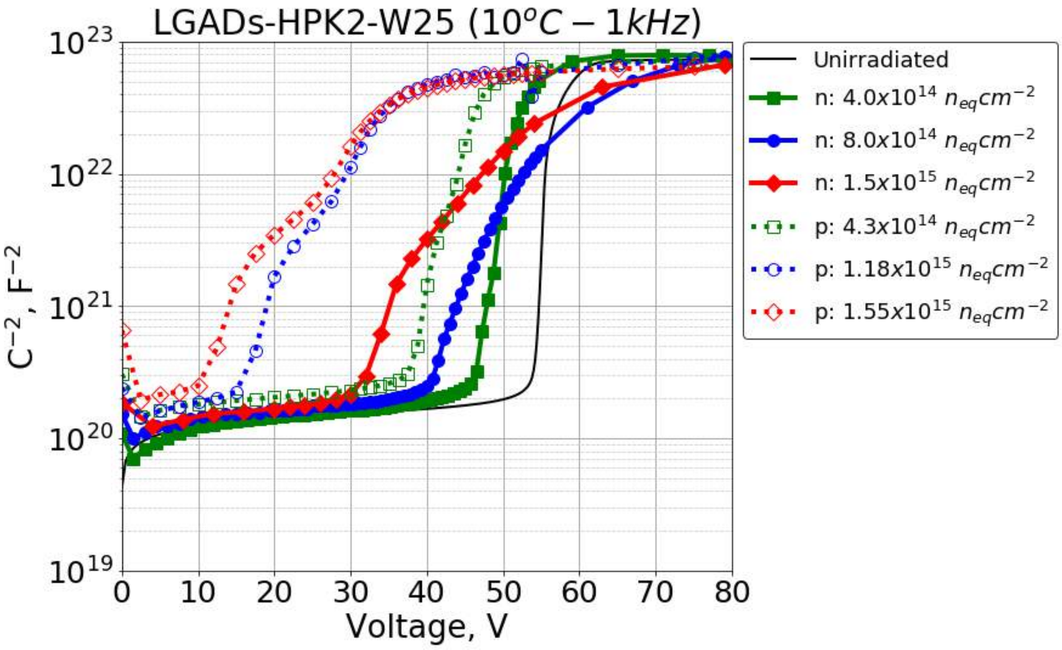

(b)

Figure 3.5: Capacitance characterization of the LGADs studied in this work. The figure shows the inverse of the squared capacitance as a function of the bias voltage for the CNM LGADs (a) and the HPK ones (b).

GHz and a sampling rate of 20 GSa/s. Additional details of the experimental setup are described in [78]. Intensity of the laser was tuned to generate a charge of ~ 1 mip for these measurements. The laser beam spot size of around 20 μm in FWHM was kept for all measurements to minimize the gain suppression effect. The measurements were performed at -20°C with the guard ring left floating.

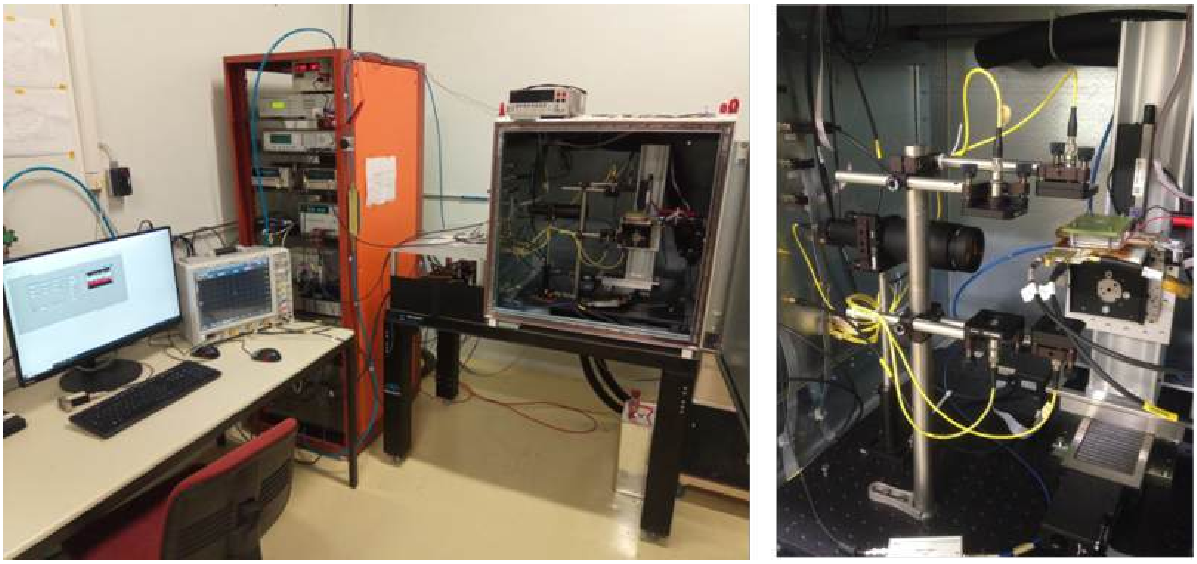

Figure 3.6: Photograph of the TCT setup in SSD lab at CERN, with all instrumentation (left), and inside the Faraday cage (right). Photo taken from [78].

The gain measurements are shown in Figure 3.7. The limit of the applied reverse bias voltage was inferred from the IV measurements, shown in the Section 3.3, and in all the cases was kept below 600 V. The method implemented in this work to calculate the gain is where the collected charge of the LGAD is compared to that of the PIN-diode after full depletion, by keeping the same set of parameters. The collected charge as a function of reverse bias voltage is then measured for all the devices individually. The gain is then calculated by the equation:

$$Gain[V] = \frac{CC_{LGAD}[V]}{CC_{PIN}[V \geq V_{FD}]} \tag{3.1}$$

3.5 Experimental results: gain layer degradation

The results presented in this chapter demonstrate an evident degradation of LGAD performance as a function of irradiation fluence. This degradation is more pronounced in the CNM-produced LGADs as compared to those produced by HPK. Furthermore, both types of LGADs exhibit greater damage from irradiation with 24 GeV/c protons than

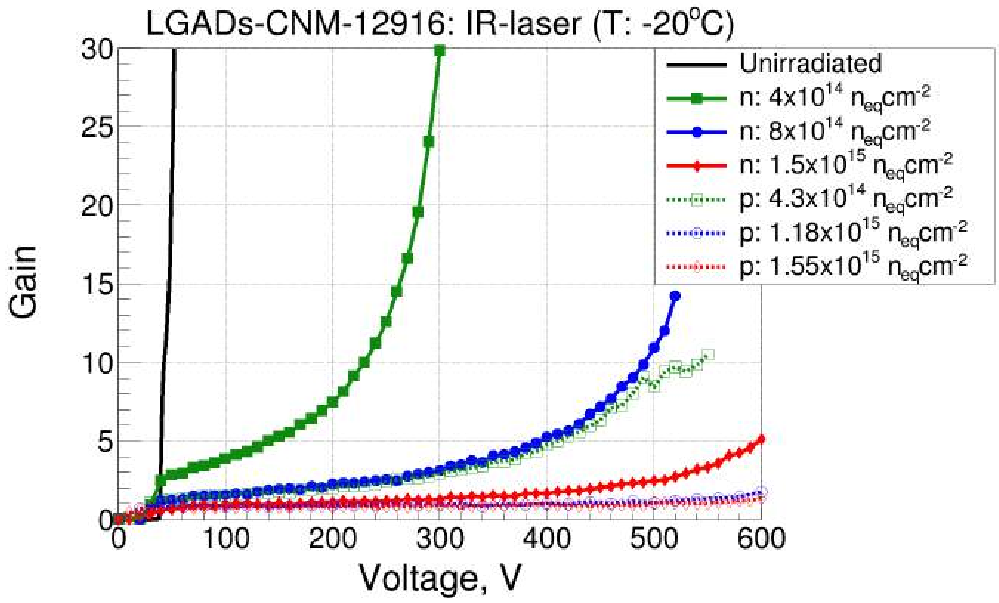

(a)

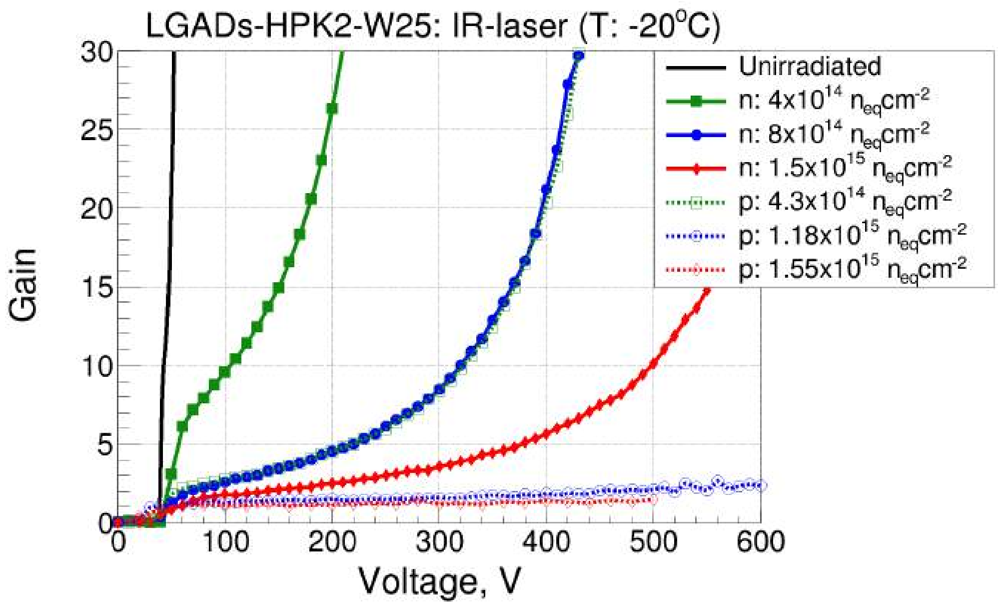

(b)

Figure 3.7: Gain measurements using an IR-laser of the LGADs studied in this work. The charge measure in the LGAD was divided by the one measured in the equivalent unirradiated PIN to evaluate the gain in the CNM LGADs (a) and HPK ones (b).

with neutrons, when normalized to the 1 MeV n_{eq} fluence. The results clearly show that the breakdown voltage increases with the irradiation fluence, which is a direct indication of degradation in the gain layer. Furthermore, proton-irradiated LGADs exhibit a higher breakdown voltage compared to neutron-irradiated devices, referring to more severe gain layer degradation in case of protons. A resemblance can also be seen in the capacitance curves presented in Figure 3.5, where the depletion voltage of the gain layer (V_{GL}) decreases progressively with irradiation fluence. Notably, this reduction in V_{GL} is more pronounced for proton-irradiated LGADs than for those exposed to neutrons, reinforcing the conclusion that protons induce stronger damage. The gain measurements shown in Figure 3.7 confirm these conclusions too.

To quantify these results, the acceptor removal effect in the GL can be evaluated. As irradiation fluence increases, the implanted boron (B) atoms in the gain layer (GL) become progressively deactivated, which directly reduces the voltage required to deplete the GL. In other words, a lower concentration of active Boron leads to a lower reverse bias voltage needed for full depletion. Based on this assumption, the V_{GL} can be extracted from the measurements, providing a direct estimate of the remaining fraction of active Boron within the GL.

The extraction of the V_{GL} was done using three different methods, as shown in Figure 3.8. Figure 3.8a shows the calculation of V_{GL} in the pad current curves, where the derivative of pad current with the bias voltage is calculated. The peak around the beginning of the avalanche region determines the V_{GL}. Figure 3.8b shows V_{GL} in the inverse of the squared capacitance curves, where V_{GL} is calculated from the first shoulder of the curve. Figure 3.8c shows the position of V_{GL} in the collected charge measurement performed with the pulsed IR-laser. All these three methods give similar results within a $\sim 3\%$ error and an average value was taken to evaluate the acceptor removal effect. The initial acceptor removal is exponentially dependent on fluence, and it is defined in Eq. 3.2, where c is the removal constant, $N_{x,0}$ is the initial doping concentration, and $V_{GL,0}$ is the initial depletion voltage of the GL [84].

$$N_x = N_{x,0}\ exp(-c\,\Phi_{eq}) \ \Rightarrow \ V_{GL} \approx V_{GL,0}\ exp(-c\,\Phi_{eq}) \tag{3.2}$$

$$GL\,fraction = \frac{V_{GL}(\phi_{eq})}{V_{GL}(0)} \tag{3.3}$$

Figure 3.9 presents the evolution of the GL fraction as a function of irradiation fluence for CNM LGADs (Figure 3.9a) and HPK LGADs (Figure 3.9b). The GL fraction is derived from the V_{GL} obtained using the methods described earlier and defined in Eq.

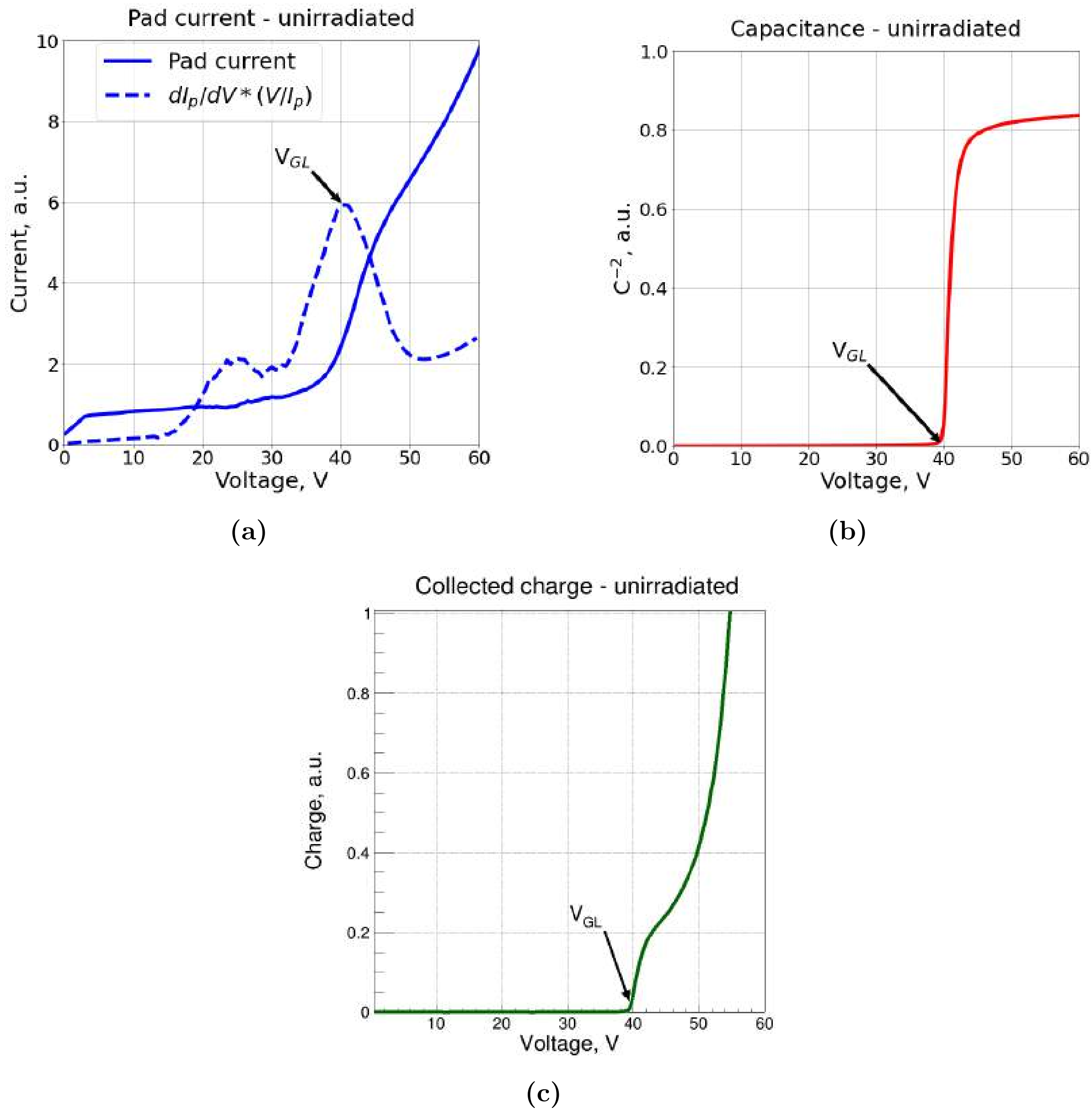

Figure 3.8: Examples of the extraction of the V_{GL} from the three different methods used in this work: (a) from the pad current curve, (b) from the capacitance curve, and, (c) from the collected charge curve.

3.3. In 3.9, the fitting curves based on the acceptor removal model (Eq. 3.2) are shown together with their corresponding removal constants. For clarity, the numerical values of these constants are summarized in Table 3.3.

The results consistently indicate that the removal constant associated with 24 GeV/c protons is approximately 2.5 times larger than that for neutrons when normalized to the 1 MeV n_{eq} fluence. In addition, the removal constants for CNM LGADs are about 1.8

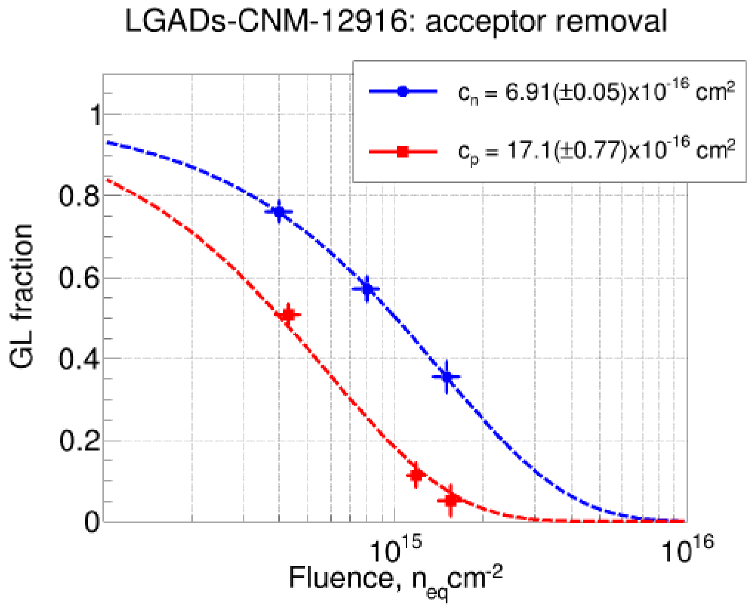

(a)

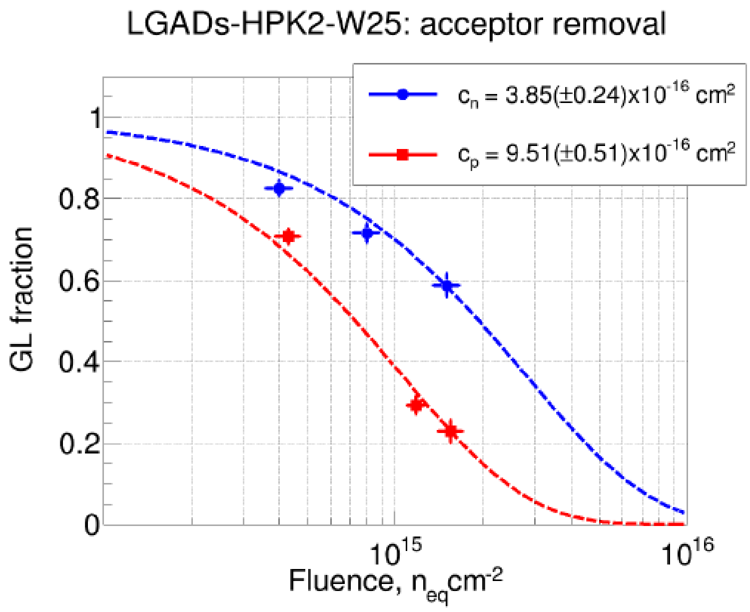

(b)

Figure 3.9: Acceptor removal parameterization using Eq. 3.2 for the CNM LGADs (a) and for the HPK ones (b).

times higher than those measured for HPK LGADs. These findings highlight both the stronger impact of proton irradiation compared to neutrons and the greater susceptibility of CNM devices relative to HPK ones.

Table 3.3: Table summarizing the acceptor removal constant (c) extracted from figure 3.9 using (Eq. 3.2).

	$c_n[cm^2]$	$c_p[cm^2]$	c_p/c_n
CNM LGADs	$6.91(\pm0.05)\times10^{-16}$	$17.1(\pm0.77)\times10^{-16}$	2.475
HPK LGADs	$3.85(\pm0.24)\times10^{-16}$	$9.51(\pm0.51)\times10^{-16}$	2.470
c_{CNM}/c_{HPK}	1.795	1.798	-

It has been demonstrated that the acceptor removal constant is influenced not only by the type of irradiation particle but also by the specific design of the GL. The extent of degradation varies among different LGADs depending on the geometry, position, and concentration of the GL doping profile. In addition, co-implantation of other elements—such as carbon—has been shown to enhance the radiation tolerance of the GL (see, for example, [85]). For this reason, it is both relevant and necessary to compare the acceptor removal constants obtained in this study with those reported in similar investigations carried out in the context of the HL-LHC upgrade. Such a comparison allows us to assess whether the values extracted here fall within the range of previously established data.

A study of the acceptor removal effect on IHEP-IMEv2 LGADs produced by the Institute of Microelectronics (Chinese Academy of Sciences) shows c_n values in the range of $3.5-6.0\times10^{-16}cm^2$ after neutron irradiation [86]. Different production runs of LGADs from HPK give c_n values in the range of $3.15-5.2\times10^{-16}cm^2$ also after neutron irradiation and, c_p values in the range of $6.5-7.0\times10^{-16}cm^2$ after irradiation with 70 MeV/c protons [87,88]. Different production runs of LGADs from CNM resulted in c_n values in the range of $5.78-8.19\times10^{-16}cm^2$ after exposure to neutrons and c_p values in the range of $18.7-19.6\times10^{-16}cm^2$ after exposure to 24 GeV/c protons [89,90]. In all these cases, LGADs show an important improvement if carbon is co-implanted in the GL. These numbers are graphically shown in Figure 3.10. Blue and grey bars represent the minimum and maximum values, respectively, that are reported in the literature, to observe the range of acceptor removal coefficient. Green bars represent the values of acceptor removal coefficient obtained in this study.

In conclusion, the results indicate that the acceptor removal constant is strongly dependent on the specific design of the GL. When fluence is normalized to the 1 MeV

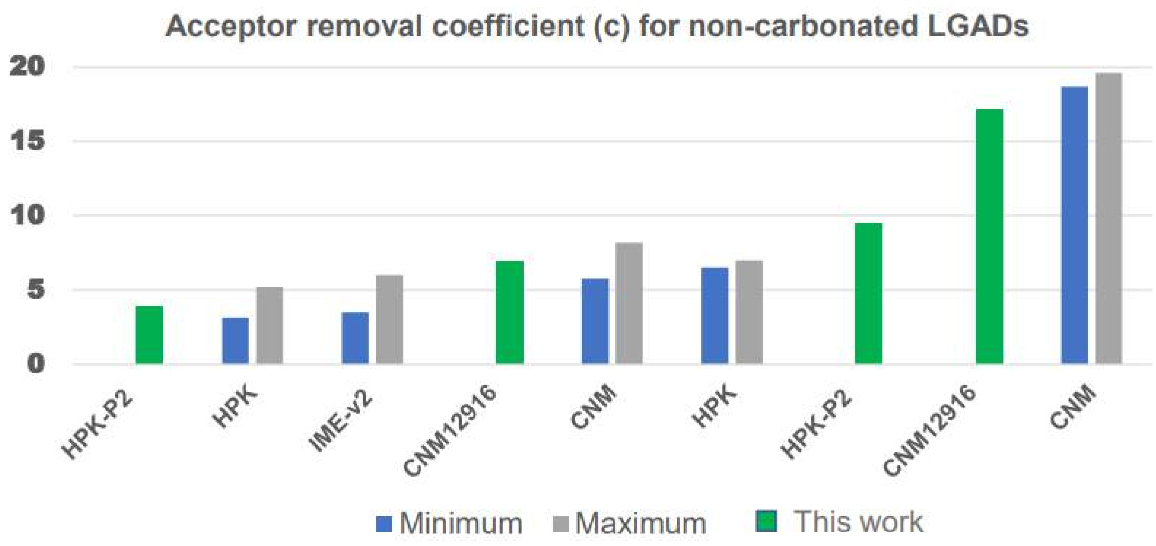

Figure 3.10: Acceptor removal coefficients for the neutron and proton irradiation, available in the literature, compared to the finding of this work. (Note: Values from the literature are not from the same batches).

n_{eq}, neutrons appear to induce less damage compared to protons. Moreover, although only a limited number of radiation damage studies involving protons are available, our observations suggest that high-energy protons cause significantly more degradation than their low-energy counterparts. This finding highlights the need for further dedicated measurements to confirm and consolidate the impact of proton energy on GL radiation damage.

3.6 Summary

A gain layer degradation study of LGADs produced by HPK and by CNM was presented in this work. The devices were irradiated with reactor neutrons and 24 GeV/c protons at varying fluences in order to assess the impact of different particle types on gain layer degradation. Electrical characterization and gain measurements using an infrared laser were performed both before and after irradiation for all samples. The acceptor removal effect in the gain layer was then evaluated through several complementary methods, leading to two main conclusions:

1: **Dependence on particle type:** The acceptor removal constant is significantly higher for proton irradiation than for neutron irradiation when normalized to the 1

MeV neutron equivalent fluence, indicating that protons induce stronger degradation of the gain layer. This was quantified with the acceptor removal constant, obtaining a ratio between protons and neutrons of $c_p/c_n \simeq 2.5$ for both types of LGADs.

2: **Dependence on LGAD design:** CNM LGADs exhibit larger removal constants compared to HPK LGADs, showing that the specific design and doping profile of the gain layer strongly influence its radiation tolerance. The acceptor removal constants (for protons and neutrons) gave a value in the CNM LGADs ~ 1.8 times higher than in the HPK ones.

Chapter 4

Advancing 4D tracking with thin LGADs: a study on BNL prototypes

4.1 Introduction

This chapter focuses on the characterization of very thin silicon detectors based on the LGAD design, targeting the timing detectors for the Electron-Ion Collider (EIC). The work consists of LGADs produced at Brookhaven National Laboratory (BNL). The strong requirements of the EIC physics program are accurate timing measurements and fine spatial resolution across several sub-detector systems, namely, TOPSiDe, hybrid LGAD/SOI trackers, time-of-flight detectors, preshower detectors, and Roman Pot detectors. To meet these requirements, LGADs provide a combination of fast charge collection and internal multiplication, making them well-suited for precision timing measurements. However, their radiation hardness needs to be investigated. This study is focused on the performance evaluation of the devices after proton irradiation. The estimated fluence for timing sub-detectors in EIC is of the order of 10^{13} $n_{eq}cm^{-2}$ [91]. Therefore, these detectors are tested for the proton fluences 1.0 x 10^{13} and 1.0 x 10^{14} $n_{eq}cm^{-2}$.

The goal of this work is to study the performance of LGADs with thicknesses of 20 μm and 30 μm, before and after irradiation with 60 MeV protons. Experiments are performed to study the breakdown and leakage current characteristics, gain degradation, acceptor removal, and timing performance.

4.2 Devices under test

The samples used for this study are LGAD and PIN sensors produced by BNL. The sensors are pad test structures from two wafers: W3082 with a thickness of 20 μm and W3108 with a thickness of 30 μm, high resistivity p-type epitaxial wafer. The sensors have two different types based on the laser opening: 1 x 1 mm^2 and 50 x 50 μm^2, as shown in Figure 4.1. The standard LGAD design contains uniform unpatterned p-spray for oxide charge compensation and n^+ electrode isolation, and a deep JTE is used for n^+ edges against protection of high electric field and breakdown, shown in Figure 4.2. Gain layer implantation energy is as per the external supplier, and the dose is optimized to have a specific breakdown voltage [92]. The doping profile of the LGAD is shown in Figure 4.3.

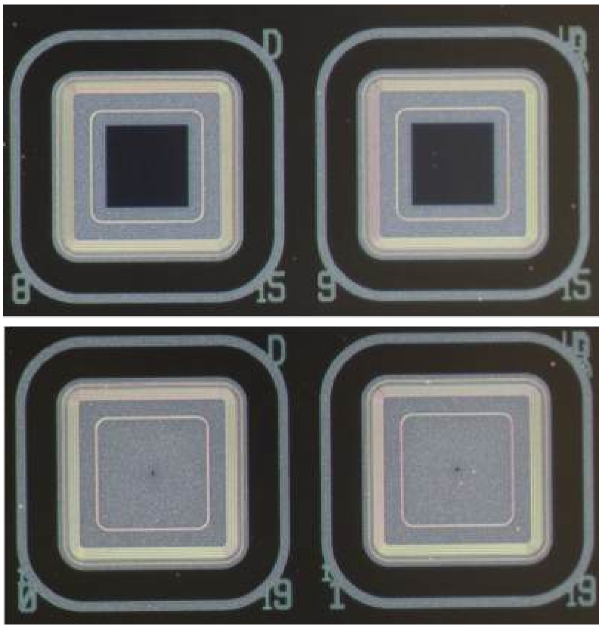

Figure 4.1: Pictures of the devices with 1 x 1 mm^2 and 50 x 50 μm^2 opening windows. Pictures taken from [92].

All sensors have an active area of 1.3×1.3 mm^2 and a guard ring structure around the central pad. There are two types of structures based on different opening windows: 1 mm x 1 mm, and 50 μm x 50 μm, in the metallization, which is provided for the laser excitation on the top side. The backside of the structures is fully metalized. In Figure 4.1, pictures of sensors with different opening windows are shown. Key parameters of the sensors are listed in the Table 4.1.

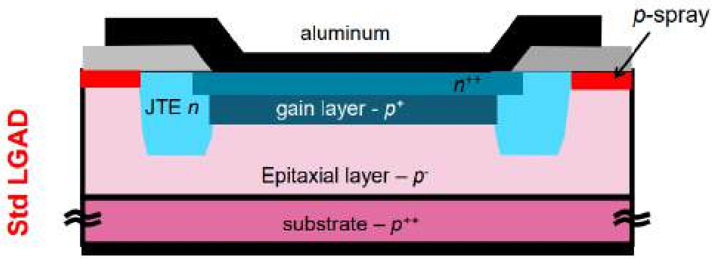

Figure 4.2: Schematics of a standard LGAD corresponding to the BNL design [92].

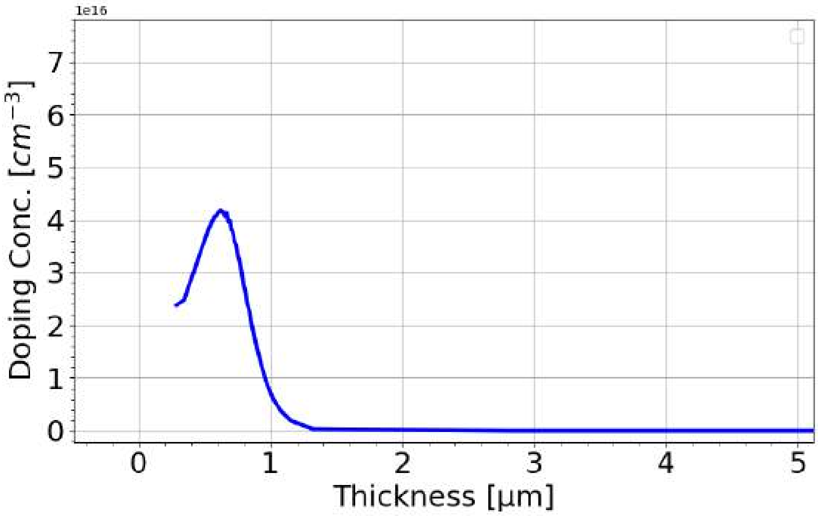

Figure 4.3: Doping concentration of the LGAD obtained from CV curves showing shallow gain layer implantation.

4.3 Irradiation campaign

PINs and LGADs from each wafer were irradiated at the Proton Irradiation Facility at the Institute of Nuclear Physics (IFJ Krakow) with 58.5 MeV protons. A hardness factor of 1.676 is applied to convert the fluences to 1 MeV neutron equivalent damage, with

Table 4.1: Key parameters for the LGAD samples used in this work: full depletion voltage (V_{dep}), gain layer depletion voltage (V_{gl}), average breakdown voltage (V_{bd}) at 20°C, capacitance reached above full depletion (C_{end}) and active thickness (d).

Wafer	V_{FD} [V]	V_{gl} [V]	V_{bd} (20°C) [V]	C_{end} [pF]	d [µm]
W3082	22	21	80	10	20
W3108	23	21	110	7	30

an error of ± 5% on the fluence values. A few PINs and LGADs were kept unirradiated for the reference measurements. Following irradiation, all samples were exposed to a controlled annealing process for 60 minutes at 80°C. A comprehensive summary of the irradiation fluences applied to the PIN detectors is presented in Table 4.2.

Table 4.2: Table summarizing the irradiations performed in the different LGADs and PINs studied in this work.

Particle	**Low fluence** $[p/cm^2]$	**Low fluence** $[n_{eq}/cm^2]$	**High fluence** $[p/cm^2]$	**High fluence** $[n_{eq}/cm^2]$
Proton	6.01×10^{12}	1.0×10^{13}	5.96×10^{12}	1.0×10^{14}

4.4 Electrical characterizations

4.4.1 Before irradiation

Electrical characterizations were carried out using the probe station present at AGH University of Krakow. The samples were placed on an electrically conductive chuck, from where the bias voltage was applied, and the tested samples were connected with micro-positioning needles to measure the current. The IV measurements of the samples before irradiation were carried out at 20°C, and the guard ring was kept floating for all the measurements. CV measurements were taken at a 1 kHz frequency.

The IV characteristics show that the PIN diodes break down in the range of 200 - 250 V, with sub-nA leakage current. The LGADs from W3082 show a breakdown in the range of 75-90 V, while for LGADs from W3108, the breakdown voltage is in the range of 110 - 120 V, as shown in Figure 4.4. The leakage current before the breakdown is in the range of nA. This shows a controlled fabrication of the devices with no premature breakdown. To further investigate the reliability of the devices, a stress test was carried out. In this study, the voltage above the breakdown is applied with current compliance increased to 1 mA, and kept in this state for 60 seconds. Afterwards, IV of the devices is performed again with 1 mA current compliance to check if the devices are in the operational conditions. The results obtained from this experiment are shown in Figure 4.5a and 4.5b, showing that the devices exhibit a similar behavior as shown in Figure 4.4.

The CV curves show that the gain layer depletes at 21 V for both the wafer thicknesses,

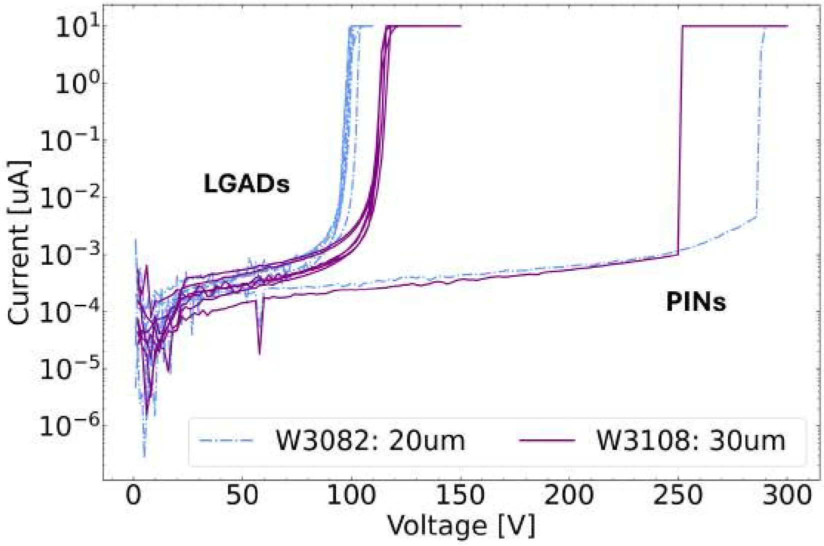

Figure 4.4: IV characteristics of the LGADs and PINs before irradiation for W3082 and W3108 at 20°C.

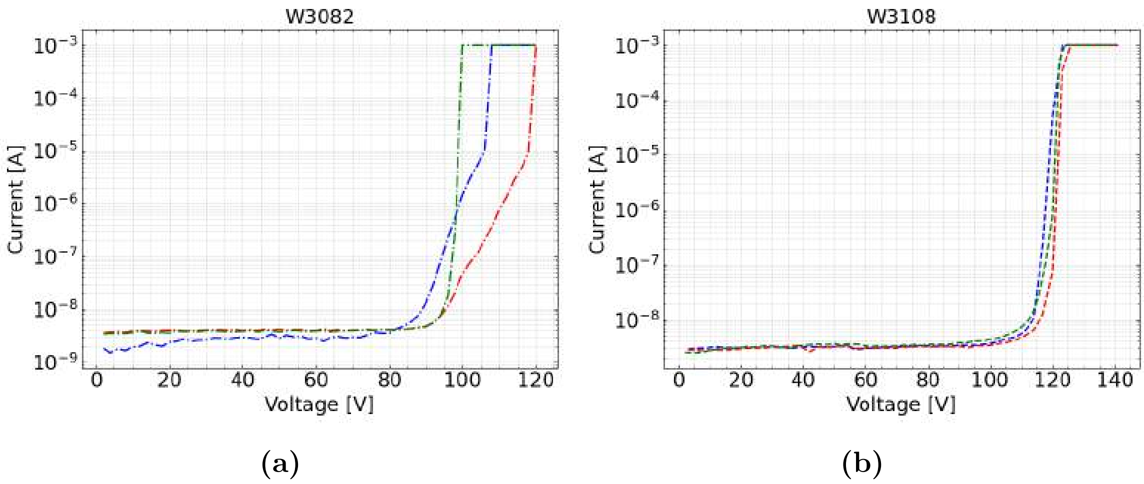

Figure 4.5: IV characteristics of the LGADs from (a) W3082 and (b) W3108, after performing the stress-test. The current compliance is set to 1 mA.

showing a consistent behavior of the doping concentration of the GL, irrespective of the device thickness. The full depletion occurs within 1 V for 20 μm thick devices, while the full depletion occurs within 2 V for 30 μm thick devices, after GL depletion. The end capacitance, i.e., capacitance value after the detector is fully depleted, is 10 pF for 20 μm and 7 pF for 30 μm thick devices, as shown in Figure 4.6. Higher capacitance values for 20 μm devices correlate with the capacitance dependence on depletion width. As the depletion width is inversely proportional to the depletion width, higher capacitance is

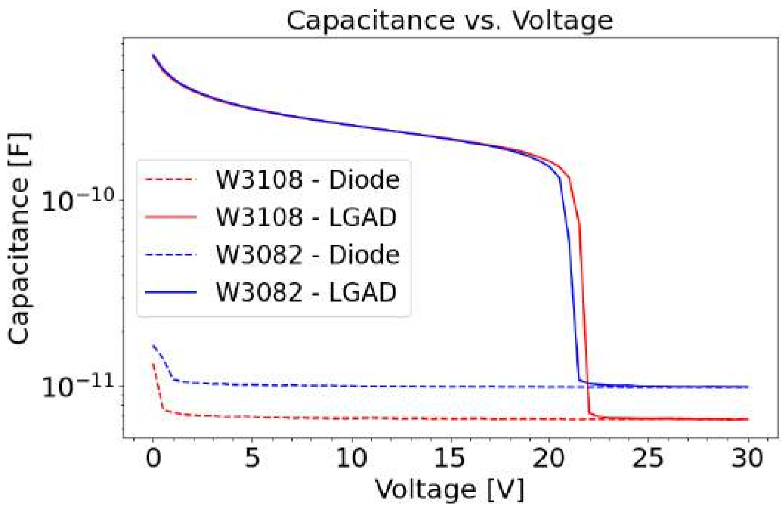

Figure 4.6: CV characteristics of the LGADs before irradiation for W3082 and W3108 at 20°C.

expected for thinner devices [93].

4.4.2 After irradiation

For the irradiated devices, the IV measurements were performed at -20°C in a climate chamber present in AGH University of Krakow. Figure 4.7a shows the IV curves of irradiated PINs from W3082 at different fluences. There is a clear increase in leakage current and the increase in breakdown voltage with the increase in fluence. The unirradiated PIN shows the breakdown at ∼ 210 V, while ∼ 350 V and ∼ 360 V represent the breakdown voltage after the irradiation fluence 1.0 x 10^{13} and 1.0 x 10^{14}, respectively. The normalized bulk current, extracted after achieving full depletion from the IV curves shown in Figure 4.7a, is plotted as a function of fluence in Figure 4.7b [13].

Figure 4.8 shows the IV curves of the LGADs from W3082 and W3108, obtained after irradiation. A significant increase in the leakage current of the LGADs after proton irradiation has been observed for both wafers. For W3082 (Figure 4.8a), the 1.0 x 10^{13} proton fluence did not effect the breakdown voltage much, as it increased by only a few volts, while the 1.0 x 10^{14} proton fluence increased the breakdown voltage from 75 V (unirradidated) to 105 V. A similar behavior is observed for W3108 (Figure 4.8b), where the breakdown voltage increase from 85 V (unirradiated) to ∼ 120 V for 1.0 x 10^{14} proton fluence.

A difference in the breakdown voltage of the unirradiated LGADs is also observed

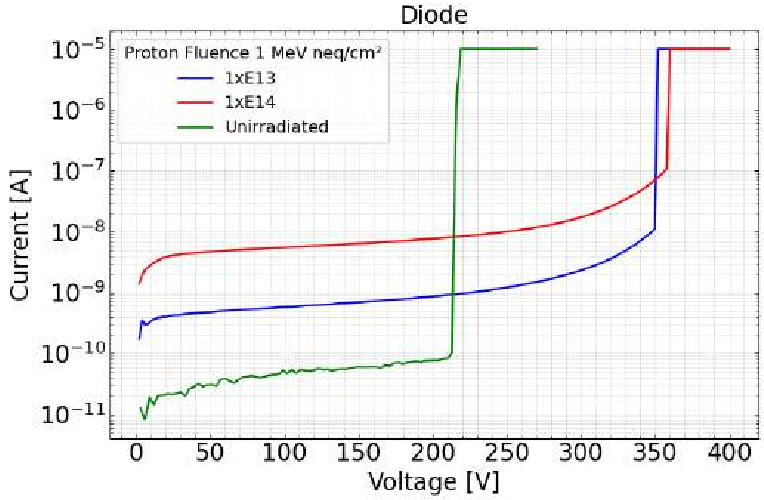

(a)

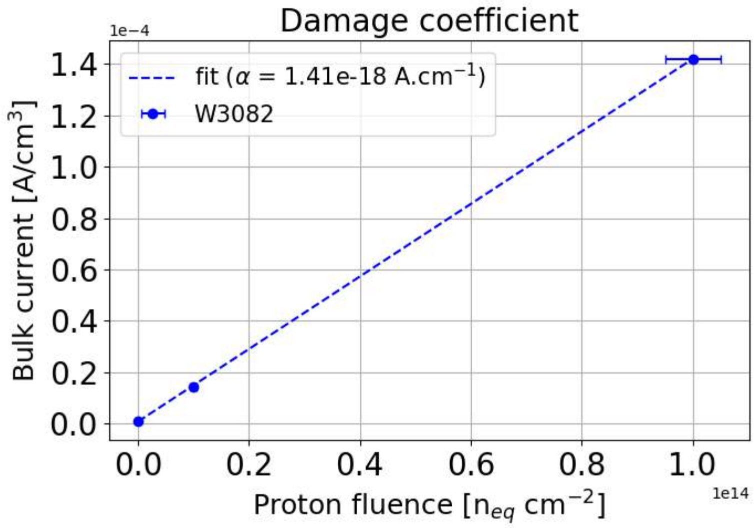

(b)

Figure 4.7: (a) IV characteristics of the PINs after irradiation for W3082 at 20°C. (b) Pad current as a function of the fluence, measured with the PIN diodes at -20°C after annealing. Dotted lines represent the linear fit to the data.

when comparing Figure 4.4 and 4.8, this is due to the difference in the measurement temperatures. In Figure 4.4, the measurements were performed at +20°C, while in Figure 4.8, the measurements were carried out at -20°C. A decrease in breakdown voltage is observed with the decrease in temperature for the avalanche devices [94].

The CV characteristics in Figure 4.9a shows a consistent behavior as seen in Figure 4.8. The V_{GL} of the unirradiated device is comparable to the V_{GL} of the device with

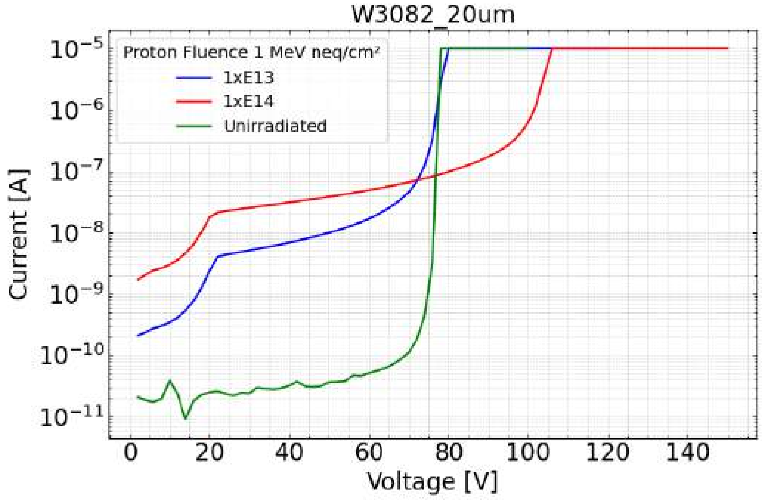

(a)

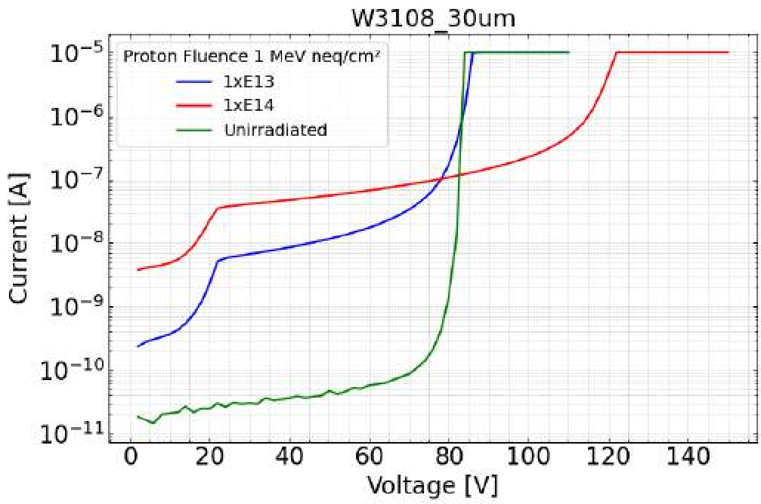

(b)

Figure 4.8: IV characteristics of (a) W3082 and (b) W3108, after 58.5 MeV proton irradiation. Measurements taken at -20°C.

fluence 1.0 x 10^{13}. While, for the 1.0 x 10^{14} fluence, the V_{GL} is reduced. This shows that V_{GL} is not much affected by the fluence 1.0 x 10^{13}.

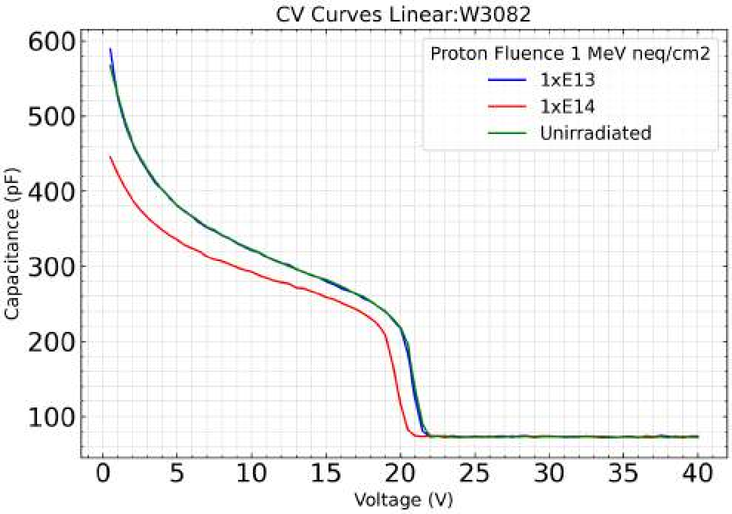

(a)

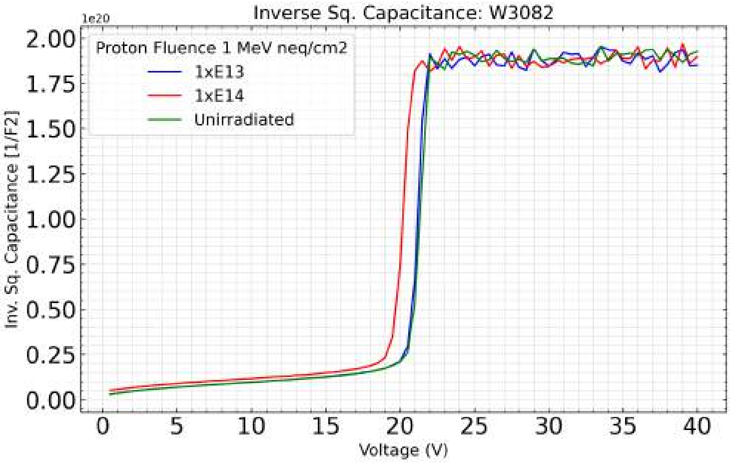

(b)

Figure 4.9: (a) Capacitance and (b) inverse squared capacitance, versus voltage of the LGADs from W3082 after irradiation at 10°C and 1kHz.

4.5 TCT measurements

4.5.1 Gain

TCT measurements were performed to evaluate the charge collection and gain in LGADs, using the TCT setup at AGH University of Krakow, as explained in Section 2.2.3. The measurements were performed with the infrared laser (1064 nm) focused to a beam spot having FWHM $\sim$ 12 μm. Laser intensity was kept to produce a charge of $\sim$ 2 mips, i.e., with a DAC value of 42.5%. The applied voltage is up to 90 V in steps of 5 V, before the avalanche breakdown, in order to avoid the amplitude saturation for the amplifier damage. The gain values from Figure 4.10, calculated from Equation 3.1, show that the gain for both the wafers (3082 and 3108) before the avalanche breakdown is ~ 20. At 60 V, devices from both wafers exhibit a gain of ~ 13, showing a similar gain behavior despite the difference in thickness, which validates the gain uniformity across the wafers.

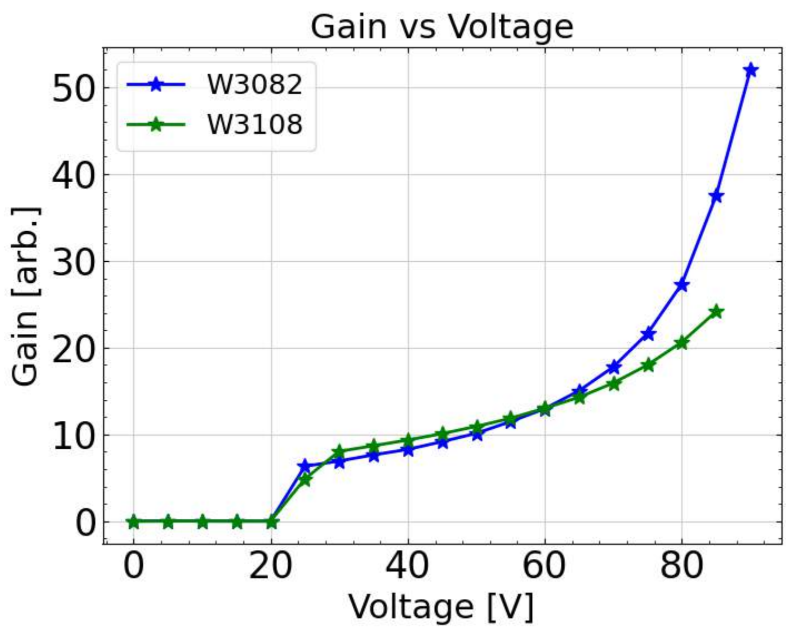

Figure 4.10: Gain of the devices from W3082 and W3108 at room temperature.

4.5.2 Gain suppression

In LGADs, gain suppression is a term that refers to a reduction in internal multiplication when the detectors are exposed to high charge densities. This phenomenon occurs because of the modification of the electric field due to high carrier density in the gain layer. This reduces the impact ionization rate and consequently reduces the gain due to the screening effect [95]. To evaluate the gain suppression in the devices, the charge collection from the PINs and LGADs of W3082 and W3108 was evaluated at different laser intensities to calculate the gain. Figure 4.11 shows the collected charge as a function of increasing laser intensity. The values in the legend represent the DAC value of the laser that quantifies the laser intensity, i.e., a higher DAC value represents a less intense laser. The increase in collected charge values represents that with increasing the laser intensity, a higher number of e-h pairs are generated in the detector, which is observed for both PINs (Figure 4.11a and 4.11b) and LGADs (Figure 4.11c and 4.11d).

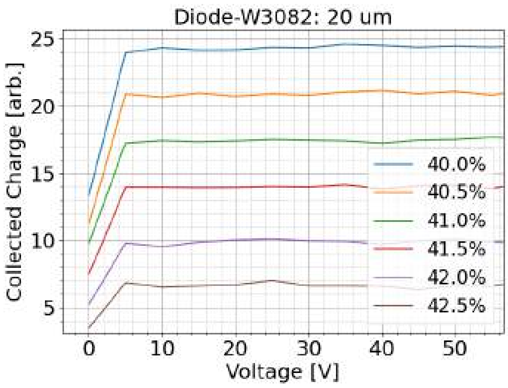

(a)

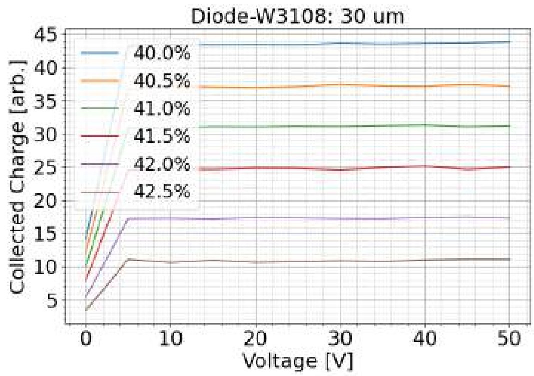

(b)

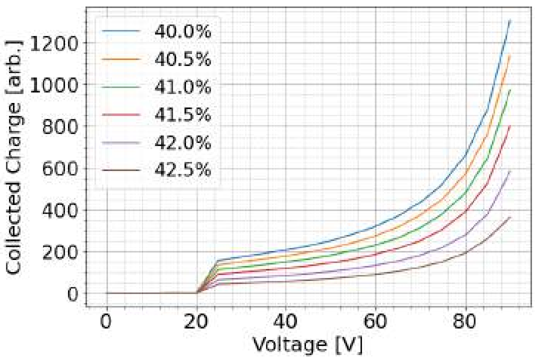

(c)

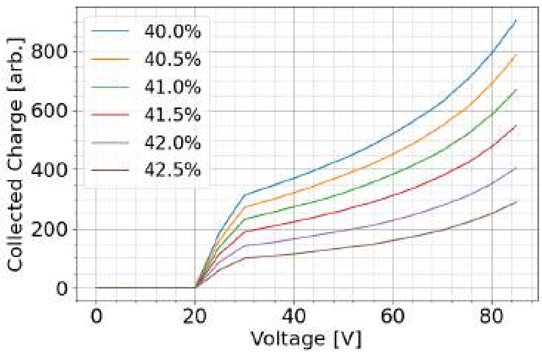

(d)

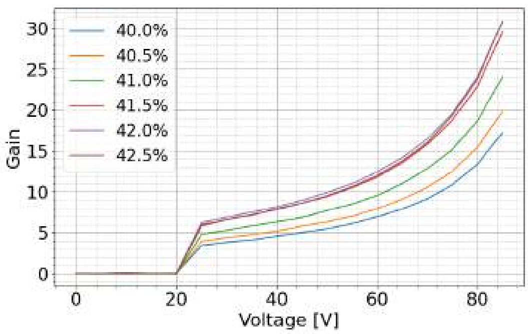

(e)

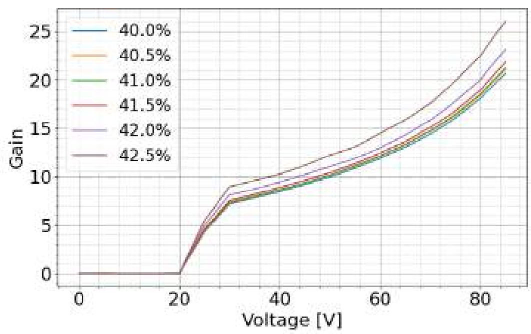

(f)

Figure 4.11: Collected charge versus applied bias as a function of increasing laser intensity obtained from the (a) PINs of W3082, (b) PINs of W3108, (c) LGADs of W3082, and (d) LGADs of W3108. Gain versus voltage at different laser intensities (e) W3082 and (f) W3108.

The calculated gain value from the collected charge is shown in Figure 4.11e and 4.11f for W3082 and W3108, respectively. Gain values show a substantial reduction with the increase in laser intensity. This gain suppression is quantified in Figure 4.12. It is deduced from the plot that the thinner detector (W3082) undergoes a reduction of ∼ 45%, while the thicker detector (W3108) experiences a reduction of ∼ 20%, at a bias voltage of 60 V for both detectors. The higher gain suppression in thinner LGADs is due to the shorter drift time and higher electric field, resulting in higher peak charge density that corresponds to the stronger gain suppression, as compared to the thicker LGADs.

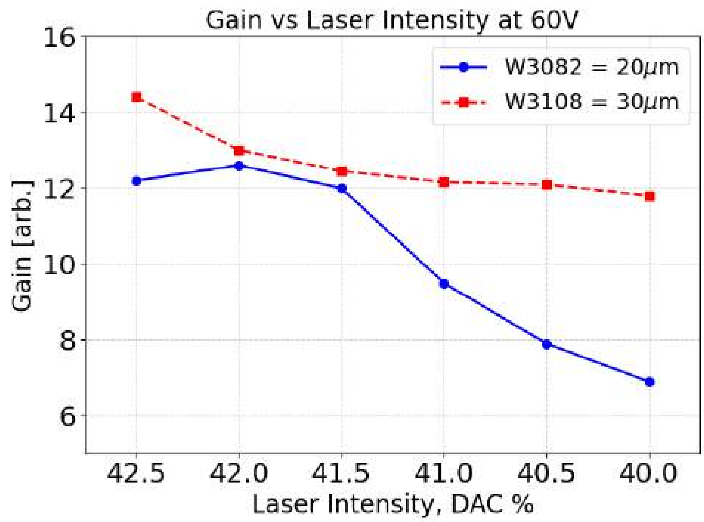

Figure 4.12: Gain of the devices from W3082 and W3108 versus increase in the laser intensity at 85 V.

4.5.3 Gain degradation after irradiation

The TCT measurements of the devices were performed at -20°C for the irradiated, and at the room temperature for unirradiated devices. All the measurements were performed with an infrared laser (1064 nm) at DAC value = 41.5% for both PINs and LGADs. Figure 4.13 shows the behavior of gain with the increasing proton fluence. At 60 V, which is well before the avalanche breakdown, the gain is ∼ 13 for unirradiated LGAD. This gain is reduced to ∼ 7 after 1.0 x 10^{13}, which is a reduction of ∼ 50%. After going higher in fluence, i.e. 1.0 x 10^{14}, the gain reduced to ∼ 4, which is a reduction of ∼ 70%.

The quantitative degradation of GL is carried out using the method of evaluating V_{GL} from the charge collection method using TCT measurements. For this purpose, a

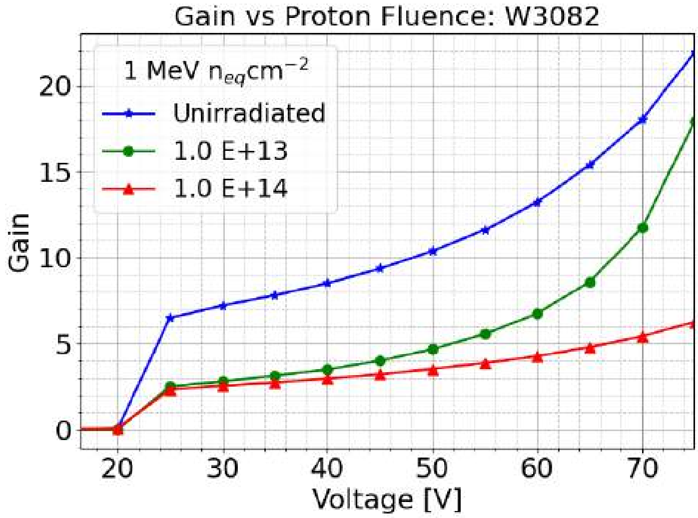

Figure 4.13: Gain of the devices from W3082 before and after proton irradiation.

fine voltage scan with a 0.5 V step is carried out near the V_{GL}. For this scan, a higher laser intensity is applied to see the depletion of the gain layer clearly. Figure 4.14a shows that the V_{GL} decreases with the increase in fluence. This decrease is quantified using Equation 3.2 and 3.3, and is shown in Figure 4.14b. Although, the value of acceptor removal coefficient (7.4 (± 2.2) x 10^{-16}cm^2 comes with a relatively large error due to less number of points (less number of fluences), but still this value lies within the acceptor removal coefficient mentioned in the literature for 60 MeV protons [87,88,96].

4.6 Time resolution

Time resolution measurements of the LGADs were performed using the timing setup explained in Section 2.2.3. For each data point, a sample of 5000 waveforms was recorded for better statistics, without averaging. To measure the time resolution in the laser-splitting configuration, as explained in Section 2.2.3, a constant fraction discriminator (CFD) algorithm is used [97]. Using CFD is a common practice for the analysis of time resolution. The basic idea is that the algorithm looks for two signals that are separated in time, and it finds the time when each signal reaches a chosen fraction of its maximum. For example, a CFD can be chosen in a way that we select the time when the first signal reaches 30% of its maximum amplitude, and compare that time with the time when the second signal reaches 70% of its maximum amplitude. The difference between these times is referred to as Δt. By repeating this practice for many waveforms (5000 in this study),

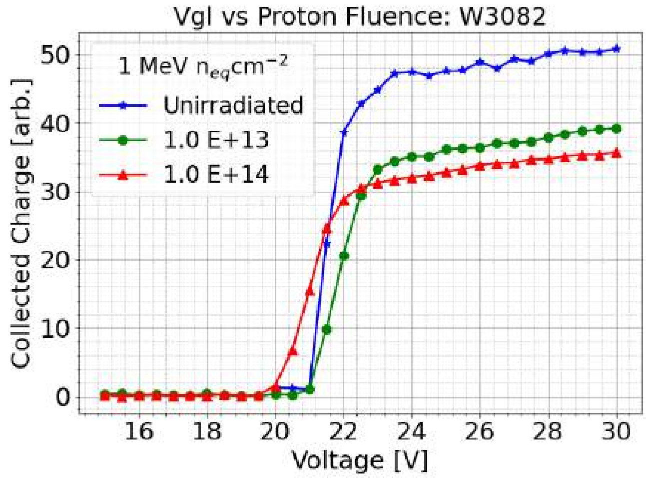

(a)

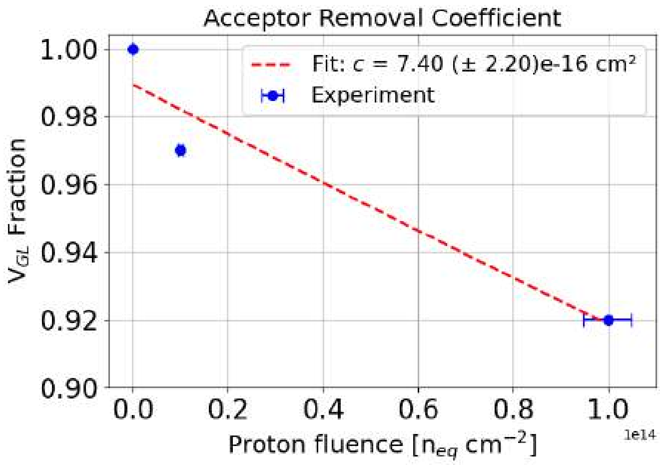

(b)

Figure 4.14: (a) Calculation of V_{GL} from the charge collection method using TCT. (b) V_{GL} fraction plotted against fluence to calculate the acceptor removal coefficient. The fitted value is mentioned in the plot legend.

a spread in Δt values is observed. This spread in Δt values is what is called *jitter*, and it tells the information of the timing resolution of the detector. If the two signals fluctuate independently, the total jitter can be written as the sum of the contributions from each signal. Since the two signals originate from the same laser source, the time resolution can be calculated from the Equation 4.1.

$$\sigma_{DUT} = \frac{\sigma_{jitter}}{\sqrt{2}} \tag{4.1}$$

In practice, Δt values follow a Gaussian distribution, so a fit is applied with a Gaussian curve and takes the width σ as the jitter. By trying different CFD fractions for each signal, a map can be generated from these values. From this map, a fraction from each signal can be chosen that gives the smallest jitter. This gives us the best possible time resolution for this setup. A higher laser intensity, $\sim$ 5 mips, was applied to separate the signal from noise. The waveforms of an unirradiated LGAD from W3082 obtained with the laser splitting configuration of the TCT setup are shown in Figure 4.15a. Two signal peaks are visible with a delay of 120 ns, as a result of laser splitting. An example of the analysis process is shown in Figure 4.15b, revealing the process of identifying peaks (red lines), maximum amplitudes (blue lines), and CFD thresholds (green lines).

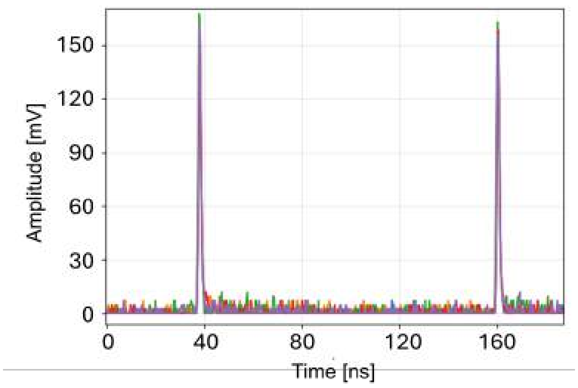

(a)

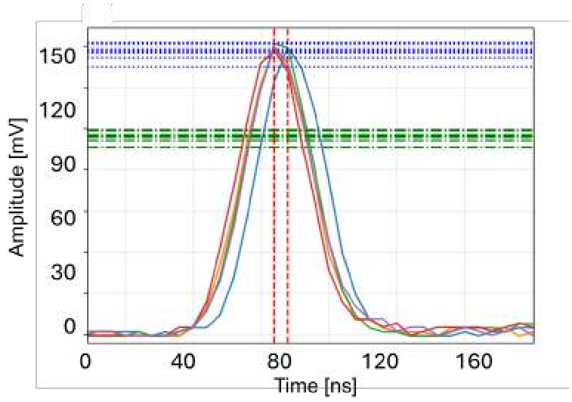

(b)

Figure 4.15: (a)A few raw TCT waveforms from two peaks obtained with the laser splitting, with a delay of 120 ns. (b) Close-up of a few waveforms from the first peak. The red lines show the peak, blue lines show the maximum amplitude of each waveform, and green lines show the marked threshold for CFD (70% in this case) for each waveform.

The spread of the time of flight (ToF) is plotted in Figure 4.16a. This spread undergoes fitting using a Gaussian distribution as shown in Figure 4.16b. The time resolution of the device is then calculated by using Equation 4.1, where σ_{jitter} is obtained from Figure 4.16b.

An example of calculating σ_{DUT} at different CFD thresholds is shown in Figure 4.17. This practice is used to plot a matrix or a map to choose the CFD thresholds for the first and second peaks to obtain the best time resolution. For most of the measurements, a CFD of 70% - 70% is applied to calculate σ_{DUT}.

Time resolution of the devices before and after irradiation is shown in Figure 4.18. With this timing setup, the LGADs show a timing resolution of $\sim$ 50 ps for both the

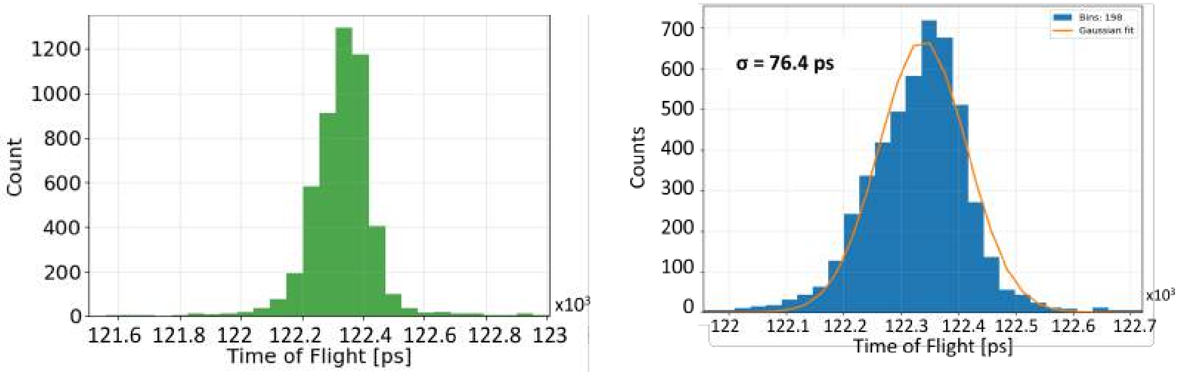

(a) (b)

Figure 4.16: (a) Histogram showing the ToF calculated from the Δt of the waveforms as seen in Figure 4.15b. (b) Gaussian fitting of the distribution of ToF to obtain the jitter of the sensor.

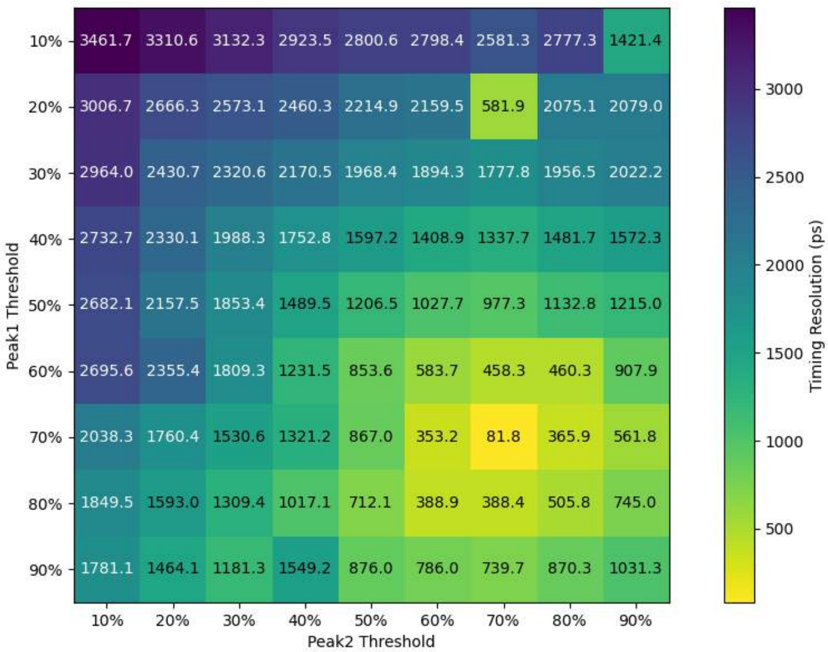

Figure 4.17: An example of a matrix of the time resolution (σ_{DUT}) calculated from different CFD thresholds for the first peak (y-axis) and second peak (x-axis).

wafers before irradiation. After irradiation, the time resolution degrades with the increase in fluence. W3108 seems to be more affected by the irradiation in terms of time resolution.

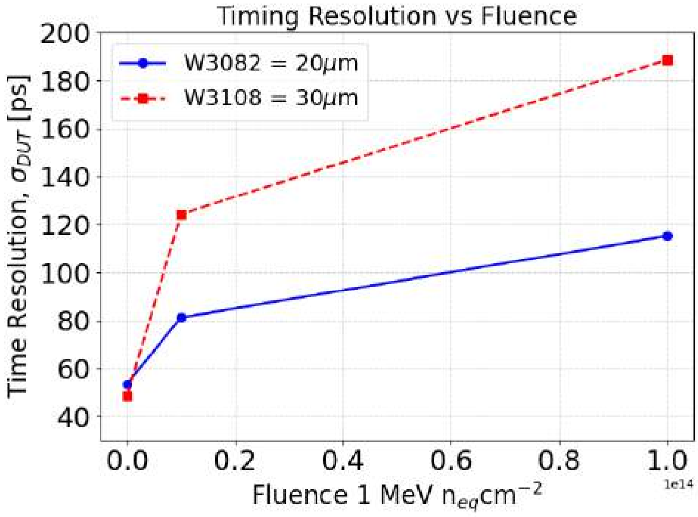

Figure 4.18: Time resolution obtained from the CFD method, before and after irradiation.

Summary

In this chapter, thin-LGADs with a thickness of 20 μm and 30 μm were studied for the timing applications in the sub-detectors of EIC. LGADs and PINs were characterized before and after irradiation. Before irradiation, the electrical characterizations show a small leakage current, and the devices break down at around 80 V and 120 V for 20 μm and 30 μm thick devices, respectively. The capacitance-voltage curves show a gain layer depletion voltage of 21 V for both thicknesses, showing a well-controlled fabrication. The devices have a gain in the range of 20-25 at around 70-80 V, depending upon how far the voltage is from avalanche breakdown. Laser characterizations at different intensities revealed the gain suppression in LGADs, with a reduction of 45% for 20 μm and 20% for 30 μm thick detectors. More suppression in thinner detectors is observed due to a more localized charge cloud near the gain region.

The devices were irradiated with 58.5 MeV protons with 1.0 x 10^{13} and 1.0 x 10^{14} fluences, when normalized to 1 MeV n_{eq} cm^{-2}. After irradiation, the leakage current increases by an order of magnitude as the fluence increases. The breakdown voltage is minimally increased after the 1.0 x 10^{13} fluence, but increases significantly after 1.0 x 10^{14} fluence, for both wafers. At 60 V, a reduction of 50% in gain is observed for 1.0 x 10^{13}, while 70% for 1.0 x 10^{14} fluence, when compared to the unirradiated LGAD. Comparison of the V_{GL} before and after irradiation gives the value of $\sim$ 7.4 x 10^{-16} cm^2, which is comparable to the values reported in literature. A time resolution of $\sim$ 50 ps is achieved from both device thicknesses, which is a great improvement in terms of time resolution obtained from the bare device connected to the simple aluminum housing. With fast timing boards, the time resolution can be improved.

The results have shown a substantial radiation hardness for the expected fluence at EIC, and for higher fluence as well. The radiation hardness allows the detectors to be implemented in timing detectors in EIC. Further investigations will be carried out in the near future based on the excitation wavelength used in the TCT setup. Furthermore, as the devices are ultra-thin, a proposal is in review to irradiate the devices with 25 MeV protons at the same fluences to compare the level of damage created in the GL for lower energy protons.

Chapter 5

Development of Trench Isolated LGADs for high energy physics and synchrotron applications

5.1 Introduction

LGADs provide internal signal amplification through a highly doped gain layer, enabling excellent timing resolution, but their capability to translate to finely pixelated detectors is limited by the presence of non-sensitive inter-pixel regions. TI-LGADs provide charge multiplication through the gain layer, which increases the signal amplitude even for small deposited energies, as many experiments operate with soft X-rays in the energy range of $1-5$ keV. As a result, low-energy X-ray photons can produce signals with a higher SNR, which makes them detectable. At the same time, the trench isolation reduces the no-gain region between pixels, which improves the fill factor and offers uniform response across the sensor area. A high fill factor is important in imaging applications, where dead regions directly reduce image quality and detection efficiency. In collaboration with UK, Czech, and Polish universities and Micron Semiconductor Ltd., they developed the TI-LGAD [98]. In this design, deep isolation trenches replace conventional junction termination extensions and p-stop implants, allowing for a near-100% fill-factor while preserving the timing resolution. This makes TI-LGADs promising candidates for applications ranging from HEP experiments to synchrotrons for the detection of soft X-rays and photon imaging.

Investigations of the prototypes of the detectors are carried out at the TCT laboratory in the AGH University of Krakow. This work also contains a comprehensive evaluation of the fill factor of pixelated TI-LGADs using both front-side and back-side illumination. The emphasis of this study is the response of the detectors to low-penetrating particles, achieved through back-side illumination with a 400 nm laser, producing a very shallow charge deposition profile that mimics soft X-rays and deep ultraviolet (DUV) radiation. This is the first extensive study reported by any group investigating TI-LGAD performance for low-penetrating particles. Detecting soft X-rays is necessary for several synchrotron techniques, such as soft X-ray diffraction, spectroscopy, and spectromicroscopy [10]. A detailed investigation of the inter-pixel distance (IPD) as a function of doping concentration of the gain layer is carried out. Fundamental electrical characterizations (IVs) and gain measurements performed at AGH University of Krakow are followed by an extensive TCT campaign at ELI beamlines using SPA-TCT and TPA-TCT. Measurements on the devices fabricated on different wafers provide new insights into the fill-factor optimization using TI-LGADs for low-penetrating particles involving shallow charge deposition.

After the successful characterization of the first batch of TI-LGADs, further efforts were made to improve the trench filling process in order to prevent over-etching of the silicon oxide. This chapter also presents the mask design simulations, along with the detailed electrical and laser characterizations carried out to evaluate the improved structures.

5.2 Fabrication of TI-LGADs

This study presents the first batch of TI-LGADs that were fabricated by Micron Semiconductor Ltd. These devices are designed to minimize the no-gain region to enhance the FF, as explained in Figure 1.19 in Section 1.7.2. Trench parameters, including width and depth, were optimized using TCAD simulations (values discussed later in this paragraph); therefore, no variations in these parameters were introduced in the fabrication of this batch. However, the major difference between the current design and the TI-LGADs designed by other foundries is that the gain layer is continuous up to the edge of the trench; therefore, no gap between the gain layer and the trench is present. The fabrication is carried out at Micron Semiconductor Ltd., Lancing, UK, whereas the trenches are fabricated at the Scottish Microelectronics Centre (SMC), Edinburgh. The optimal trench design is limited by the capabilities of the tools at the SMC, which uses Deep Reactive

Ion Etching (DRIE) [99], to etch trenches into the silicon. The key to the design is the control of the aspect ratio of the trenches. Careful control of the etching parameters allows the control of the depth and width of the trenches. TCAD simulation shows that narrower trenches provide better isolation and that the depth of the trench does not have a significant effect on the isolation as long as the trench is deeper than the gain region, as shown in Figure 5.1a.

In the simulation, isolation is evaluated by measuring the resistance between two adjacent pixels at a voltage above the full depletion, as described in Ref. [100]. In these simulations, a fixed oxide charge was present at the interface of the trench with a value of 1 x 10^{12} cm^{-2}. Based on feasible processing capabilities and simulation results, the optimized trench is 1 μm wide and 5 μm deep. Figure 5.2 shows an scanning electron microscopy (SEM) image of the edge of a cleaved device. The trench is clearly seen surrounding the active region, left of the image. The image on the right of Figure 5.2 shows the dimensions of the trench with a width of 2 μm and a depth of 7 μm. This is slightly deeper than the expected trench depth due to a slight over-etch of the trench to ensure the depth was greater than the critical value of 2 μm. However, this increase in the trench dimension as compared to the design is because the silicon is consumed for the growth of silicon oxide in the trench. One can see that the trench is not completely filled with oxide; this was due to the etching of the oxide before the junction implantation. The etching of the trench is caused by insufficient thermal oxide growth while filling the trenches, which resulted in an "open" trench. As the trench was slightly open, while performing the wet etch of the junction window, the etchant could enter the trench, and therefore 2 μm silicon oxideon the top was etched because of wet etching. The trench was chemically etched away. However, based on simulations and experimental results, this does not affect the isolation capability of the trench. This is shown in Figure 5.1a where the inter-pixel resistance is simulated as a function of the trench width and depth. One can see that by reducing the width of the trench, the resistance increases; changing the depth of the trench has no significant impact on the resistance. It should be noted that for a trench with a depth of less than 2 μm, the simulation showed early breakdown, hence these depths were not considered for the fabrication.

Simulations were performed using other typical isolation structures, such as the p-stop and p-spray, to verify that the inter-pixel resistance achieved by the trenches is sufficient. Figure 5.1b shows the inter-pixel resistance for the different isolation methods, including a no-isolation method. The no-isolation method is used as a reference, which is the same

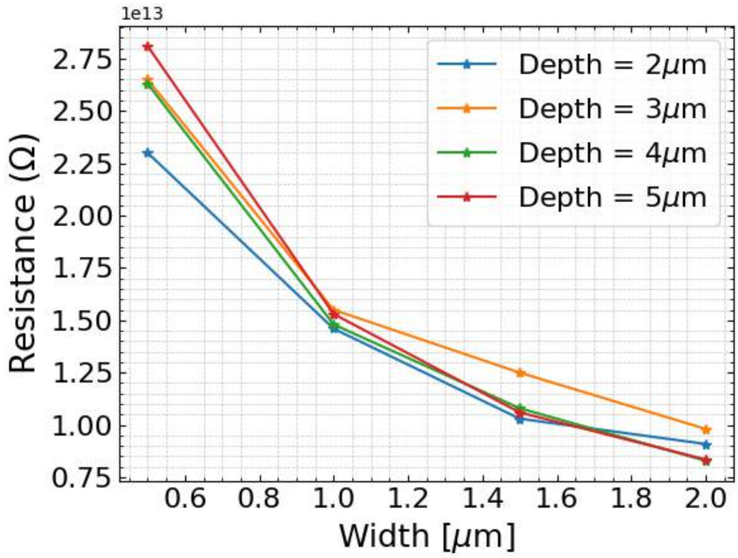

(a)

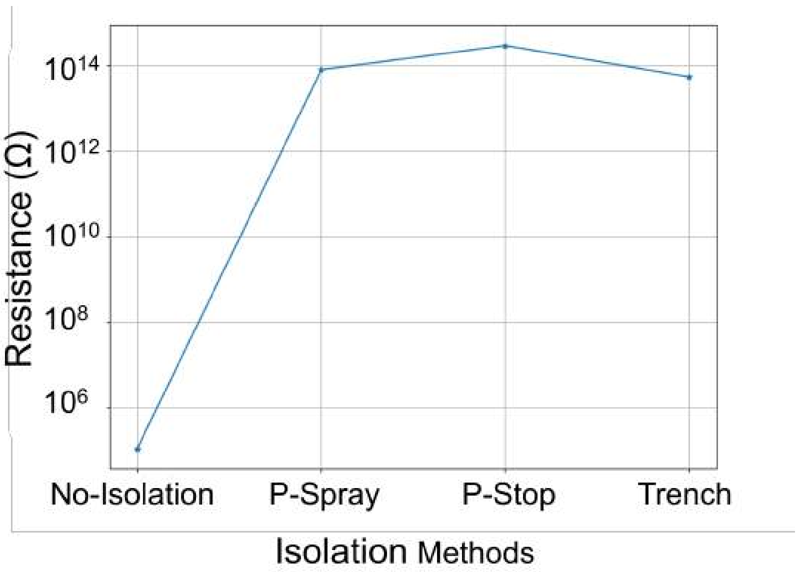

(b)

Figure 5.1: (a) Simulation of the dependence on the resistance between adjacent pixels as a function of trench width and trench depth. (b) Simulation of the dependence on the resistance between adjacent pixels for a variety of isolation methods, where, the trench parameters are 1 μm wide and 5 μm deep [98].

structure as the p-spray method but without the p-spray implantation. Generally, Micron Semiconductor Ltd. uses p-spray as a standard. The resistance is measured for the case of a fixed oxide charge of 1 x 10^{12} cm^{-2}, where the inter-pixel resistance shows comparable

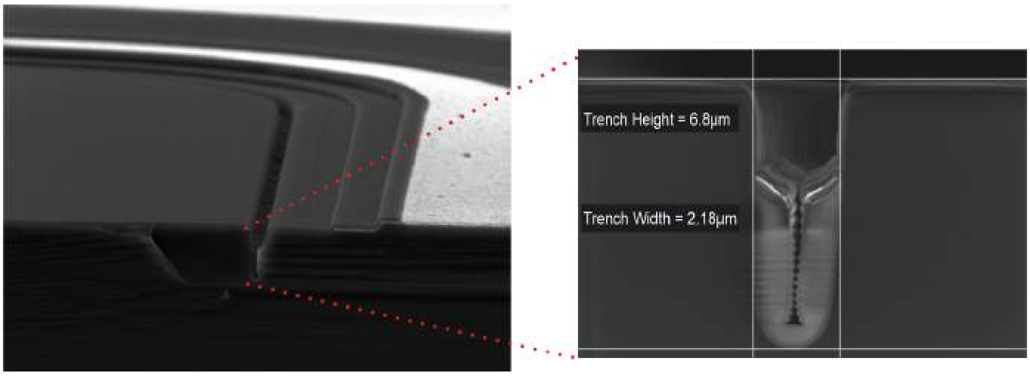

Figure 5.2: The image on the left is an SEM image that shows a cleaved detector and the fabricated trench that surrounds the active region. The image on the right shows a close-up of the trench with the final dimensions of the oxide-filled trench. Width ≈ 2.18 μm, depth ≈ 6.8 μm.

results for the p-spray, p-stop, and trench isolation methods. This verifies that the trench isolation method developed shows good isolation. As explained earlier, the fabrication process of trenching was limited in terms of the width of the trench; the final fabricated trench is 2 μm. The fabrication of the TI-LGAD was performed on 200 μm thick, high resistivity, 6-inch p-type silicon wafers. Although fabrication on a 200 μm thick substrate is not ideal for timing studies, it serves as a proof-of-concept and may be useful in other applications that do not require a fast timing response. A detailed fabrication process of the standard LGAD used by Micron Semiconductor Ltd. is described in Section 2.6.5 of the thesis mentioned in [15].

Table 5.1: Fabrication details of the first batch of TI-LGADs showing process parameters [15].

Wafer No.	Relative Boron dose	Relative Phosphorus dose
W1	1.4	1
W5	1.3	1
W6	1.2	1
W10	1.1	1

This batch consists of 4 wafers, differing only in the doping concentrations of the gain layer, described in Table 5.1. The results from this work are focused on W5 and W6 with a gain of 2-4, based on the fabrication process discussed in [15]. The wafer layout contains both full-sized TimePix3 sensor arrays and pad test structures. There are five

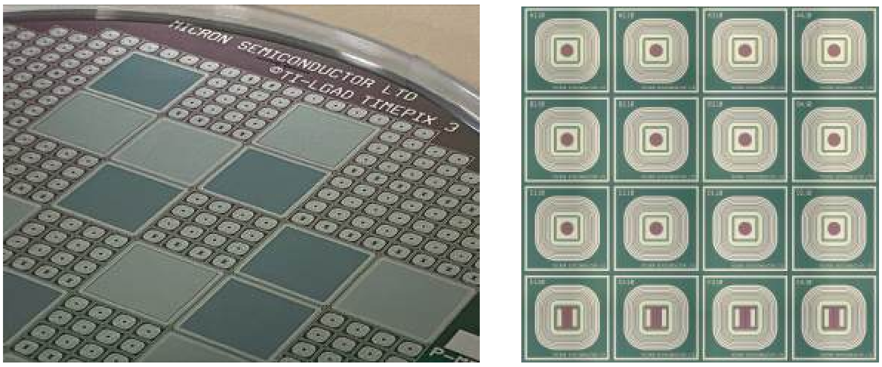

(a) **(b)**

Figure 5.3: (a) Processed TI-LGAD wafer, (b) Pad test structures, 1st line contains A devices: LGADs with JTE, 2nd line contains B devices: LGADs with Trench and JTE, 3rd line contains C devices: PIN, and D devices: LGADs with Trench, and bottom line are E devices: 2x1 Pixels with trench in the middle and around the pad.

types of pad test structures with an active area of 1x1 mm^2, described as follows:

- **A-devices:** 1x1 Standard LGAD pad with JTE used as the terminating structure.
- **B-devices:** 1x1 LGAD Pad with a combination of the JTE and the trench used as the terminating structure. The trench is located 5 μm from the inner part of the JTE towards the active area.
- **C-devices:** 1x1 PIN Diodes Pad with JTE used as the terminating structure.
- **D-devices:** 1x1 LGAD Pad with a trench used as the terminating structure.
- **E-devices:** 2x1 LGAD Pixels with a trench used as the terminating structure, and also to isolate the pixels. These devices' pixels have a size of 500 μm x 1mm.

In addition to pad devices, there are pixelated devices with a 55 μm and 110 μm pixel pitch compatible with the Timepix3 ASIC [101]. Figure 5.3 shows a fabricated wafer with Timepix3 sensors and pad devices. The results of the Timepix3 sensors will not be discussed in this thesis.

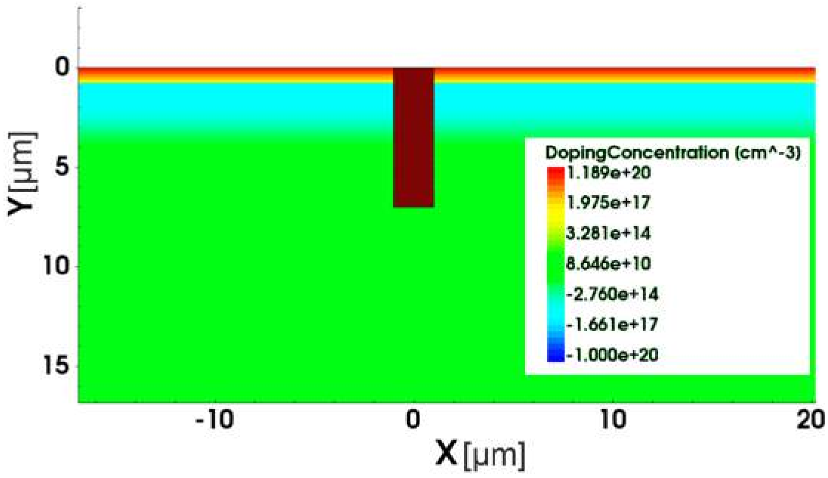

(a)

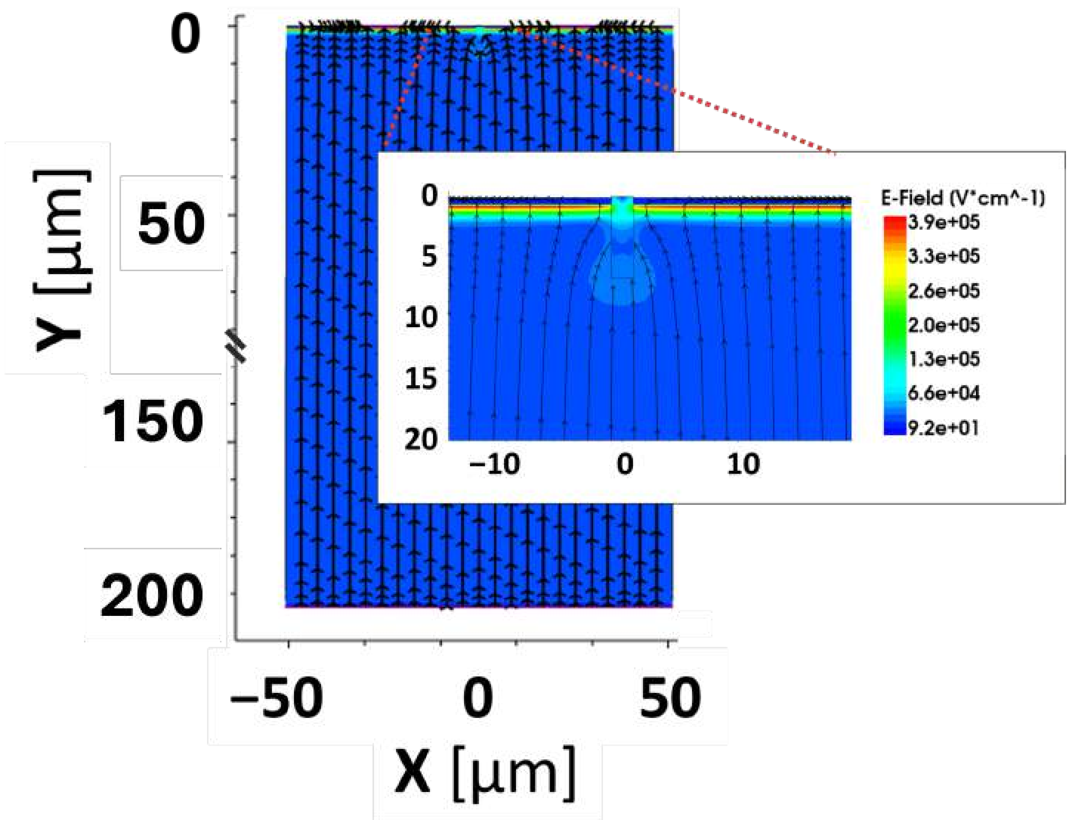

(b)

Figure 5.4: Simulated TI-LGAD structure in Sentaurus TCAD shows (a) doping concentrations across the device, (b) Electric field at 500 V.

5.3 Methodology

5.3.1 TCAD simulation

TI-LGAD simulation studies were performed using Sentaurus TCAD. The device geometry was generated using the Structure Editor (SDE) tool. The device structure is 100 μm wide and 200 μm thick p-type silicon. A 2 μm wide and 7 μm deep trench, filled with silicon oxide, is placed at a position marked X = 0 μm, between two pixels. The structure is designed so that the edges of the detector are far from the trench, and just the region around the trench is simulated, i.e., inter-pixel distance. A uniform highly doped n^{++} implant is present on either side of the trench, that is, from position X = –50 μm to X = −1 μm (Pixel1) and X = 1 μm to X = 50 μm (Pixel2), as shown in Fiure 5.4a. A p^{+} gain layer is implanted below the n^{++} layer to create the typical gain layer doping profile, as described in Ref. [44]. The simulated doping profiles presented in this study are derived from secondary ion mass spectrometry (SIMS) measurements performed on real devices fabricated at Micron Semiconductor Ltd, as shown in Ref. [44]. These profiles were subsequently adjusted to account for an additional thermal processing step required for the production of TI-LGADs. The device simulation includes a fixed oxide charge of 1 x 10^{12} cm^{-2} in order to better represent a real working device with a saturated fixed oxide charge. Figure 5.4a shows the simulated TI-LGAD structure with the doping concentrations, and Figure 5.4b shows the electric field at 500 V in the region around the trench.

The simulation of the IPD is carried out using the transient simulations within the TCAD SDEVICE tool. Transient simulations are carried out with the charge injection using infrared (1064 nm) wavelength from a monochromatic source. A 1-dimensional laser scan is performed in the simulation by injecting light at a range of positions along the surface, starting at X = –40 μm to X = +40 μm. The simulations are performed at a range of voltages, 0-300 V, to understand the behavior of the IPD as a function of voltage.

5.3.2 Transient Current Technique

In this work, a TCT setup installed in the AGH University of Krakow was used to study the isolation and determine the IPD experimentally. The experimental setup is explained in Section 2.2.3.

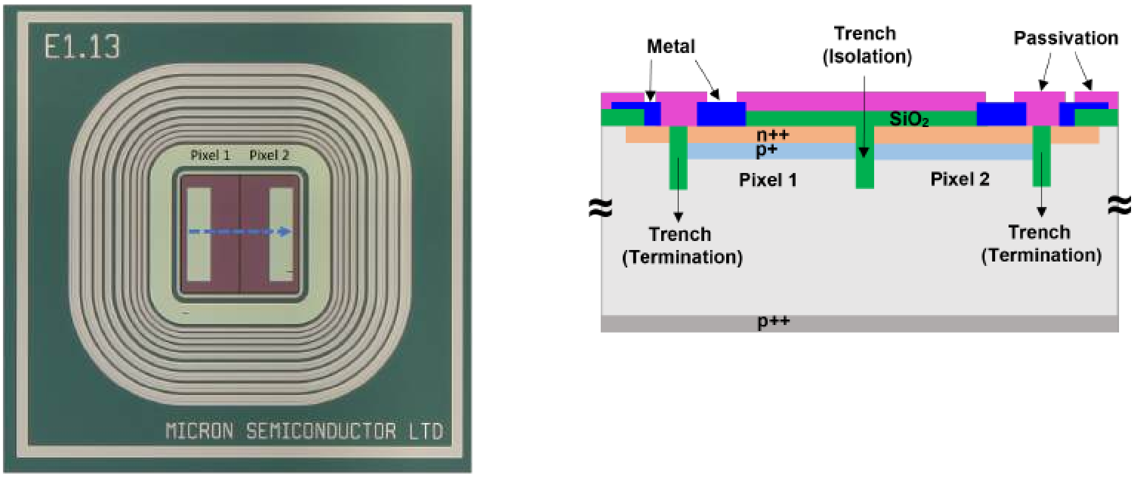

(a) (b)

Figure 5.5: a) Device E, 2x1 pixels. The arrow indicates the direction of the 1-D linescan with the measurements starting on top of the electrode of Pixel1 and finishing on top of the electrode of Pixel2. b) Cross-section of the device E.

The DUT was mounted on a 4-channel readout board, the Chubut-2 [102]. As we are working with a 2x1 pixel device, pixels are connected to two channels of the Chubut-2, and the remaining two channels are grounded by a 50 Ω resistor. The bias voltage is applied through an HV line. Chubut-2 comes with built-in broadband amplifiers with a 40 dB gain and 50 MHz to 4 GHz bandwidth, allowing both outputs to be directly connected to the oscilloscope. This enables us to record signals from both pixels at once. A 1D scan in the x-direction is performed where the laser traverses from metal (left) to metal (right) in 1 μm steps, so that it moves across Pixel1, trench, and then Pixel2, as shown in Figure 5.5a.

5.4 Results and discussions

5.4.1 Electrical characterizations: simulation and experiment

Electrical characterization of this batch is carried out using the probe station in the Glasgow Laboratory for Advanced Detector Development (GLADD) at the University of Glasgow, where the current-voltage (IV) and capacitance-voltage (CV) characteristics were observed. Figure 5.6a shows the leakage current (I_{leak}) of a standard LGAD with JTE (A-devices) is of the order of 100s of picoamperes (pA). LGAD with a combination of JTE and trench as the termination structure (B-devices) has a slightly higher leakage current than A devices. For the devices that include only a trench as the termination structure around the pad periphery (D-devices), and devices that have a trench in the middle of the two pixels as well as around the pad periphery (E-devices), the leakage current increases by almost an order of magnitude. I_{leak} does not increase significantly with an increase in voltage as the gain is ~ 3, which refers to a lower electric field in the multiplication region, and no breakdown is observed up to 300 V.

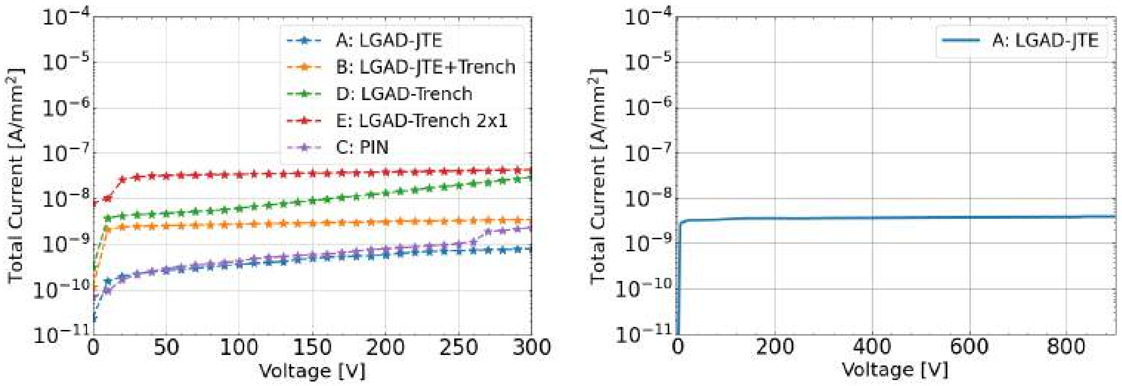

(a) (b)

Figure 5.6: (a) Leakage current of diode and LGADs with various termination structures from Run 3455, W6. (b) IV measurement of the standard LGAD (A-Device) from the same wafer shows no breakdown up to 900 V.

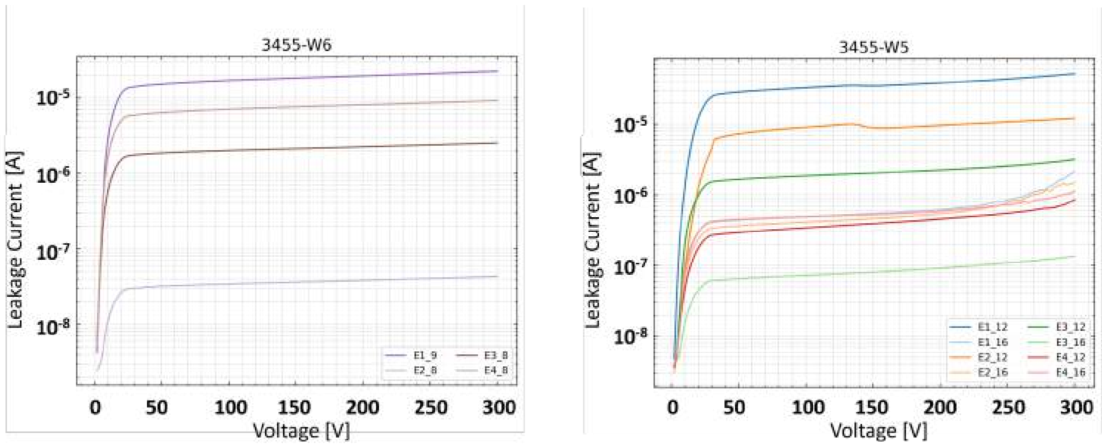

(a) (b)

Figure 5.7: Leakage current from a) W6 (lower doping) b) W5 (higher doping) Trench isolated E-devices. No premature breakdown is observed for these devices.

These results show that the trench has a direct impact on the leakage current, but does not cause early breakdown. A few pad devices are tested for voltages up to 900 V, and no breakdown voltage is observed, as shown in Figure 5.6b. The 2x1 pixel devices show good uniformity in terms of the leakage current for several devices, with some devices showing higher current (> 1 μA) as shown in Figure 5.7b, showing a well-controlled fabrication. The CV curves show that the depletion voltage of the gain layer (V_{GL}) is $\sim$ 24 V and the full depletion voltage (V_{FD}) is $\sim$ 120 V for all devices, as shown in Figure 5.8a. The simulation of the CV curves shows excellent agreement with the experimental measurements in terms of V_{GL} and V_{FD}. Figure 5.8b represents the charge collection from the devices, showing a difference in V_{GL} for both wafers. W5 shows a higher V_{GL} due to a higher GL doping.

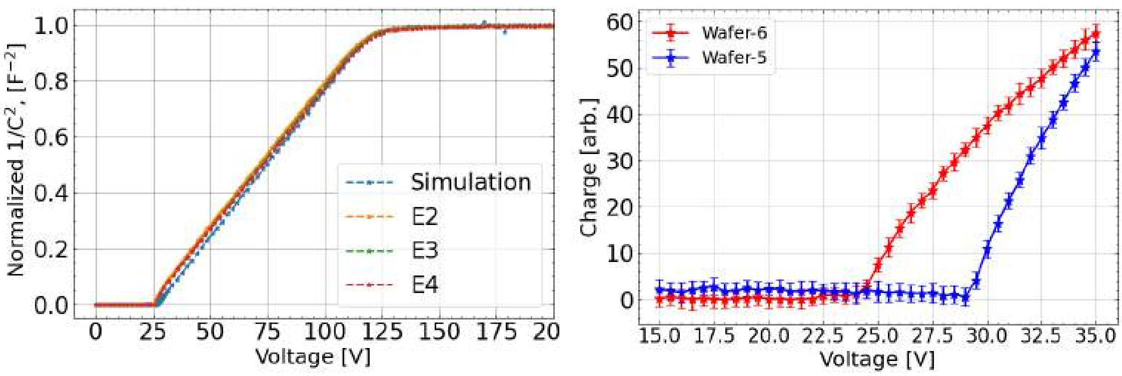

(a) (b)

Figure 5.8: (a) Experimental and simulated inverse square of capacitance as a function of the reverse bias voltage curves, which explains the good agreement between experimental measurements and simulations. (b) V_{GL} of W5 and showing different gain layer doping concentrations.

5.4.2 Gain

After successful electrical characterization of the sensors, charge collection (CC) measurements were performed using the TCT setup as described in Section 5.3.2. The IR laser of wavelength 1064 nm was used for CC measurements as it traverses the sensor thickness, hence mimicking a mip. Therefore, the laser intensity was calibrated to the most probable value (MPV) of a mip to induce charge in the sensor [96]. The laser intensity was kept the same for all scans and sensor types, creating $\sim$ 2.6 fC charge. The gain of the devices was obtained by comparing the charge collection with a PIN, using Eq. 3.1. Since the wafer under test has the second lowest GL doping, the results in Figure 5.9 show that the gain is between 2.5 and 3 for bias voltages above V_{FD}. TCAD simulations show a good agreement with a gain in the range of 3 - 4.

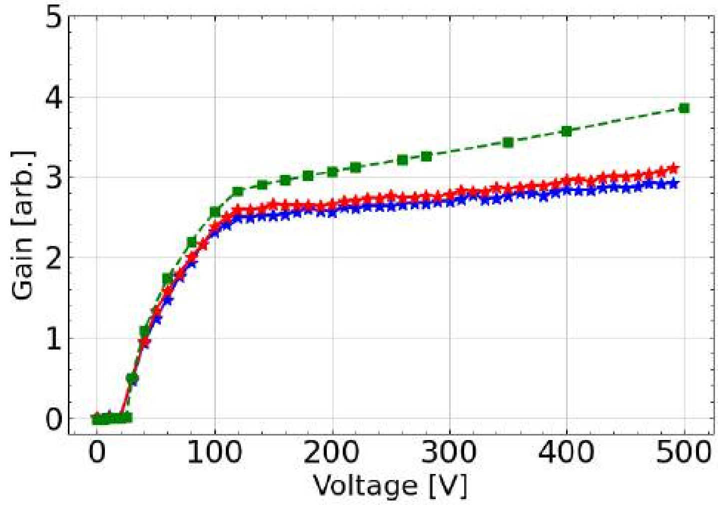

Figure 5.9: Gain of the standard (blue) and TI-LGAD (red) from the same wafer, as a function of voltage. The gain from simulations (green) agrees well with the experimental measurements.

5.4.3 Isolation: simulation and experiment

Pixel isolation

One of the key requirements of a pixelated detector is that the pixels are isolated, i.e., each pixel only registers a signal if there is a charge interaction within the pixel area. The laser response from the TI-LGADs is observed to validate the pixel isolation via trenches. For this study, the TCT system is used with an IR laser (1064 nm) and focused to a spot size of 10 μm to observe the signal on each pixel of a 2x1 pixel sensor when the laser traverses the detector thickness. To perform the electrical isolation measurement, 2D charge collection maps of Pixel1 and Pixel2 are generated by performing a 2D TCT raster scan of the entire pixel array. Figure 5.10a plots the charge collected on Pixel1 as a function of laser position. One can see the structure of the 2x1 array, with Pixel1 on the left (Red) and Pixel2 on the right (Blue) of the image.

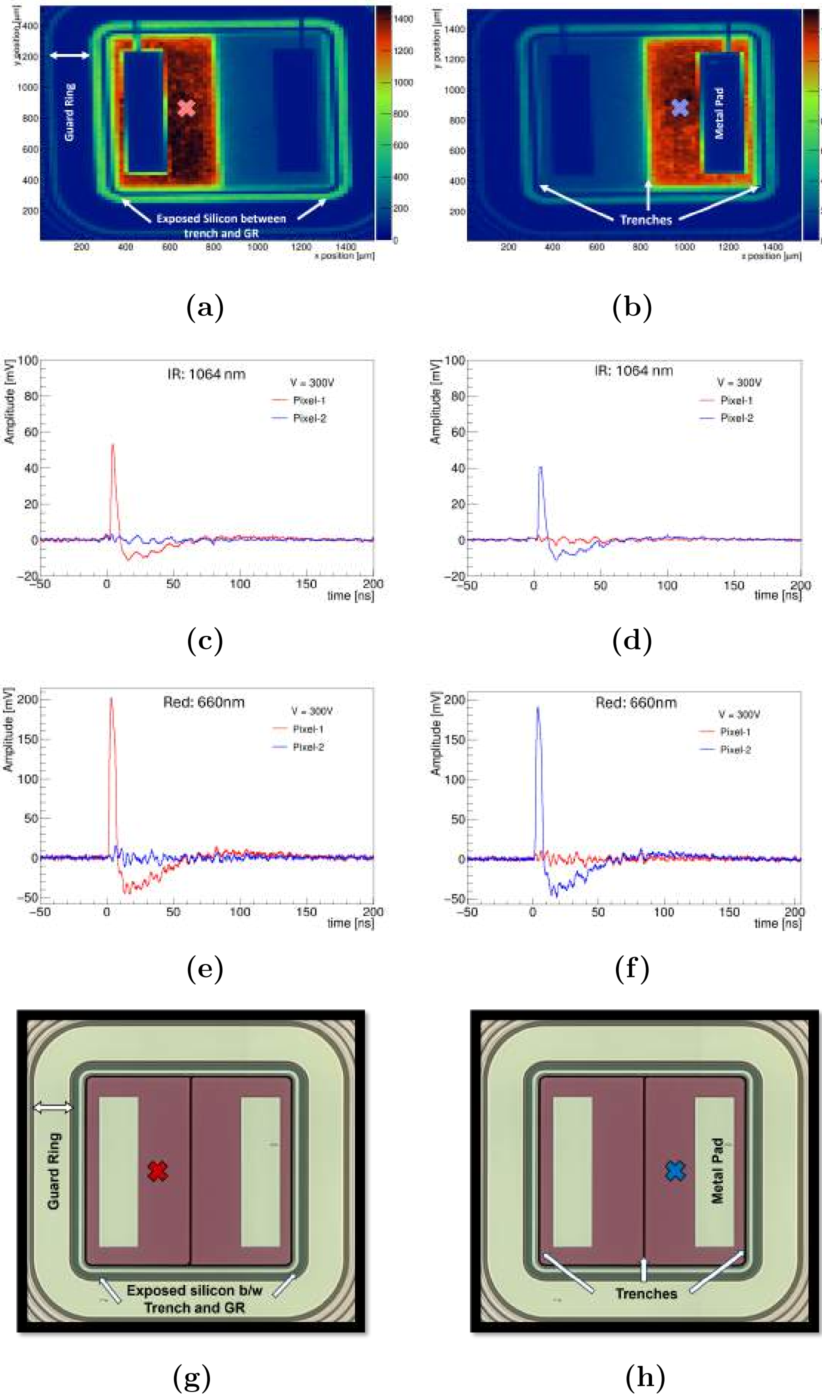

Figure 5.10: Charge collection 2D maps of the TI-LGAD demonstrating excellent isolation between Pixel1 and Pixel2: (a,b) independent pixel response; (c,d) IR laser waveforms for Pixel1 and Pixel2; (e,f) red laser waveforms for Pixel1 and Pixel2. Crosses in (a,b) indicate the laser positions. Schematics of the scan and representative waveforms are shown in (g,h).

The rectangular regions in the center of each pixel are metal electrodes that reflect the laser, and thus, no charge is seen when the laser hits these regions. The gap between the GR and the 2x1 pixel array can also be seen. Figure 5.10a shows that when the laser illuminates the region of Pixel1, the charge collected from Pixel1 is high, and when the laser illuminates the region of Pixel2, the charge collected from Pixel1 is close to zero. The response of Pixel2 is similar, as shown in Figure 5.10b. This result confirms that the pixel isolation is effective, although a small collected charge can be observed on the adjacent pixel. However, looking at the waveforms observed for both pixels when the infrared laser illuminates Pixel1 (Figure 5.10c) and Pixel2 (Figure 5.10d), no clear signal is present on the adjacent pixel. Similar is the case with the red laser, as shown in Figure 5.10e and 5.10f.

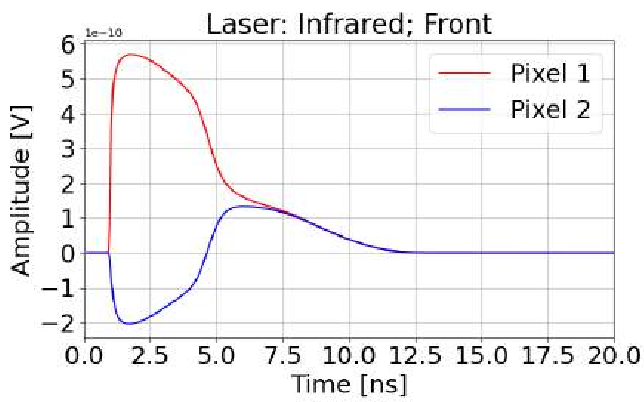

(a)

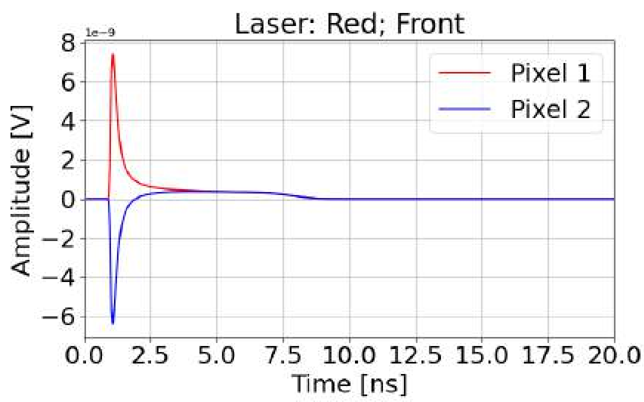

(b)

Figure 5.11: TCT waveforms obtained using TCAD simulations with (a) infrared (front illumination) and (b) red laser (front illumination), at 20 μm away from the trench.

To investigate the issue of small charge collection observed on adjacent pixels, we analyzed the simulated TCT waveforms on Pixel1 and Pixel2 using infrared (Figure 5.11a) and red (Figure 5.11b) lasers. Pixel1—the pixel under test—exhibits the collected signal. In contrast, Pixel2 displays a bipolar signal. This bipolar response arises from the movement of charge carriers that do not ultimately contribute to the collected charge on Pixel1. Despite not being collected, these carriers still induce a transient current in Pixel2. The current reverses direction during the process, resulting in a bipolar waveform that integrates to zero, consistent with the principles described in [93]. We further observed that the amplitude of the bipolar signal on Pixel2 diminishes as the laser injection point moves away from the trench, indicating a spatial dependence. The apparent charge collection on adjacent pixels, as shown in Figure 5.10, may thus be attributed to a coarse resolution of the bipolar signal. When the bipolar signal is not fully resolved, its integral can yield a small non-zero value, falsely suggesting a net charge collection.

Calculation of inter-pixel distance

IPD plays a crucial role in determining the fill factor of the device. The IPD was measured using the TCT setup described in Section 5.3.2. In this setup, a 1D scan is performed where waveforms are recorded as a function of laser position on the top surface of the detector. The laser moves from the metal electrode on top of Pixel1 to the metal electrode on top of Pixel2, crossing the trench (Figure 5.5a). The laser travels a distance of 700 μm for each scan in steps of 1 μm. The collected charge is calculated for each waveform by integrating the signal. The charge collected is plotted as a function of laser position, and the profile can be represented by an s-curve function [61], which is defined as

$$f(x) = \left[erf\left(\pm \frac{x - c_1}{c_2} \right) + 1 \right] * c_3 + c_4 \ , \tag{5.1}$$

where x is the laser position, and c_1, c_2, c_3, and c_4 are free fitting parameters. The erf is the Gauss-error function given by

$$erf(x) = \frac{2}{\sqrt{\pi}} \int_0^x e^{-t^2} dt \ . \tag{5.2}$$

The IPD is then calculated by the difference of the laser position where the normalized charge reaches 50% of the normalized charge of both pixels, as shown in Figure 5.12a. An example of the charge profiles obtained from 1D laser scans and the s-curve fitting is shown in Figure 5.12b.

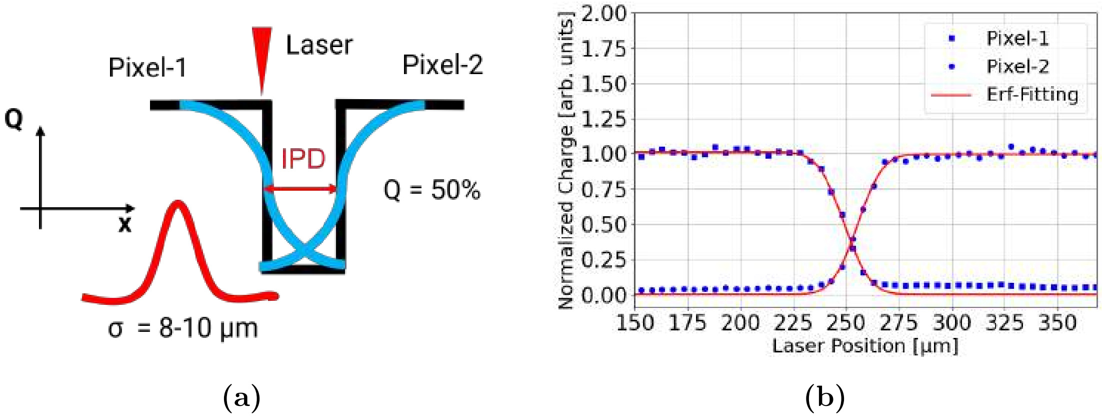

Figure 5.12: a) Schematics of the calculation method of the inter-pixel distance. b) Example of an IPD calculation using s-curve fitting using Eq. 5.1.

The laser scans as a function of position are performed with increasing voltage, 60 V to 300 V in steps of 30 V, as shown in Figure 5.13. Figure 5.13a shows the collected charge obtained from W6, while Figure 5.13b shows the collected charge of W5. The difference in the gain can also be observed from these plots. An unusual kink is observed at the trench position, which is more pronounced in the W5. This kink appears to be related to the doping profile and may arise from the continuous nature of the gain layer, which does not include a gap at the trench interface. This kink is studied in detail with the TPA-TCT, and is discussed in the later section.

Figure 5.14 shows the experimental and simulated CC profiles versus laser position on the device at a reverse bias of 300 V. The 1-dimensional charge collection profile obtained from the simulations is slightly different compared to the experimental results due to the difference in the laser beam profile in the simulation and experiment. This can be compared by looking at the FWHM (σ) of both curves. Figure 5.14a is obtained from the infrared laser (1064 nm) while Figure 5.14b is the result of the red laser (660 nm). While the laser is illuminating Pixel1, a small amount of collected charge is seen on Pixel2, and vice versa. Quantitatively, this charge is smaller for the infrared laser than the red laser and can be referred to as the charge sharing. However, this charge sharing produces no clear signal on the adjacent pixels, as shown in Figure 5.10. Section 5.4.3 explains the phenomenon that might be the reason for crosstalk. The red laser was used as it penetrates only a few microns in silicon, while the IR penetrates the entire thickness of the device under test. The IPD obtained from the above-mentioned

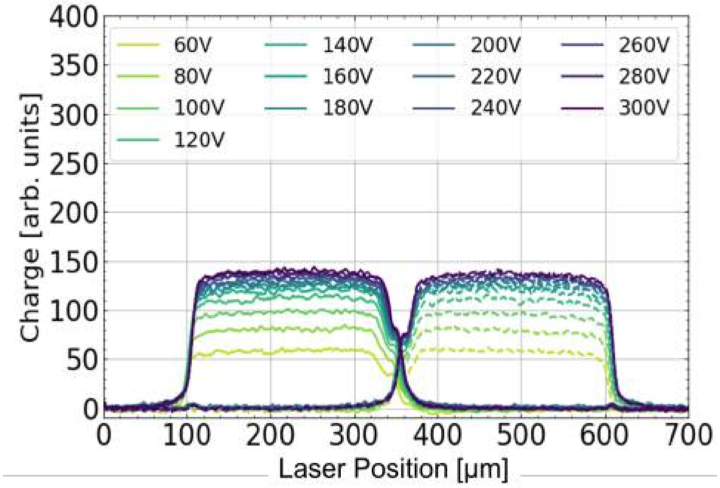

(a)

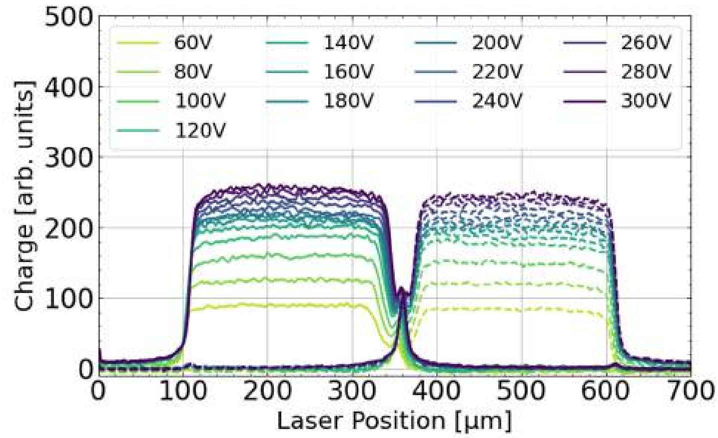

(b)

Figure 5.13: Plots showing line scans as a function of voltage for (a) W6 (low doping), (b) W5 (high doping).

configurations is shown in Figure 5.15. The plot shows results for both red and infrared lasers illuminating from the front. The systematic uncertainty of 1 μm in experimentally obtained values is due to the stage movement. Figure 5.15 shows that the simulation underestimates IPD. At 300 V, the simulation predicts an IPD of 2.5 μm, while the infrared laser measurements give an IPD of $\approx$ 6 μm. Within the uncertainties, the IPD is not affected significantly by the applied bias voltage above V_{FD}, which is in agreement with the simulation. The measurements with the red laser illuminating the front side of the detector show a very similar response to the simulation.

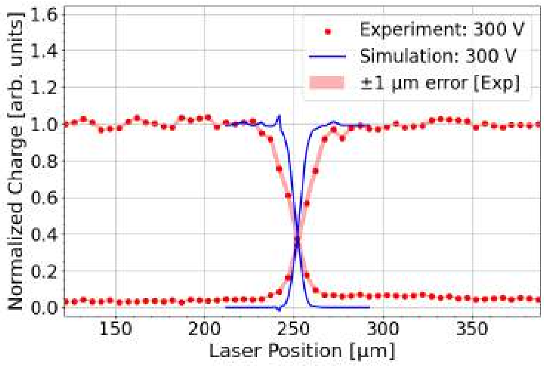

(a)

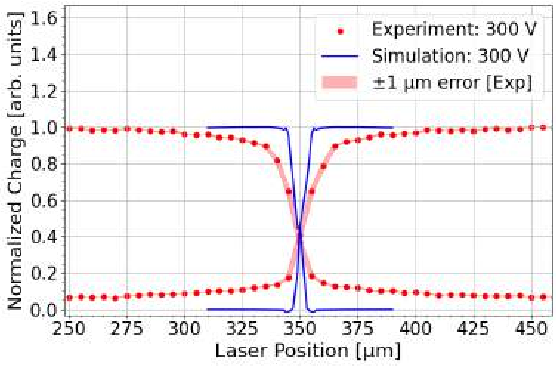

(b)

Figure 5.14: Comparison of the experimental and simulated 1-dimensional laser scan of the device using (a) Infrared (1064 nm) and (b) Red (660 nm) laser.

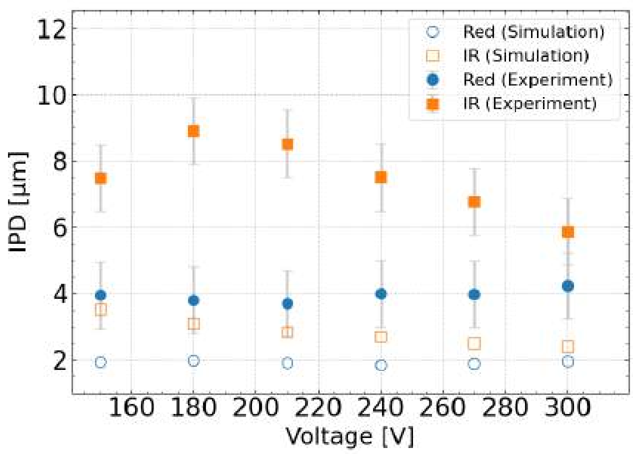

Figure 5.15: Experimental and simulated IPD value of W6, using Red (660 nm) and Infrared (1064) laser from the front side of the device, using the TCT setup at AGH.

The difference in the IR laser measurements and the simulation can be partly explained by the differences between the simulation and reality. In the simulation, the laser profile is a ~ 10 μm beam, which enters the detector exactly perpendicular to the surface, and the beam profile remains constant throughout the full thickness of the device. In the TCT measurements, although the laser is focused to approximately ~ 10 μm at the detector surface, it spreads as it propagates through the silicon. This causes the resulting beam profile to form a cone-shaped induced charge cloud, leading to reduced spatial precision and an increased IPD. The angle of incidence can also be taken into account, which, due to the mounting of the detector on the PCB, may not be exactly perpendicular to the laser beam, resulting in an increased IPD. Considering only the results from the red laser, the device characteristics can be better understood. When the red laser illuminates the front side, the results match those of the simulation. These differ from the results obtained by using the IR laser because the light penetrates only a few microns and thus produces a well-focused charge cloud, unlike the IR laser. These results are reported in [98].

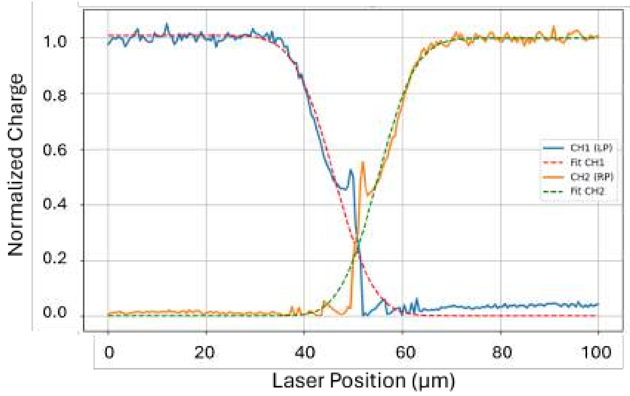

Figure 5.16: Example of charge collection profile at different laser position for Pixel1 (blue) and Pixel2 (orange). The dashed lines show the fitting of the s-curves for IPD calculation.

Similar studies were performed at ELI Beamlines using the SPA-TCT setup explained in the Section 2.2.5. The motivation for using the ELI facility is that the laser spot (FWHM) is $\sim 1.7\ \mu$m and the trench width is 2 μm. These comparable dimensions can provide a better spatial resolution to study the trench parameters. The wavelengths used for this study were 800 nm, providing 20-30 μm penetration depth in silicon, and 400 nm, providing very shallow penetration depth, mimicking low penetrating particles (e.g., soft X-rays). Figure 5.16 shows an example of the charge collection at 300 V, for different laser positions on the device, carried out at ELI. Here, the kink shown in Figure 5.13 is more resolved and becomes more prominent with the increase in voltage. Figure 5.17a shows the simulated charge collection profiles as a result of 1D laser excitation traversing from Pixel1 to Pixel2, with simulation configurations similar to the ones used in the ELI TCT setup. The simulated charged profiles also reveal a difference when passing through the trench, validating the kink observed in Figure 5.16. This kink is further investigated with TPA-TCT, which is explained in the following section.

The IPD values shown in Figure 5.19 show that for top illumination, the IPD decreases with the increase in voltage, and decreases sharply for W5 (highly doped) as compared to W6 (lower doped). For W5, the IPD decreases from $\sim 13.5\ \mu$m to $\sim 10\ \mu$m at 60V

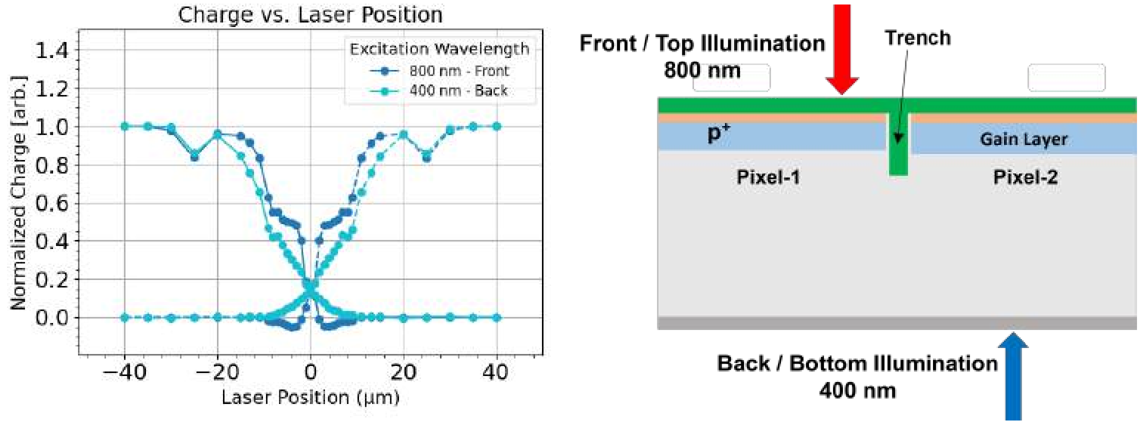

(a) (b)

Figure 5.17: (a) TCAD Simulations of collected charge as a result of laser excitation at different x-positions using the ELI-TCT setup configurations. (b) Schematics of laser illumination using top (800 nm) and bottom (400 nm) configurations.

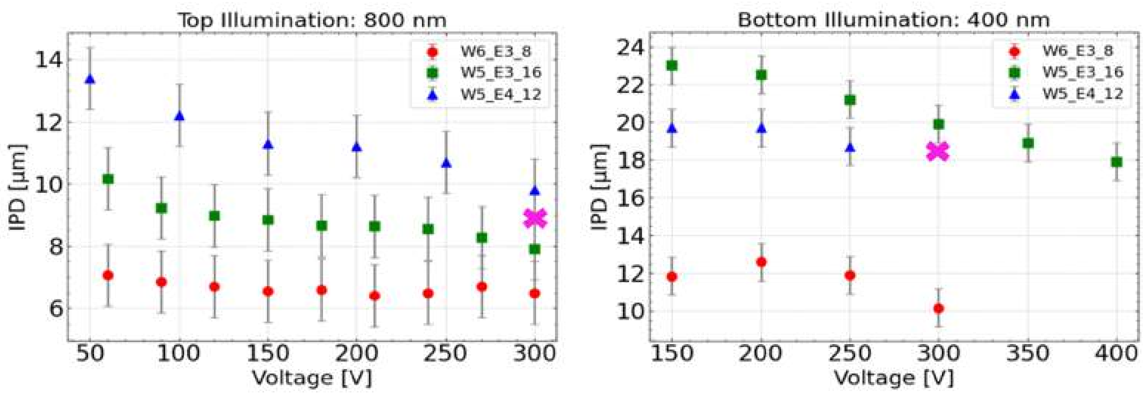

(a) (b)

Figure 5.18: The plots show IPD as a function of voltage, obtained with the TPA-TCT setup at ELI. (a) Top illumination with 800 nm. (b) Bottom illumination with 400 nm. The additional cross shows the simulated IPD, calculated from Figure 5.17a.

and 300V, respectively. Whereas for W6, the IPD is not much effected by the voltage, and stay in the range of $6 - 7$ μm. The results shown in Figure 5.18a are comparable to the experimental values shown in Figure 5.15 for the infrared laser for W6. The results shown in Figure 5.18b reveals that for 400 nm bottom illumination, the IPD reduces from 12 μm at 150V to 10 μm at 300V for W6. Whereas for W5 device E4, it reduces from $\sim$ 20 μm at 150V to $\sim$ 18 μm at 250V. The simulated IPD values are also shown in Figure 5.19, represented with a magenta cross. The simulated values lie within the error of experimental IPD values at 300 V for the devices from W5. This indicates that close to the gain layer, the electric field is sufficiently strong and laterally well-confined. In this region, carriers are rapidly collected before significant diffusion or lateral drift can occur, leading to a small IPD and an optimal fill-factor. As the interaction depth increases, the IPD increases, reflecting enhanced lateral carrier spreading before reaching the multiplication region. Therefore, these values suggest that the fill factor is reduced for low penetrating particles entering from the back side. The differences in the IPD values of the two devices from the same wafer (W5) indicate that the performance of trenches across the wafer is not uniform, which can also be seen from the IV curves where the leakage current is higher for some devices.

5.5 TPA – TCT measurements

The TPA-TCT setup at ELI Beamlines, as explained in 2.2.5, was used to carry out the measurements explained in this section. The motivation behind using the TPA-TCT is the 3-dimensional spatial resolution, where it is possible to perform the line scans as a function of depth. This can provide us with the values of IPD through the whole device thickness. For the IPD calculation, the measurements were performed in two configurations: illumination from the front side of the device and illumination from the back side of the device. This procedure is opted to observe if there is scattering involved from the front side due to the presence of a trench. A line scan at different depths is shown in Figure 5.19a, which shows the collected charge throughout the depth of the device, and the red dashed lines show the calculation of IPD values.

The line scans at different depths were performed for one device from W6 and two devices from W5. The calculated IPD values using both measurement configurations, i.e., top and bottom illumination, are shown in Figure 5.20. An important thing to notice is that the *0 μm* position on the axis with depth values always refers to the front side of the device, which is where the trench is present.

The calculated IPD values obtained with TPA-TCT are in good agreement with those measured using the SPA-TCT setup at ELI. A direct comparison of the IPD values from Figure 5.19 at 300 V, both at the front surface (depth = 0 μm) and at the back surface (depth = 200 μm), illustrates this consistency. For W6, the IPD values at 300 V are approximately 6.5 μm with SPA and 6 μm with TPA under front illumination. For W5, the corresponding IPD values fall within the range of 10–14 μm for both SPA and TPA.

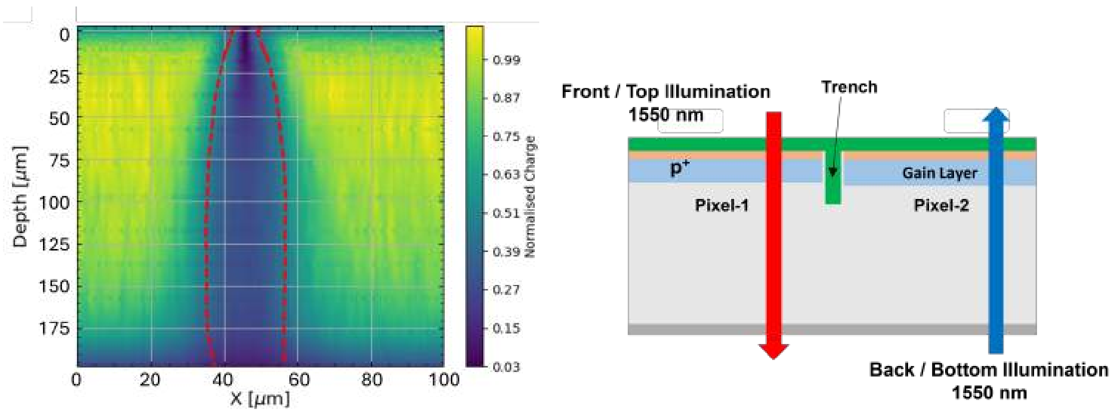

(a) **(b)**

Figure 5.19: (a) Example of charge collection profile versus laser position as a function of depth, at 300 V. The red dashed lines show the calculated IPD values from fitting s-curves on individual measurements. (b) Schematics of TPA laser illumination for top and bottom configurations using 1550 nm wavelength.

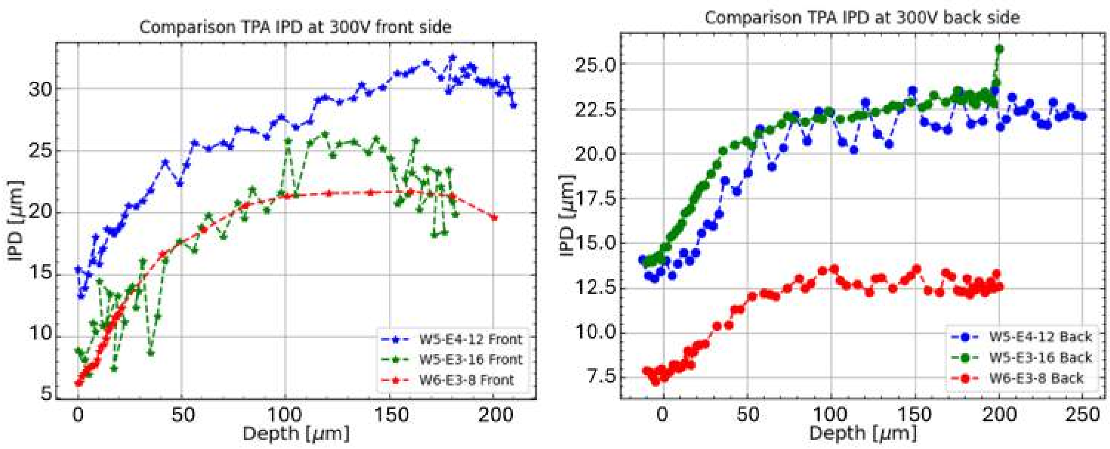

(a) **(b)**

Figure 5.20: The plots show IPD as a function of depth at 300 V, obtained with the TPA-TCT setup at ELI. (a) Top illumination (b) Bottom illumination. Depth = 0 μm refers to the front side of the device.

It is further observed that TPA measurements from front illumination yield better results at the surface but degrade as the laser propagates toward the back side of the device. Conversely, when TPA is applied from the back illumination, the results are improved both at the back surface and at the front surface, highlighting the dependence of measurement quality on the illumination geometry. The comparison between front and back illumination using TPA is shown in Figure 5.21. Only one device from each wafer is shown. These results suggest that TPA from back-side illumination is more effective and shows better IPD as compared to the front side illumination, which is an effect of laser scattering from the trench [103].

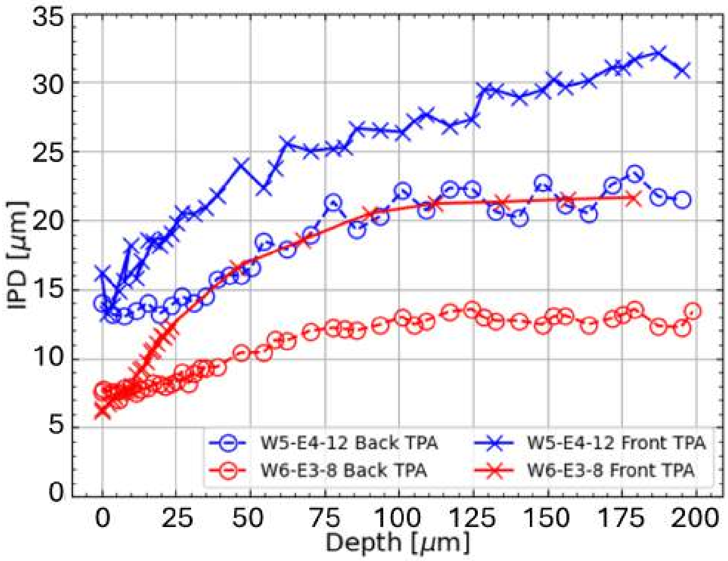

Figure 5.21: Comparison of IPD values obtained using TPA from front and back illumination.

Since the kink observed in the line scans at the trench, shown in Figure 5.16, is more prominent in the devices from W5, 2D maps of the device from W5 showing charge collection, signal time, and rise time are shown in Figure 5.22. The rise time shows how quickly the charge carriers are collected and the signal time reveals effective measurement of the charge. These maps show an increase in the signal time and rise time near the trench edges that reflects the slow collection of the carriers near trench edges, producing signals with larger collection time. Larger signal result in higher charge value, which might be the reason for the kink in charge collection profiles.

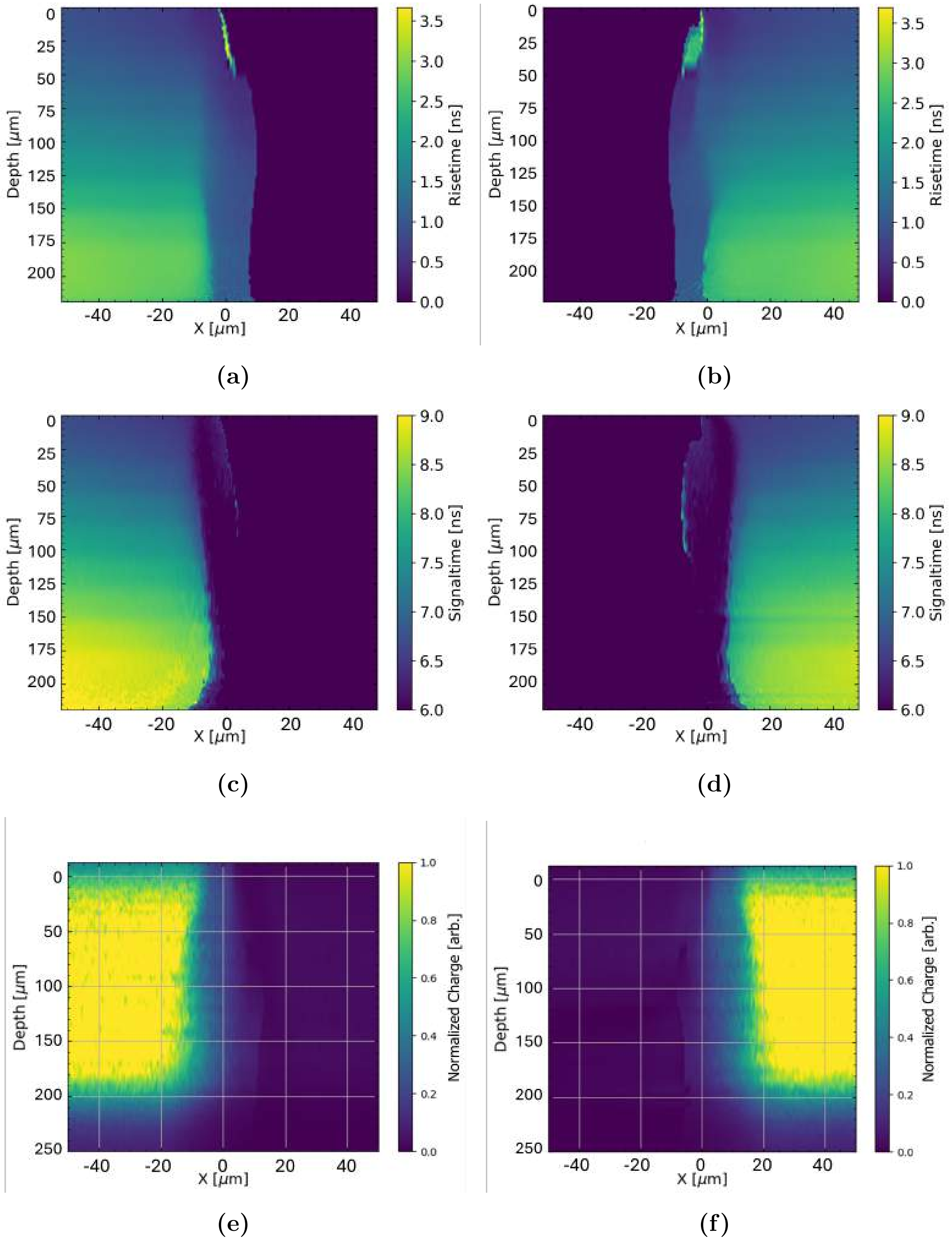

Figure 5.22: 2D maps of the device from W5, showing: rise time from Pixel1 (a) and Pixel2 (b), signal time from Pixel1 (c) and Pixel2 (d), and collected charge from Pixel1 (e) and Pixel2 (f) at 300 V.

To further investigate the kink, depth scans using TPA were performed at three different x-positions, i.e., center of the trench, edge of the trench, and center of the pixel. These scans were performed as a function of voltage to validate how the kink behaves with an increase in voltage. The plots shown in Figure 5.23 depict no peak at the surface of the device, i.e., z = 0 μm when the laser illuminated the center of the pixel (Figure 5.23a) and at the center of the trench (Figure 5.23b). Whereas, a sharp increase in the charge collection can be seen at depths z $\simeq$ 0 to 10 μm, in Figure 5.23c. This peak increases with the increase in voltage, which links the kink directly with the gain layer. This confirms that the kink originates at the edge of the trench due to high field regions present at the interface of the gain layer and the trench itself.

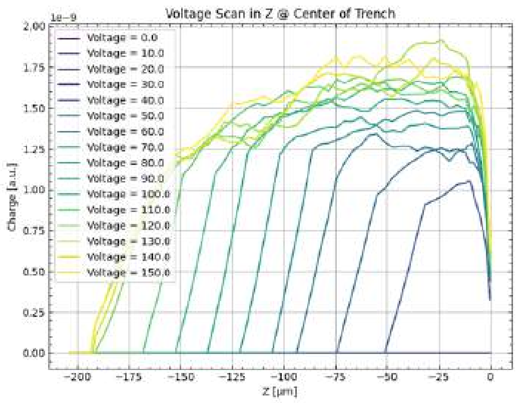

(a)

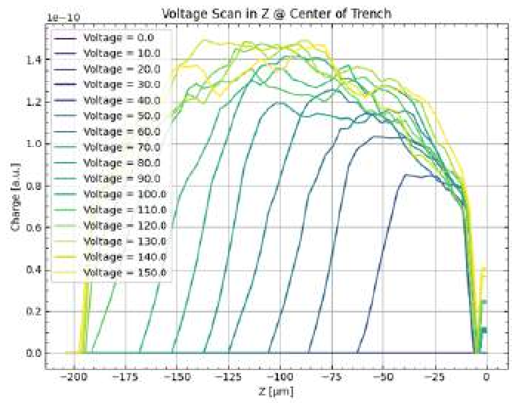

(b)

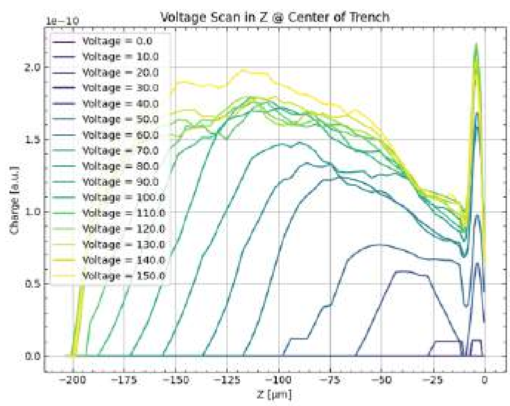

(c)

Figure 5.23: Charge collection depth scans using TPA, with increasing bias voltage with illumination at (a) center of the pixel, (b) center of the trench, and (c) edge of the trench.

From Figure 5.23a, the thickness of the device can also be calculated. The depletion depth increases with the increase in voltage, until it reaches a certain point where it does not change with an increase in voltage. This is referred to as full depletion voltage, and the depth at that voltage is the thickness of the detector. Figure 5.24 shows that the device fully depletes at 120 V, and the detector's thickness corresponding to that voltage is 200 μm.

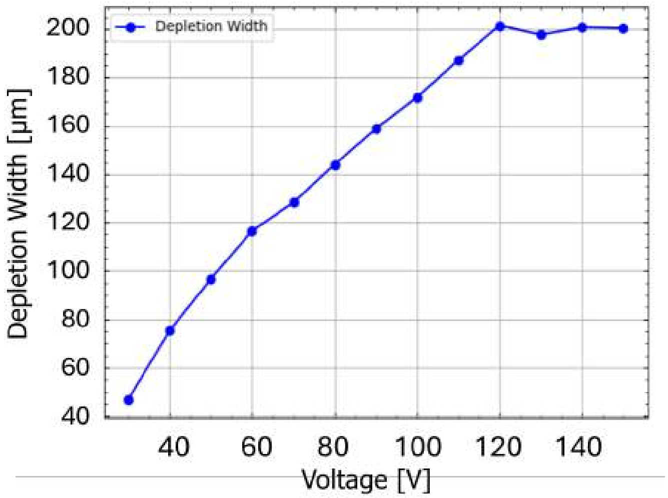

Figure 5.24: Depletion depth of the detector as a function of voltage.

Fabrication and characterization of the first batch of TI-LGADs was successful and is presented in the preceding sections. However, the over-etching of silicon oxide inside the trench makes the trench not completely filled with silicon oxide. This led to the presence of metal debris inside the trench, as shown in Figure 5.2. The energy dispersive X-ray spectroscopy (EDS) [104] is used for elemental analysis, after cleaving some of the devices from different parts of the wafer. This technique help to identify the presence of any contaminants.The EDS spectra shown in Figure 5.25 confirms the presence of aluminum along with silicon, oxygen and other contaminants inside the trench. To resolve this issue, version-2 of the TI-LGADs was produced. The details are given in the following sections.

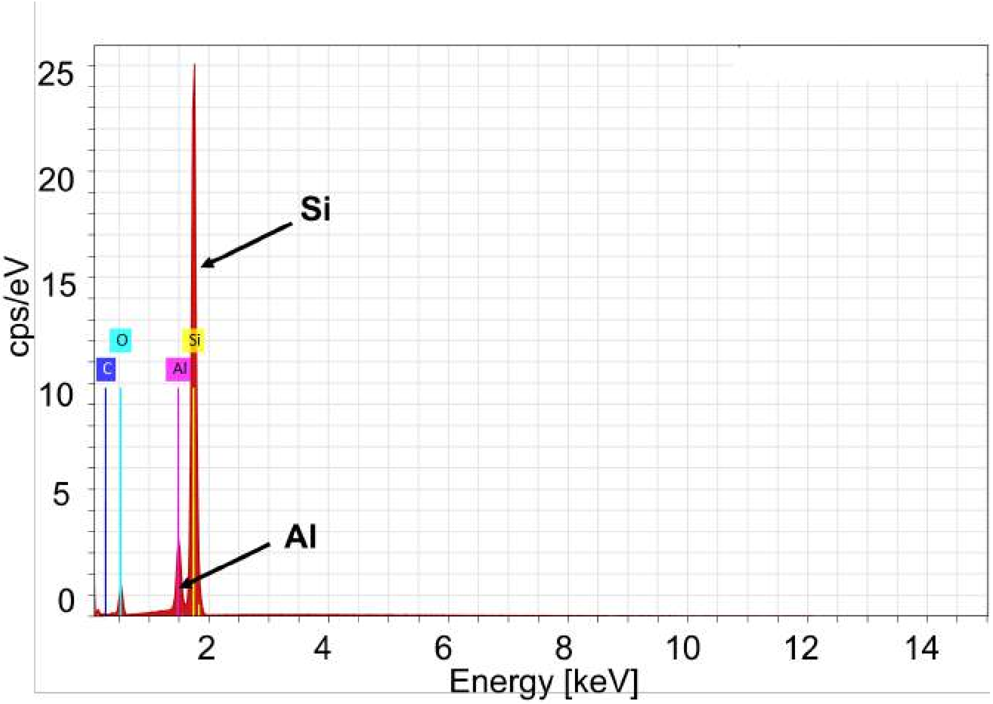

Figure 5.25: EDS spectra of TI-LGAD from W6 showing the presence of aluminum in the elemental analysis.

5.6 TI-LGADs: version 2

Version-2 of TI-LGADs is fabricated to ensure complete filling of the trench with silicon oxide. Version-2 differs from version-1 only in the mask design of the oxide to open for the junction implant; the rest of the device parameters are kept the same. In this design, an oxide layer with ~ 2 μm thickness is grown over the trench, which will be referred to as an *oxide cap* in this chapter, as shown in Figure 5.26. The width of the oxide cap is determined with TCAD simulations.

5.6.1 Design simulations

To create the device structure, simulations were performed using the Structure Editor (SDE) tool of the Sentaurus TCAD, where the gap between the n^+ layer (red) and the edge of the trench (green), as shown in Figure 5.26, is parametrized. Gap $= 0$ μm means there is no gap between the n^+ layer and the trench. The structures were created to study the gap ranging from 0 to 5 μm, with a step size of 0.5 μm, on each side of the trench. The simulated TI-LGAD device is 200 μm thick, where Y $= 0$ μm is the surface, and 20 μm in width, where the trench is at the center of the device at X $= 10$ μm. The

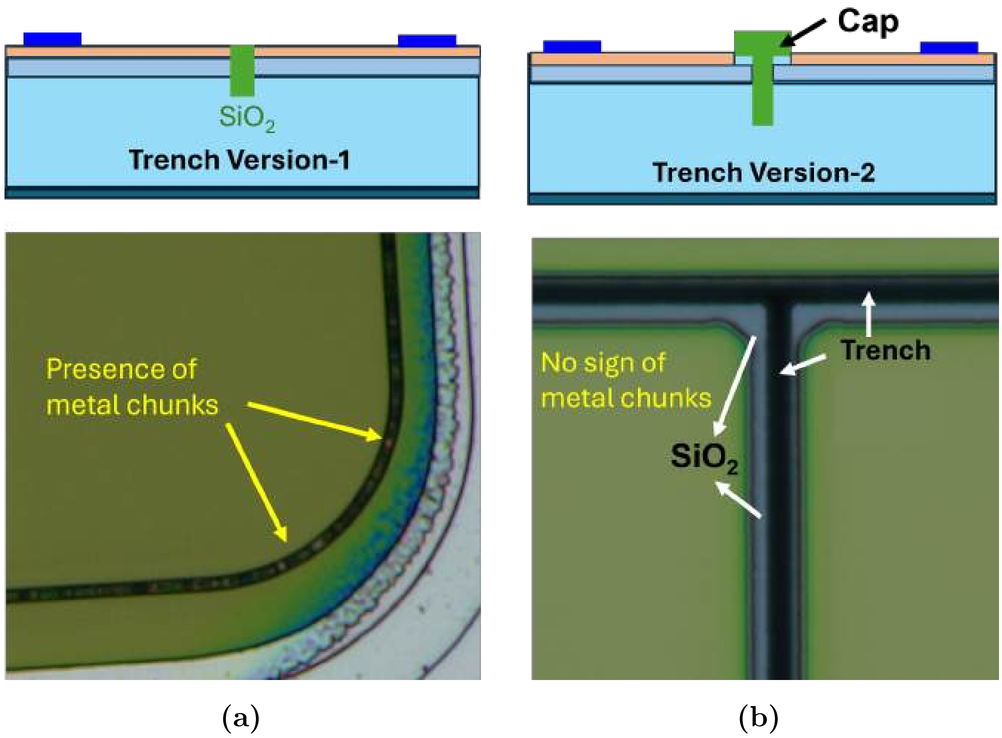

Figure 5.26: Device schematics of 2x1 TI-LGAD version-2 (right), as compared to version-1 (left). The picture is not to scale.

doping profiles and the rest of the parameters were kept similar as discussed in Section 5.3.1.

The device simulations were performed using the SDEVICE tool of the Sentaurus TCAD to simulate the electric field in the device. The applied bias voltage was up to 1000 V. The simulated IV curves were obtained to observe the leakage current and breakdown of the device as the gap between the n^+ layer and the trench edge is varied. IV curves show that no breakdown is observed for the device with a gap up to 2.5 μm. For gap = 3 μm, the device breaks down at 500 V and goes to breakdown for the rest of the gap values immediately after the depletion of the gain layer, as shown in Figure 5.27. The choice of the gap between the n^+ layer and the edge of the trench is crucial. If the gap is too large, the electric field near the surface may become distorted and unevenly distributed, leading to premature breakdown of the device. Positive charge at the silicon-oxide interface attracts electrons and forms a surface accumulation layer. Charge carriers drifting toward the n^+ implants can then be guided toward the surface, where the electric field is locally enhanced. This leads to increased surface leakage current and can cause premature breakdown of the device [31]. Therefore, the fabrication of version-2 was carried out

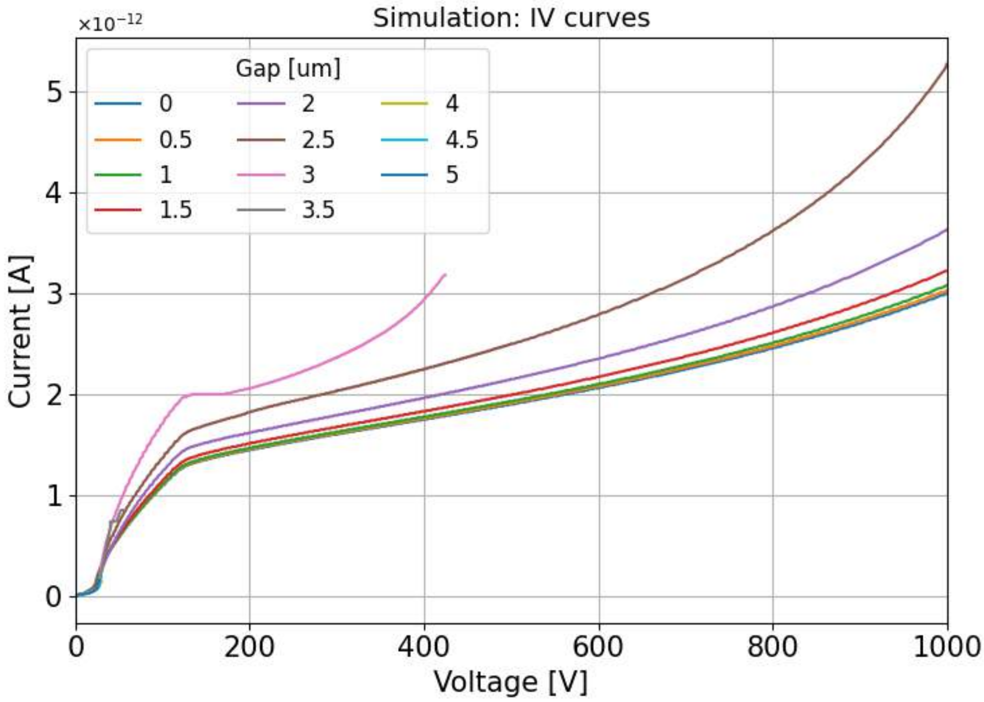

Figure 5.27: Simulated IV curves of the TI-LGAD based on the gap variation. The applied voltage is $0 - 1000$ V.

using the gap $= 1$ μm. This value was chosen due to the limitation of the mask aligner that has an error of $\pm$ 0.5 μm. So, even if the mask is misaligned, it is not so much that it crosses the limit where the device breaks down, i.e., gap > 2.5 μm. The mean ionization integral (MII) maps of the devices are shown in Figure 5.28. The MII is the spatial integral of the local impact ionization coefficient along a carrier path, and it measures the presence of avalanche multiplication. This is a critical parameter because it links microscopic impact-ionization models to the macroscopic device behaviors such as avalanche multiplication, leakage current, and breakdown voltage. If the MII is < 1, the device is in a safe zone and is operational. But if its value equals unity, then the device is in the state of high electric field and going towards or already in the breakdown region [16]. This makes MII useful for analyzing breakdown in devices, where the electric field is highly non-uniform and often increases near junctions, device edges, or hetero-interfaces.

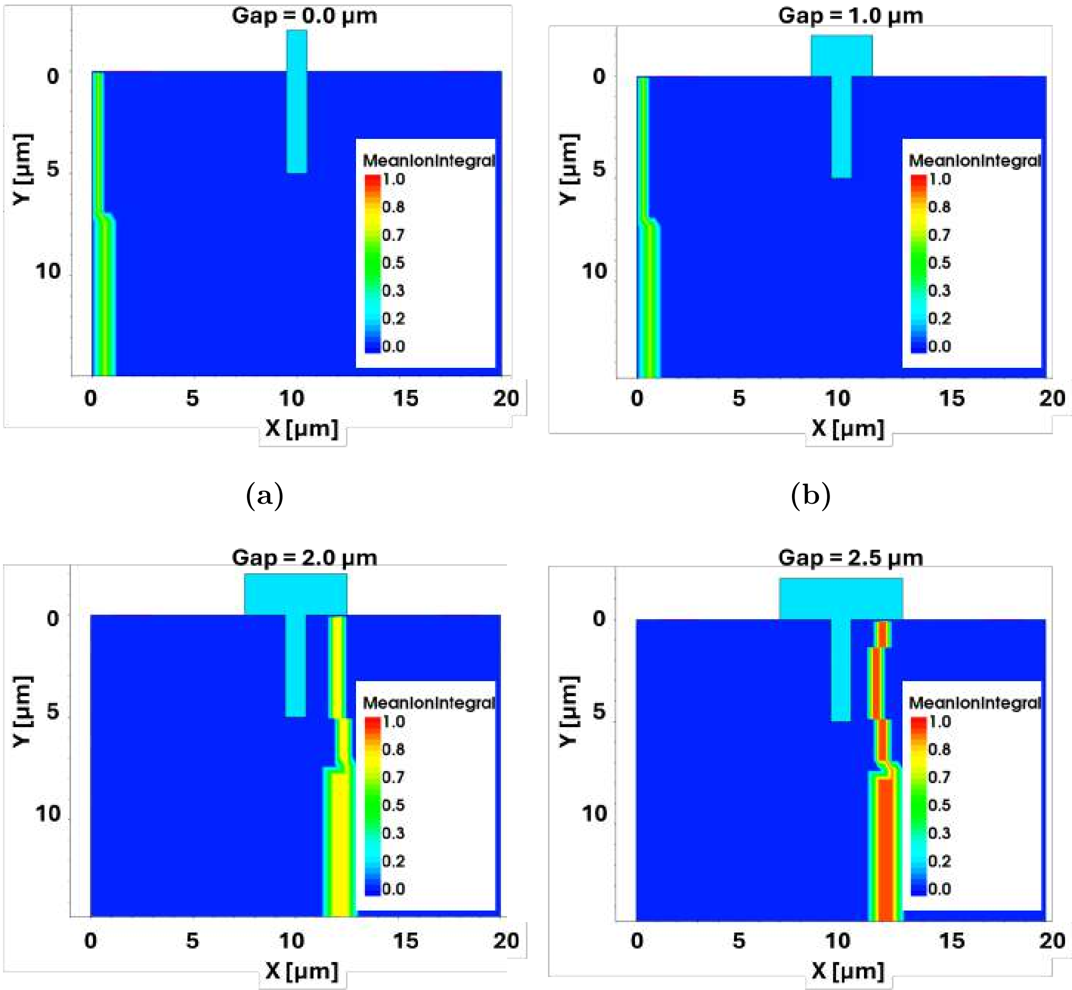

(a) (b)

(c) (d)

Figure 5.28: Simulated mean ion integral maps of the TI-LGAD based on the gap variation. The applied voltage is 1000 V.

Table 5.2: Fabrication details of the second batch of TI-LGADs showing process parameters [15].

Wafer No.	Relative Boron dose	Relative Phosphorus dose
W2	1.4	1
W4	1.3	1
W8	1.2	1
W9	1.1	1

5.6.2 Electrical characterizations

The electrical characterization of the TI-LGADs was carried out with a semi-automatic probe station present at the University of Glasgow. Random blocks were chosen from each wafer (details in Table 5.2) to probe the IVs and check the breakdown behavior. The IV curves show that for the pixelated devices (E-devices), the leakage current jumps to 10s of μA, as soon as the gain layer is depleted, showing breakdown. While for the standard PIN and LGAD devices with p-stop and JTE, the leakage current is in operational ranges, i.e., $< 1\ \mu$A. A few blocks from W9 contained some E-devices that were breaking down in the range of $60 - 80$ V. This provided sufficient opportunity to perform further characterizations to identify the underlying cause of the early breakdown.

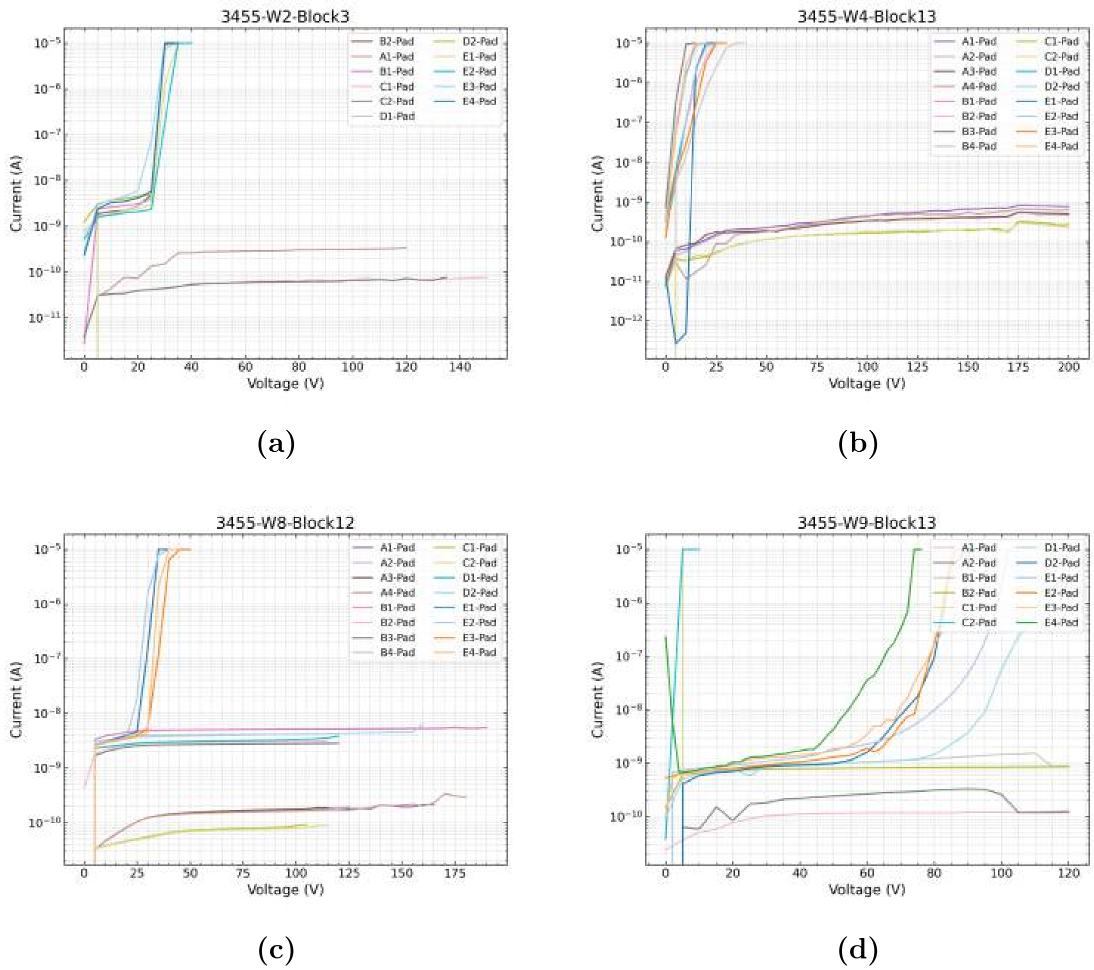

Figure 5.29: IV curves of TI-LGADs version-2. Wafers differ in the doping concentration of the gain layer.

5.6.3 Transient Current Technique measurements

Devices from W9 were diced and wire-bonded to the Chubut-2 board for laser characterizations using the TCT setup explained in Section 2.2.3. The line scans were performed as a function of increasing bias voltage up to 80 V, as shown in Figure 5.30a. The plot shows ideal isolation between the pixels, since no cross-talk is observed. Charge collection also shows a gain of $\sim$ 2 at 80 V. The IPD was calculated from Figure 5.30a, and is shown in Figure 5.30b. The values show an IPD of $\sim$ 5 μm at 80V, which is even before the full depletion of the device. The IPD is expected to decrease further after the device is fully depleted. It is an indication that IPD has improved with the new design, but the devices break down early. This needs to be further investigated.

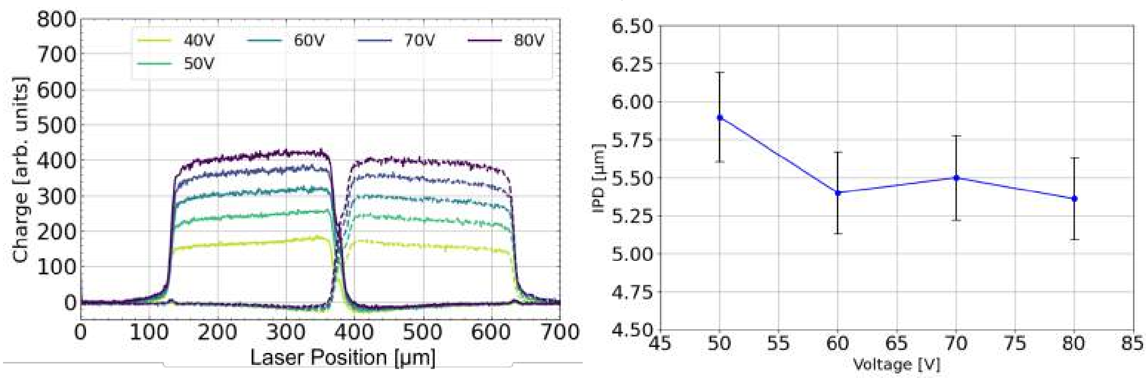

(a) (b)

Figure 5.30: (a) 1-dimensional laser scan of a device from W9 as a function of increasing voltage. (b) IPD values extracted from (a).

5.6.4 Infrared lock-in thermography

Infrared lock-in thermography (IR-LIT) is a non-destructive technique used to study the generation of heat with high sensitivity on semiconductor devices. In the case of LGADs, this technique is very useful as it can reveal high electric field and leakage current regions that lead to the breakdown of the device. These regions appear as hotspots on the device surface, identifying the weak points that cause breakdown. The idea behind this technique is to detect repetitive small temperature changes that originate from the modulated electric signal. The devices are studied under reverse electrical bias conditions (Small Signal Modulation for Thermal Analysis approach - SIMTA). This modulation of the bias voltage causes power dissipation in high leakage current or the multiplication areas. This results in a change in temperature on the device surface at the same frequency as the applied signal [105].

An IR camera records the heat produced from the surface of the device. The IR camera does not measure the absolute temperature; it only measures the change in temperature that oscillates with the electrical signal. The thermal and the electrical signal are synchronized at a lock-in frequency, where the noise is suppressed, and only the temperature change at locked-in frequency is visible in phase and amplitude images. The amplitude image shows the strength of the thermal response of the detector, while the phase image shows the delay between the thermal and electric signal. The phase information is more useful because it is less prone to external noise or intrinsic properties. This makes the phase images more reliable for detecting the defects. For example, if a hotspot is visible in the amplitude image, it may appear due to external noise or surface contamination. But if the same spot appears in the phase image, this confirms the presence of a defect at that spot.

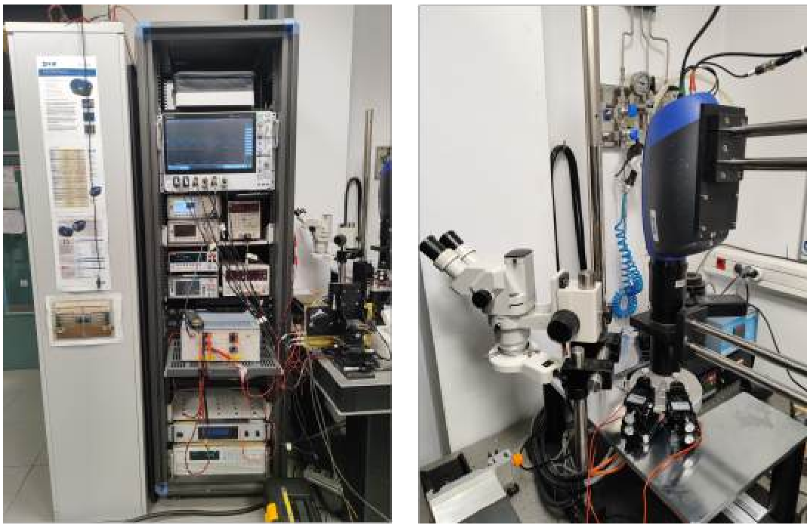

Figure 5.31: Infrared lock-in thermography setup present at CNM Barcelona.

In this work, the IR-LIT setup at CNM Barcelona is used. The setup uses an FLIR SC5500 IR camera with an internal lock-in module and a microscopic lens with a resolution of 6 μm [106]. The chuck is thermally conductive to apply the desired temperature, probes are used to apply bias voltage, and the IR camera is used to capture the thermal signal originating from the device. The setup is shown in Figure 5.31. These measurements were made possible through the efforts of the Power Devices Group (Xavier Perpiñà and

Conrad Ferrer) at CNM, whose support is gratefully acknowledged.

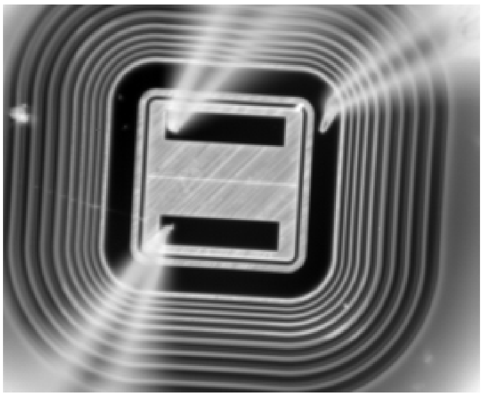

(a)

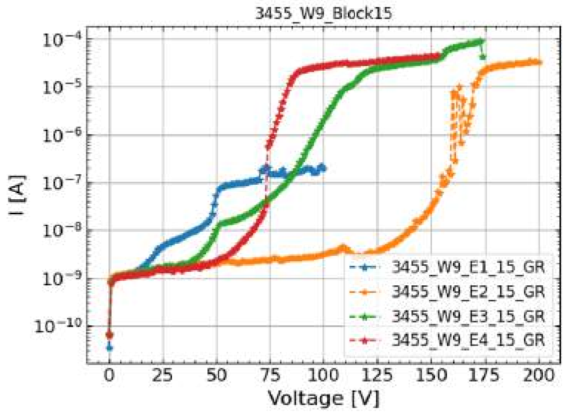

(b)

Figure 5.32: (a) Picture obtained using an IR camera to show the probe connections for IV and LIT measurements. (b) Obtained IV curves from the same setup.

E-devices from block-15 were used to investigate the breakdown spots. Figure 5.32 shows the image of how the devices were connected and the IV of those devices performed in the same setup. The applied DC bias was selected based on the breakdown voltage of each device, and the AC modulation was chosen so that the voltage oscillated between the low and high leakage current regions, to generate a contrast image.

Figure 5.33 shows the images of signal and phase for each device. The parameters used for the detection are listed above the images, for example, DC bias, AC voltage, lock-in frequency, and the applied temperature to the chuck. The contrast images show the bright spots as the hotspots where the leakage current is very high and is responsible for the early breakdown of the device. The phase image confirms that this hotspot does not come from the external noise or contamination. The images reveal that all the devices are breaking down at the trench that is present between the two pixels; however, the exact place of the hotspot varies for each device.

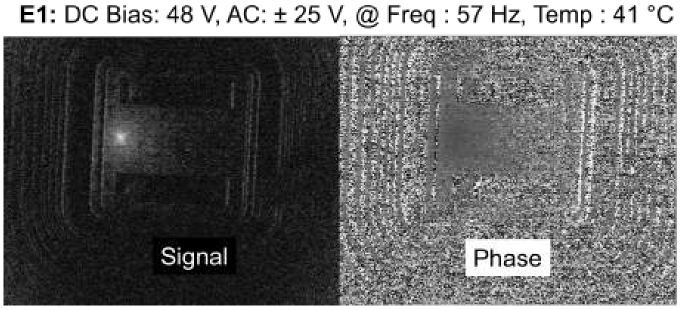

(a)

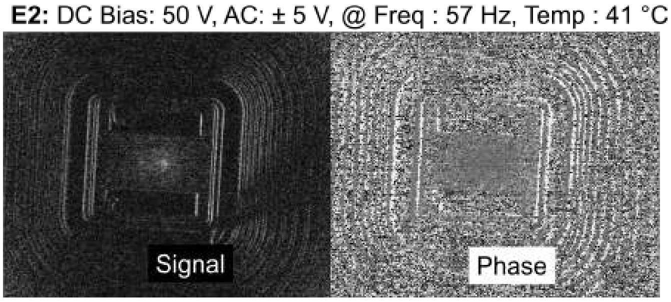

(b)

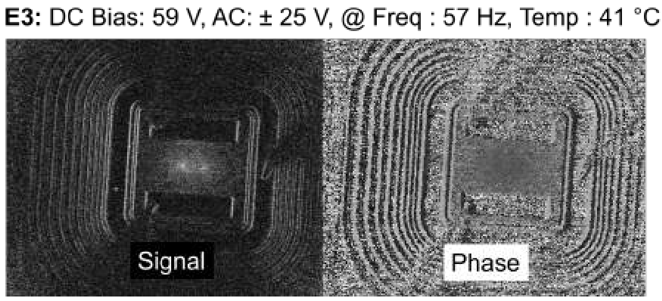

(c)

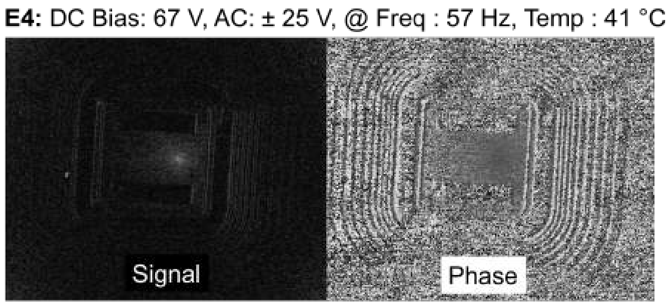

(d)

Figure 5.33: Signal and phase images of the devices from block 15 of the W9 showing hotspots on the signal image (left) and confirmation of the hotspot in the phase image (right). The devices are (a) E1, (b) E2, (c) E3, and (d) E4.

5.6.5 Structural investigations

Based on the results from IR-LIT, the next step was to correlate the mask design of the oxide cap with the measurements. According to the measurements, the gap of 2.5 μm was acceptable for bias up to 1000 V and 3 μm for bias up to 500 V. Therefore, the microscope images of the pixelated devices were taken to check the alignment of the oxide cap with the trench. Figure 5.26 shows that the mask is slightly misaligned; however, the distance between the trench edge and oxide cap edge is less than 2 μm on either side of the trench. This reflects that even though the mask is misaligned, the gap is less than 3 μm, which is safe in terms of early breakdown of the devices.

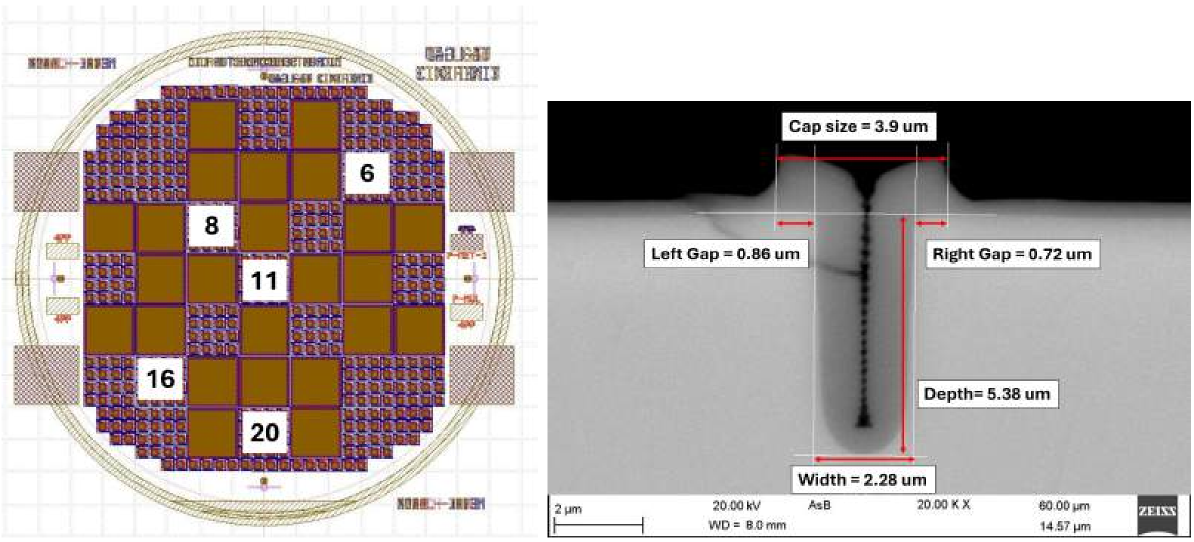

(a) (b)

Figure 5.34: (a) Map of the wafer from where the random pixelated devices were chosen for SEM and EDS. (b) SEM image of a device from block 16.

A detailed study of the trench width and depth, and the size and misalignment of the oxide cap was performed using SEM and EDS. These studies were performed in University of Glasgow by Parisa. An example of the SEM-EDS images and elemental analysis plot is shown in Figure 5.35. The spectra shows no aluminum peak inside the trench as it was observed for first batch, as shown in Figure 5.25. A slight misalignment of the oxide cap can also be seen from the images. All observed parameters are presented in detail in Table 5.3. The misalignment shown in Figure 5.35 is different based on different parts of the wafer. The blocks near the center have better alignment than the blocks that are away from the center.

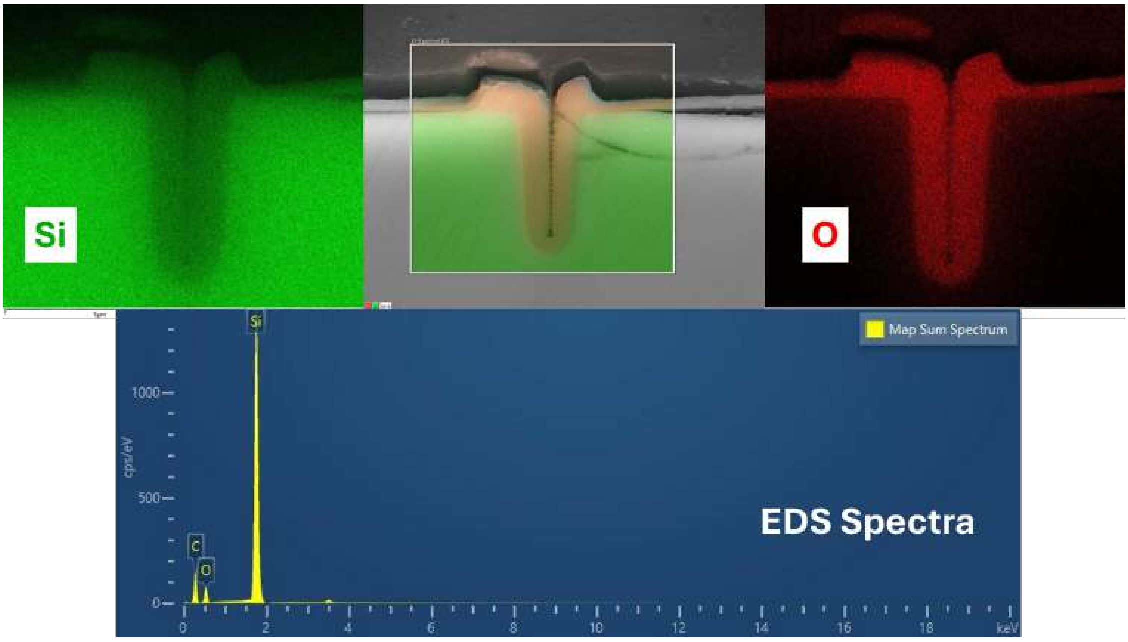

Figure 5.35: SEM-EDS images of the pixelated device from block-8 of W9. The plot shows the EDS spectra containing elemental analysis.

Table 5.3: Trench parameters obtained from SEM imaging from different parts of the W9.

Sample	**Tr. Width [μm]**	**Cap size [μm]**
Block-6	2.91	4.35
Block-8	2.20	3.94
Block-11	2.29	3.96
Block-16	2.05	3.75

Summary

In this work, two batches of TI-LGADs produced by Micron Semiconductors Ltd. were characterized. A detailed study of the 2×1 pixel TI-LGADs was carried out to evaluate pixel isolation and the IPD evaluation.

For the first batch, the IV measurements show stable operation with no premature breakdown caused by the trench structures. No breakdown was observed up to 1000 V. The leakage current remains low, around 10–100 nA/mm^2 at operating voltages. The measured gain of both standard LGADs and TI-LGADs is similar, in the range of 2–3, which agrees well with transient simulations using an IR laser. The laser scans of the

2×1 TI-LGADs show very good pixel isolation. The IPD is reduced from about 50−70 μm in standard LGADs to less than 10 μm in TI-LGADs. This is a clear improvement and leads to a much higher fill factor. It also supports the use of smaller pixel sizes in future devices.

SPA-TCT and TPA-TCT measurements were used to study charge transport, electric field distribution, and fill factor. The results show that the IPD depends on gain layer doping, bias voltage, laser wavelength, and injection side. For example, in SPA-TCT with 800 nm front illumination, the IPD decreases with increasing voltage. W5 shows a stronger voltage dependence than W6 due to differences in the electric field near the gain layer. Back-side illumination with 400 nm gives larger IPD values, especially for W5. This indicates that particles interacting deeper in the device can lead to a larger no-gain region. In general, a higher gain layer doping reduces the fill factor. The observed increase in IPD under back illumination indicates that carriers generated deep in the bulk experiences a significant amount of lateral diffusion before reaching the gain layer. As the drift path length increases, the probability of lateral spreading grows, effectively increasing the IPD. This leads to a reduction in the effective fill factor for low-penetrating particles compared to particles interacting near the gain layer. The future work includes reducing the detector thickness, which will help in minimizing the effects of long carrier drift paths. In thinner devices, charge carriers reach the gain layer more quickly, confining the lateral diffusion. This leads to improved fill factor, better hit efficiency, and enhanced timing performance for low-penetrating particles.

Depth-resolved TPA-TCT measurements provide a 3D view of the electric field. The results show that the effective IPD depends not only on the trench geometry but also on carrier drift and diffusion in the bulk. The smallest IPD is obtained near the gain layer, around 7 μm for W6, because the electric field is strong and carriers are immediately collected. At larger depths, the IPD increases due to longer drift paths and stronger lateral spreading. The increase is more pronounced for front illumination, where carriers must travel through the full thickness of the sensor. Similar behavior is observed for W5, but with overall larger IPD values.

The second batch of TI-LGADs shows improved IPD values even before full depletion. However, an early breakdown is observed in the IV curves. This was further studied using IR-LIT measurements, which point to issues near the trench structures. These effects will be addressed in future designs. Despite this, the first batch of TI-LGADs already demonstrates a clear improvement in fill factor compared to standard LGADs.

Chapter 6

Double-sided 3D column detectors for timing applications

6.1 Introduction

In the HL-LHC era, the CMS and ATLAS experiments will operate in a much harsher radiation environment. To meet the new performance requirements, both experiments have chosen thin LGADs as their solid-state timing detectors. LGADs can provide time resolution of around 30 ps per detector layer [6], which is essential for precise event reconstruction at high particle rates. However, LGADs have some important limitations, as discussed in Section 3.6.

Because of these limitations, other detector technologies are being explored. One promising solution that addresses radiation hardness and meets comparable timing requirements is the technology of 3D detectors. Several efforts are being carried out at CNM for the fabrication of 3D detectors, and have reported impressive results in terms of radiation hardness and timing performance. Test beam measurements and studies with ^{90}Sr electrons demonstrate only a small degradation of charge collection across the full HL-LHC fluence range [107].

3D detectors have several features that make them favorable for timing applications in extreme radiation environments. Their geometry allows for short drift distances, which results in faster signal formation and short induced current pulses. Although 3D detectors are very radiation hard, there are some challenges when used for timing applications. Since the geometry of 3D detectors is very complex compared to the planar detectors, it suffers from a non-uniform electric field and weighting field through the bulk. This non-uniformity originates due to the p- and n-electrodes that are embedded in the silicon bulk [108].

This chapter involves the characterization of double-sided 3D pixel detectors for timing applications fabricated by CNM, reported in [71]. After introducing the design of the hexagonal and square pixel configurations of the 3D detectors, electrical characterizations are performed to validate the response from the detectors. Afterwards, charge collection and time of arrival (ToA) studies are performed for both pixel configurations using the TCT setup, and time resolution using jitter is also investigated with the laser-splitting TCT setup.

6.2 Detector design and geometry

The architecture of 3D detectors makes the collection time independent of the active thickness, as discussed in Section 1.7.3. However, the amount of charge generated by an ionizing particle depends on the active thickness because the charge is generated within the active thickness of the sensor. Therefore, a larger active thickness results in a greater charge collection, producing larger induced signals. This improves SNR and time resolution, as discussed in [71]. The schematics of the 3D detector are shown in Figure 1.20. This production involves a run at CNM where 3D detectors are fabricated on 285 μm thick wafers using a double-sided fabrication process. In this process, the p- and n-electrodes (columns) are etched from both sides of the silicon wafer, allowing the full wafer thickness to function as the active region.

Fabrication of 3D column detectors is limited by the aspect ratio (AR), defined as the ratio of column depth to width, which is used in the DRIE process for etching columns. The highest aspect ratio achieved at CNM is 25. Furthermore, it is crucial to prevent the diffusion of dopants from highly doped electrodes through the other side of the silicon. Therefore, a gap of 45 μm is designed from the tip of the n-column to the back side of the silicon, and from the tip of the p-column to the front side of the silicon bulk to prevent the short connection between both sides, as shown in Figure 1.20. Given the gap, active thickness, and AR, the depth of the column is approximately 250 $\pm$ 10 μm, and a diameter of 8-10 μm is designed on high-resistivity float-zone p-type silicon with a resistivity of 5 kΩ-cm. The run is 16069 with the CNM-987 mask set, as shown in Figure 6.1. The wafers contain several test structures with square and hexagonal geometries having different pixel arrays and cell sizes. The test structures under the investigation in

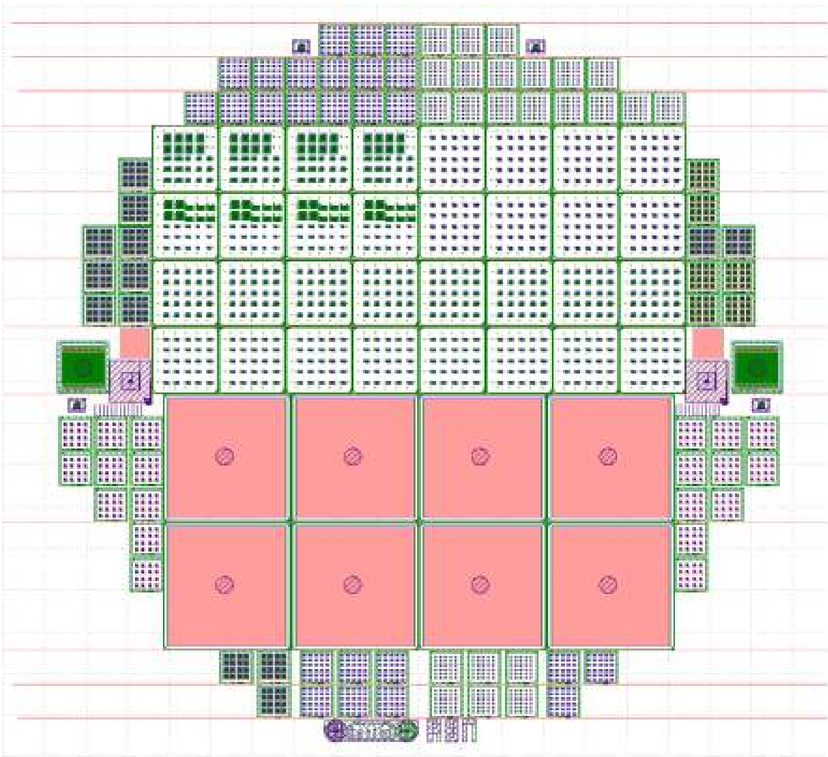

Figure 6.1: Mask 987 of the production run 16069 of the double-sided 3D column detectors for timing applications at CNM.

this work are the single pixel cells surrounded by a guard ring from wafer-6, containing 86 μm column pitch for hexagonal geometry surrounded by 6 surrounding pixels, referred to as 2-X, and 55x55 μm pixel size for square geometry with 8 surrounding pixels, referred to as 1-X, as shown in Figure 6.2a and 6.2b, respectively.

6.3 Electrical characterizations

The electrical characterization of the 1-X and 2-X devices was carried out at the Radiation Detector Laboratory at CNM using a Cascade probe station. The measurements setup contains two 2410 Keithley voltage sources, used to record the leakage current from the central pixel (labeled as "C") and the guard ring (labeled as "G") separately, as shown in Figure 6.2. The bias voltage is applied through the probes on C and G contacts, and the back side of the detectors is grounded. Therefore, a positive voltage is applied to reversely bias the detectors. Details of the setup are explained in [71], and the images of the 2-X and 1-X devices on the probe-station can be seen in Figure 6.3.

The IV curves of the hexagonal devices (2-X) from block-1 are shown in Figure 6.4,

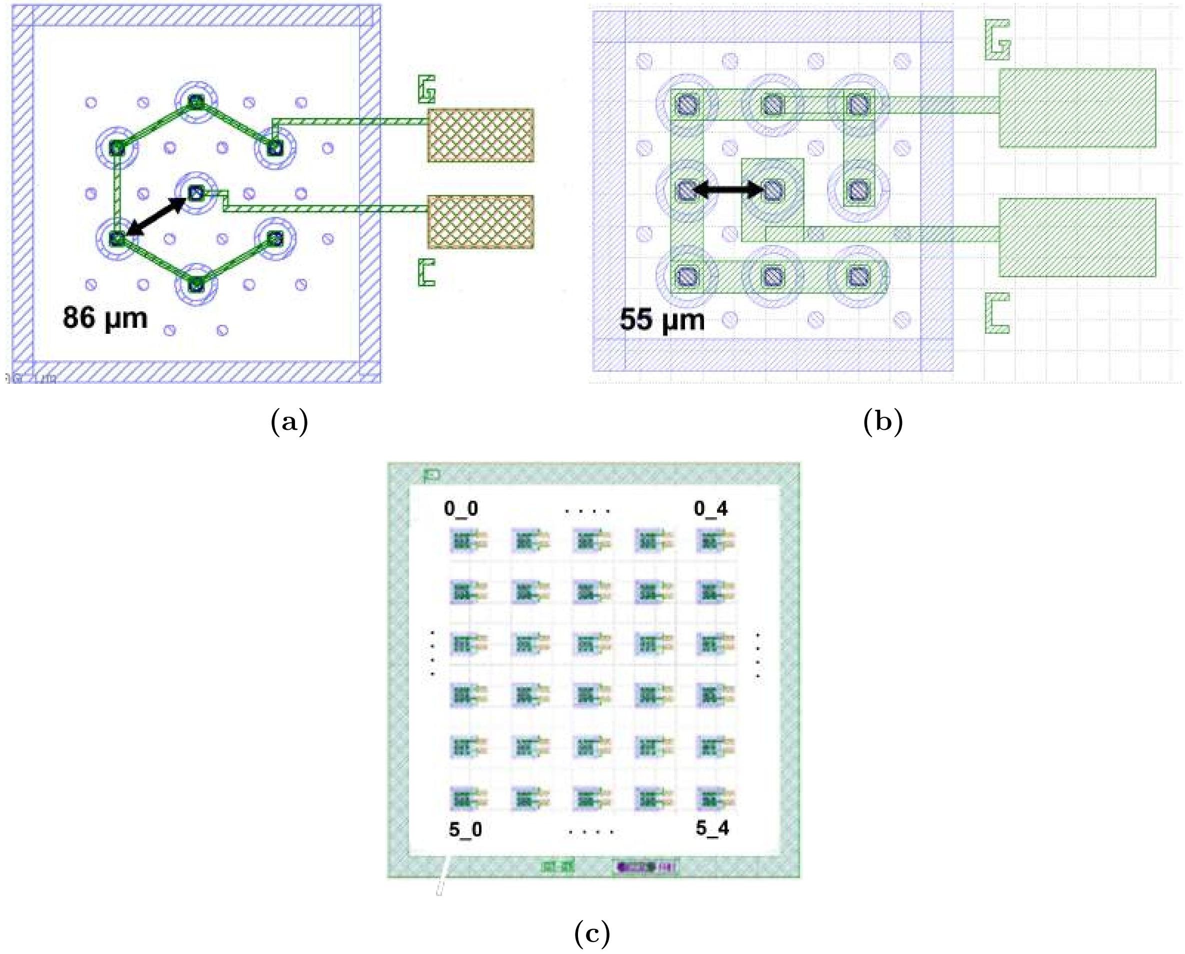

Figure 6.2: Detector design of the (a) hexagonal- and (b) square-3D pixel detectors with the column pitches. The green layer represents the metal routing used to connect the guard ring pixels through a short connection and to link each pixel to its corresponding readout pad. (c) A block consisting of 30 devices representing the device labels.

and for squared devices (1-X) are shown in Figure 6.5a and 6.5b. The IVs do not show the expected ideal diode-like behavior where the leakage current saturates after the detector is fully depleted; rather, the leakage current keeps increasing with the applied bias voltage. The current compliance is set to 10 μA.

IV curves show that the leakage current is higher for the 1-X devices as compared to 2-X. By setting a criteria based on no specific motivation, yield is calculated for both 1-X and 2-X devices for the test devices that do not reach current compliance (10μA) until 20 V. With that criteria, 2-X devices with hexagonal geometry yields 70-75 % and the yield of 1-X devices that have square geometry is 50-55 %. The values suggest that the hexagonal pixels are better in performance than the square pixels in terms of leakage

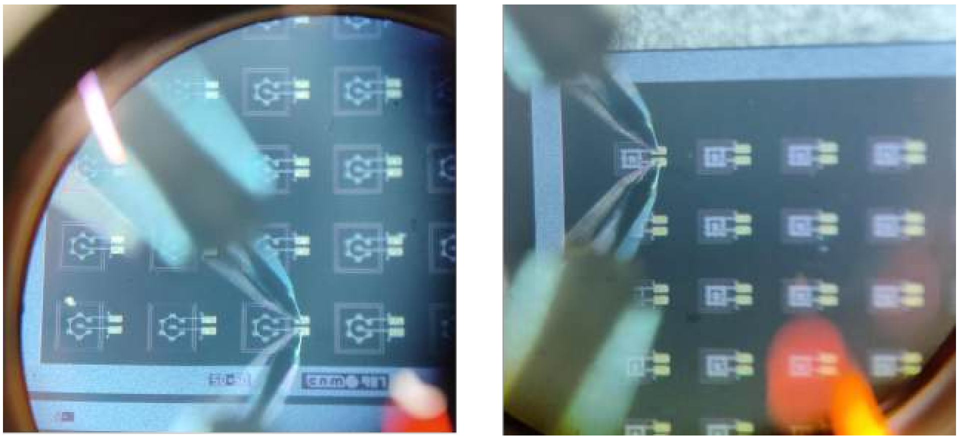

Figure 6.3: Images from the microscope showing the probes with central and guard ring connections of hexagonal pixels (left) and square pixels (right)

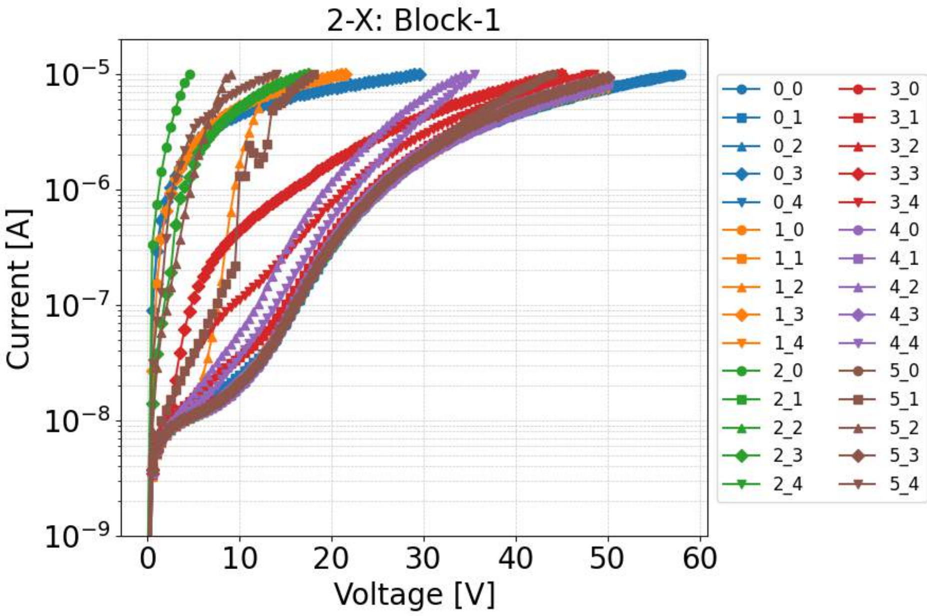

Figure 6.4: IV curves obtained from the hexagonal (2-X) devices from block-1. Different colors represent the rows of block and symbols represent the device in that row.

current. Since the yield of 1-X devices was lower, IV measurements on another block of 1-X devices were performed to validate the yield, and it remains the same. By looking at the leakage current, the device 0_0 from 2-X, and 0_1 from 1-X were wire-bonded for the charge collection, ToA, and time resolution studies.

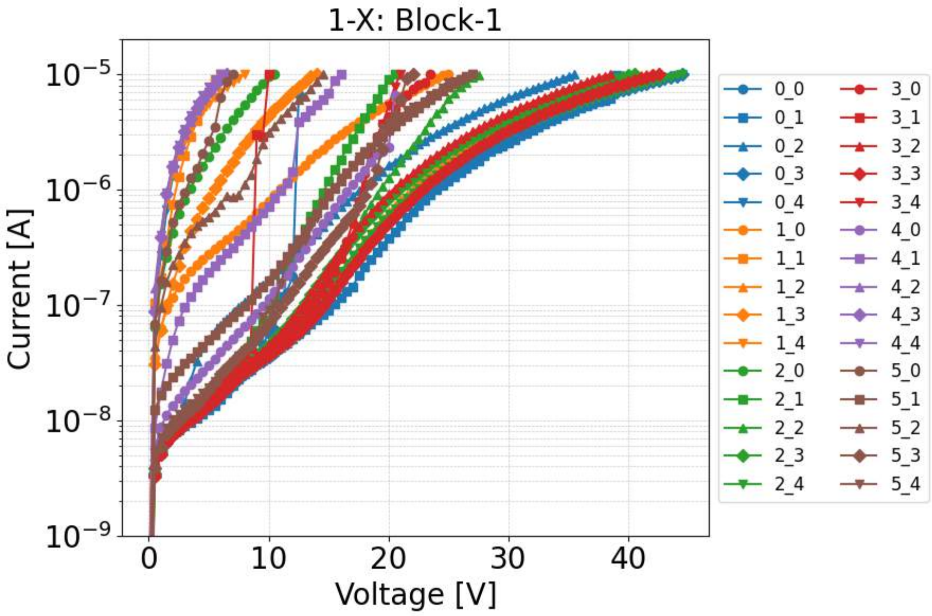

(a)

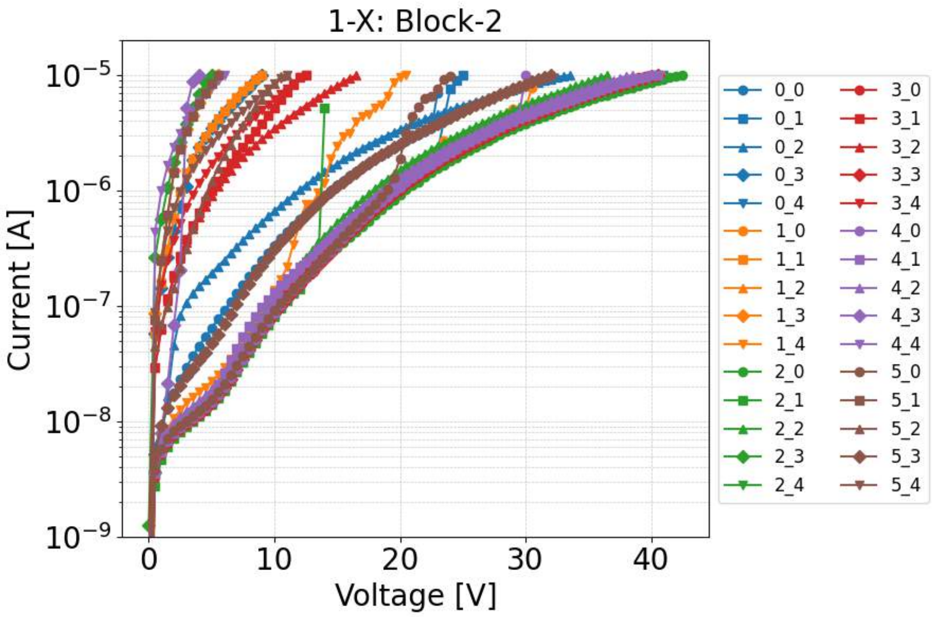

(b)

Figure 6.5: IV curves obtained from the square (1-X) devices from (a) Block-1 and (b) Block-2. Different colors represent the rows of block and symbols represent the device in that row.

6.4 Backside metal removal

As described in Section 6.2 and shown in Figure 6.2, the area for laser injection is very limited due to the presence of metal structures surrounding the central pixel for 2-X devices, and is even reduced for 1-X devices. The area available for laser injection in 1-X devices is 10-15 μm, which is of the order of the laser beam spot. In this scenario, the reflections and beam clipping are anticipated, which can influence the results. Therefore, the removal of metal (aluminum) from the backside of a few of the devices was carried out at CNM after the fabrication. The mask is designed in strips of the order of the pixel size, as shown in Figure 6.6a, and the fabrication steps involved in the removal of metal are shown in Figure 6.6b.

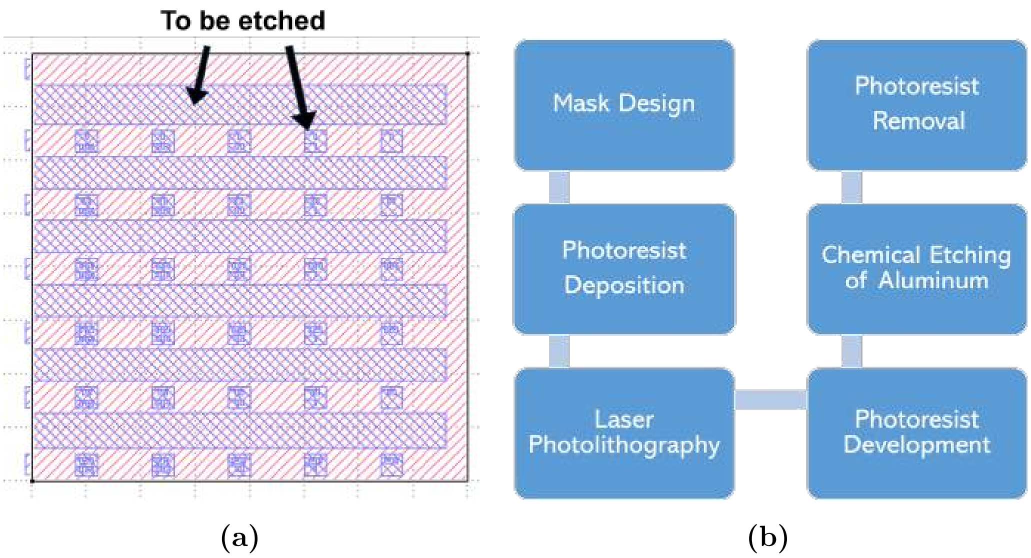

Figure 6.6: (a) Mask design for the metal removal from the backside. (b) Steps involved in the fabrication process.

The mask deposition was carried out using laser photolithography. The etching of the aluminium from the backside of the detector was successful. The post-fabrication images of the 2-X and 1-X blocks are shown in Figure 6.7a and 6.7b, respectively. Since the devices are completely metalized from the backside, the mask is slightly misaligned for 2-X devices, but the central pixel is clearly visible for all devices, as it can be seen in Figure 6.7a. After the backside metal removal, IV measurements on a few devices from 2-X and 1-X blocks were performed, which ensured the backside contact is still in place and the devices are getting biased. An important thing to remember is the presence of titanium/titanium oxide (Ti/TiO_2) with a thickness of approximately 30 nm.

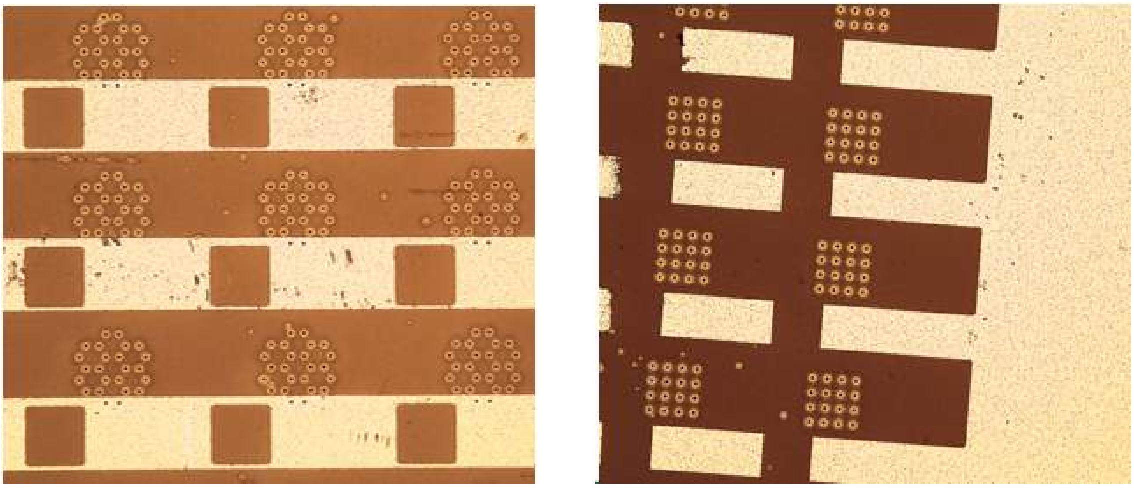

(a) (b)

Figure 6.7: Post-fabrication images of the backside metal removal of (a) 2-X (hexagonal) and (b) 1-X (square) devices.

6.5 Transient Current Technique measurements

The TCT measurements were performed using the setup at AGH University of Krakow, as described in Section 2.2.3. The measurements were carried out using an IR laser (1064 nm) focused to a beam spot with FWHM $\sim$ 15 μm. Laser intensity was calibrated with a 300 μm thick PIN diode and was kept equivalent to $\sim$ 5 mips at 1 kHz repetition rate.

6.5.1 Charge collection: front

The charge collection (CC) is one of the crucial aspects of studying 3D detectors for timing applications. The CC explains how the charge is collected at different positions of the pixel. In this study, the CC of 3D detectors is evaluated by acquiring TCT waveforms in 2D (x-y) scans and integrating each waveform at the specified position to obtain the charge. This generates a 2D map of the pixel in terms of charge collection, revealing the high- and low-charge collection points in the pixel. Obtaining these maps over certain voltages also reveals the drift of carriers with increasing electric field. Figure 6.8 shows the CC obtained from the 2-X device, showing the hexagonal geometry of the pixel. The 2D maps reveal a central n-column and the surrounding 6 n-columns that are interconnected to form a guard ring, which are clearly resolved. The boundaries near the p-columns become more defined with the increase in voltage, as shown in Figure 6.8 (a-e). Figure 6.8 (f) shows the region where the scans are performed. Similar scans were performed for the 1-X device, and the results are shown in Figure 6.9. The laser intensity was kept the same as for the 2-X devices, i.e., 5 mips, but the CC values are reduced by 3 times as compared to 2-X devices. This difference is due, not entirely, to a large laser beam spot as compared to the available opening in silicon for laser injection in 1-X devices. The reduced CC in square pixels can also be attributed to their less uniform electric field distribution and longer maximum drift paths. The corners of the square geometry create low-field regions where carriers drift more slowly. In contrast, hexagonal pixels provide a more symmetric field and shorter drift distances, resulting in more efficient charge collection [109]. For 1-X devices, the p- and n-columns are not finely resolved due to the large metalization areas around. Figure 6.9 (a-e) shows the 2D maps with increasing voltage, and Figure 6.9 (f) shows the region of the scan.

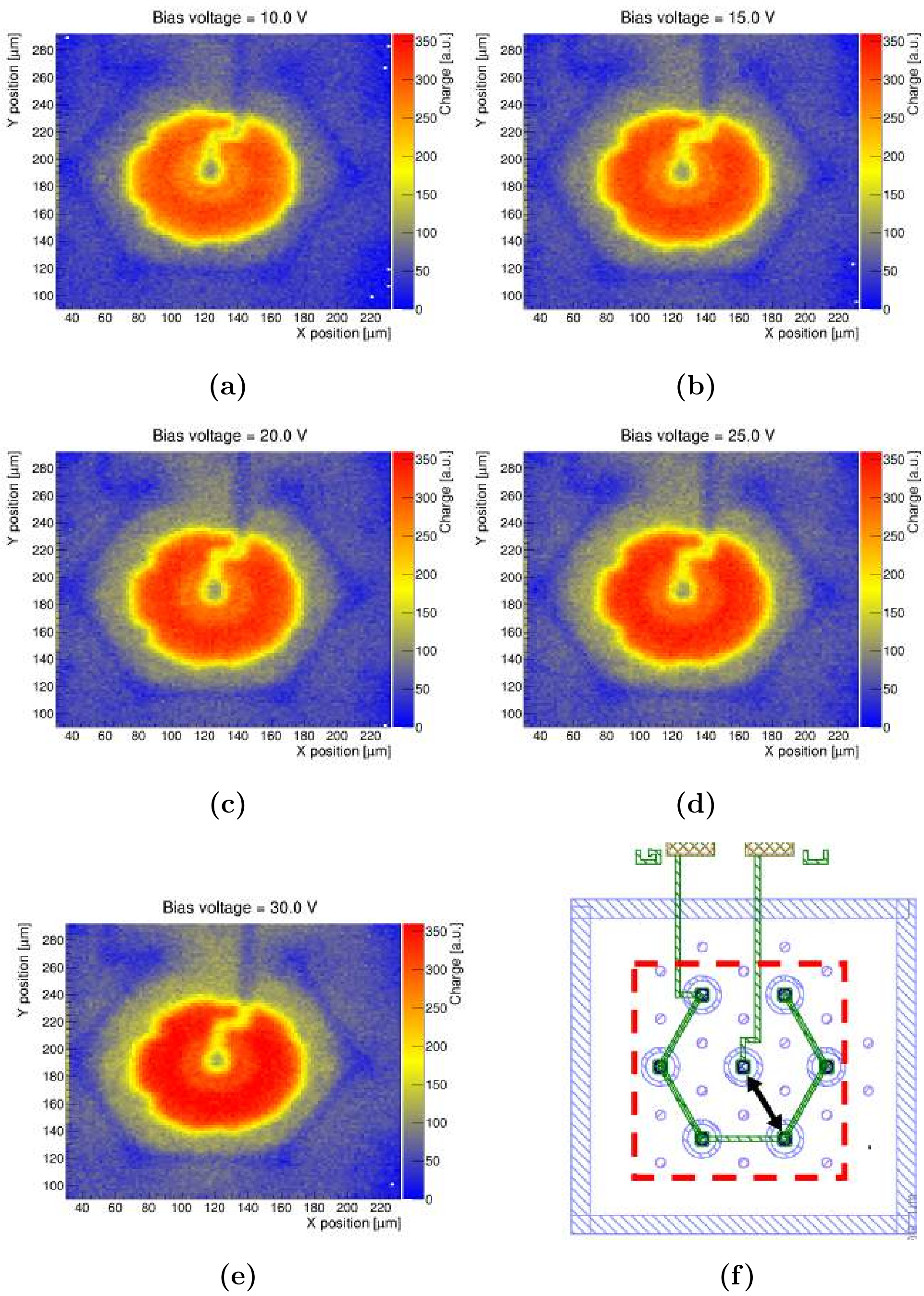

Figure 6.8: Charge collection 2D maps obtained from the front side of 2-X devices showing the hexagonal geometry of the pixels at (a) 10 V, (b) 15 V, (c) 20 V, (d) 25 V, (e) 30 V, and (f) the region of scan.

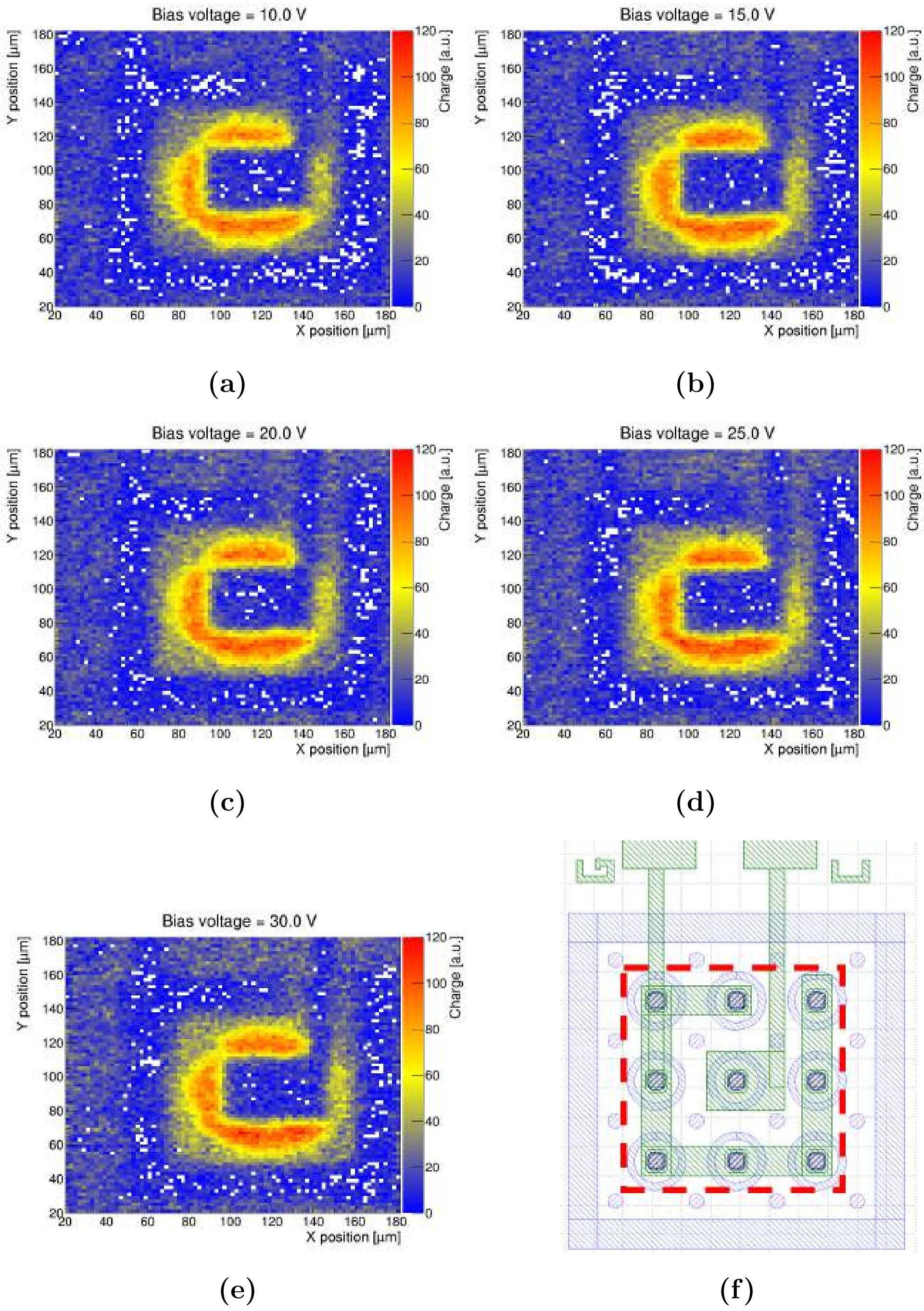

Figure 6.9: Charge collection 2D maps obtained from the front side of 1-X devices showing the squared geometry of the pixels at (a) 10 V, (b) 15 V, (c) 20 V, (d) 25 V, (e) 30 V, and (f) the region of scan.

6.5.2 Charge collection: back

Similar scans were performed from the back side of the 2-X and 1-X devices due to the presence of large metalization areas, especially in the case of 1-X devices, as discussed in Section 6.5.1. The charge collection from the backside of the 2-X device is shown in Figure 6.10. When the laser intensity was kept the same as used in the front illumination, the signal amplitude was reduced by a factor of 10.

Due to the presence of $\sim$ 30 nm thick Ti/TiO_2 on the backside, there is an optical attenuation through the Ti layer. Therefore, the laser intensity was optimized to generate approximately the same amount of charge as it was generated by the laser intensity calibrated to $\sim$ 5 mips when injecting the laser from the front side. After optimizing the laser intensity for the 2-X device, the same laser intensity was used for the 1-X device. From backside injection, the CC value for 1-X is reduced by 20% only when compared to the 2-X device.

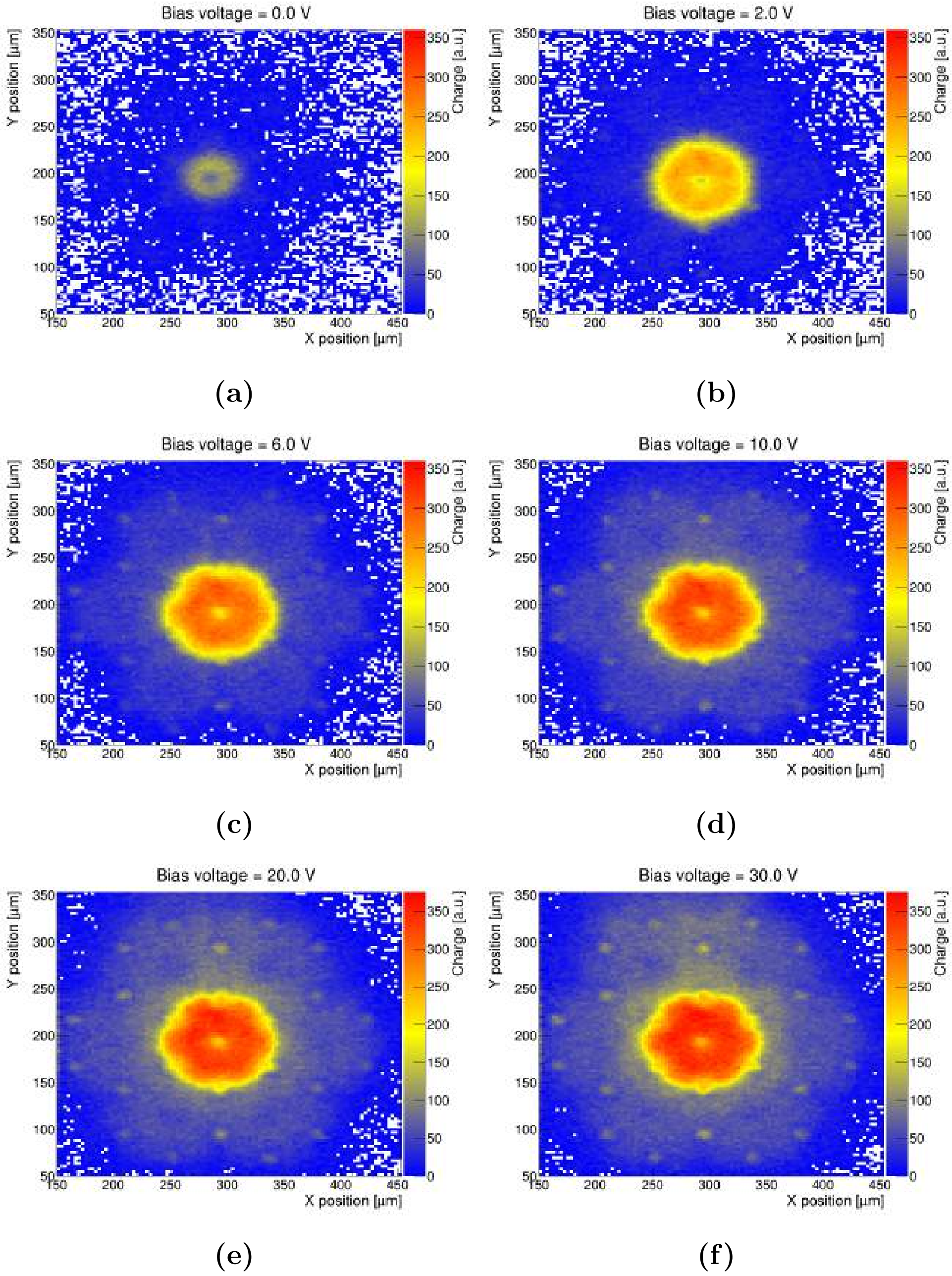

Figure 6.10: Charge collection 2D maps obtained from the back side of the 2-X devices showing the hexagonal geometry of the pixels at (a) 0 V, (b) 2 V, (c) 6 V, (d) 10 V, (e) 20 V, and (f) 30 V.

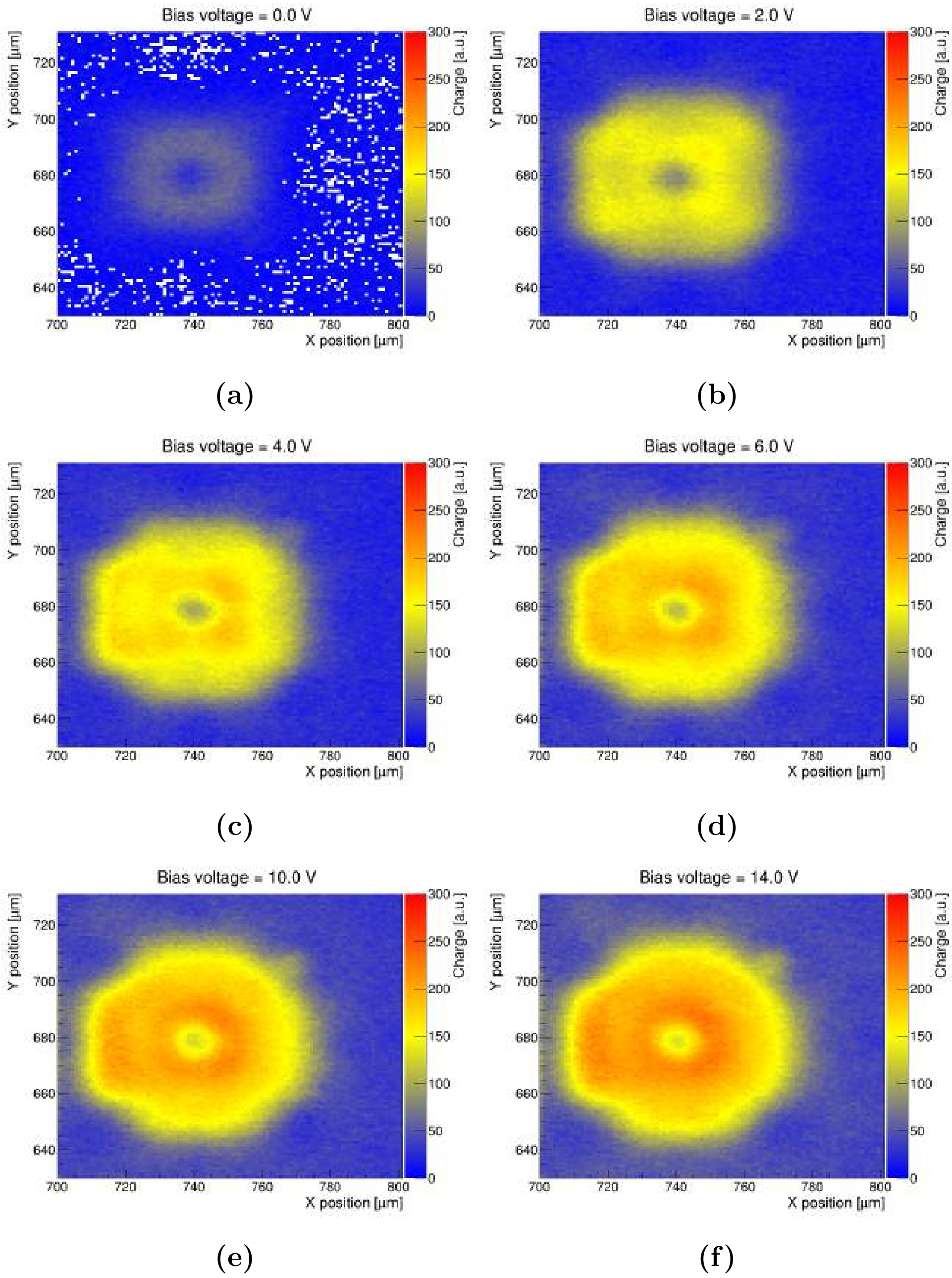

Figure 6.11: Charge collection 2D maps obtained from the back side of the 1-X devices showing the sqaure geometry of the pixels at (a) 0 V, (b) 2 V, (c) 4 V, (d) 6 V, (e) 10 V, and (f) 14 V.

6.5.3 Time of arrival (ToA)

The time of arrival (ToA) is a key parameter in timing detectors, which describes the duration between charge generation and charge collection at a specified threshold. In simpler words, ToA represents how fast a detector responds to a particle hit. After carrier generation, electrons and holes drift to their respective electrodes under the influence of the electric field. As they move from the point of interaction to their electrodes, a signal is generated based on the weighting field. The shape and risetime of this signal define when the hit is registered. Therefore, ToA depends on carrier drift velocity, drift distance, electric field, and the sensor geometry. As explained in Section 6.1, in 3D silicon detectors, the electrodes are etched vertically into the depth of the silicon substrate, penetrating the bulk material; therefore, the electric field and the weighting field are non-uniform across the detector [108]. Carriers generated close to the column are collected very quickly. In contrast, the carriers generated far from the electrodes will need more time to reach the electrodes. This position dependence leads to a variation in ToA within a pixel. The spread of ToA values across the pixel cell contributes directly to the time resolution of the detector. For this reason, understanding and quantifying the ToA distribution in 3D detectors is essential [110].

Since the sensors contain columnar electrodes, the phenomenon of laser beam clipping can occur. This can change the charge created in the sensor volume, producing smaller signals. The signal intensity may vary not only because of sensor properties, but also because of the geometrical effects as well. Therefore, for ToA measurements, a CFD threshold of 50% is applied to the signal to minimize the effect of geometry in the ToA evaluation [110]. The absolute values on the scale represent the ToA spread at different positions on the device.

Hexagonal pixels (2-X)

The ToA was evaluated from the backside of the 2-X device across the pixel to observe the differences with reference to different positions on the pixel, as shown in Figure 6.12. 2D maps of the ToA are shown at multiple voltages to observe the behavior of ToA at different electric field strengths. The highest ToA values are observed near the edges of the pixels where the p^+ columns are present, where there is a minimum or almost no electric field, while the lowest ToA values are observed near the central n^+ column, where the electric field is maximum. Validation of the spread in ToA is carried out by plotting waveforms at different positions on the pixel (Figure 6.13a). The dotted lines represent the amplitude, whereas the solid lines represent the time at 50% threshold. Each color represents the position labelled on the 2D map, as shown in Figure 6.13b.

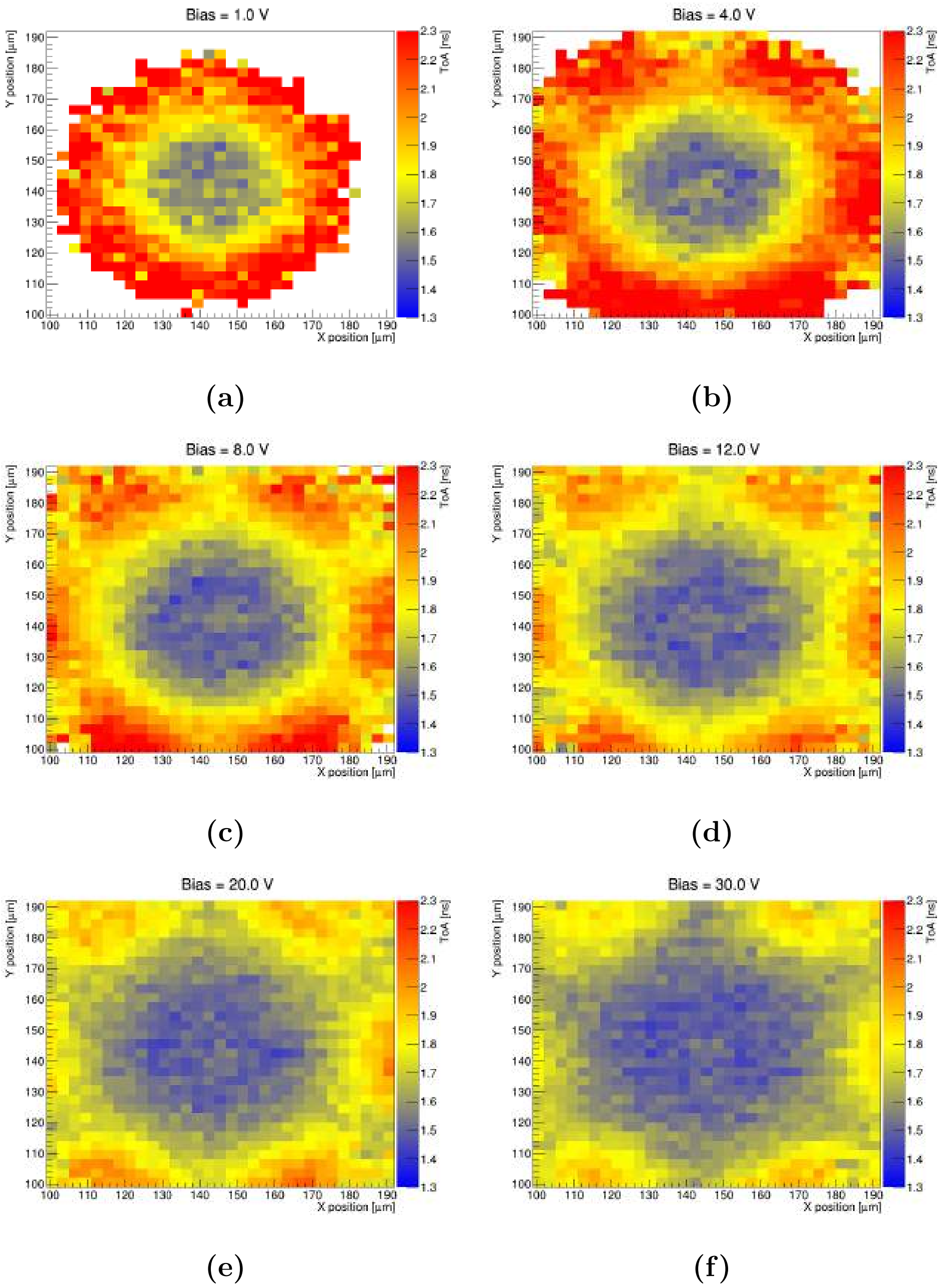

Figure 6.12: ToA 2D maps obtained from the back side of the 2-X devices showing spread of the ToA across the pixel at (a) 1 V, (b) 4 V, (c) 8 V, (d) 12 V, (e) 20 V, and (f) 30 V.

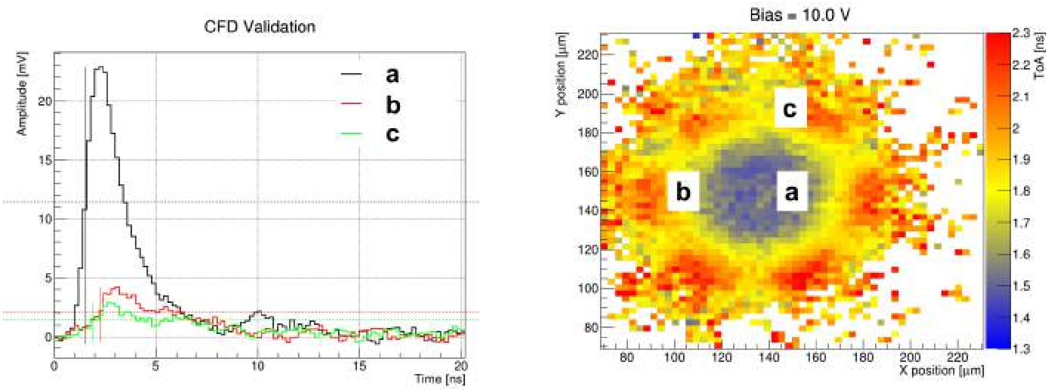

(a) (b)

Figure 6.13: (a) Waveforms plotted from different pixel positions of 2-X device. Dotted and solid lines represent the CFD of 50% threshold. (b) ToA 2D map of 2-X device showing the positions.

The one-dimensional ToA distribution for the 2-X device is shown in Figure 6.14. The distribution of ToA across the pixel is quantified using the Median Absolute Deviation (MAD). The MAD is used instead of Root Mean Square (RMS) because it provides a more robust measure of the spread. The MAD is less affected by the long tails in the distribution that arise from localized field variations or fluctuations in measurements. Using the MAD, therefore, gives a more reliable estimate of the intrinsic ToA variation across the pixel cell, and thus a more realistic evaluation of its contribution to the overall time resolution [110].

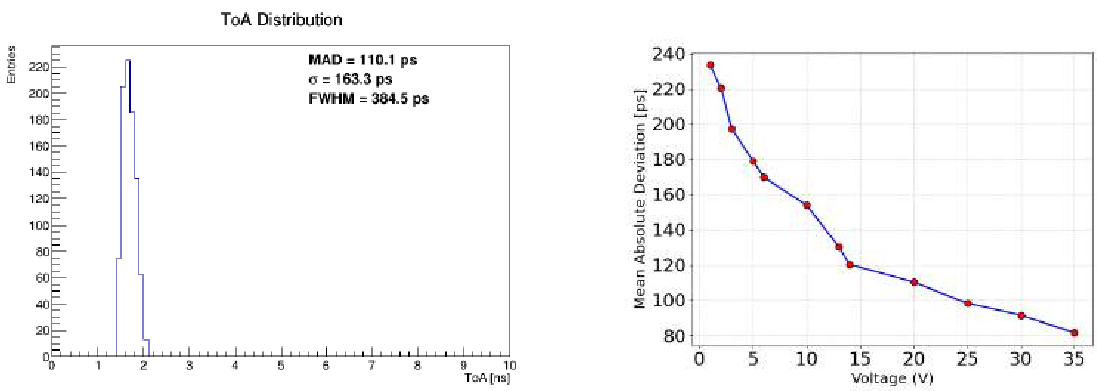

(a) (b)

Figure 6.14: (a) Spread of the ToA values for hexagonal geometry (2-X) at 20 V. (b) Evolution of the MAD values as a function of increasing bias voltage.

The MAD values show a spread of 110 ps across the pixel for hexagonal geometry at 20 V, as shown in Figure 6.14a. The evolution of MAD values as a function of increasing electric field is shown in Figure 6.14b. A rapid decrease in the spread is observed up to 15 V. After that, the decrease in MAD values becomes less steep and follows a linear behavior. The lowest MAD value is observed to be ~ 81 ps at 35 V.

Square pixels (1-X)

Validation of spread in ToA is carried out by plotting waveforms at different positions on the pixel (Figure 6.15a). The dotted lines represent the amplitude, whereas the solid lines represent the time at 50% threshold. Each color represents the position labelled on the 2D map, as shown in Figure 6.15b. Similar measurements as performed for hexagonal pixels (2-X) were performed for the square pixels (1-X) as well, to evaluate the ToA from the backside, as shown in Figure 6.16. 2D maps of the ToA for 1-X are shown for different voltages to observe the behavior of ToA at different electric field strengths. The highest ToA values are observed near the edges of the pixels where the p^+ columns are present, having minimum or almost no electric field, while the lowest ToA values are observed near the central n^+ column, where the electric field is maximum.

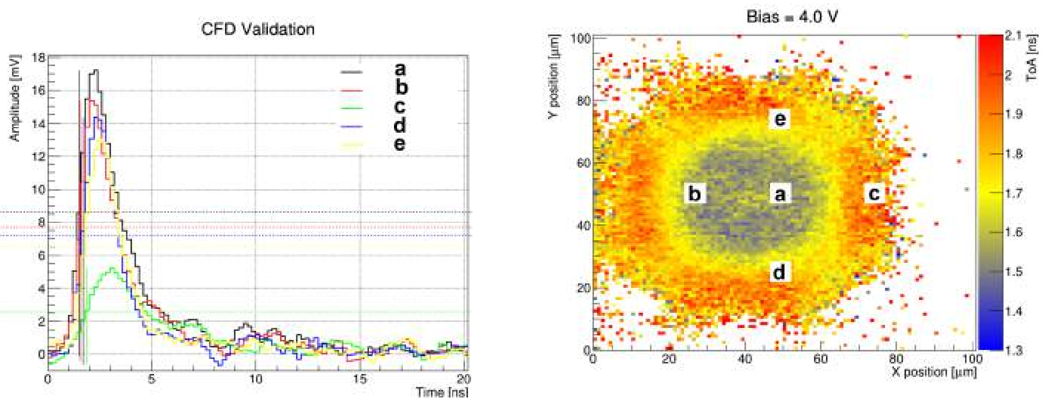

(a) (b)

Figure 6.15: (a) Waveforms plotted from different pixel positions of the 1-X device. Dotted and solid lines represent the CFD of 50% threshold. (b) ToA 2D map of 1-X device showing the positions.

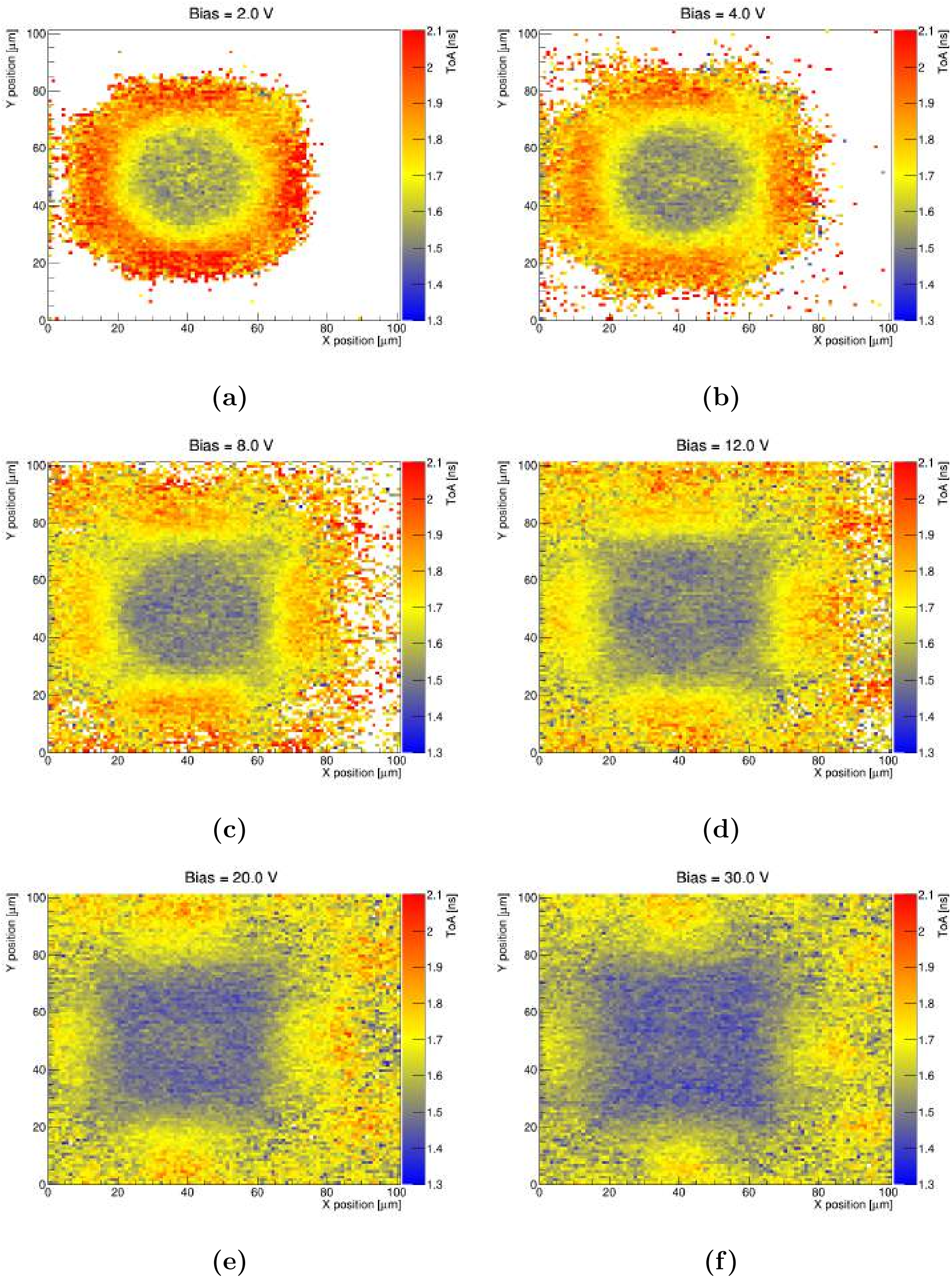

Figure 6.16: ToA 2D maps obtained from the back side of the 1-X devices showing spread of the ToA across the pixel at (a) 2 V, (b) 4 V, (c) 8 V, (d) 12 V, (e) 20 V, and (f) 30 V.

Similar to the 2-X device, one-dimensional ToA distribution for 1-X device is shown in Figure 6.17. The MAD values show a spread of $\sim$ 110 ps across the pixel for square geometry at 20 V, as shown in Figure 6.17a. The evolution of MAD values as a function of increasing electric field is shown in Figure 6.17b. A rapid decrease in the spread is observed up to 6 V. After that, the decrease in MAD values becomes less steep and follows a linear behavior up to 30 V. The lowest MAD value is seen for 30 V, which is $\sim$ 67 ps.

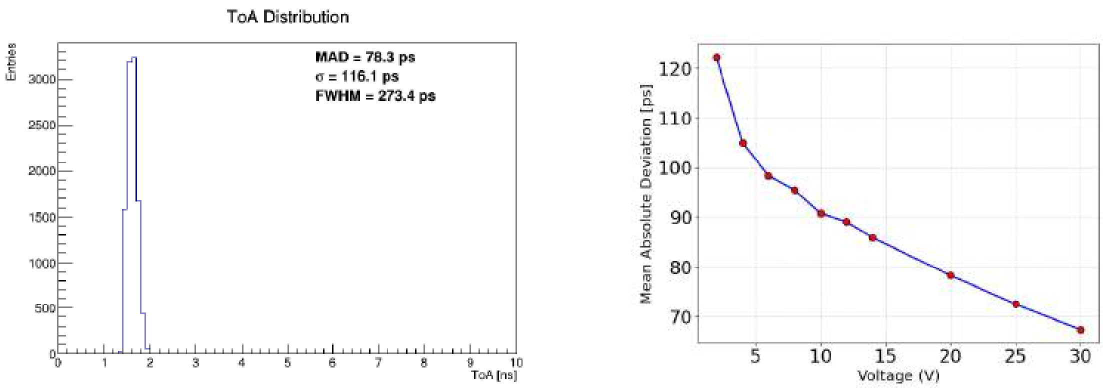

(a) (b)

Figure 6.17: (a) Spread of the ToA values for square geometry (1-X) at 20 V. (b) Evolution of the MAD values as a function of increasing bias voltage.

6.6 Summary

The fabrication of the double-sided 3D column detectors for timing applications was performed at CNM with two pixel geometries: hexagonal (2-X) and square (1-X). The IV curves show that hexagonal pixels have lower leakage current and breakdown later as compared to square pixels. Hexagonal pixels also produce larger signals, resulting in greater charge collection, as compared to square pixels. Interestingly, the timing behavior differs between the two pixel designs. Square pixels demonstrate a more consistent and less dispersed ToA distribution (from MAD analysis), whereas hexagonal pixels show a broader spread.

At 30V, the squared pixels reveal a ToA spread of 67 ps, while for the hexagonal pixels it is 94.5 ps. One important difference between the two designs is the distance between the n^+ and p^+ columns. In the hexagonal geometry, this distance is larger. This leads to a weaker electric field in some regions between the columns. As a result, charge carriers drift more slowly, and their collection time becomes more dependent on the exact position of generation. This explains the larger spread in ToA observed for the hexagonal pixels.

Chapter 7

Summary and Conclusions

Every result here is a small defiance of chaos — a reminder that nature, even in its complexity, carries a rhythm.

This thesis focuses on the development and characterization of advanced silicon detectors for precise timing and tracking in high-energy physics experiments. The motivation comes from the growing demands of future facilities such as the HL-LHC and other next-generation colliders like the FCC, where detectors must combine excellent spatial resolution, fast timing performance, and strong radiation tolerance. The work addresses these challenges by studying Low Gain Avalanche Diodes (LGADs), trench-isolated LGADs (TI-LGADs), and 3D silicon detectors.

The first part of the thesis investigates radiation effects in LGADs. A detailed gain layer degradation study was performed on devices fabricated by HPK and CNM. The sensors were irradiated with neutrons and high-energy protons to evaluate the impact of different particle types. The results show that proton irradiation causes stronger degradation of the gain layer compared to neutrons when normalized to 1 MeV neutron equivalent fluence. In addition, the gain layer design plays a key role in radiation tolerance, as CNM devices show higher acceptor removal constants than HPK devices. These results highlight the importance of gain layer engineering for long-term operation in harsh radiation environments.

The thesis then studies ultra-thin LGADs with thicknesses of 20 μm and 30 μm for timing applications. Before irradiation, the devices show low leakage current and stable electrical behavior. Gains in the range of 20–25 are achieved close to the breakdown voltage. After irradiation with protons, an increase in leakage current and a gain reduction are observed, as expected. The sensors maintain good timing performance, achieving time resolutions of about 50 ps before irradiation, and degrade after the irradiation. The results confirm that thin LGADs produced by BNL are promising candidates for precision timing in moderate radiation environments.

A major part of the work focuses on improving the fill factor of segmented LGADs. Standard LGADs suffer from inactive regions between pixels, which reduce detection efficiency. To overcome this limitation, trench-isolated LGADs (TI-LGADs) were developed and characterized. Two fabrication batches were studied. The first batch shows stable operation, low leakage current, and no premature breakdown up to high bias voltages. Laser measurements demonstrate a strong reduction of the inter-pixel dead region from 50–70 μm in standard LGADs to less than 10 μm in TI-LGADs. This represents a clear improvement in fill factor and supports fine segmentation. Detailed SPA-TCT and TPA-TCT measurements provide insight into charge transport and electric field distribution. The results show that the effective inactive region depends not only on geometry but also on electric field strength, gain layer doping, and interaction depth. The second batch shows improved isolation but early breakdown effects, which will guide future design improvements.

The final technical part of the thesis investigates double-sided 3D column detectors for timing applications. Two pixel geometries, square and hexagonal, were studied. Electrical measurements show that hexagonal pixels have lower leakage current and higher collected charge. However, timing studies reveal that square pixels provide a more uniform ToA response. The ToA spread is 67 ps for square pixels and 94.5 ps for hexagonal pixels at 30 V. The difference is explained by the larger electrode spacing in the hexagonal design, which leads to weaker electric fields and stronger position dependence of charge collection time. These results show that pixel geometry strongly affects timing performance and must be carefully optimized for 4D tracking.

Overall, this thesis provides a systematic study of timing performance as a unifying metric. It begins with understanding gain degradation under irradiation, continues with establishing operating points for thin LGADs, advances to trench isolation for improved segmentation, and finally explores 3D detectors as an alternative technology for extreme radiation environments. The work demonstrates that both LGAD-based and 3D detector technologies have strong potential for future high-luminosity experiments, provided that geometry, doping, and operating conditions are carefully optimized.

The work carried out in this PhD was not limited to experimental measurements and data analysis. A major part of the effort was dedicated to the development and commissioning of the detector characterization laboratory at AGH University of Krakow. This included the setup and optimization of TCT systems, implementation of measurement procedures, and establishment of reliable analysis methods. The laboratory has become an active center for silicon detector research.

In addition, strong international collaborations were built and strengthened with institutes such as CERN, CNM Barcelona, the University of Glasgow, IFJ Krakow, BNL, and ELI Beamlines. The author actively participated in joint measurement campaigns, internships, test beams, and collaborative R&D projects. Through these activities, the institute gained visibility and recognition within the international detector community.

Bibliography

[1] G. Charpak and F. Sauli, *High-resolution electronic particle detectors*, Annu. Rev. Nucl. Part. Sci. **34** (1984), no. CERN-EP-84-35 285.

[2] ATLAS Collaboration, *ATLAS prepares for High-Luminosity LHC*, `https://atlas.cern/Updates/News/ATLAS-Prepares-HLLHC`.

[3] *The Large Hadron Collider Experiment*, `https://home.cern/science/accelerators/large-hadron-collider`.

[4] J. Pinol Bel, *The High-Granularity Timing Detector for ATLAS at HL-LHC*, tech. rep., ATL-COM-HGTD-2024-039, 2025. doi: 10.3390/particles8020036.

[5] F. Cossutti, *Precision Timing with the CMS MIP Timing Detector for High-Luminosity LHC*, tech. rep., 2024. doi: 10.1088/1742-6596/1162/1/012035.

[6] R. Moriya *et al.*, *30 ps time resolution with 50 μm thick silicon Low Gain Avalanche Detectors fabricated by Micron Semiconductor Ltd*, Nuclear Instruments and Methods in Physics Research Section A: Accelerators, Spectrometers, Detectors and Associated Equipment **1080** (2025) 170775.

[7] V. Hinger *et al.*, *Resolving soft X-ray photons with a high-rate hybrid pixel detector*, Frontiers in Physics **12** (2024) 1352134.

[8] T. Poikela *et al.*, *Timepix3: a 65K channel hybrid pixel readout chip with simultaneous ToA/ToT and sparse readout*, Journal of instrumentation **9** (2014), no. 05 C05013.

[9] J. Fink, E. Schierle, E. Weschke, and J. Geck, *Resonant elastic soft X-ray scattering*, Reports on Progress in Physics **76** (2013), no. 5 056502.

[10] A. P. Hitchcock, *Soft X-ray spectromicroscopy and ptychography*, Journal of Electron Spectroscopy and Related Phenomena **200** (2015) 49.

[11] G. Paternoster *et al.*, *Trench-isolated low gain avalanche diodes (TI-LGADs)*, IEEE Electron Device Letters **41** (2020), no. 6 884.

[12] LHCb Collaboration, *Technology developments for LHCb Upgrade II*, , CERN-LHCb-PUB-2025-002.

[13] M. Moll, *Radiation damage in silicon particle detectors: Microscopic defects and macroscopic properties*, PhD thesis, Hamburg U., 1999, https://bib-pubdb1.desy.de/record/300958/files/desy-thesis-99-040.pdf?subformat=pdfa.

[14] G. Lindström *et al.*, *Radiation hard silicon detectors—developments by the RD48 (ROSE) collaboration*, Nuclear Instruments and Methods in Physics Research Section A: Accelerators, Spectrometers, Detectors and Associated Equipment .

[15] N. Moffat, *Low gain avalanche detectors for particle physics and synchrotron applications*, PhD thesis, Glasgow U., 2020, https://theses.gla.ac.uk/81281/.

[16] S. M. Sze, *Semiconductor devices: physics and technology*, John wiley & sons, 2008. https://openlibrary.org/works/OL5474647W/Semiconductor_devices_physics_and_technology.

[17] C. Kittel and H. Kroemer, *Thermal Physics. WH Freeman*, New York (1980), https://books.google.com/books/about/Thermal_Physics.html?id=52-BOAEACAAJ.

[18] A. S. Ansari *et al.*, *Oxides and metal oxide/carbon hybrid materials for efficient photocatalytic organic pollutant removal*, Catalysts **15** (2025), no. 2 134.

[19] J. A. Villegas Dominguez, *Development of Low Gain Avalanche Detectors (LGAD) for high- and low-penetrating particles in silicon* , May, 2024. http://hdl.handle.net/10803/693186.

[20] W. Maes, K. De Meyer, and R. Van Overstraeten, *Impact ionization in silicon: A review and update*, Solid-State Electronics **33** (1990), no. 6 705.

[21] S. M. Sze, Y. Li, and K. K. Ng, *Physics of semiconductor devices*, John wiley & sons, 2021. https://onlinelibrary.wiley.com/doi/book/10.1002/0470068329.

[22] K. Thornber, *Applications of scaling to problems in high-field electronic transport*, Journal of Applied Physics **52** (1981), no. 1 279.

[23] M. Krammer, *Silicon detectors*, praktikum lecture notes, Institute of High Energy Physics (HEPHY), Vienna, 2010-2011. https://particles.ipm.ac.ir/conferences/DetectorSchool2011/lectures/Thomas2.pdf.

[24] A. Sinha, *Built-in voltage of a silicon pn junction having a heavily doped region*, Journal of applied physics **55** (1984), no. 2 460.

[25] M. D. L. Hanlon, *The development of p-type silicon detectors for the High Radiation Regions of the LHC*, , https://livrepository.liverpool.ac.uk/3188334/.

[26] E. Cavallaro, *Novel silicon detector technologies for the HL-LHC ATLAS upgrade*, 2019. https://ddd.uab.cat/record/207901.

[27] L. Rossi, P. Fischer, T. Rohe, and N. Wermes, *Pixel detectors: From fundamentals to applications*, Springer, 2006. https://link.springer.com/book/10.1007/3-540-28333-1.

[28] D. McGregor and J. K. Shultis, *Radiation detection: concepts, methods, and devices*, CRC Press, 2020. https://www.routledge.com/Radiation-Detection-Concepts-Methods-and-Devices/McGregor-Shultis/p/book/9781439819395.

[29] M. Wiehe *et al.*, *Development of a tabletop setup for the transient current technique using two-photon absorption in silicon particle detectors*, IEEE Transactions on Nuclear Science **68** (2020), no. 2 220.

[30] S. Ramo, *Currents induced by electron motion*, Proceedings of the IRE **27** (2006), no. 9 584.

[31] F. Hartmann, *Evolution of silicon sensor technology in particle physics*, vol. 43, Springer, 2009. https://link.springer.com/book/10.1007/978-3-319-64436-3.

[32] F. Ravotti, *Development and Characterisation of Radiation Monitoring Sensors for the High Energy Physics Experiments of the CERN LHC Accelerator*, cern-thesis-2007-013, Université Montpellier II, 2006, https://repository.cern/legacy/record/1014776.

[33] D. Pitzl *et al.*, *Type inversion in silicon detectors*, Nuclear Instruments and Methods in Physics Research Section A: Accelerators, Spectrometers, Detectors and Associated Equipment **311** (1992), no. 1 98.

[34] R. Wunstorf *et al.*, *Investigations of donor and acceptor removal and long term annealing in silicon with different boron/phosphorus ratios*, Nuclear Instruments and Methods in Physics Research Section A: Accelerators, Spectrometers, Detectors and Associated Equipment **377** (1996), no. 2-3 228.

[35] J. C. Lange, *Differential Top-Quark-Pair Cross Sections in pp Collisions at $\sqrt{s} = 7$ TeV with CMS and Charge Multiplication in Highly-Irradiated Silicon Sensors* , May, 2013. https://bib-pubdb1.desy.de/record/154110/files/DESY-2013-00813.pdf.

[36] G. Kramberger *et al.*, *Determination of effective trapping times for electrons and holes in irradiated silicon*, Nuclear Instruments and Methods in Physics Research Section A: Accelerators, Spectrometers, Detectors and Associated Equipment **476** (2002), no. 3 645.

[37] V. Cindro *et al.*, *Readout of non-irradiated and irradiated strip detectors with fast analogue electronics*, Nuclear Instruments and Methods in Physics Research Section A: Accelerators, Spectrometers, Detectors and Associated Equipment **439** (2000), no. 2-3 337.

[38] J. Kemmer, *Fabrication of low noise silicon radiation detectors by the planar process*, Nuclear Instruments and Methods **169** (1980), no. 3 499.

[39] A. Vacchi *et al.*, *Performance of the UA6 large-area silicon drift chamber prototype*, Nuclear Instruments and Methods in Physics Research Section A: Accelerators, Spectrometers, Detectors and Associated Equipment **306** (1991), no. 1-2 187.

[40] G. Pellegrini *et al.*, *Technology developments and first measurements of Low Gain Avalanche Detectors (LGAD) for high energy physics applications*, Nuclear Instruments and Methods in Physics Research Section A: Accelerators, Spectrometers, Detectors and Associated Equipment **765** (2014) 12.

[41] M. Casado, A. H. Group *et al.*, *A high-granularity timing detector for the ATLAS phase-II upgrade*, Nuclear Instruments and Methods in Physics Research Section A: Accelerators, Spectrometers, Detectors and Associated Equipment, https://doi.org/10.1016/j.nima.2022.166628.

[42] M. Carulla *et al.*, *50 μm thin Low Gain Avalanche Detectors (LGAD) for timing applications*, Nuclear Instruments and Methods in Physics Research Section A: Accelerators, Spectrometers, Detectors and Associated Equipment **924** (2019) 373.

[43] V. Sola *et al.*, *First FBK production of 50 μm ultra-fast silicon detectors*, Nuclear Instruments and Methods in Physics Research Section A: Accelerators, Spectrometers, Detectors and Associated Equipment **924** (2019) 360.

[44] N. Moffat *et al.*, *Low Gain Avalanche Detectors (LGAD) for particle physics and synchrotron applications*, Journal of Instrumentation **13** (2018), no. 03 C03014.

[45] W. Krüger *et al.*, *LGAD technology for HADES, accelerator and medical applications*, Nuclear Instruments and Methods in Physics Research Section A: Accelerators, Spectrometers, Detectors and Associated Equipment **1039** (2022) 167046.

[46] C. Royon and F. Gautier, *Fast timing detectors with applications in cosmic ray physics and medical science*, Nuclear Instruments and Methods in Physics Research Section A: Accelerators, Spectrometers, Detectors and Associated Equipment **1058** (2024) 168886.

[47] N. Cartiglia *et al.*, *Tracking in 4 dimensions*, Nuclear Instruments and Methods in Physics Research Section A: Accelerators, Spectrometers, Detectors and Associated Equipment **845** (2017) 47.

[48] H. F. Sadrozinski, A. Seiden, and N. Cartiglia, *4D tracking with ultra-fast silicon detectors*, Reports on Progress in Physics **81** (2017), no. 2 026101.

[49] P. Fernández-Martínez *et al.*, *Design and fabrication of an optimum peripheral region for low gain avalanche detectors*, Nuclear Instruments and Methods in Physics Research Section A: Accelerators, Spectrometers, Detectors and Associated Equipment **821** (2016) 93.

[50] N. Moffat and R. Bates, *Simulation of the small pixel effect contributing to a low fill factor for pixellated Low Gain Avalanche Detectors (LGAD)*, Nuclear Instruments and Methods in Physics Research Section A: Accelerators, Spectrometers, Detectors and Associated Equipment **1018** (2021) 165746.

[51] G. Pellegrini *et al.*, *Recent technological developments on LGAD and iLGAD detectors for tracking and timing applications*, Nuclear Instruments and Methods in Physics Research Section A: Accelerators, Spectrometers, Detectors and Associated Equipment **831** (2016) 24.

[52] E. Currás *et al.*, *Inverse low gain avalanche detectors (iLGADs) for precise tracking and timing applications*, Nuclear Instruments and Methods in Physics Research

Section A: Accelerators, Spectrometers, Detectors and Associated Equipment **958** (2020) 162545.

[53] G. Giacomini, W. Chen, G. D'Amen, and A. Tricoli, *Fabrication and performance of AC-coupled LGADs*, Journal of Instrumentation **14** (2019), no. 09 P09004.

[54] G. D'Amen *et al.*, *Measurements of time and spatial resolution of AC-LGADs with different designs*, Journal of Instrumentation **17** (2022), no. 08 C08007.

[55] S. Ayyoub *et al.*, *A new approach to achieving high granularity for silicon diode detectors with impact ionization gain*, , 10.1088/1742-6596/2374/1/012171.

[56] A. Tournier *et al.*, *Pixel-to-pixel isolation by deep trench technology: application to CMOS image sensor*, in *Proc. Int. image sensor workshop*, pp. 12–15, 2011. doi: 10.60928/w9fx-zmiy.

[57] C. Piemonte *et al.*, *Performance of NUV-HD Silicon Photomultiplier Technology*, IEEE Transactions on Electron Devices **63** (2016), no. 3 1111.

[58] X. Cai *et al.*, *Vertical 4h-SiC nipn APDs with partial trench isolation*, IEEE Photonics Technology Letters **30** (2018), no. 9 805.

[59] G. Paternoster *et al.*, *Novel strategies for fine-segmented low gain avalanche diodes*, Nuclear Instruments and Methods in Physics Research Section A: Accelerators, Spectrometers, Detectors and Associated Equipment **987** (2021) 164840.

[60] M. Senger *et al.*, *A comprehensive characterization of the TI-LGAD technology*, Sensors **23** (2023), no. 13 6225.

[61] A. Bisht *et al.*, *Characterization of novel trench-isolated LGADs for 4D tracking*, Nuclear Instruments and Methods in Physics Research Section A: Accelerators, Spectrometers, Detectors and Associated Equipment **1048** (2023) 167929.

[62] S. I. Parker, C. J. Kenney, and J. Segal, *3D—a proposed new architecture for solid-state radiation detectors*, Nuclear Instruments and Methods in Physics Research Section A: Accelerators, Spectrometers, Detectors and Associated Equipment **395** (1997), no. 3 328.

[63] H. V. Jansen *et al.*, *Black silicon method X: a review on high speed and selective plasma etching of silicon with profile control: an in-depth comparison between Bosch and cryostat DRIE processes as a roadmap to next generation equipment*, Journal of micromechanics and microengineering **19** (2009), no. 3 033001.

[64] K. Wang *et al.*, *Design and simulation of a novel 4H-SiC LGAD timing device*, Radiation Detection Technology and Methods **8** (2024), no. 2 1140.

[65] C. Jain *et al.*, *Modelling the effect of neutron damage on low-gain avalanche detectors.*, Acta Physica Polonica: A **146** (2024), no. 5 .

[66] J. Alda, *Laser and Gaussian beam propagation and transformation*, Encyclopedia of optical engineering **999** (2003) 1013.

[67] M. Milovanović, *Electric field and charge multiplication in radiation-damaged silicon detectors*, PhD thesis, University of Ljubljana, 2016, https://repozitorij.uni-lj.si/IzpisGradiva.php?id=83819.

[68] I. Abt *et al.*, *Characterization of silicon microstrip detectors using an infrared laser system*, Nuclear Instruments and Methods in Physics Research Section A: Accelerators, Spectrometers, Detectors and Associated Equipment **423** (1999), no. 2-3 303.

[69] E. Belau *et al.*, *Charge collection in silicon strip detectors*, Nuclear Instruments and Methods in Physics Research **214** (1983), no. 2-3 253.

[70] Particulars. *Large scanning TCT*, "https://www.particulars.si/products.php?prod=LargeScanTCT.html", 2015. Accessed: 2025-12-20.

[71] Ò. Ferrer Naval, *Radiation Hard Timing 3D Detectors for Future Colliders*, PhD thesis, Universitat Autonoma de Barcelona, 2024, https://ddd.uab.cat/pub/tesis/2024/hdl_10803_692821/odfn1de1.pdf.

[72] M. Goppert-Mayer, *Über elementarakte mit zwei quantensprüngen*, Annalen der Physik **401** (1931), no. 3 273.

[73] W. Kaiser and C. Garrett, *Two-photon excitation in CaF_2: Eu^{2+}*, Physical review letters **7** (1961), no. 6 229.

[74] E. Ejopu, *Advancing Solid-State Sensor Technology For the Next-Generation LHCb Detector With Two-Photon Absorption*, PhD thesis, The University of Manchester (United Kingdom), 2025, https://research.manchester.ac.uk/en/studentTheses/advancing-solid-state-sensor-technology-for-the-next-generation-l/.

[75] ELI, *Time-resolved Spectroscopic Ellipsometry (trELIps) and Transient Current Technique (TCT) using the Coherent Astrella laser*, "https://up.eli-laser.eu/equipment/trelips-tct-561971438". Accessed: 2025-12-23.

[76] G. Laštovička-Medin *et al.*, *Femtosecond laser studies of the single event effects in low gain avalanche detectors and pins at ELI beamlines*, Nuclear Instruments and Methods in Physics Research Section A: Accelerators, Spectrometers, Detectors and Associated Equipment **1041** (2022) 167321.

[77] G. Medin, *TPA/SPA SET UP AT ELI BEAMLINES*, PowerPoint Presentation, November, 2020. https://indico.cern.ch/event/896954/contributions/4106493/attachments/2146181/3621008/TCT%20setup%20at%20ELI%20Beamlines-GM.pdf.

[78] M. O. Wiehe, *Development of a two-photon absorption-TCT system and study of radiation damage in silicon detectors*, PhD thesis, Austrian Academy of Sciences (AT), 2021, https://repository.cern/records/0babt-1xj88/files/CERN-THESIS-2021-225.pdf.

[79] ATLAS Collaboration, *Technical Design Report: A High-Granularity Timing Detector for the ATLAS Phase-II Upgrade*, tech. rep., CERN, Geneva, 2020. CERN-LHCC-2020-007.

[80] CMS Collaboration, *A MIP Timing Detector for the CMS Phase-2 Upgrade*, tech. rep., CERN, Geneva, 2019. CERN-LHCC-2019-003.

[81] M. Moll, *SISSA: Acceptor removal-Displacement damage effects involving the shallow acceptor doping of p-type silicon devices*, PoS (2020) 027.

[82] P. Allport *et al.*, *Experimental determination of proton hardness factors at several irradiation facilities*, Journal of Instrumentation **14** (2019) P12004.

[83] S. Otero Ugobono, *Characterisation and optimisation of radiation- tolerant silicon sensors with intrinsic gain*, Nov., 2018. https://repository.cern/records/jfsqq-xfc25/files/CERN-THESIS-2018-264.pdf.

[84] G. Kramberger *et al.*, *Radiation effects in Low Gain Avalanche Detectors after hadron irradiations*, Journal of Instrumentation **10** (2015) P07006.

[85] E. Currás, *Low Gain Avalanche Detectors for 4-dimensional Tracking Applications in Severe Radiation Environments*, Proc. 29th Int. Workshop on Vertex Detectors (VERTEX2020) (2020) .

[86] Y. Feng *et al.*, *Study of the Acceptor Removal Effect of LGAD*, IEEE Transactions on Nuclear Science **69** (2022), no. 12 2324.

[87] Y. Jin *et al.*, *Experimental Study of Acceptor Removal in UFSD*, Nuclear Instruments and Methods in Physics Research Section A: Accelerators, Spectrometers, Detectors and Associated Equipment **983** (2020) 164611.

[88] A. Howard *et al.*, *LGAD measurements from different producers*, in *37th RD50 Workshop, Zagreb*, 2020. https://indico.cern.ch/event/896954/contributions/4106306/attachments/2146559/3618285/AHoward_RD50_Nov2020_ProducersComparison.pdf.

[89] E. Currás *et al.*, *Timing performance and gain degradation after irradiation with protons and neutrons of Low Gain Avalanche Diodes based on a shallow and broad multiplication layer in a float-zone 35 µm and 50 µm thick silicon substrate*, Nuclear Instruments and Methods in Physics Research Section A: Accelerators, Spectrometers, Detectors and Associated Equipment **1055** (2023) 168522.

[90] E. Gkougkousis, *Acceptor removal - Radiation Hardness and breakdown*, in *36th RD50 Workshop, Geneva*, 2020. https://indico.cern.ch/event/918298/contributions/3880598/attachments/2050927/3438310/RD50_2020_Gkougkousis.pdf.

[91] X. Li, *Advanced silicon tracking detector developments for the future electron-ion collider*, Nuclear Instruments and Methods in Physics Research Section A: Accelerators, Spectrometers, Detectors and Associated Equipment **1057** (2023) 168687.

[92] G. Giacomini, M. Boukhicha, and T. Tsang, *Optical characterization of low-gain avalanche diodes*, doi: 10.1109/NSS/MIC/RTSD57106.2025.11287424.

[93] H. Spieler, *Semiconductor detector systems*, vol. 12, Oxford university press, 2005. https://global.oup.com/academic/product/semiconductor-detector-systems-9780198570737.

[94] V. Kraus *et al.*, *Studies on the effect of low-fluence proton and neutron irradiation on n-type LGADs*, Nuclear Instruments and Methods in Physics Research Section A: Accelerators, Spectrometers, Detectors and Associated Equipment (2025) 171138.

[95] E. Currás, M. Fernández, and M. Moll, *Gain reduction mechanism observed in low gain avalanche diodes*, Nuclear Instruments and Methods in Physics Research Section A: Accelerators, Spectrometers, Detectors and Associated Equipment **1031** (2022) 166530.

[96] E. C. Rivera, A. La Rosa, M. Moll, and F. Zareef, *Gain layer degradation study after neutron and proton irradiations in low gain avalanche diodes*, Journal of Instrumentation **18** (2023), no. 10 P10020.

[97] M. Ferrero *et al.*, *An Introduction to Ultra-Fast Silicon Detectors*, CRC press, 2021. `https://www.routledge.com/An-Introduction-to-Ultra-Fast-Silicon-Detectors/Lucchini-Dinardo/p/book/9780367379534`.

[98] F. Zareef *et al.*, *Achieving near 100% fill factor for small pixel LGADs: Study of first trench isolated LGADs fabricated at Micron Semiconductor Ltd*, Journal of Instrumentation **20** (2025), no. 07 P07037.

[99] E. H. Klaassen *et al.*, *Silicon Fusion Bonding and Deep Reactive Ion Etching a New Technology for Microstructures*, in *Proceedings of the International Solid-State Sensors and Actuators Conference - TRANSDUCERS '95*, vol. 1, pp. 556–559, 1995. doi: 10.1109/SENSOR.1995.717285.

[100] T.-E. Hansen *et al.*, *First fabrication of full 3D-detectors at SINTEF*, Journal of Instrumentation **4** (2009) P03010.

[101] T. Poikela *et al.*, *Timepix3: a 65K channel hybrid pixel readout chip with simultaneous ToA/ToT and sparse readout*, Journal of Instrumentation **9** (2014) C05013.

[102] M. Senger, *Chubut 2: Readout board for LGADs*, `"https://sengerm.github.io/Chubut_2/doc/testing/index.html"`, 2023. Accessed: 2025-06-04.

[103] S. Pape, E. Currás, M. Fernández García, and M. Moll, *Techniques for the investigation of segmented sensors using the two photon absorption-transient current technique*, Sensors **23** (2023), no. 2 962.

[104] P. D. Ngo, *Energy dispersive spectroscopy*, in *Failure analysis of integrated circuits: Tools and techniques*, pp. 205–215. Springer, 1999. https://link.springer.com/chapter/10.1007/978-1-4615-4919-2_12.

[105] O. Breitenstein, W. Warta, and M. C. Schubert, *Lock-in thermography: Basics and use for evaluating electronic devices and materials*, vol. 10, Springer, 2019. https://link.springer.com/book/10.1007/978-3-319-99825-1.

[106] J. Leon *et al.*, *Local non invasive study of SiC diodes with abnormal electrical behavior*, Solid-State Electronics **113** (2015) 35.

[107] J. Lange *et al.*, *Radiation hardness of small-pitch 3D pixel sensors up to a fluence of* $3{\times}10^{16}$ n_{eq}/cm^2, Journal of Instrumentation **13** (2018), no. 09 P09009.

[108] A. Loi, A. Contu, and A. Lai, *Timing optimisation and analysis in the design of 3D silicon sensors: the TCoDe simulator*, Journal of Instrumentation **16** (2021), no. 02 P02011.

[109] C. Da Via *et al.*, *3d silicon sensors: Design, large area production and quality assurance for the atlas ibl pixel detector upgrade*, Nuclear Instruments and Methods in Physics Research Section A: Accelerators, Spectrometers, Detectors and Associated Equipment **694** (2012) 321.

[110] C. Lasaosa *et al.*, *The influence of pixel cell layout on the timing performance of 3D sensors*, Journal of Instrumentation **20** (2025), no. 06 C06080.

List of Figures

List of Tables